PHYSICAL MODELLING OF LEADING EDGE CAVITATION: COMPUTATIONAL METHODOLOGIES AND APPLICATION TO HYDRAULIC MACHINERY

THÈSE N^{O} 3353 (2005)

PRÉSENTÉE À LA FACULTÉ SCIENCES ET TECHNIQUES DE L'INGÉNIEUR

Institut des sciences de l'énergie

SECTION DE GÉNIE MÉCANIQUE

ÉCOLE POLYTECHNIQUE FÉDÉRALE DE LAUSANNE

POUR L'OBTENTION DU GRADE DE DOCTEUR ÈS SCIENCES

PAR

Youcef AIT BOUZIAD

Ingénieur d'état en hydraulique, Ecole nationale polytechnique d'Alger, Algérie
DEA de conversion de l'énergie, Université Paris VI, France
et de nationalité algérienne

acceptée sur proposition du jury:

Prof. F. Avellan, Dr M. Farhat, directeurs de thèse
Prof. J.-L. Kueny, rapporteur
Prof. A. Pasquarello, rapporteur
Dr G. Scheuerer, rapporteur
Prof. R. Susan-Resiga, rapporteur

Lausanne, EPFL
2006

A mes chers parents
$\mathcal{E}$ Yemma, $\mathcal{E}$ Vava ...

Remerciements

Je tiens à adresser mes plus sincères remerciements à toutes les personnes qui ont été impliquées de près ou de loin dans ce travail de quatre ans au laboratoire.

Que tous les membres du jury soient remerciés pour leur intérêt, leurs critiques enrichissantes et l'attention qu'ils ont portés à ce travail.

Mes premiers égards vont tout naturellement au Professeur François Avellan, directeur de thèse, pour sa confiance en me permettant d'effectuer ce travail au sein du Laboratoire de Machines Hydrauliques. Son soutien, son implication personnelle ainsi que ses conseils ont été un gage de réussite.

Tous mes remerciements vont au Docteur Mohamed Farhat, codirecteur de thèse et responsable du groupe cavitation, pour son enthousiasme, son implication et sa grande disponibilité.

Une attention particulière au Professeur Jean-Louis Kueny, au Professeur Roméo Susan-Resiga et à Alex Guedes, pour leur contribution et leur disponibilité.

La réalisation de ce travail n'aurait pu être possible sans l'appui scientifique et financier du Fond National Suisse et de Mitsubishi Heavy Industry. A ce titre, je remercie M. Kazuyoshi Miyagawa et toute son équipe pour leur implication dans le projet.

Mes remerciements vont à l'ensemble des membres du LMH, pour leur sympathie et leur soutient. Je remercie Isabelle, Maria, Anne, Shadje, Louis et toute l'équipe des mécaniciens, Philippe et le bureau d'études ainsi que Henri-Pascal et le groupe GEM. Je remercie également les anciens et les nouveaux doctorants et assistants pour l'ambiance qu'ils ont su instaurer au sein du laboratoire: Coutix, Sebastiano, Jorge, Bartu, Gabi, Tino, Azzdin, Stefan, Monica, Lavinia, Georgiana, Silvia, et tous les oubliés.

Durant ces années, j'ai eu l'occasion de rencontrer des personnes aussi exceptionnelles les unes que les autres, qui m'ont toujours aidé et soutenu. Je remercie infiniment Sonia pour son aide, ses encouragements et sa patience. Je remercie Faiçal, Lluis, Christophe et Ali pour leurs conseils, et leur bonne humeur, ainsi qu'Alexandre, Philippe et Olivier pour leur aide et leur soutient.

Enfin, je tiens à exprimer ma profonde gratitude à ma famille. Je vous serai éternellement reconnaissant, toi Yemma pour ton attention et ton dévouement, toi Vava pour m'avoir toujours soutenu et encouragé. Un grand merci à Karim, Kahina et Larvi ainsi qu'à Krimo, Hakima et Anis pour tout ce qu'ils m'apportent dans la vie.

Résumé

La cavitation est l'un des phénomènes physiques les plus contraignants en ce qui concerne les performances des machines hydrauliques. A cet effet, il est primordial de savoir prédire son apparition, son développement ainsi que de fixer un seuil des pertes de performances qui lui sont associées.

Les modèles de prédiction, basés sur des simulations numériques, sont généralement dédiés à la reproduction des propriétés globales de l'écoulement résultant, l'intérêt étant de prédire l'apparition et le développement de la cavité. Dans la présente étude, différents modèles sont évalués et des méthodes adaptées aux zones de détachement et de fermeture de la cavité sont proposées. Un cas concret industriel est étudié afin d'analyser, en régime de cavitation, les mécanismes à l'origine de la chute des performances dans les machines hydrauliques.

Différents modèles de simulation des écoulements en régime de cavitation sont évalués dans le cas d'un profil hydraulique bidimensionnel. Un modèle monophasique à suivi d'interface, un modèle multiphasique à équation d'état, ainsi qu'un modèle multiphasique à équation de transport sont comparés en terme de prédiction du coefficient d'apparition de la cavitation, de son développement, de la distribution de pression correspondante sur le profil, ainsi que du champ de vitesse de l'écoulement résultant.

Une approche originale basée sur une formulation des contraintes locales est introduite. Le seuil classique d'apparition de la cavitation, basé sur la pression statique, est corrigé par la composante non isotrope des contraintes de cisaillement, composante prise en compte par le concept de la contrainte maximale de traction. Cette dernière, formulée en terme de taux des contraintes de cisaillement, est introduite dans les calculs CFD et validée par des calculs de couche limite sur une géométrie de type parabolique. Cette approche, testée dans le cas d'un profil hydraulique, s'avère prometteuse par la prise en compte des effets de Reynolds et des effets de rugosité de surface, tels qu'observés expérimentalement.

Le modèle multiphasique à équation de transport est testé dans le cas d'un régime de cavitation instationnaire caractérisé par une instabilité de type jet rentrant conduisant à des lâchers cycliques de cavités transitoires. Une comparaison entre différents modèles de turbulence démontre que les modèles classiques à 2 équations ne parviennent pas à reproduire ce phénomène. L'utilisation de modèles plus adaptés tels que des modèles de type LES, ou par la modification de la viscosité effective du mélange liquide-vapeur conduisent à la prédiction de lâchers de cavités en régime instationnaire. Les fréquences de lâchers sont validées expérimentalement démontrant que le phénomène modélisé obéit à la loi de Strouhal.

Finalement, le modèle est utilisé dans le cas d'un inducteur en régime de cavitation. Les résultats obtenus concernant la topologie de la poche de cavitation et des pertes

des performances concordent avec les résultats expérimentaux. Une analyse des transferts énergétiques dans la machine ainsi qu'une analyse de l'effet de la cavitation sur l'écoulement global mettent en évidence l'origine des pertes. Ces pertes sont principalement dues à la réduction du couple fourni et aux pertes additives induites par la désorganisation de l'écoulement due à la présence de la poche. Ces deux phénomènes sont observés successivement lorsque la cavitation de bord d'attaque atteint le niveau du col de la machine introduisant des changements importants dans la structure de l'écoulement.

Abstract

Cavitation is usually the main physical phenomenon behind performance alterations in hydraulic machinery. For this reason, it is crucial to accurately predict its inception and development and to highlight a comprehensive relation between the cavitation development and the performances drop associated.

The common cavitation models, based on numerical flow simulations, are intended to reproduce the general cavitation behavior, and their major focus is the cavitation onset and developed cavity shape prediction. In the present study, various methods in cavitation modelling are investigated. Specific computational methods are outlined for the two sensitive zones of cavity detachment and closure. Finally, an industrial case is investigated in order to highlight the mechanisms of head drop phenomenon in hydraulic machines.

Current modelling techniques are reviewed together with physical arguments concerning the cavitation phenomenon, and a 2D hydrofoil test case is used to evaluate the models. A mono-fluid interface tracking model, a multiphase state-equation based model, and a multiphase transport-equation based model are discussed in terms of reproducing the cavitation flow characteristics as the cavitation inception, development, pressure distribution and velocity profiles in cavitation regimes.

An innovative approach based on the local stress formulation is proposed. The non-viscous anisotropic stress is taken into account through the maximum tensile stress criterion for cavitation inception instead of the classical pressure threshold. The maximum tensile stress criterion, formulated using the shear strain rate formulation is used for CFD computations. The method is evaluated with the case of a parabolic nose leading edge flow with comparison to the boundary layer computations. The developed model is tested in the case of a 2D hydrofoil in both smooth and rough walls under different flow conditions. The ability of the model to take into account Reynolds and surface roughness effects, as observed in experimental investigations, is demonstrated.

A comparative study of turbulence modelling for unsteady cavitation is presented which indicates a strong correlation between the cavitation unsteadiness predictions and the turbulence modelling. The adapted techniques in reproducing the unsteady cavitation flow are found to be either using an accurate filtering turbulence model to correctly capture the large eddies, or to modify the turbulent viscosity function, and thereby introducing an artificial compressibility effect. The simulated leading edge cavitation instability, in our case, occurs at a certain cavity length where the cavity closure corresponds to the high pressure gradient region and is governed mainly by the occurrence of the reentrant jet at the cavity closure. This phenomenon is found to be periodic and the shedding frequencies matches to the Strouhal law as observed in experiments.

Finally, the multiphase mixture model is used in the case of an industrial inducer. The model provides satisfactory results for the prediction of the cavitation flow behavior and performance drop estimation for the operating points studied. An analysis based on global energy balance and local flow analysis demonstrates that the head drop is mainly caused by the lower torque generation and the hydraulic losses induced by the secondary flows. These phenomena occur when the cavity extends towards the throat region, leading to important changes in the flow structure.

Contents

Notations

Latin

a	Speed of sound: $a \simeq 1500$ m/s @ water	[m s^{-1}]
c	Chord length	[m]
c_p, c_v	Specific heat at constant pressure and temperature	[–]
f	Frequency	[Hz] [s^{-1}]
g	Gravitational acceleration: $g \simeq 9.81$ m/s^2	[m s^{-2}]
h	Static enthalpy	[m^2 s^{-2}]
i	Hydrofoil incidence angle	[$^\circ$]
k	Turbulent kinetic energy	[m^2 s^{-2}]
k_s	Surface roughness high	[m]
$\dot{m}$	Cavitation mass source term	[kg m^{-3} s^{-1}]
n	Rotational speed	[s^{-1}]
$\vec{n}$	Normal vector	[–]
p	Static pressure	[Pa]
p_t	Total pressure	[Pa]
p_v	Saturation vapor pressure: $p_v \simeq 2300$ Pa @ 20°C	[Pa]
s, n	Curvilinear coordinates	[m]
t	Time	[s]
x, y, z	Cartesian coordinates	[m]
y	Mass fraction (quality)	[–]
y^+	Dimensionless sublayer-scaled distance: $y^+ = \frac{C_\tau y}{\nu}$	[–]
A	Surface	[m^2]
C	Absolute velocity	[m s^{-1}]
C_u	Angular absolute velocity	[m s^{-1}]
C_m	Meridian absolute velocity	[m s^{-1}]
C_τ	Friction velocity: $C_\tau = \frac{\tau_w}{\rho}$	[m s^{-1}]
$\bar{\bar{D}}$	Rate of deformation tensor	[s^{-1}]
E	Specific hydraulic energy: $E = gH$	[J kg^{-1}]
E_r	Specific hydraulic energy loss	[J kg^{-1}]

E_k	Specific hydraulic kinetic energy	[J kg^{-1}]
F	Force	[N]
F^c, F^v	Vaporization and condensation factors	[–]
F, f	Complex potential (appendix B)	[m^2 s^{-1}]
F', f'	Complex velocity potential (appendix B)	[m s^{-1}]
H	Net hydraulic head	[m]
	Boundary layer shape factor: $H = \frac{\delta^*}{\theta}$	[–]
I	Rothalpy	[J kg^{-1}]
$\bar{\bar{I}}$	Identity matrix	[–]
L	Characteristic length scale	[m]
N	Rotational speed: N=60n (Hydraulic machine)	[min^{-1}]
	Bubble number density (RP model)	[m^{-3}]
$NPSE$	Net positive suction energy	[J kg^{-1}]
Q	Flow rate	[kg s^{-1}] [m^3 s^{-1}]
R	Radius	[m]
	Perfect gas constant: R=8.32	[J mol^{-1} $^\circ$K^{-1}]
$\mathcal{R}$	Curvature	[m^{-1}]
S	Surface tension: $S_{lv} = 0.0728$ N/m @ 20°C	[Nm^{-1}]
$\bar{\bar{S}}$	Deviator tensor	[s^{-1}]
T	Temperature	[$^\circ$C] [$^\circ$K]
	Period	[s]
$\vec{T}$	Impeller torque	[N m]
$\bar{\bar{T}}$	Stress tensor	[s^{-1}]
U	Peripheral velocity: $U = \omega R$	[m s^{-1}]
V	Volume	[m^3]
W	Relative speed	[m s^{-1}]

Greek

α	Volume fraction	[–]
β	Conformal mapping stagnation point parameter	[–]
δ	Boundary layer thickness	[m]
δ^*	Boundary layer displacement thickness: $\delta^* = \int_0^\delta \left(1 - \frac{C}{C_e}\right)$	[m]
ε	Turbulent dissipation rate	[m^2 s^{-3}]
	Arbitrary small value	[–]
γ	Specific heat ratio: $\gamma = \frac{c_p}{c_v}$	[–]
Γ	Mass source term	[kg m^{-3} s^{-1}]

$\dot{\gamma}$	Shear strain rate: $\dot{\gamma} = \sqrt{\bar{\bar{D}} : \bar{\bar{D}}}$	[s^{-1}]
λ	Thermal conductivity	[W m^{-1} K^{-1}]
μ_{eff}	Effective viscosity: $\mu_{\text{eff}} = \mu + \mu_t$	[kg m^{-1} s^{-1}]
μ	Dynamic (molecular) viscosity	[kg m^{-1} s^{-1}]
μ_t	Turbulent (eddy) viscosity	[kg m^{-1} s^{-1}]
ν	Kinematic viscosity: $\nu = \frac{\mu}{\rho}$	[m^2 s^{-1}]
Φ	Potential function	[m^2 s^{-1}]
Ψ	Stream function	[m^2 s^{-1}]
ρ	Density	[kg m^{-3}]
τ	Shear stress	[Pa]
θ	Boundary layer momentum thickness: $\delta^* = \int_0^\delta \frac{C}{C_e}\left(1 - \frac{C}{C_e}\right)$	[m]
ξ, η, ζ	Body (curvilinear) coordinates	[m]
$\vec{\Omega}$, ω	Rotational velocity (Hydraulic machines)	[rad s^{-1}]
ω	Specific dissipation rate (Turbulence)	[s^{-1}]

Subscripts

l, v	Liquid, vapor phase
n	n^{th} phase
g	Gas
m	Mixture
e	Boundary layer edge value
ref	Reference value
∞	Free-stream value
t	Transition, Turbulent
i, j, k	Reference to grid directions
x, y, z	Reference to cartesian directions

Superscripts

v, c	Vaporization, condensation
$*$	Referenced to the cavitation free regime
$**$	Referenced to the best efficiency (design) point

Dimensionless Numbers

C_f	Skin friction coefficient	$C_f = \frac{\tau}{\frac{1}{2}\rho C_\infty^2}$

C_p	Pressure coefficient	$C_p = \frac{p - p_\infty}{\frac{1}{2}\rho C_\infty^2}$
C_{p_t}	Total pressure coefficient	$C_{p_t} = \frac{p - p_\infty}{\rho E}$
C_D	Drag coefficient	$C_D = \frac{F_D}{\frac{1}{2}\rho C_\infty^2 A}$
C_L	Lift coefficient	$C_L = \frac{F_L}{\frac{1}{2}\rho C_\infty^2 A}$
M	Mach number	$M = \frac{C}{a}$
Pr_l	Prandtl laminar number	$Pr_l = \frac{\mu c_p}{\lambda}$
Re	Reynolds number	$Re = \frac{C_\infty L}{\nu}$
St	Strouhal number	$St = \frac{fL}{C_\infty}$
φ	Flow rate coefficient	$\varphi = \frac{Q}{\pi\omega R^3}$
ψ	Specific energy coefficient	$\psi = \frac{2E}{\omega^2 R^2}$
ψ_c	Net positive specific energy coefficient (cavitation number)	$\psi_c = \frac{2NPSE}{\omega^2 R^2}$
σ	Cavitation number (Thoma number)	$\sigma = \frac{p_\infty - p_v}{\frac{1}{2}\rho C_\infty^2}$

Abbreviations

EPFL	Ecole Polytechnique Fédérale de Lausanne
LMH	Laboratoire de Machines Hydrauliques
BL	Boundary Layer
LE	Leading Edge
NS	Navier-Stokes
RP	Rayleigh-Plesset
RANS	Reynolds Averaged Navier-Stokes
Model 1	Interface tracking model (single phase)
Model 2	State equation based model (multiphase homogeneous mixture)
Model 3	Transport equation based model (multiphase homogeneous mixture)

Introduction

The Cavitation Phenomenon

Cavitation is the formation of vapor or gas cavities within a given liquid due to pressure drop. It may be observed in various engineering systems such as hydraulic constructions, aeronautics, aerospace, power systems and turbomachinery. In the case of hydraulic machinery, modern design requirements lead to more compact machines with higher rotation speeds and higher cavitation risk. This makes cavitation an important issue in turbomachinery design and operation, which should be controlled, or at least well understood.

The cavitation development may be the origin of several negative effects, such as noise, vibrations, performance alterations, erosion and structural damages. These effects make a cavitation regime a situation to be avoided. Among the cavitation types that may develop, the "leading edge cavitation" is often observed in hydraulic machines and is known to be responsible for severe erosion. This kind of cavitation is characterized by a partial vapor cavity that detaches from the leading edge of a streamlined body and extends downstream. To alleviate the negative effects of cavitation, both experimental and computational studies have been undertaken. So far, the efforts to predict and model cavitation have been driven mainly by the turbomachinery, ship propeller and aerospace industries.

Although the numerical modelling of such cavitation has received a great deal of attention, it is still a very difficult and challenging task to predict such complex unsteady and two-phase flows with an acceptable accuracy. The cavitation inception which mainly occurs at vapor pressure is highly dependent on the flow conditions, water nucleation, and especially on the local surface roughness. The complex interaction of the vapor cavity with the turbulent flow, which is not yet fully understood, can be responsible for flow instabilities leading to complex phenomena such as the re-entrant jet and the generation of U-shaped vapor vortices transported by the mean flow to the pressure recovery region where they collapse.

Fundamentals of Cavitation

Physics of the Phenomenon

Cavitation in flowing liquids is a particular two-phase flow with phase transition (vaporization/condensation) driven by pressure change without any heating. It can be interpreted as the rupture of the liquid continuum due to excessive stresses [59]. In a phase diagram (Fig. 1), the liquid to vapor transition may be obtained whether by heating the liquid at constant pressure, which is well known as boiling, or by decreasing the pressure in

the liquid at constant temperature, which corresponds to the cavitation phenomenon. Although the cavitation process is not strictly isothermal, thermodynamic effects are usually neglected for liquids like water at ambient temperature. It is commonly admitted that cavitation occurs at a given location M and a given temperature T whenever the pressure p in the liquid reaches the saturated vapor pressure $p_v(T)$, namely :

$$p_M(T) \leq p_v(T) \tag{1}$$

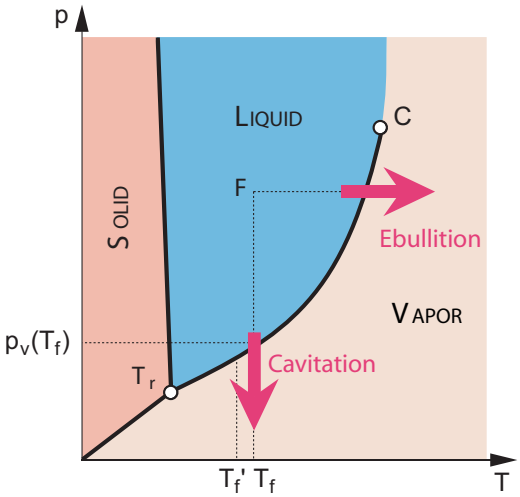

Figure 1: State phase diagram and phase change curves [59]

It should be noticed that under particular conditions, liquids may withstand significant tension without vaporizing. Many researchers (Donny 1846, Reynolds 1882) have already reported that the tensile strength significantly increases for still degassed liquids. Nevertheless the above cavitation inception criterion ($p_M(T) \leq p_v(T)$) remains valid for industrial liquids due to the existence of weak sites made of gas and vapor micro bubbles in the liquid, and usually called "cavitation nuclei". The compressibility coefficient of the liquid is very small, so that due to negative pressures (tension), the liquid continuum can easily break depending on the liquid nucleation, which significantly reduces the liquid traction properties.

Using the interfacial equilibrium condition and assuming that the transformation of the gas is isothermal, Blake (1949) has highlighted the critical values for the stability of a given nucleus of vapor and gas in an infinite volume of liquid. He deduced the critical values of the nucleus radius and the corresponding critical pressure as a function of the initial radius, the gas pressure and the surface tension. Rayleigh (1917) has introduced the dynamic effect on the liquid-vapor equilibrium. The equation which is known today as the Rayleigh-Plesset equation (1949) is certainly the most used mathematical model describing the growth and collapse of a spherical cavity in an infinite liquid volume. The equation describes the evolution of a bubble radius as a function of the imposed pressure signal time.

Cavitation Types

Different types of cavitation can be observed depending on the flow configurations (Fig. 2). Many authors have proposed a classification of cavitation types depending on certain parameters. Two main classification families can be derived; the attached cavitation, where the cavity interface is partly attached to the solid surface, and the convected cavitation where the entire interface is moving with the flow.

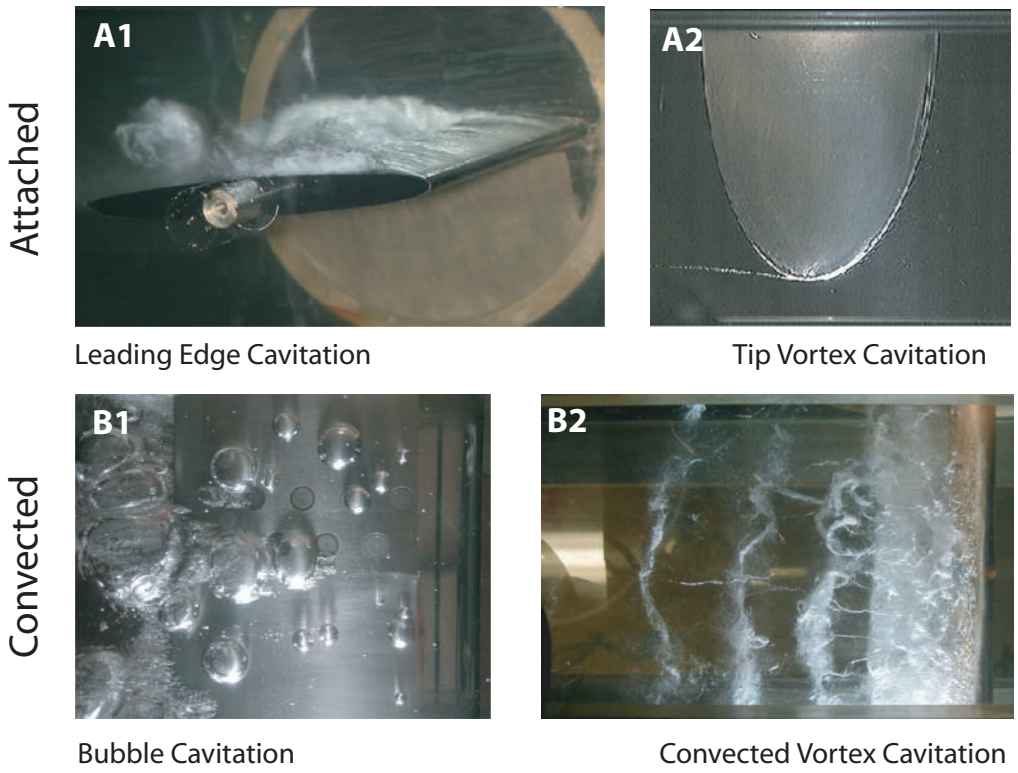

Figure 2: Different types of cavitation (flow from right to left).
A1) Leading edge cavitation, A2) Tip vortex cavitation
B1) Bubble cavitation, B2) Convected vortex cavitation behind a cylinder

- Attached cavitation
  - A1. Leading edge cavitation, also known as attached cavity, occurs at depression zones of the blade surface; it is usually called sheet cavitation, when the cavity is considered as a thin and quasi-steady stable cavity. The liquid-vapor interface can be smooth and transparent or has the shape of a highly turbulent boiling surface. It is also called cloud cavitation when the generated transient cavities are of the same order as the main attached cavity. Leading edge cavitation can be partial or appear as super-cavitation when the cavity grows in such a way to envelop the whole solid body. The leading edge cavitation is commonly observed when a hydraulic machine operates under off-design conditions.

  - A2. Attached tip vortex cavitation, which occurs generally at blade (or rotating blade) extremities. It occurs in the vortex core, characterized by high shear and low pressure fields.

- Convected cavitation
  - B1. Bubble cavitation, or travelling bubble cavitation where individual transient bubbles generate in the liquid and move with it as they expand and collapse during their life cycles. It occurs for low pressure gradients resulting from low foil incidence angles. It is observed at adapted mass flow in hydraulic machines.
  - B2. Convected vortex cavitation as cavitating Von-Kàrmàn street.

Causes and Effects

The principal cavitation apparition circumstances are:

- Depression due to local flow over-speed caused by change in streamlines curvatures (machine blades, restricted section passage);
- Pressure fluctuations caused by flow instabilities (diesel injectors, water hammer);
- Solid surface imperfections (hydraulic constructions);
- High shear and high vortex flows (cavitating jet, turbine vortex rope)

The cavitation occurring in a system initially designed to operate in homogeneous fluid can have several consequences:

- Performance alteration which appears as an increase of the losses, decrease in efficiency or limitation of the blade torque, flow disorganization by a passage blockage...
- Noise and vibrations
- Structure alteration by erosion in the region where travelling bubbles collapse

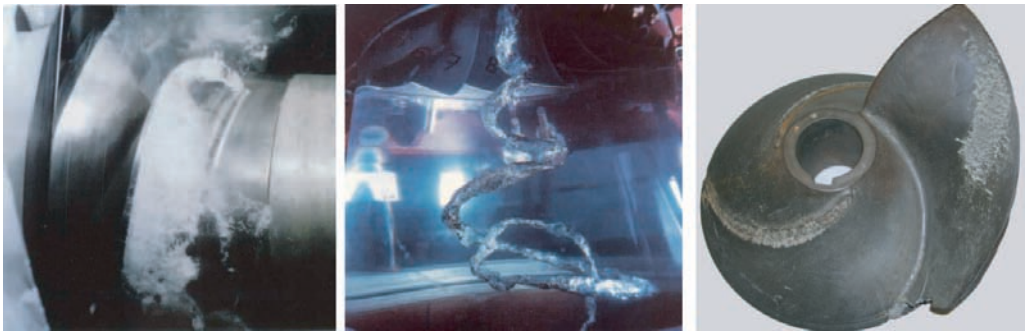

Figure 3: Typical developed cavitation on rotating inducer (left), cavitation vortex rope downstream a Francis turbine (center), cavitation erosion on pump impeller (right).

Context of the Study

The cavitation phenomenon is highly complex since it induces physical properties change of the initial fluid; the fluid mixture becomes compressible and the flow structure changes involving two-phase flow including continuous interfacial changes of mass and momentum. The two phases have two different physical properties and flow fields, and may have no distinguished interface between them. The time characteristics of the phase change are very small compared to the main flow characteristics and the turbulence behavior of the initial fluid changes with the presence of cavitation. As a result, the two-phase structure of such flow can be highly unorganized and unstable.

The complexity of the phenomenon make cavitation modelling difficult in the sense that experimental investigations require specific instrumentation for the multiphase environment, and the modelling strategies have to be based on empirical hypothesis.

Nevertheless the researchers have made great efforts, starting from the work of Rayleigh (1917) up to today, a lot of theoretical and experimental research has been conducted in order to analyze and understand the cavitation phenomenon. In experimental studies, an extensive amount of literature exists, dealing with different aspects of cavitation. Most of them are dedicated to fundamentals aspect, and the physics of cavitation.

Numerical studies and simulations of cavitation have been pursued for years, even if the Navier-Stokes based simulations emerged only in the last decade. Existing cavitation models compute the overall behavior of cavitating flows which implies that the major goal of a cavitation model should be to predict the onset, growth, and collapse of bubbles in cavitating flows. There is no comprehensive model in the literature that can simulate various types of cavitation and provide a detailed description of the flow field.

Literature Review

Leading Edge Cavitation Physics

The interest in the leading edge cavitation is motivated by two reasons; first this is the main cavitation type encountered in hydraulic machinery and is at the origin of the head drop phenomenon, and second, the leading edge cavitation is known as the most erosive one, because of its attachment to the blade and near-wall induced bubbles collapse.

Leading edge cavitation presents different aspects. Starting from the quasi-steady state partial attached cavitation to the super-cavitation regime, where the cavity envelops the entire blade and develops downstream, the flow can have a complex behavior where the cavity is characterized by a strong unsteadiness, transient cavities shedding downstream

and a completely 3D flow even in a 2D configurations as reported in Fig. 4, which illustrates a typical case of unsteady leading edge cavitation over a hydrofoil. In addition to the phase change phenomenon (i.e. liquid-vapor interfacial change), two regions are generally of interest and are driving the cavitation pattern; the cavity detachment region which is related to the cavitation onset, and the cavity closure which is the heart of the cavity instability.

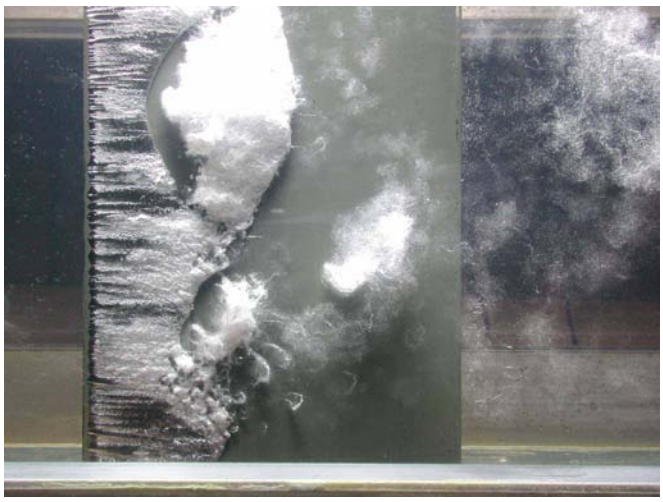

Figure 4: Typical leading-edge cavitation on a hydrofoil
Top view (flow from left to right), i=3° σ=0.8, C_{ref}=18 m/s

Cavitation Inception

The cavitation inception over hydraulic bodies is function of several parameters such as liquid nucleation, wall surface, and boundary layer state. A commonly used criterion for cavitation inception is based on a static approach and states that the cavities occur when the hydrodynamic pressure drops below the vapor pressure of the liquid at the free stream temperature. This is true in most cases, but not any more when using highly gaseous water or dealing with a rough surface wall [70].

Arndt and Ippen [7] illustrate the sensitivity of cavitation inception to the turbulence intensity of the boundary layer, which may be amplified in the case of non polished surface. Numachi [103] illustrates the roughness effect on cavitation inception and on its detachment position. Concerning isolated cavities, Knapp et al. [83] and Arndt [6] have studied the effect of tridimensional roughness elements and state a correlation between the cavitation inception and relative distance of the roughness relative to the boundary layer thickness.

In a different manner, Keller [82] has reported comprehensive test series for cavitation inception and the influence of induced scale effect. The main parameter affecting the cavitation inception criteria were found to be principally water quality with regard to its cavitation susceptibility (tensile strength, concentration and size of nuclei) and flow and fluid parameters (flow velocity, viscosity of the fluid, turbulence).

The pressure threshold, called also the critical pressure, is dependent on the water nuclei and on the local stresses. Joseph [79] has proposed an improved criterion, which can account for anisotropic flow structures. It is formulated in terms of the principal stresses occurring in a moving fluid rather than the pressure in a static fluid. The formulation is based on the idea that the liquid will rupture in the direction of maximum tension.

Cavitation Detachment

Various cavitation patterns can occur on a hydrofoil and various authors have investigated the governing parameters that allow for cavity attachment to a solid surface. Besides the flow parameters (Reynolds number, angle of attack, pressure), the state of the boundary layer as well as the surface roughness and water nucleation have been widely studied. The issue is to provide physical modelling that can predict the occurrence of attached cavitation or travelling bubbles.

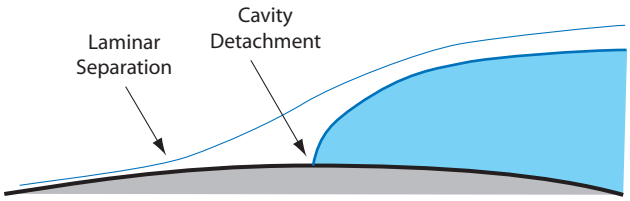

Figure 5: Schematic representation of the flow near the cavity detachment [3; 59]

The first studies which reported the effect of the boundary layer are those relating the laminar boundary layer separation to the presence of an attached cavity. Arakeri and Acosta [4] and Arakeri [3], using the Schlieren visualization technique on axisymmetric bodies, have stated that cavitation occurs after a laminar boundary layer separation and developed a correlation between the position of the separation point and the cavity detachment. Franc and Michel [61], by using dye injection on a polished hydrofoil have confirmed this statement and posed the 'cavity detachment paradox' assuming that the liquid should be in tension upstream the cavity detachment. From the physical point of view, they assumed that the boundary layer separation offers a shelter protecting the vapor cavity from being swept by the incoming flow. Tassin and Ceccio [141] have confirmed these observations with the help of dye injection, Schlieren visualization and Laser Doppler Velocimetry (LDV) techniques.

Farhat et al. [55; 57] have questioned necessity of laminar separation for the occurrence of attached cavitation. According to PIV measurements in the cavity detachment region, they have shown that cavitation may attach to the foil without any measurable boundary layer separation. They have also demonstrated that the liquid upstream of the cavity detachment can withstand negative pressures (liquid in tension). Values as low as -1 bar absolute pressure have been recorded with the help of miniature pressure sensors flush mounted to the hydrofoil leading edge.

Indeed, there are two ways to consider the leading edge cavitation. On the one hand the attached cavity may be seen as an obstacle facing to the incoming flow. In this case the laminar separation of the boundary layer stands for a necessary condition to ensure

the mechanical equilibrium of the cavity. On the other hand, the cavity interface may be considered as a non material surface corresponding to the transition to vapor of the incoming liquid. In this case, there is no need of boundary layer separation to allow the cavity to attach.

Cavity Closure and Instability

The cavity closure is a critical region where the vapor produced at the front part of the interface turns into liquid state. It is characterized by its unsteady and unstable character. In this region, liquid and vapor are highly mixed experiencing a strong interaction of the cavity with the outer flow. Most of the erosion occurs in the vicinity of the closure region and is caused by the collapse of travelling cavities. The vapor structures formed in the low pressure zones are transported downstream and collapse violently when they reach the higher pressure zone. A physical modelling of such two-phase flows have to take into account two different time scales. One is related to the liquid motion and the other, which is several order of magnitude smaller, is associated with the collapse of travelling cavities. Despite of the 2D configurations, the cavity closure always exhibits strong 3D pattern and is tightly related to the instabilities that develop in the main cavity.

Farhat [54] observed that at low values of incidence angle, upstream velocity and cavity length, the main cavity remains stable with shed cavities having small dimensions compared to the main cavity length. He stated that this kind of cavitation is associated with low erosion risk and induced vibration as well as a random generation process of travelling cavities. He also observed that hydrodynamic instabilities may develop within the main cavity whenever the velocity, the incidence angle or the cavity length are increased beyond a threshold value. Unstable cavitation is characterized by large shed cavities with a tremendous increase of erosion risk and vibration levels. In this case the shedding frequency is found to be governed by a Strouhal law based on the cavity length. The Strouhal number value is in a range of 0.2–0.4 depending on the flow conditions and hydrofoil geometry [106; 41; 81].

The hydrodynamic mechanism of the generation of travelling cavities has been widely investigated by Avellan et al [15; 14] with the help of Laser Doppler Anemometry (LDA) measurements. They have pointed out a strong interaction of the main cavity with the outer flow, which leads to the development of Kelvin-Helmoltz instability and the formation of large discrete swirling structures at the leading edge of the main cavity. The energy transfer from the mean flow to these structures induces the formation of U-shaped vortices in the cavity closure as illustrated on Fig. 6.

The cavity closure is the region where the liquid flow surrounding the cavity reattaches to the wall, and is splits in two. One fraction in the main flow direction and a second reentering the cavity, and called "the reentrant jet". Both fractions are separated by a streamline which ideally ends to a stagnation point on the hydrofoil (Fig. 7). As the cavity thickness increases, the reentrant jet front moves towards the leading edge of the foil. As soon as the jet reaches the cavity detachment, the main cavity is entirely swept away and transported downstream. The cavity formation and its shedding and collapse take place in a cyclic way [59].

Callenaere et al. [26; 27] have used a particular experimental arrangement to control independently the adverse pressure gradient and the cavity thickness. They have found,

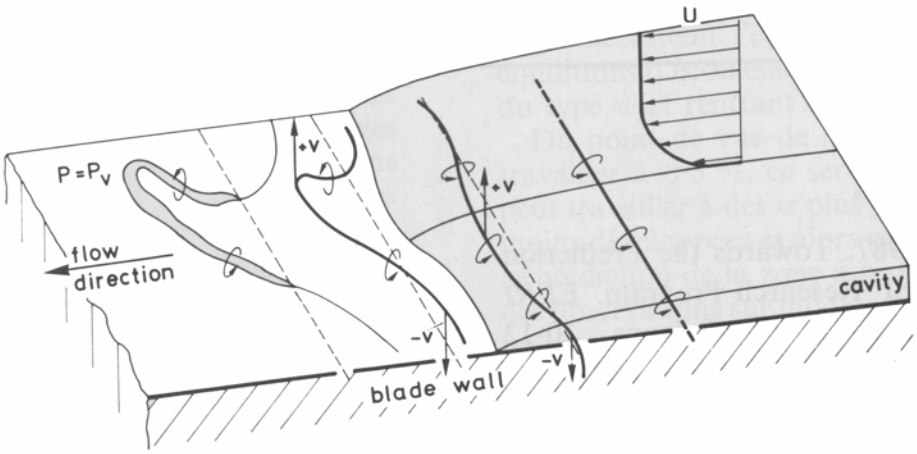

Figure 6: U-Shape cavitation vortex generation mechanism [15]

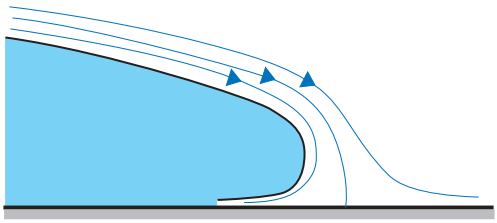

Figure 7: Schematic presentation of the flow near the cavity closure zone [59]

using LDV measurements, a good correlation between the cloud cavitation instability and the region of high pressure gradient. They deduced a map of different instabilities represented by a graphic of the cavity thickness as a function of the cavitation number. They defined five main zones: the cloud cavitation, surrounded by four other types; reentrant jet without shedding for low incidence angles, continuous shedding for long cavities, long non-oscillating cavities, and shear cavitation. The authors also found that the reentrant jet instability occurs when two conditions are satisfied: first, the adverse pressure gradient must be large enough, which imposes a maximum cavity length, second, the cavity must be not too thin, which imposes a minimum cavity length.

Leading Edge Cavitation Modelling

Although the numerical modelling of leading edge cavitation has received a great deal of attention, it is still a challenging investigation to predict such unsteady, turbulent and two-phase flows. Tulin [147] and Wu [155] were the pioneers in the domain using indirect conformal mapping methods and free-streamline theory in the 50's. Yamagushi & Kato [156] and Lemonier and Rowe [93] have investigated singularity methods in the 80's, whereas Dupont and Avellan [50; 51] have investigated Navier-Stokes corrections on classical potential computations. These preliminary methods were based on empirical correlations for the cavity closure and/or cavity length. In the last few years, more

generalized models were introduced, and studies were focused on the single-fluid Navier-Stokes model. In the literature, two different approaches have been mainly proposed for leading edge cavitation simulation.

In the first approach, called Interface-Tracking or Interface-Fitting Model (mainly monophasic steady-state approach), only the liquid phase is resolved and the vapor phase is not considered and replaced by an interface boundary condition. The cavity interface is considered as a free surface boundary of the computation domain, and the computational grid includes one phase only. The cavity is then deformed every time step in order to reach the vapor pressure at its border stating that no mass flux is allowed across the interface. This method was designed to predict steady-state attached partial cavities, and the initial shape of the cavity and a closure region model (wake model) have to be provided. First approaches were introduced by Desphande et al. [44] and Chen and Heister [33] using Euler and Navier Stokes equations in 2D formulations respectively. They have used the static vapor pressure criteria ($p < p_v$) for the initial shape estimation and the cavity closure region. Desphande et al. [45] provide an additional energy equation to take into account the thermodynamic effects in cryogenic fluids. Hirschi et al. [72; 73] proposed an approximation of the initial cavity shape by the envelope of a travelling bubble which is computed by the Rayleigh-Plesset equation, and the same approach is used in the unsteady region of two-phase closure. The method was used in 2D configuration as well as full 3D formulations for hydraulic machines.

The second approach is an Interface-Capturing Model (mainly unsteady multiphasic approach), where the vapor-liquid interface is directly derived from the flow calculation using mixture model assumptions. In this approach, a pseudo-density function of the liquid-vapor mixture is used to close the equations system. In the 90's, and motivated to model the vapor phase flow and cavitation unsteadiness, Delannoy and Kueny [85] proposed a barotropic law relating pressure to density, where Ventikos [149] investigated a model where the fluid state is governed by an enthalpy equation. Kubota et al. [84] introduced the pseudo density calculation with the help of Rayleigh-Plesset model and the assumption is made about the bubble number density distributed in a continuous liquid phase.

Cavitation modelling through a multiphase mixture model, based on a transport equation for the phase change, has been introduced in the last few years. Chen and Heister [34; 35] proposed an additional density transport equation to reproduce the non-equilibrium phase change instead of the classical static formulation. Singhal et al. [134] and Merkle et al. [101], introduced an additional equation for the vapor (or liquid) volume fraction including source terms for vaporization and condensation processes (i.e. bubble growth and collapse). Kunz et al. [86; 87; 88; 89; 90] and Singhal et al. [133; 131; 132] used similar techniques with differences in deriving the source terms. A comparative study of these models and their differences are given by Sennocak & Shyy [126; 127; 128]. Sauer and Schnerr [122] and Tani and Ngashima [140] investigated the extension of the model to thermosensitive fluids by resolving the energy equation and making hypotheses for the temperature changes of the fluid.

Cavitation Instability

Among the different types of cavitation unsteadiness, it is useful to distinguish two categories; the system instability and the intrinsic instability. The system instability is when the cavity instability is system fluctuations dependent or due to interaction with other cavities. Surge instability is an example of the system instability, and a simple 1D model is given by Watanabe et al. [152] where the unsteady behavior of a cavity in a duct is governed by the inlet conditions. Duttweiller and Brennen [52] and Watanabe and Brennen [151] have also proposed a model of cavitation surge instability on a cavitating propeller in a water tunnel. The rotating cavitation in inducers [143; 144; 75] and cavitation in a hydrofoil cascade [76] are typical cases where the instability does not originate from the cavity itself but requires other cavities to develop.

Intrinsic instability is when the instability or the unsteadiness originates from the cavity itself. Preliminary unsteady computations have been undertaken by Furness and Hutton [66] and were based on an interface tracking methodology. A constant vapor pressure and no slip boundary conditions are applied to the cavity interface, and the cavity is adjusted at each time step, so that the normal velocity vanishes at the cavity interface. They have obtained a reentrant jet at the cavity closure, but the computations were stopped at this level due to the difficulty of cavitation shedding with this configuration. The unsteady character of an attached cavity including transient cavity shedding, is often obtained for very high adverse pressure gradients (high incidence angle), and the first successful unsteady formulations have been achieved using mixture model formulations.

Reboud and Delannoy [115] have already highlighted, in the case of a 2D hydrofoil that a classical barotropic model leads to an unsteady flow with transient cavities shedding in the case of Euler computations but not with the RANS k-ε turbulence model. Reboud et al. [116; 39] have investigated the ability of two-equation turbulence models to reproduce the cavity unsteadiness in the case of a venturi nozzle [138; 139]. They have stated that the use of the k-ε turbulence model leads to a steady-state cavity because of the high turbulent viscosity level induced by the turbulence model. They have proposed an empirical reduction for the eddy viscosity in the cavitating regions which results in an unsteady flow with shedding of transient cavities. The authors have also obtained the same results using a compressible formulation of the k-ω turbulence model [153] based on a local Mach number formulation.

Song and He [135], using a barotropic cavitation model and a Large Eddy Simulation Smagorinsky's SGS model, have reproduced an unsteady cavitation regime. Qin et al. [112; 111] have used the same model in the case of a 2D hydrofoil. They obtained a large vortex and periodic shedding of transient cavities. Shin and Ikohagi [130] have simulated unsteady cavity flow around a flat plate (cavitating Von Karman street) and a flow in a bend using a compressible vapor-liquid two-phase flow formulation. They have taken into account the effect of the apparent compressibility of the mixture and used a non homogeneous formulation of the viscosity as well as a non isotropic formulation of the stress tensor. Saito et al. [121] have used the same approach in the case of a 2D hydrofoil and obtained a shedding of transient cavities.

Wu et al. [154] and Kunz et al. [90] have compared a classical k-ε model to the hybrid Detached Eddy Simulation approach on the same 2D hydrofoil case (geometry of the CAV03, physical models and CFD tools for computation of cavitating flows workshop).

Wu et al. have established a big difference in the predicted eddy viscosity of the different models, even if no model predicts transient cavity shedding. They explain that by the similarity in the near wall treatment by both models. Kunz et al. have obtained an unsteady flow field and transient cavity shedding with both models. They stated that, even if the predicted pressure and lift values are the same between the models, the DES simulation leads to more separated vapor structures and an increase of the size of transported cavities. On the same geometry, Pouffary et al. [109], Delgosha et al. [38], and Saito et al. [121] using RANS computations and different formulations for the multiphase effective viscosity obtained the same results as Kunz et al., where Qin et al. [113] with their model do not predict any transient cavity shedding. It results that the unsteady modelling of cavitation, depends in addition to the cavitation model itself, on the turbulent modelling assumptions (turbulence modelling approach and near-wall treatment) as well as the numerical algorithm used for the simulation (same models used with the same geometry have different results).

All these works were dedicated to model the unsteady cavitation flow and mainly to reproduce the shedding of transient cavities in the unsteady cavitation regime. There is no comparative study with experimental data. However, the results were considered satisfactory when the Strouhal law is satisfied.

Liquid Nucleation and Gas Effects

Liquids contain a finite amount of non-condensable gas in dissolved or non dissolved states. The so-called nucleation is the physical and chemical processes through which microbubbles filled with gas and vapor are generated inside the liquid. Jones [78] provided a review of nucleation in supersaturated liquids. He differentiated between the homogeneous nucleation, which takes place inside the liquid, and the surface nucleation, which occurs at the wall surface. The liquid nucleation can have considerable effect on the cavitating flow, and the phase change threshold can be strongly affected.

Multiphase flow models based on the Rayleigh-Plesset equation use the nuclei volume fraction only for the vaporization and condensation processes by specifying an average distribution with typical radius and bubble number density. The dynamic of the non condensable gas is not taken into account. However, more elaborate models including the non-condensable gas as third inert phase with its own transport equation are proposed for ventilated cavities [132]. A first attempt to take into account the dissolved gas effect was undertaken by Qin et al. [112].

Surface Tension

In a pure liquid, surface tension is the macroscopic manifestation of the intermolecular forces that tend to hold molecules together and prevent the formation of holes. The liquid pressure p_l, exterior to a vapor bubble of radius R, is related to the interior pressure, p_v, by : $p_l = p_g + p_v - \frac{2S}{R}$, where S is the surface tension.

It is assumed that the concept of surface tension can be extended down to bubbles or vacancies a few intermolecular distances in size [25; 59]. In interface tracking models, the surface tension can be easily taken into account by including the resulting forces in the deformation algorithm. On the other hand, in the homogeneous or two-fluid multiphase

models, the difficulty consists in the absence of an explicit physical interface between the both phases.

One of the first successful approaches to include surface tension in two-phase homogeneous media is developed by Brakbill et al. [22]. The article describes the "Continuum Surface Force Model", that implements surface forces such as surface tension through volume source terms distributed around the fluid interphase and concentrated at the interface. For the liquid-vapor set, the surface tension force given by the continuum surface force model is: $F_{lv} = f_{lv}\delta_{lv}$. The δ_{lv} term is often called the interface delta function; it is zero away from the interface, thereby ensuring that the surface tension force is active only near to the interface as: $\delta_{lv} = |\nabla\alpha_{lv}|$. f_{lv} is the surface force, and $f_{lv} = -S_{lv}\mathcal{R}_{lv}\vec{n}_{lv} + \vec{\nabla}_s S$. The two terms on the right hand side of the equation reflect the normal and tangential components of the surface tension force respectively. The normal component arises from the interface curvature and the tangential component from variations in the surface tension coefficient (the Marangoni effect). S is the surface tension coefficient, $\vec{n}_{lv}$ is the interface normal vector pointing from the primary fluid to the secondary fluid (calculated using the volume fraction gradient), ∇_s is the gradient operator on the interface and $\mathcal{R}$ is the surface curvature.

Thermal Effects

Most of the cavitation models suppose an equilibrium system based on the saturation vapor pressure, $p_v(T)$, which corresponds to the free-stream fluid temperature T. In this system, the liquid-vapor exchanges follow instantaneously the required volume variations driven by the pressure and inertial forces.

On the contrary as considered, cavitation phenomenon is not made at constant temperature. The thermal exchange necessary to phase change need a phase change temperature below the upstream temperature. This phenomenon called "Cavitation Thermal Delay", becomes important when the liquid temperature is close to the liquid critical temperature. In addition for these kind of fluids the vapor pressure-temperature curve can be much steeper than that for water. For fluids considered as thermo-sensitive, a non negligible thermal effect can appear. The temperatures inside the cavity are below the one of the free-stream fluid, and the vapor pressure inside the cavity $p_v(T)$ corresponding to the local temperature is also smaller. This means that cavitation development is less important that the one intended by neglecting thermal effect [59; 60; 62] and the use of vapor pressure of bulk temperature can lead to scale effect for developed cavitation [5]

In modelling, and for thermo-sensitive fluids like cryogenic fluids, usually used in aerospace and rocket engine technology, the phenomenon imposes that vaporization and condensation require an energy transfer (i.e. existence of temperature gradients and heat exchange at the liquid-vapor interface) on the one hand, and the phase change requires a finite laps time and disequilibrium conditions at the interface on the other hand.

Earlier procedures consisted in defining a non dimensional temperature difference number, the so-called the Stepanoff B-Factor method (Stahl and Stepanoff; 1956). The temperature depression in the cavity is given by: $\triangle T = B(\rho_l/\rho_v)(H_{fg}/c_p)$, where B is a constant and expresses the ratio between the volume of vapor and the liquid volume. The value of B is correlated based on experiments over simple geometries as a function of non-dimensional

parameters characterizing the flow conditions and fluid characteristics [102; 119]. On the other hand Fruman et al. [64; 65; 63] applies the concepts of the "Entrainment Theory" (the vapor production is equal to the air injection necessary to sustain a ventilated cavity of equal mean length) to improve the experimental correlations and estimate the thermal boundary layer effects on the basis of rough flat plate turbulent boundary layer theory.

In CFD, different approaches are proposed. In interface tracking methods the classical deformation algorithm is supplied by an additional deformation routine according to the thermodynamic effect. A normal temperature gradient is used as a boundary condition for the energy equation and gives the temperature depression on the cavity interface [45]. In state equation models, various approaches based on the modification of the homogeneous mixture density calculation taking into account the thermal effect are proposed [114]. Promising methods are those based on the resolution of the full energy equation. Sauer et al. [122] proposed a simplified equation for the mixture enthalpy (Avva, 1995) and a thermal bubble growth model (thermal controlled growth, Plesset 1977), where they relate the thermal change to the volume fraction change to take into account the thermal effect. Tani et al. [140] proposed the resolution of the energy equation and their hypothesis is based on computing the equivalent mixture density. Both liquid and vapor densities are functions of the temperature (perfect gas for the vapor, and Tamman type for the liquid). Then, the equivalent density is a function of both temperatures, pressure and volume fractions. The volume fraction is computed via the volume fraction transport equation using the Rayleigh source terms.

Alternatives Approaches

For developed 3D cavitation, averaged formulations are the most adapted ones regarding to the computation cost and the description level of interest. These models are not suited for some specific cases of cavitation. The typical case is the modelling of an isolated cavity collapse, where the interfaces between the liquid and the vapor are very distinct and the time and space scales are very small but on the same order. For these cases, methods based on interface tracking strategies to avoid diffusion at the interfaces are developed. The typical higher accuracy in grid discretization are those based on the sub-grid method (using one field formulation of Navier-Stokes equations) and usually called "Immersed Boundary Methods". They are divided into two main families; the first is the front capturing method where the front is captured directly on regular, stationary grid using marker function to locate the interface. It includes the VOF (zero thickness) and the Level Set methods (finite thickness). The second family is Front Tracking methods where the interface is localized through an adaptive grid.

The volume of fluid method (VOF) (Harlow and Welch 1965, see [123]) is the most popular one because of its use in several commercial codes. It locates the interface using a marker function which corresponds to the local volume fraction of a phase. It is equal to one in the phase itself and zero otherwise, and a reconstruction algorithm is used for the interface. The Level Set Method (cf. Osher's group works [104]) uses a distance function to the interface and has the advantage to be continuous in all the domain, relating different liquid properties to the distance to the interface. In addition, a hybrid formulation between the Front Tracking and Front Capturing methods, is called Embedded Interface Methods (cf. Trygvason's works [142]). A stationary regular grid is used for the fluid flow, and the

interface is tracked by a separate grid of lower dimension.

Concerning cavitation modelling, Chahine and his co-workers have undertaken a large amount of work concerning the dynamic of single bubble or interaction of several bubbles surrounded by a fluid [31; 32] or near a solid wall [158]. The method is an interface tracking method using a potential theory with a boundary element method (BEM) developed in 3D, axisymmetric and 2D versions [M11]. On the same topic (isolated bubble collapse), one can find works concerning Direct Navier-Stokes simulations with front tracking methods taking into account viscosity and surface tension terms [157; 108].

The Present Work

Purpose and Proposed Approach

As matters stand, the existing models are aimed to reproduce the overall pattern of a cavitation flow. The main effort in cavitation modelling in multiphase flow is centered about the formulation of the density-pressure relationship, and the main goals are to reproduce cavitation inception, development and eventually head drop prediction in hydraulic machines. The different models reported in the literature reproduce more or less the cavity length and pressure distribution in a correct manner. There is no comprehensive analysis concerning sensitive regions as cavitation detachment and closure. The same observation is made regarding to the hydraulic machinery where the cavitation behavior and estimation of the head drop level are the main interest of the manufacturer.

The present work is an investigation to develop a relevant physical model for the leading edge cavitation. The main goal is the development of computational methodologies which can provide detailed description of the leading edge cavitation flows as well as to highlight the mechanisms of the performances alteration related to it in hydraulic machines.

To this end, firstly we propose to evaluate the different cavitation models in the case of a 2D geometry and to compare the results to experimental data. The cavitation modelling is regarded in the specific case of the cavitation detachment and instability. The basic idea is to highlight the main driving parameters for each specific phenomenon and to evaluate the possibility of developing adapted physical models. Secondly, the models are used in the case of a hydraulic machine in order to summarize the developed cavitation effects on the machine and to highlight a comprehensive threshold related to the performances drop.

Structure of the Document

Besides the introduction, which presents the objective of our study and a literature review, the document is organized in five parts.

Part I is the theoretical part of the present work, which draws up the theory in modelling the general turbulent multiphase flow and cavitation flow, including the different models used for the present work.

Part II details the numerical tools used in the present work as well as the experimental facilities. A description of the used hydrofoil and measurements techniques is provided.

Part III concerns the case study of a 2D hydrofoil in steady-state cavitation regime. It is a comparative study between the different techniques of cavitation modelling and measurement, giving a summary of the different models and the ability of each one to reproduce the behavior of cavitating turbulent flow. Computations are compared to experimental data and an assessment is made regarding the model performances. This part includes the development of a modelling technique in order to take into account the surface roughness and Reynolds number effects on cavitation inception. It includes a phenomenological presentation of the maximum tensile stress theory, and test cases for the method evaluation. A parabolic nose case study is adopted to evaluate the CFD computations in reproducing correctly the added correction as well as the NACA0009 case in both configurations of smooth and rough walls.

Part IV is devoted to the cavitation intrinsic instability over a 2D hydrofoil. It includes a comparative study of the cavitation-turbulence interaction and summarizes the ability of each model to reproduce the unsteady cavitation flow. Computations are then compared to experimental data.

Part V draws up a numerical simulation dealing with a cavitating inducer. A comparative study of the models in terms of predicting the main cavity development and head drop threshold is done. It includes a physical analysis of the breakdown phenomenon and details the major reasons and mechanisms at the origin of the cavitation induced performance losses in hydraulic machinery.

In the last part, a general conclusion is drawn and suggestions for future work are provided to improve the physics of cavitation modelling.

Part I

Physical Modelling of Leading Edge Cavitation

Chapter 1

Turbulent Two-Phase Flow Modelling

Two-phase flow is the flow characterized by the presence of one or several interfaces separating the phases or components. Examples of flow systems can be found in a large number of engineering systems and wide varied natural phenomena. Two-phase flow can be without phase change as free surface flow, or with phase change as ebullition and cavitation. Cavitation modelling techniques are often derived from the general two-phase flow theory which is itself derived from the general flow mechanics and continuum mechanics. Before addressing different cavitation modelling strategies, it is necessary to expose the conservation equation in flow mechanics and multiphase flow theory.

In analyzing two-phase flows, it is evident that we first follow the standard method of continuum mechanics. Thus a two-phase flow is considered as a field which is divided into single phase regions with moving boundaries between the phases. The standard differential balance equations hold for each subregion with appropriate jump and boundary conditions to match the solutions of these equations at the interfaces. In theory, it is possible to formulate a two-phase flow problem in terms of the local instant variables and called "Local Instant Formulation". When each subregion which is bounded by interfaces can be considered as a continuum, the local instant formulation is mathematically rigorous. Consequently, all the two-phase flow models should be derived from this formulation by proper averaging methods [77].

1.1 Basic Flow Mechanics and Conservation Equations

The general integral balance can be written by introducing the fluid density ρ, the efflux $\bar{\bar{J}}$ and the body source Φ of any quantity ψ, as below:

$$\frac{d}{dt}\int_{V_m}(\rho\psi)\,dV = -\oint_{A_m}\left(\vec{n}\cdot\bar{\bar{J}}\right)dA + \int_{V_m}(\rho\Phi)dV \tag{1.1}$$

Eq. 1.1 states that the time rate of change of $\rho\psi$ in a material volume V_m is equal to the fluxes through the material surface A_m plus the body source.

Using Green's theorem and Leibnitz rule we obtain the differential balance equation:

$$\frac{\partial \rho\psi}{\partial t} + \vec{\nabla} \cdot \left(\vec{C}\rho\psi\right) = -\vec{\nabla} \cdot \bar{\bar{J}} + \rho\phi \tag{1.2}$$

where the first term is the time rate of change of the quantity per unit volume, and the second term is the rate of convection per unit volume. The right hand side represents the diffusive fluxes and the volume source.

Mass Conservation

In a given volume V, the flow mass $M_V(t)$ at time t, can be expressed in the integral form as:

$$M_V(t) = \int_V \rho\left(\vec{x}, t\right) dV \tag{1.3}$$

The differential mass conservation equation, which can be derived from the general balance equation with no surface and volume sources, becomes:

$$\frac{\partial \rho}{\partial t} + \vec{\nabla} \cdot (\rho\vec{C}) = 0 \tag{1.4}$$

It expresses the conservation of mass, and is called the **Continuity Equation**.

Momentum Conservation

Momentum conservation is given by the equation:

$$\rho\frac{\partial \vec{C}}{\partial t} + \rho(\vec{C} \cdot \vec{\nabla})\vec{C} = \vec{\nabla} \cdot \bar{\bar{T}} + \vec{f} \tag{1.5}$$

where $\vec{f}$ denotes body forces and $\bar{\bar{T}}$ the stress tensor. For a viscous, Newtonian and incompressible fluid, the tensor $\bar{\bar{T}}$ can be divided into the pressure term p and viscous stresses $\bar{\bar{\tau}}$ as:

$$\bar{\bar{T}} = -p\bar{\bar{I}} + \bar{\bar{\tau}} \tag{1.6}$$

Finally we can derive the momentum equation of a Newtonian, incompressible fluid, known as **Navier-Stokes** equation, as:

$$\rho\frac{\partial \vec{C}}{\partial t} + \rho(\vec{C} \cdot \vec{\nabla})\vec{C} = -\vec{\nabla}p + \vec{\nabla} \cdot \bar{\bar{\tau}} + \vec{f} \tag{1.7}$$

- $\vec{f}$ denotes the body force term, and represents typically the gravitational field in hydraulic systems as :

$$\vec{f} = \rho\vec{g} = \vec{\nabla}(-\rho g z) \tag{1.8}$$

- $\bar{\bar{\tau}}$ denotes the viscous stress tensor and is related to the deformation stress tensor $\bar{\bar{D}}$ (symmetric part of the velocity gradients) as:

$$\bar{\bar{\tau}} = 2\mu\bar{\bar{D}} \tag{1.9}$$

- For a turbulent flow, the Reynolds decomposition is used to describe the turbulent quantities as the sum of mean and fluctuant values. For a given variable u the decomposition gives :

$$u = \bar{u} + u' \tag{1.10}$$

then the turbulent stress term $\bar{\bar{\tau}}_t$ is introduced in eq. 1.7 :

$$\rho\frac{\partial\vec{\bar{C}}}{\partial t} + \rho(\vec{\bar{C}}\cdot\vec{\nabla})\vec{\bar{C}} = -\vec{\nabla}\bar{p} + \vec{\nabla}\cdot(\bar{\bar{\tau}} + \bar{\bar{\tau}}_t) + \vec{f} \tag{1.11}$$

and is known as the **Reynolds equation**.
$\bar{\bar{\tau}}_t$ is the Reynolds stress tensor given by:

$$\bar{\bar{\tau}}_t = -\rho\overline{\vec{C'}\otimes\vec{C'}} = -\rho\begin{pmatrix} \overline{C'^2_x} & \overline{C'_xC'_y} & \overline{C'_xC'_z} \\ \overline{C'_yC'_x} & \overline{C'^2_y} & \overline{C'_yC'_z} \\ \overline{C'_zC'_x} & \overline{C'_zC'_y} & \overline{C'^2_z} \end{pmatrix} \tag{1.12}$$

This term should be represented by turbulence models assuming a relation between the Reynolds stress tensor and the flow field.

Energy Balance

The balance of energy can be written by considering the total energy of the fluid in the differential form:

$$\frac{De}{Dt} + p\frac{D}{Dt}\frac{1}{\rho} = \frac{1}{\rho}\Phi - \frac{1}{\rho}\vec{\nabla}\cdot\vec{q} = \frac{1}{\rho}\Phi - \frac{1}{\rho}\vec{\nabla}\cdot(\lambda\vec{\nabla}T) \tag{1.13}$$

where e is the internal energy of the fluid, Φ is the dissipation and $\vec{q}$ the heat flux vector.

1.2 Two-Phase Flow Theory

In multi-phase or multi-component flows, the presence of interfacial surfaces introduces great difficulties in the mathematical and physical formulation of the problem [77].

From the mathematical point of view, a multi-phase flow can be considered as a field which is divided into single phase regions with moving boundaries separating the constituent phases. The differential balance holds for each subregion, however, it cannot be applied to the set of these sub-regions in the normal sense without violating the above conditions of continuity.

From the point of view of physics, the difficulties which are encountered in deriving the field and constitutive equations appropriate to multi-phase flow systems from the presence of the interface and the fact both the steady state and dynamic characteristics of dispersed two-phase flow systems depend upon the structure of the flow.

1.2.1 Two-Fluid Model

The two-fluid model (often called Euler-Euler model) is formulated by considering each phase separately. Thus the model is expressed in terms of two sets of conservation equations governing the balance of masses, momentum and energy for each phase. However, since the averaged fields of one phase are not independent of the other phase, we have interaction terms appearing in these balance equations (mass, momentum and energy transfers to the n^{th} phase from the interfaces). Consequently six differential field equations with interfacial conditions govern the macroscopic two-phase flow system.

In two-fluid model formulations, the transfer processes of each phase are expressed by their own balance equations. This means that this model is highly complicated not only in terms of the number of field equations involved but also in terms of the necessary number of constitutive equations.

The real importance of two-fluid model is that it can take into account the dynamic interactions between phases. This is accomplished by using momentum equations for each phase and two independent velocity fields in the formulation. On the other hand the constitutive equations should be highly accurate, since the equations of the two phases are completely independent and the interaction terms decide the degree of coupling between the phases, thus the transfer processes between the phases are greatly influenced by these terms [77].

Continuity Equation

The two-fluid model is characterized by two independent velocity fields which specify the velocity of each phase. The most natural choice are the mass-weighted mean phase velocities $\vec{C}_n$. The suitable form of the continuity equation is:

$$\frac{\partial \alpha_n \rho_n}{\partial t} + \vec{\nabla} \cdot (\alpha_n \rho_n \vec{C}_n) = \Gamma_n \tag{1.14}$$

with the interfacial mass transfer condition:

$$\sum_{n=1}^{2} \Gamma_n = 0 \tag{1.15}$$

where Γ_n represents the rate of production of the n^{th} phase mass from the phase changes at the interfaces and α_n is the local volume fraction and :

$$\sum_{n=1}^{2} \alpha_n = 1 \tag{1.16}$$

Momentum Equation

In the two-fluid model formulation, the conservation of momentum is expressed by two momentum equations (one for each phase), such as:

$$\frac{\partial}{\partial t}(\alpha_n \rho_n \vec{C}_n) + \alpha_n \rho_n (\vec{C}_n \cdot \vec{\nabla}) \vec{C}_n = -\vec{\nabla}(\alpha_n p_n) + \vec{\nabla} \cdot (\alpha_n \bar{\bar{\tau}}_n + \alpha_n \bar{\bar{\tau}}_{t,n} + \vec{M}_n) + \vec{f} \tag{1.17}$$

We note that the momentum equation for each phase has a "n" interfacial source term $\vec{M}_n$ which couples the motions of the two phases. The interfacial transfer condition has the form:

$$\sum_{n=1}^{2} \vec{M}_n = \vec{M}_m \tag{1.18}$$

and :

$$\vec{M}_m = 2R_{21}S\vec{\nabla}\alpha_2 + \vec{M}_m^R \tag{1.19}$$

where R_{21} denotes the average mean curvature of the interfaces, S the surface tension , and $\vec{M}_m^R$ takes into account the effect of the changes in the mean curvature.

Constitutive Equations

In the previous formulations, the number of dependent variables exceeds those of the field equations, thus the balance equations with proper boundary conditions are insufficient to yield any specific answer. Consequently it is necessary to supplement them with various constitutive equations (usually of four types; state, mechanical, energetic and turbulent) which define a certain type of ideal materials.

The constitutive equations of state express the fluid proprieties like density $\rho_n(T_n, p_n)$, enthalpy $h_n(T_n, p_n)$ and surface tension $S(T_n)$ as functions of thermodynamic properties.

In point of view of mechanics, the most used one is the linearly viscous fluid of Navier-Stokes and has a constitutive equation of the form:

$$\tau_n = \mu_n \left[\nabla\vec{C}_n + \left(\nabla\vec{C}_n\right)^T\right] - \left(\tfrac{2}{3}\mu_n - \lambda_n\right)\left(\nabla\cdot\vec{C}_n\right)\bar{\bar{I}}$$

The contact heat transfer is expressed by the heat flux vector $\vec{q}_n$, and the energetic constitutive equation specifies the nature and mechanism of the contact energy transfer. Most fluids obey the generalized Fourier's law of heat conduction.

The difficulties encountered in writing the constitutive equations for turbulent fluxes even in single phase flow are quite considerable. The formulations of the turbulent stress tensor are usually the same as for the homogeneous mixtures.

1.2.2 Mixture and Homogeneous Models

The basic concept of the 'Mixture model' (or Diffusion model) is to consider the mixture as a whole. This formulation is more simple than the two-fluid model, however it requires some drastic constitutive assumptions involving some of the important characteristic of two-phase flow to be lost. Nevertheless it is exactly this simplicity of the model which makes it very useful in many two-phase flow system dynamics where the required information is often the one of the total mixture.

The most important aspect of the diffusion model is the reduction in the total number of field and constitutive equations required. The system is expressed in terms of four field equations; the mixture continuity, momentum and energy. These three macroscopic

mixture conservation equations are supplemented by a diffusion equation which takes into account for the concentration (i.e. volume fraction) change [77]. This lack should be expressed by additional constitutive equations (the lack of dynamic interactions in the relations is replaced by the constitutive laws). This approach is appropriate to mixtures, where the dynamic of the two components are locally closely coupled and the whole system is resolved in a macroscopic point of view.

If the system is phase change controlled (negligible drift or diffusion of mass in the diffusion equation), the system can be simplified and called "Homogeneous Model".

Continuity Equation

The mixture continuity equation can be written as follows:

$$\frac{\partial \rho_m}{\partial t} + \vec{\nabla} \cdot (\rho_m \vec{C}_m) = 0 \tag{1.20}$$

It has exactly the same form as the single-phase continuity equation without internal discontinuities, where the mixture quantities are defined as:

$$\rho_m = \sum_{n=1}^{2} \rho_n \alpha_n \tag{1.21}$$

$$\vec{C}_m = \sum_{n=1}^{2} \frac{\rho_n \vec{C}_n}{\rho_m} \tag{1.22}$$

$$p_m = \sum_{n=1}^{2} p_n \alpha_n \tag{1.23}$$

Diffusion Equation

On the other hand the diffusion equation, which expresses the change in concentration α_n (i.e. the mixture density ρ_m), is derived as:

$$\frac{\partial \alpha_n \rho_n}{\partial t} + \vec{\nabla} \cdot (\alpha_n \rho_n \vec{C}_m) = \Gamma_n - \nabla \cdot \left(\alpha_n \rho_n \vec{C}_{12} \right) \tag{1.24}$$

where Γ_n accounts for the mass transfer at the interface, and the second right side term is the diffusion flux term, since the convective flux are expressed by the mixture center of mass velocity. It should be noticed that in this equation (1.24), we have explicitly the diffusion terms, which is due to the development based on the mixture center of mass.

In the case where the relation is expressed through the center of mass velocities of each phase, C_n, the equation will be:

$$\frac{\partial \alpha_n \rho_n}{\partial t} + \vec{\nabla} \cdot (\alpha_n \rho_n \vec{C}_n) = \Gamma_n \tag{1.25}$$

On the other hand, if the system is phase change controlled (negligible drift or diffusion of mass in the diffusion equation), i.e. the relative motion between the two phases is negligible or not taken into account, the model is simplified and called **Homogeneous Model**. The diffusion equation in this case is given by ($C_{12} \sim 0$):

$$\frac{\partial \alpha_n \rho_n}{\partial t} + \vec{\nabla} \cdot (\alpha_n \rho_n \vec{C}_m) = \Gamma_n \tag{1.26}$$

In the opposite, it may be appropriate to call the mixture model where the effects of relative motions between 2 phases are taken into account by the drift velocities ($\vec{C}_{12} \neq 0$) the **Drift Model** .

Momentum Equation

The general formulation of the conservation of momentum has the same form as the single phase theory for the whole mixture:

$$\frac{\partial}{\partial t}(\rho_m \vec{C}_m) + \rho_m (\vec{C}_m \cdot \vec{\nabla}) \vec{C}_m = -\vec{\nabla}(p_m) + \vec{\nabla}(\bar{\bar{\tau}} + \bar{\bar{\tau}}_t) + \vec{M}_m + \vec{f} \tag{1.27}$$

$\vec{M}_m$ is the interfacial momentum source and the surface tension term is neglected. There is no direct terms in the mixture momentum equation.

It is clear that the choice of the model depends on the phenomena we need to reproduce and the time and space scales resolution involved for. The two-fluid model is suited for two-phase flow, where the two phases have a sharp interface. Cavitation and especially leading edge cavitation have a well mixed multiphase behavior at cavity closure region, where the interface between liquid and vapor is not clearly identified, and the two-fluid modelling in sense of resolving each phase separately leads to unrealistic small scales resolution. With these limitations the two-fluid model returns automatically to a mixture model, and appears to be the best choice regarding the computation effort versus the physics reproduction pair for leading edge cavitation modelling.

Using a mixture model (drift or homogeneous) for modelling a turbulent cavitation flow, the system needs two closure assumptions: one for the turbulent (fluctuations) terms in the momentum equation and the other for the interphase mass source for the mixture density (i.e. volume fraction equation).

1.3 Turbulence Modelling

The instantaneous continuity and Navier-Stokes equations form a closed set of four equations with four unknowns C_x, C_y, C_z and p. However time-averaged procedure in momentum equations does not consider all details concerning the state of the flow contained in the instantaneous fluctuations. As result, the time averaged Navier-Stokes equations (Reynolds equation) presented contain six extra terms, $C_i' C_j'$, called the Reynolds stress tensor ($\bar{\bar{\tau}}_t$) representing the turbulent fluctuations.

The complexity of the turbulence and its random characteristics, constrain us to use a simple formulation for the extra stresses. Also the cavitation, as the multiphase turbulence formulations are simplified to homogeneous formulations, that means that transport equations for turbulence are restrained to the whole fluid mixture.

Usually the turbulence models can be classified as :

- Reynolds averaged models	[RANS, based on time-averaged NS equations]
- Eddy viscosity models	[based on Boussinesq eddy-viscosity concept]
	- Algebraic models: uniform μ_t, mixing length
	- One-equation models: turb. kinetic energy model
	- Two-equations models: k-ε, k-ω, SST
- Reynolds stress models	- Seven-equations models: Re-stress, Re-stress-ω
- Detached Eddy Simulation	[DES, based on hybrid RANS-LES formulation]
- Large Eddy Simulation	[LES, based on space-filtered equations]

The investigated models k-ε, k-ω, SST, and DES are described in detail according to: [150; 153; 107; 30; 100].

1.3.1 Eddy Viscosity Turbulence Models

The first approximation in turbulence modelling suggests that the Reynolds stresses are assumed to be proportional to mean velocity gradients. This defines the 'Eddy Viscosity Model'. The analogy between the stress and strain tensors is made similar to laminar Newtonian flow:

$$-\rho C_i' C_j' \sim \mu_t \left(\frac{\partial C_i}{\partial x_j} + \frac{\partial C_j}{\partial x_i} \right) - \frac{2}{3} \rho k \delta_{ij} \tag{1.28}$$

where μ_t is the eddy (turbulent) viscosity and δ_{ij} is the Kronecker symbol.

This equation is the basis of the eddy viscosity models and expresses the Reynolds stresses if the turbulent viscosity μ_t is known. The models described below provide this variable.

Two-equation turbulence models are very widely used, as they offer a good compromise between numerical effort and computational accuracy. The velocity and length scale are obtained from separate transport equations (hence the two-equation term). The turbulent viscosity is modelled as the product of a turbulent velocity and turbulent length scale.

In two-equation models, the turbulent length scale is estimated from two properties of the turbulence field, usually the turbulent kinetic energy and its dissipation rate. The turbulence velocity scale is computed from the turbulent kinetic energy. The turbulent kinetic energy and dissipation rate (of the turbulent kinetic energy) are provided from the solution of their own transport equations.

k-ε Turbulence Model

Based on semi-empirical equations, the standard (original) k-ε model (Jones and Launder 1972, Launder and Spalding, 1974) has two equations, one for the turbulent kinetic energy (k) and one for its rate of viscous dissipation (ε).

The velocity and length scale are assumed as:

$$C \sim \sqrt{k} \qquad L \sim \frac{k^{\frac{2}{3}}}{\varepsilon} \tag{1.29}$$

With the Prandtl-Kolmogorov analogy, the eddy viscosity is specified as:

$$\mu_t = C^{ste}\rho CL = \rho C_\mu \frac{k^2}{\varepsilon} \tag{1.30}$$

relating the variables k and ε via a dimensionless constant C_μ.

The model uses the following transport equations:

Turbulence Kinetic Energy:

$$\frac{\partial \rho k}{\partial t} + \frac{\partial \rho C_j k}{\partial x_j} = \frac{\partial}{\partial x_j}((\mu + \frac{\mu_t}{\sigma_k})\frac{\partial k}{\partial x_j}) + \tau_{ij}\frac{\partial C_i}{\partial x_j} - \rho\varepsilon \tag{1.31}$$

Dissipation Rate :

$$\frac{\partial \rho \varepsilon}{\partial t} + \frac{\partial \rho C_j \varepsilon}{\partial x_j} = \frac{\partial}{\partial x_j}\left((\mu + \frac{\mu_t}{\sigma_\varepsilon})\frac{\partial \varepsilon}{\partial x_j}\right) + \frac{\varepsilon}{k}\left(C_{\varepsilon 1}\tau_{ij}\frac{\partial C_i}{\partial x_j} - C_{\varepsilon 2}\rho\varepsilon\right) \tag{1.32}$$

The model contains five adjustable constants derived from experiments:

$C_\mu = 0.09;$ $\sigma_k = 1.00;$ $\sigma_\varepsilon = 1.30;$ $C_{1\varepsilon} = 1.44;$ $C_{2\varepsilon} = 1.92.$

The Reynolds stress is computed using an extended Boussinesq relationship (Eq. refboussinesq1) with auxiliary relations :

$$\omega = \frac{\varepsilon}{C_\mu k} \qquad L_t = C_\mu \frac{k^{3/2}}{\varepsilon} \tag{1.33}$$

k-ω Turbulence Model

One of the advantages of the k-ω formulation is the near wall treatment for low-Reynolds number computations. The model does not involve the complex non-linear damping functions required for the k-ε model and is therefore more accurate and more robust. The k-ω model assumes that the eddy viscosity is linked to the turbulence kinetic energy and turbulent frequency via the relation:

$$\mu_t = \rho\frac{k}{\omega} \tag{1.34}$$

The standard (original) k-ω model (Wilcox, 1988) solves two transport equations, one for the turbulent kinetic energy k, and one for the specific dissipation rate ω (rate of dissipation per unit of turbulence kinetic energy, often called turbulent frequency) and the stress tensor is computed from the eddy-viscosity concept.

Turbulence Kinetic Energy :

$$\frac{\partial \rho k}{\partial t} + \frac{\partial \rho C_j k}{\partial x_j} = \frac{\partial}{\partial x_j}\left((\mu + \sigma^*\mu_t)\frac{\partial k}{\partial x_j}\right) + \tau_{ij}\frac{\partial C_i}{\partial x_j} - \beta^*\rho k\omega \tag{1.35}$$

Specific Dissipation Rate :

$$\frac{\partial \rho \omega}{\partial t} + \frac{\partial \rho C_j \omega}{\partial x_j} = \frac{\partial}{\partial x_j}\left((\mu + \sigma\mu_t)\frac{\partial \omega}{\partial x_j}\right) + \frac{\omega}{k}\left(\alpha\tau_{ij}\frac{\partial C_i}{\partial x_j} - \beta\rho k\omega\right) \tag{1.36}$$

Closure Coefficients :

$\alpha = 5/9; \qquad \beta = 3/40; \qquad \beta^* = 9/100; \quad \sigma = 1/2; \qquad \sigma^* = 1/2.$

Auxiliary Relations :

$$\varepsilon = \beta^* \omega k \qquad\qquad L_t = \frac{k^{1/2}}{\omega} \tag{1.37}$$

SST Turbulence Model

A problem with the original k-ω model is its strong sensitivity to free-stream conditions. In order to solve the problem, a blending between the k-ω model near the surface and the k-ε model in the outer region was developed by Menter [98].

The model called Shear Stress Transport model (SST) solves the above equations: (by multiplying the Wilcox k-ω equations by function (F_1), and the transformed Launder-Spalding k-ε equations by $(1 - F_1)$, such as:

Turbulence Kinetic Energy :

$$\frac{\partial \rho k}{\partial t} + \frac{\partial \rho C_j k}{\partial x_j} = \frac{\partial}{\partial x_j}\left((\mu + \frac{\mu_t}{\sigma_{k3}})\frac{\partial k}{\partial x_j}\right) + \tau_{ij}\frac{\partial C_i}{\partial x_j} - \beta^* \rho k \omega \tag{1.38}$$

Specific Dissipation Rate :

$$\rho\frac{\partial \omega}{\partial t} + \rho C_j \frac{\partial \omega}{\partial x_j} = \frac{\partial}{\partial x_j}\left((\mu + \frac{\mu_t}{\sigma_{\omega 3}})\frac{\partial \omega}{\partial x_j}\right) + \frac{\omega}{k}\left(\alpha_3 \tau_{ij}\frac{\partial C_i}{\partial x_j} - \beta_3 \rho k \omega\right) + (1 - F_1) 2\rho \frac{1}{\omega \sigma_{\omega 2}} \frac{\partial k}{\partial x_j}\frac{\partial \omega}{\partial x_j} \tag{1.39}$$

where the coefficients of the model are a linear combination of the corresponding coefficients of the k-ω and modified k-ε models ($\Phi = F_1 \Phi_{k\omega} + (1 - F_1)\Phi_{k\varepsilon}$).

Closure coefficients :

k-ω:	$\alpha_1 = 5/9;$	$\beta_1 = 3/40;$	$\sigma_{k1} = 2;$	$\sigma_{\omega 1} = 2;$	$\beta^* = 9/100;$
k-ε:	$\alpha_2 = 0.44;$	$\beta_2 = 0.0828;$	$\sigma_{k2} = 1;$	$\sigma_{\omega 2} = 1/0.856;$	$C_\mu = 0.09;$

The model combines the advantages of the Wilcox k-ω and the Launder-Spalding k-ε model, but still fails to properly predict the onset and amount of flow separation from smooth surfaces due to the over-prediction of the eddy-viscosity (the transport of the turbulent shear stress not properly taken into account). The proper transport behavior can be obtained by a limiter added to the formulation of the eddy-viscosity:

$$\mu_t = \rho \frac{k}{\max(\omega, SF_2)} \tag{1.40}$$

F_2 is a blending function, which restricts the limiter to the wall boundary layer, as the underlying assumptions are not correct for free shear flows. S is an invariant measure of the strain rate.

The blending functions F_1 and F_2 are critical to the success of the method. Their formulation is based on the distance to the nearest surface and on the flow variables [30]. The model as described accounts for the transport of the turbulent shear stress and should gives more accurate predictions of the onset and the amount of flow separation under adverse pressure gradients.

Non Homogeneous Two-Equations Models

In the presence of a multiphase flow, the natural modelling of turbulence would be to have separate models and a set of equations defining each phase separately. The complexity of this approach leads major workers to deal with classical homogeneous turbulence formulation. The induced neglected effects can be more or less important in multiphase flows. This led some researchers to the idea of the modification of classical two-equation turbulence models.

Vaidyanathan and Senocak [148; 125], proposed a non-equilibrium k-ε, based on the correction of the model coefficients to fit the experimental data based on optimization techniques. The difference between the computational and experimental results is used to judge the model fidelity. Reboud et al. [116; 39] have introduced an artificial compressibility effect on the classical incompressible k-ε. The idea is to avoid the high diffusivity of the numerical model, caused by the addition of the artificial viscosity (μ_t). The model assumes a low and non linear turbulent viscosity on the multiphasic media as:

$$\mu_t = f(\rho) C_\mu \frac{k^2}{\varepsilon} \tag{1.41}$$

where $f(\rho)$ is a power function as:

$$f(\rho) = \rho_v + \left(\frac{\rho_v - \rho_m}{\rho_l - \rho_v}\right)^n (\rho_v - \rho_l) \qquad n \gg 1 \tag{1.42}$$

1.3.2 Reynolds Stress Turbulence Models

The Reynolds stress equation models (RSM), also called second-order or second-momentum closure models are based on transport equations for all the components of the Reynolds stress tensor and the dissipation rate. These models which originate from Launder (1975) do not use the eddy viscosity hypothesis, but solve an equation for the transport of Reynolds stresses in the fluid (algebraic equations for the Algebraic-RSM (ASM) and individual differential equation for each Reynolds stress component for the original RSM). Theoretically, the modelling of stress anisotropy (directional effects of the Reynolds stress field) makes Reynolds stress models more suitable to complex flows. The exact differential equations describing the Reynolds-stress tensor $-\rho\overline{C_i' C_j'}$ are:

$$\frac{\partial \rho \tau_{ij}}{\partial t} + \frac{\partial \rho C_k \tau_{ij}}{\partial x_k} = -P_{ij} + \varepsilon_{ij} - \Pi_{ij} + \frac{\partial}{\partial x_k}\left[\mu \frac{\partial \tau_{ij}}{\partial x_k} + C_{ijk}\right] \tag{1.43}$$

where

$$P_{ij} = \tau_{ik}\frac{\partial C_j}{\partial x_k} + \tau_{jk}\frac{\partial C_i}{\partial x_k} \tag{1.44}$$

$$\varepsilon_{ij} = \overline{2\mu \frac{\partial C_i'}{\partial x_k}\frac{\partial C_j'}{\partial x_k}} \tag{1.45}$$

$$C_{ijk} = \overline{\rho C_i' C_j' C_k'} + \overline{p' C_i'}\delta_{jk} + \overline{p' C_j'}\delta_{ik} \tag{1.46}$$

$$\Pi_{ij} = \overline{p' \left(\frac{\partial C_i'}{\partial x_j} + \frac{\partial C_j'}{\partial x_i} \right)} \tag{1.47}$$

are respectively the production, dissipation, turbulent transport and pressure-strain correlation tensors, which should be modelled to close the system equations.

Reynolds stress-ω Turbulence Model

The Reynolds Stress-ω turbulence model is a Reynolds stress model based on the ω-equation (instead of ε-equation). The advantage is the same of the k-ω model allowing an accurate near wall treatment. The modelled equations for the Reynolds stresses can be written as follows:

Reynolds-Stress Tensor (Six differential equations):

$$\frac{\partial \rho \tau_{ij}}{\partial t} + \frac{\partial \rho C_k \tau_{ij}}{\partial x_k} = -P_{ij} + \varepsilon_{ij} - \Pi_{ij} + \frac{\partial}{\partial x_k} \left[\mu \frac{\partial \tau_{ij}}{\partial x_k} + C_{ijk} \right] \tag{1.48}$$

Specific Dissipation Rate :

$$\rho \frac{\partial \omega}{\partial t} + \rho \bar{C}_j \frac{\partial \omega}{\partial x_j} = \frac{\partial}{\partial x_k} \left((\mu + \sigma \mu_t) \frac{\partial \omega}{\partial x_k} \right) + \frac{\omega}{k} (\alpha \tau_{ij} \frac{\partial C_i}{\partial x_j} - \beta \rho k [\omega + \hat{\xi} \sqrt{2 \Omega_{mn} \Omega_{mn}}]) \tag{1.49}$$

Auxiliary Closure Relations :

$$\mu_t = \rho \frac{k}{\omega} \qquad \varepsilon = \beta^* \omega k \tag{1.50}$$

$$P_{ij} = \tau_{ik} \frac{\partial C_j}{\partial x_k} + \tau_{jk} \frac{\partial C_i}{\partial x_k} \qquad D_{ij} = \tau_{ik} \frac{\partial C_k}{\partial x_j} + \tau_{jk} \frac{\partial C_k}{\partial x_i} \tag{1.51}$$

$$\begin{aligned} \Pi_{ij} = {} & \beta^* C_1 \omega \left(\tau_{ij} + \frac{2}{3} \rho k \delta_{ij} \sigma \right) - \hat{\alpha} \left(P_{ij} + \frac{2}{3} P \delta_{ij} \sigma \right) \\ & - \hat{\beta} \left(D_{ij} + \frac{2}{3} P \delta_{ij} \sigma \right) - \hat{\gamma} \rho k \left(S_{ij} + \frac{1}{3} S_{kk} \delta_{ij} \sigma \right) \end{aligned} \tag{1.52}$$

Closure coefficients :

$\alpha = 4/5; \quad \beta = 3/40; \quad \beta^* = 9/100; \quad \sigma = 1/2; \quad \sigma^* = 1/2;$
$\hat{\alpha} = 42/55; \quad \hat{\beta} = 6/55; \quad \hat{\gamma} = 1/4; \quad \hat{\xi} = 1;$
$C_1 = 1 + 4(1 - e/k)^3/2;$

1.3.3 Space-Filtered Equations Based Models

Large Eddy Simulation

Large Eddy Simulation (LES) are the turbulence models where the time-dependent flow equations are solved for the mean flow and the largest eddies (large scale) and where the effects of the smaller eddies (small scale) are neglected. The model filters the equation of motion. The computational expense of LES lies between RANS and DNS simulations and is motivated by the limitations of each of this approach. There are four conceptual steps in LES; three modelling issues, and one numerical simulation issue:

First, a filtering operation is defined to decompose the velocity C into the sum of filtered (resolved) components $\bar{C}(x,t)$, which represent the motion of large eddies, and a residual (sub-grid, SGS) component $C'(x,t)$, as: $(C = \bar{C} + C')$, with:

$$\bar{C}(x,t) = \int G(x-x')C(x',t)dx' \tag{1.53}$$

where G is the filter function. This appears analogous to Reynolds decomposition. Important differences are that $\bar{C}(x,t)$ is a random field and the filtered residual $C'(x,t)$ is not always zero.

Second, the filtered velocity field is derived for Navier-Stokes equations. There are of the standard form with the momentum containing the residual stress tensor (SGS stress tensor). The filtered Navier-Stokes equations show a non linear transport term which can be developed as:

$$\overline{C_iC_j} = \overline{\bar{C}_i\bar{C}_j} + \overline{\bar{C}_iC'_j} + \overline{C'_i\bar{C}_j} + \overline{C'_iC'_j} \tag{1.54}$$

where the second and the third terms vanish in time averaging formulation but not in the case of volume averaging. Then the model introduces the sub-grid scale (SGS) stresses, τ_{ij}, as:

$$\begin{aligned}\tau_{ij} &= \overline{C_iC_j} - \bar{C}_i\bar{C}_j \\ &= \overline{\bar{C}_i\bar{C}_j} + \overline{\bar{C}_iC'_j} + \overline{C'_i\bar{C}_j} + \overline{C'_iC'_j} - \bar{C}_i\bar{C}_j\end{aligned} \tag{1.55}$$

Third, the closure is obtained by modelling the residual-stress tensor most simply by an eddy-viscosity model.

Finally, the filtered equations are solved numerically for $\bar{C}$, which provides an approximation to the large-scale motions. The different LES variants are based on the filtering techniques and the modelling of the sub-grid scale τ_{ij}.

Detached Eddy Simulation

The use of LES in boundary layer flows at high Reynolds numbers is very expensive and therefore not useful for common industrial simulations. On the other hand, turbulent structures can be resolved in massively separated regions, where the large turbulent scales are of the same dimensions as the geometrical structure generating them.

Detached Eddy Simulation (DES) [137; 136; 99] is an attempt to combine elements of RANS and LES formulations, where the RANS formulation is used inside attached and

mildly separated boundary layers and LES is applied in massively separated regions. While this approach offers many advantages, it is clearly not without problems, as the model has to identify automatically the different regions.

The used version of the DES model (Menter-CFX [99; 100]) is based on the SST-LES formulation. The advantage of this combination is that the accurate prediction of turbulent boundary layers up to separation and in mildly separated regions carries over from the SST model.

The idea behind the original DES model of Strelets [137] is to switch from the RANS model to an LES model in regions where the turbulent length L_t predicted by the RANS model is larger than the local grid spacing. In this case, the length scale $L_t = \sqrt{k}/\beta^*\omega$, used in the computation of the dissipation rate ε in the equation for the turbulent kinetic energy k, is replaced by the local grid spacing $\Delta = \max(\Delta_{ijk})$:

$$L_t \rightarrow C_{DES}\Delta \qquad \text{for: } C_{DES}\Delta < L_t \qquad \text{with: } (C_{DES} = 0.61)$$

The practical reason for choosing the maximum edge length in the DES formulation is that the model should return the RANS formulation in attached boundary layers. The maximum edge length is therefore the safest estimate to ensure that request. The DES modification of Strelets can be formulated as a multiplier to the destruction term in the k-equation:

$$\varepsilon = \beta^* k\omega \rightarrow \beta^* k\omega \cdot F_{DES} \qquad \text{with: } F_{DES} = \max\left(\tfrac{L_t}{C_{DES}\Delta}, 1\right)$$

The used formulation in this work is the Zonal SST-DES formulation (Menter-CFX). The model offers a zonal formulation with new limiter based on the blending functions of the SST model in order to prevent the flow separation in attached portion of the boundary layer due only to local grid spacing:

$$F_{DES} = \max\left(\frac{L_t}{C_{DES}\Delta}(1 - F_{SST}), 1\right) \qquad \text{with: } F_{SST} = 0, F_1, F_2 \tag{1.56}$$

The Strelets model is recovered when F_{SST} is set to 0. $F_{SST} = F_1$ offers the highest level of protection against grid-induced separation, but might also be less responsive in LES regions.

1.3.4 Used Models

The turbulence models detailed in this chapter are the main one used in literature for fluid mechanics and turbo-machinery flows. In our work we used them depending of the need of the simulations. For steady state flows and poor mesh resolution near the wall (using log-law wall functions), there is a priori no difference between the two equations formulations. The use of k-ε in the case of 2D steady hydrofoil and inducer steady computations instead of k-ω or SST is justified in this way. Several works reported the diffusive character of classical eddy viscosity models. To this end, several turbulence models, starting with the classical two equations model to the multi-scale DES models are used in the time-dependant simulations to make a turbulence comparative study in the case of unsteady cavitation.

Chapter 2

Cavitation Modelling

Summary of used models in the present study, and the assumed hypotheses are presented in Fig. 2.1. Single-phase interface tracking model, homogeneous multi-phase state-equation based model, and homogeneous multi-phase transport-equation based model are detailed in the following.

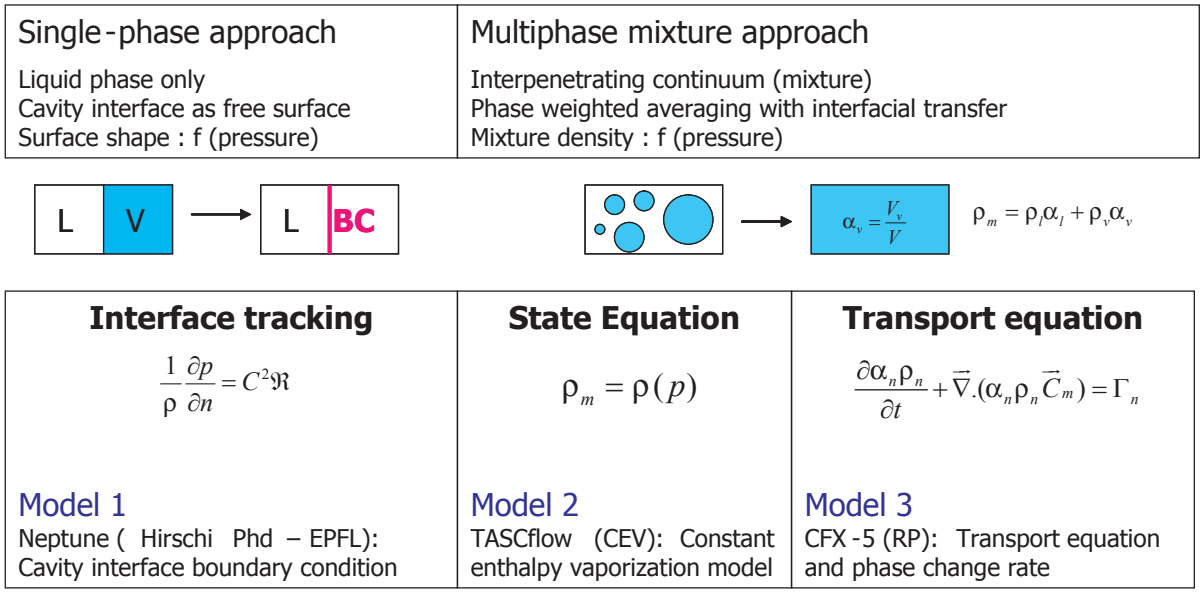

Figure 2.1: Cavitation models

2.1 Single-Phase Interface Tracking Model

The Single-Phase Interface Tracking Model was one of the first modern methods of cavitation modelling. It is based on the same idea used in Boundary Layers computations by dividing the domain into two regions and deforming the interface in an iterative way until the convergence ($p = p_v$ at the liquid-vapor interface). The method was used with potential flow theory [93; 50; 51; 44] and also in 2D Euler or Navier-Stokes computation [33; 45] and recently in fully 3D Navier-Stokes with application to hydraulic machinery [72; 73].

Most of the models use an iterative procedure based on the static liquid-vapor interface equilibrium condition:

$$p_l = p_g + p_v - \frac{2S}{R_0} \tag{2.1}$$

and by neglecting the surface tension and the inert gas contributions, the relation is simplified to:

$$p_l = p_v \tag{2.2}$$

In the following, we will give more details about the method developed by Hirshi [74; 72; 73] (the one used in the present work) which it differs from the others concerning the initial cavity shape estimation and the treatment of the cavity closure.

2.1.1 Interface Tracking Methodology

The deformation algorithm of the cavity interface is based on the idea of adapting the cavity shape in an iterative way until the vapor pressure is reached in the cavity boundary (free surface-like). The deformation procedure is performed according to the pressure distribution on the blade obtained from the liquid flow computation (of the previous iteration). A similar idea has also been used in the past by Dupont & Avellan [50; 51] and Chen & Heister [33] . For a given cavitation number σ, the modified cavity thickness $\vec{e}$ at time step ($t' = t + 1$) corresponding to the abscissa ξ along the streamline η is given by:

$$\vec{e}(\xi, \eta, t') = \vec{e}(\xi, \eta, t) + \lambda C_2 [C_p(\xi, \eta, t) + \sigma] \cdot \vec{n}(\xi, \eta, t) \tag{2.3}$$

where $\vec{n}$ is the normal vector to the cavity interface at the point (ξ, η, t) and λ is a function of the flow confining. C_2 is a factor depending on the relaxation coefficient C_1 given by the term $[C_p(\xi, \eta, t) + \sigma]$ and the local curvature $\mathcal{R}$, which overcomes oscillations in high thickness gradients.

$$C_2 = \frac{\left[2 - 2^{(1-C_1)}\right]}{1 + \mathcal{R}(\xi, \eta, t)} \qquad [0 \leq C_2 \leq 1] \tag{2.4}$$

$$C_1 = \begin{cases} 1 & \text{if } |C_p(\xi, \eta, t) + \sigma| > S_{cp} \\ \frac{|C_p(\xi, \eta, t) + \sigma|}{S_{cp}} & \text{if } |C_p(\xi, \eta, t) + \sigma| \leq S_{cp} \end{cases} \tag{2.5}$$

where S_{cp} is the standard deviation of the difference $\delta(\xi, \eta, t)$ between the pressure coefficient C_p and the cavitation number σ over the cavity length (L_c).

$$S_{cp} = \sqrt{\frac{1}{L_c} \int_{\xi=0}^{\xi=L_c} \left[\delta(\xi, \eta, t) - \bar{\delta}(\xi, \eta, t)\right]^2 d\xi} \tag{2.6}$$

with $\bar{\delta}(\xi, \eta, t)$ the mean value of $\delta(\xi, \eta, t)$ over the cavity length.

$$\delta(\xi, \eta, t) = C_p(\xi, \eta, t) + \sigma \tag{2.7}$$

$$\bar{\delta}(\eta,t) = \frac{1}{L_c}\int_{\xi=0}^{\xi=L_c} \delta(\xi,\eta,t)d\xi \tag{2.8}$$

Finally, the convergence criteria can be done by setting an order of magnitude ε:

$$S_{cp} < \varepsilon \tag{2.9}$$

2.1.2 Initial Cavity Estimation

In contrast to classical models using the p_v iso-surface as an initial form for the computation, the initial shape of the vapor cavity is estimated by the envelope of a travelling bubble along the suction side of the hydrofoil. The Rayleigh-Plesset equation is used to calculate the evolution of a nucleus placed in an infinite water volume on the blade surface. The driving pressure field is derived from the cavitation free calculation along streamlines (or mesh line for technical considerations). It should be noticed that only half of the bubble diameter is considered for the cavity thickness. The Rayleigh-Plesset equation is given by:

$$\rho\left[R\ddot{R} + \frac{3}{2}\dot{R}^2 + \frac{4\nu}{R}\dot{R}\right] = (p_v - p(t)) - \frac{2S}{R} + \left[\frac{2\gamma}{R_0} - (p_v - p_0)\right]\left(\frac{R_0}{R}\right)^{3\Gamma} \tag{2.10}$$

The resolution of the non linear differential equation (2.10) is obtained using a variable step Runge-Kutta algorithm. With a given pressure distribution, the initial conditions for the equation are imposed as: $R(0) = 0$ and $\dot{R} = 0$.

The different terms of the equation are:

$R\ddot{R} + \frac{3}{2}\dot{R}^2$	Inertial term
$(p_v - p(t))$	Rayleigh motor term
$\frac{2S}{R}$	Surface tension term
$\left[\frac{2\gamma}{R_0} - (p_v - p_0)\right]\left(\frac{R_0}{R}\right)^{3\Gamma}$	Bubble state term, (Γ the polytropic coefficient)
$\frac{4\nu}{R}\dot{R}$	Viscous term

(2.11)

The use of the envelope of a travelling bubble for initial cavity estimation is justified by the physics of leading edge cavitation. Indeed, we have already shown how attached cavity may originate from a smooth and continuous transition from bubble to sheet cavitation [55; 9; 70].

2.1.3 Closure Region Treatment

The interface tracking model, based on the free surface flow hypothesis assumes a constant pressure at the cavity interface. This is not the case of a developed cavity in the biphasic and unsteady closure region. To overcome this problem, we assume that the cavity may be approximated from its maximum thickness to its closure by the envelope of a collapsing bubble as already suggested by Yamagushi & Kato [156]. The initial radius is taken equal

to the maximum thickness of the cavity and the Rayleigh equation is used. This describes the spherical bubble radius evolution through a constant pressure field with neglecting viscous terms, surface tension and initial bubble internal state, and is given by:

$$\rho\left[R\ddot{R}+\frac{3}{2}\dot{R}^2\right]=p_v-p(t) \tag{2.12}$$

The equation can be described using the distance formulation instead of time by introducing the local velocity at the initial location $\frac{dR}{dT}=\frac{dR}{ds}C_{\xi_{max}}$. Thus we obtain the closure model based on the Rayleigh equation.

2.2 Homogeneous Multi-phase State Equation Based Model

The model assumes a homogeneous mixture with variable density ρ_m, generally related to the pressure via a state relationship or state diagram, generally considered as isothermal. The state equation serve to introduce a phase change, or rather a density change, when the pressure decreases below the vapor pressure. The density is kept constant in pure liquid and vapor regions and the density variation is dependent on the equation of state. The mixture density is defined as:

$$\rho_m=\alpha_l\rho_l+\alpha_v\rho_v \tag{2.13}$$

where α_l and α_v are respectively the liquid and vapor volume fractions and satisfy the equation:

$$\alpha_v+\alpha_l=1 \tag{2.14}$$

The volume fractions are related to the density according to:

$$\alpha_v=\frac{\rho-\rho_l}{\rho_v-\rho_l} \tag{2.15}$$

The whole system is then represented with Navier-Stokes equations for a homogeneous mixture plus a constitutive equation of state relating the pressure to density.

$$\frac{\partial\rho_m}{\partial t}+\vec{\nabla}\cdot(\rho_m\vec{C}_m)=0 \tag{2.16}$$

$$\frac{\partial}{\partial t}(\rho_m\vec{C}_m)+\rho_m(\vec{C}_m\cdot\vec{\nabla})\vec{C}_m=-\vec{\nabla}(p_m)+\vec{\nabla}(\bar{\bar{\tau}}+\bar{\bar{\tau}}_t)+\vec{M}_m+\vec{f} \tag{2.17}$$

$$\rho_m=\rho(p) \tag{2.18}$$

2.2.1 Constant Enthalpy Vaporization Model

The state equation model we are using in our study is the Constant Enthalpy Vaporization Model (CEV) [29]. Here, the cavitation phenomenon is assumed to follow a constant enthalpy vaporization-condensation processes, beginning from the sub-cooled liquid region and expanding into the two-phase zone.

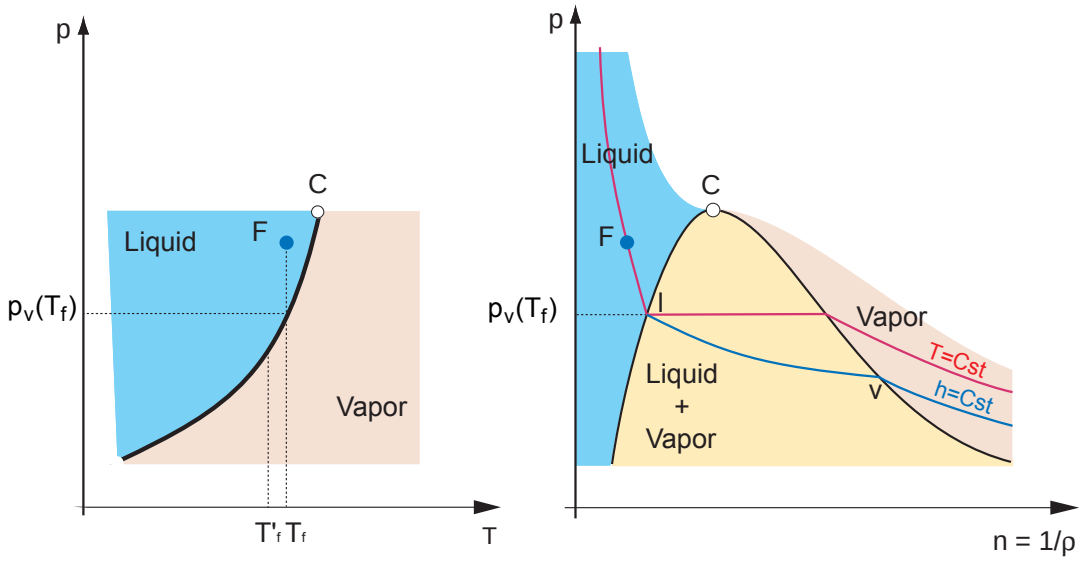

Figure 2.2: CEV Liquid-Vapor phase diagram
Saturation and Clapeyron curves with Andrews Isothermals [20; 59]

For a given local temperature T and with the local pressure p calculated by the resolution of the full Navier-Stokes equations (continuity, momentum and energy), saturation enthalpy values $h_v(p)$ and $h_l(p)$ are obtained from the liquid-phase diagram (Fig. 2.2) and the pseudo-density function as well as the mass fraction of the liquid y_l are derived as follows:

$$y_l = \frac{h_v(p) - h}{h_v(p) - h_l(p)} \tag{2.19}$$

$$\rho_m = \frac{1}{\frac{1}{\rho_v} + y_l \left(\frac{1}{\rho_l} - \frac{1}{\rho_v}\right)} \tag{2.20}$$

This model is developed on the same idea that as can be found in literature [149; 53] where the models include thermal proprieties of the mixture. Most of these models are based on the resolution of full Navier-Stokes equations including enthalpy (or energy) equation and the constitutive equation of state is based on steam water tables.

2.2.2 Other Models

Barotropic Model (Delannoy & Kueny [43])

The fluid is considered as single-phase with variable density according to a barotropic equation of state, which is based on the mixture speed of sound formulation.

$$\frac{\partial \rho}{\partial p} = \frac{1}{a_{min}^2} \tag{2.21}$$

The equation $\rho(p)$ looks like an 'S' function (sinus-hyperbolic type) with a constant slope of $\frac{1}{a^2}$ at the location ($p = p_v$). The authors adjusted the mixture speed of sound according to experimental data. As the method is compressible, one of the numerical difficulties of the model is the Mach number in the mixture region (can be supersonic : $a \ll C_{\text{ref}}$). On the other hand, authors used the same approach using a variable speed of sound function of the local mixture based on polynomial equation [37] or an empirical expression of a two-phase media [49].

Rayleigh Plesset Model (Kubota et al. [84])

The model developed by Kubota et al. [84] and named Bubble Two-Phase Flow (most known as Bubble Model) is not really a state equation model. Even if it employs a constitutive equation, it is based on Rayleigh-Plesset model. The fluid is considered as compressible continuum with widely varied density. An uniform distribution of a nuclei in the domain governs the growth and collapse of the bubble and is given by a modified Rayleigh equation solution imbedded in the Navier-Stokes equations for every point in the flow field.

2.3 Homogeneous Multi-phase Transport Equation Based Model

The cavitation modelling including a phase transport equation to model the liquid-vapor phase change (i.e. cavity growth and collapse) is the principal idea of the model. The model is a mixture multi-phase model including mass/volume fraction transport equation, with appropriate source terms to regulate the mass transfer between the phases.

The principal advantage of the model is the modelling of the phase change via a transport equation, which has a great contribution of reproducing the physics of cavitating flows :

- Cavity Detachment: the model, by the character of the transport equation can reproduce the cavitation delay as shown in experimental studies [59; 55].
- Cavity Closure: in contrast to barotropic models, in transport equation based models, the density is a function of the transport process. Consequently, gradients of density and pressure are not necessarily parallel, suggesting that the model can accommodate the baroclinic vorticity $\nabla\frac{1}{\rho}\nabla p$ generation as highlighted by recent experimental studies [67].

Different forms of the transport equation and source terms have been proposed in literature. So far, satisfactory results have been obtained with these models. All of them have introduced empirical factors to regulate the mass transfer, these factors are resulting from experiment/numerical calibrations.

2.3.1 Governing Equations

A truncated form of the Rayleigh-Plesset (RP) equation is used and assumes thermal equilibrium between the liquid and vapor phases. The RP equation provides the basis for

the rate equation controlling vapor generation/destruction, and is implemented through a volume fraction equation with a source term using a multiphase mixture theory [30].

The governing continuity and momentum equations for a classical RANS and homogeneous mixture multiphase flow are described below. Additional transport equation for the inter-phase mass transfer is added for the liquid phase.

$$\frac{\partial \rho_m}{\partial t} + \vec{\nabla} \cdot (\rho_m \vec{C}_m) = 0 \tag{2.22}$$

$$\frac{\partial}{\partial t}(\rho_m \vec{C}_m) + \rho_m (\vec{C}_m \cdot \vec{\nabla}) \vec{C}_m = -\vec{\nabla}(p_m) + \vec{\nabla}(\bar{\bar{\tau}} + \bar{\bar{\tau}}_t) + \vec{M}_m + \vec{f} \tag{2.23}$$

$$\frac{\partial \alpha_n \rho_n}{\partial t} + \vec{\nabla} \cdot (\alpha_n \rho_n \vec{C}_m) = \Gamma_n \tag{2.24}$$

2.3.2 Mass-Fraction Transport Equation

The governing equations describe the cavitation process involving 2-phase 3-component system, where we assume no-slip between all phases. The three components are: vapor (v), water (w), and non-condensable gas in the form of micro-bubbles nuclei (nuc). The relative quantity of each of the components is described by a volume fraction scalar, as:

$$(\alpha_w + \alpha_{nuc}) + \alpha_v = 1 \tag{2.25}$$

In many cavitation problems, the non-condensable gas phase is assumed to be well mixed in the liquid phase with a constant volume fraction α_{nuc}. On this basis the mass fractions α_w and α_{nuc} can be combined and treated as one. The volume scalar α_l is introduced as: $\alpha_w + \alpha_{nuc} = \alpha_l$. Choosing the scalar α_l to solve the transport equation, the governing equation for the liquid phase including non-condensable gas becomes :

$$\frac{\partial}{\partial t}(\alpha_l \rho_l) + \vec{\nabla} \cdot (\alpha_l \rho_l \vec{C}_m) = \Gamma_l = \dot{m}_l^v + \dot{m}_l^c \tag{2.26}$$

where: $\alpha_v = 1 - \alpha_l$ and $\dot{m}_l^v, \dot{m}_l^c$ are the source terms respectively associated to the vaporization and condensation processes (ie. growth and collapse). Their units are $kg/m^3/s$ and account for mass exchange between the vapor and liquid during cavitation.

2.3.3 Rayleigh-Plesset Source Term

The cavitation model is implemented based on the use of the Rayleigh-Plesset equation to estimate the rate of vapor production. For a vapor bubble nucleated in a surrounding liquid, the dynamic of the bubble can be described by the RP equation, by neglecting viscous terms and surface tension, such as :

$$\rho \left[R\ddot{R} + \frac{3}{2}\dot{R}^2 \right] = p_v - p \tag{2.27}$$

$$\Gamma_l = N \rho_l 4\pi R_0^2 \dot{R} \tag{2.28}$$

where R is the radius of the bubble, p_v the vapor pressure in the bubble, p the pressure in the surrounding liquid and ρ_l the liquid density. The first order approximation is used,

where the growth or collapse of a bubble follows the RP equation, neglecting higher order terms and bubbles interactions ($\dot{R} = \sqrt{\frac{2}{3}\frac{|p_v - p|}{\rho_l}}$). The number of bubble per unit volume of the mixture, N, available as nucleation sites is given by:

during vaporization:

$$N^v = \frac{3\alpha_l \alpha_{nuc}}{4\pi R_0^3} \tag{2.29}$$

and during condensation:

$$N^c = \frac{3\alpha_v}{4\pi R_0^3} \tag{2.30}$$

In practice, the vaporization and condensation processes have different time scales. Empirical constants, F^c and F^v, are introduced to take into account these constraints. By replacing Eq. 2.27, 2.29 and 2.30 in Eq. 2.28, we have:

$$\dot{m}_l^v = -F^v \frac{3\rho_v \alpha_{nuc} \alpha_l}{R_0} \sqrt{\frac{2}{3} \text{Max}\left(\frac{p_v - p}{\rho_l}, 0\right)} \tag{2.31}$$

$$\dot{m}_c^v = F^c \frac{3\rho_v (1 - \alpha_l)}{R_0} \sqrt{\frac{2}{3} \text{Max}\left(\frac{p - p_v}{\rho_l}, 0\right)} \tag{2.32}$$

The non-condensable gas, assumed as spherical bubbles, provide nucleation sites for the cavitation process. The default value for α_g is taken equal to 10^{-5} and a typical initial radius for the nuclei as $R_0 = 10^{-6}$ m. Using a simple 2D hydrofoil [129], the derived values which allow the best prediction of cavity dimensions are: $F^v = 50$, and $F^c = 0.015$ [30].

2.3.4 Other Models

Different variants of the transport-equation based models are used in literature. Most of them use the same experimental database. They use the pressure distribution of Rouse and Mc Known [117] over hemispherical cavitating headforms and the velocity profile measurements of Stutz et al. [138; 139] in the case of converging diverging nozzle.

Density Based Model (Chen & Heister [34; 35])

The density is the dependent variable in the transport equation. It was the first attempt to model the phase change through an additional transport equation. Evaporation and condensation are derived from the same transport equation. Density transport equation (2.33) is added to the NS system and the pressure difference governs the cavity growth and collapse introducing the pressure history concept (non-equilibrium model) [34]

$$\frac{D\rho}{Dt} = C(p - p_v) \tag{2.33}$$

The model is derived in another form using the Rayleigh-Plesset model to define the right hand of the density transport equation to describe the model as [35]:

$$\frac{D\rho}{Dt} = f(p, R_0, \alpha) \tag{2.34}$$

Pressure Based Model (Singhal et al. [134], Merkle et al.[101])

The liquid or vapor mass fraction is the dependent variable in the transport equation.

- Evaporation and condensation terms are function of the pressure (Singhal et al. [134], Merkle et al. [101], Ahuja et al. [1], Senocak et al. [126]). Both volume and mass fraction forms of the model are adopted . The liquid volume fraction formulation is presented below:

$$\frac{\partial}{\partial t}\left(\alpha_l \rho_l\right) + \nabla \cdot \left(\alpha_l \rho_l \vec{C}_m\right) = \dot{m}^v + \dot{m}^c \tag{2.35}$$

$$\dot{m}^v = \frac{F^v}{t_\infty}\left[\frac{p - p_v}{\frac{1}{2}\rho_l C_{\text{ref}}^2}\right]\rho_l \alpha_l \qquad p \leq p_v \tag{2.36}$$

$$\dot{m}^c = \frac{F^c}{t_\infty}\left[\frac{p - p_v}{\frac{1}{2}\rho_l C_{\text{ref}}^2}\right]\rho_v \alpha_v \qquad p \geq p_v \tag{2.37}$$

Empirical factors are determined through numerical/experimental results and make it dimensionless with free stream values. $t_\infty = L_{\text{ref}}/C_{\text{ref}}$ is the flow time characteristic.

- The evaporation terms are function of the pressure whereas the condensations term are function of the volume fraction (Kunz et al. [86; 87; 88; 94])

$$\frac{\partial}{\partial t}\left(\alpha_l \rho_l\right) + \nabla \cdot \left(\alpha_l \rho_l \vec{C}_m\right) = \dot{m}^v + \dot{m}^c \tag{2.38}$$

$$\dot{m}^v = \frac{F^v}{t_\infty}\left[\frac{p - p_v}{\frac{1}{2}\rho_l C_{\text{ref}}^2}\right]\rho_l \alpha_l \qquad p \leq p_v \tag{2.39}$$

$$\dot{m}^c = \frac{F^c}{t_\infty}\left[\frac{(\alpha_l)^2(1-\alpha_l)}{\rho_l}\right] \qquad p \geq p_v \tag{2.40}$$

Empirical factors are used and adjusted for different geometries and different flow conditions.

Rayleigh Plesset Based Model (Singhal et al. [133], Sauer & Schnerr [122])

The liquid or vapor mass fraction is the dependent variable in the transport equation. The phase change rate terms are dependent of the pressure, and are deduced from a simplified Rayleigh-Plesset equation. The Singhal model [133; 131; 132] is presented below :

$$\frac{\partial}{\partial t}\left(y_l \rho_m\right) + \nabla\left(y_l \rho_m \vec{C}_m\right) = \left(\dot{m}^v + \dot{m}^c\right) \tag{2.41}$$

$$\dot{m} = \frac{3\alpha}{R_0}\frac{\rho_v \rho_l}{\rho}\left[\frac{2}{3}\frac{|p_v - p|}{\rho_l}\right]^{1/2} Y_l \qquad p \leq p_v \tag{2.42}$$

Using correlations and assumptions, the equations are turned as:

$$\dot{m}^v = F^v \frac{\sqrt{k}}{\sigma} \rho_l \rho_v \left[\frac{2}{3}\frac{p_v - p}{\rho_l}\right]^{1/2} Y_l \qquad p \leq p_v \tag{2.43}$$

$$\dot{m}^c = F^c \frac{\sqrt{k}}{\sigma} \rho_l \rho_l \left[\frac{2}{3}\frac{p - p_v}{\rho_l}\right]^{1/2} Y_v \qquad p \geq p_v \tag{2.44}$$

The phase-change threshold pressure is corrected by an estimation of the local values of the turbulent pressure fluctuations as:

$$p_v = p_{sat} + (p'_{turb}/2) = p_{sat} + (0.39\rho k/2) \tag{2.45}$$

- Sauer and Schnerr [122] used a Rayleigh-Plesset source term for the bubble growth and collapse. They added also to the system a simplified equation for the mixture enthalpy coupled with a thermal bubble growth model to take into account the thermal effect on cryogenic fluids.

- Alajbegovic [2] used a Rayleigh-Plesset based model in a two-fluid configuration. The vapor and liquid phases have different speed, taking into account the slip velocity. Unfortunately the closure equation is based on the pressure ($p = p_{1,2}$) preventing the possibility of introducing surface tension as an interphase momentum source [22] in the multi-fluid system.

Interfacial Dynamics Based Models (Senocak et al. [127; 125])

Using the equations of mass and normal momentum at the liquid/vapor interface (neglecting viscous and surface tension effects), and using dimensional analysis, Senocak [127; 125] introduced mass source terms based on interfacial liquid/vapor dynamics as:

$$\frac{\partial}{\partial t}(\alpha_l) + \nabla \cdot (\alpha_l \vec{C}_m) = \dot{m}^v + \dot{m}^c \tag{2.46}$$

$$\dot{m}^v = F^v \frac{(p - p_v)}{(C_{v,n} - C_{I,n})^2(\rho_l - \rho_v)} \frac{\rho_l \alpha_l}{\rho_v t_\infty} \qquad p \leq p_v \tag{2.47}$$

$$\dot{m}^c = F^c \frac{(p - p_v)}{(C_{v,n} - C_{I,n})^2(\rho_l - \rho_v)} \frac{1 - \alpha_l}{t_\infty} \qquad p \geq p_v \tag{2.48}$$

where $C_{v,n}$ $C_{I,n}$ are the vapor and interface normal velocities. The current model uses the interface velocity for time dependent problems (equal to zero in steady state problem) and it requires additional methods to track the interface. However Senocak [125] proposed a simplification of the problem as:

$$C_{v,n} = \vec{C} \cdot \vec{n} = \vec{C} \cdot \frac{\nabla \alpha_v}{|\nabla \alpha_v|} \quad \text{and} \quad C_{I,n} = \frac{1 - \frac{C_{l,n}}{C_{v,n}}\frac{\rho_l}{\rho_v}}{1 - \frac{\rho_l}{\rho_v}} C_{v,n} \tag{2.49}$$

and a value of 0.90 is used for $\frac{C_{l,n}}{C_{v,n}}$

Part II

Numerical and Experimental Tools

Chapter 3

Numerical Infrastructure and Tools

The presented cavitation models describe the physical models which should be discretized and numerically solved. Usually in fluid mechanics the use of finite volume method is taken. Today, several commercial softwares offer at least one of multiphase cavitation model, generally a law state model or a Rayleigh-Plesset transport equation base model (RP-TEM). In addition, some codes offers the possibility of introducing user mass transfer rates via user defined functions.

FineTurbo Numeca CFD group [M8] includes a barotropic model [43] as a cavitation model. The solver is based on an artificial compressibility method (preconditioning technique) with dual time stepping, adapted to the large variation of the Mach number. Star-CD [M10] proposed two models, a barotropic model and a VOF version of RP-TEM. Fluent5 [M7] and CFD-RC [M9] adopted the full cavitation model of Singhal [131]. Fluent code has the choice between a homogeneous and drift models as well as two-fluid formulation. Several segregated solvers as well as coupled preconditioned time-marching solver can be used.

In this present work we are using the commercial codes CFX-TASCflow[M3] and CFX-5[M1] from ANSYS. TASCFlow includes the CEV state equation model and the RP-TEM in VOF configuration. CFX-5 has included the RP-TEM model and can be used either in mixture or two fluid Euler-Euler configurations. Inert phases can be added to the system, and user defined functions for the phase change (cavitation rate) as well as for the turbulence modelling are also included. Finally, we will give detailed informations about the used CFD codes CFX-TASCflow and CFX-5.

3.1 The Solver

The CFX-TASCflow [M3] and CFX-5 [M1] commercial codes, which served as a platform for the present work is a three-dimensional block-structured (TASCflow)/ unstructured (CFX-5) mesh code that solves the Reynolds-Averaged Navier-Stokes equations with a finite volume method.

The solver is fully coupled and solves the hydrodynamic equations (C_x, C_y, C_z, p) in a single system. This solution approach uses a fully implicit discretization of the equations at any given time step. For steady state problems, the time-step behaves like an "under-relaxation parameter", to guide the approximate solutions in a physically based manner to

a steady-state solution. The solver uses a Multigrid accelerated Incomplete Lower Upper (ILU) factorization technique for solving the discrete system of linearized equations. It is an iterative solver whereby the exact solution of the equations is approached during the course of several iterations. An algebraic Multigrid technique is used carrying out early iterations on a fine mesh and later iterations on progressively coarser virtual ones. The results are then transferred back from the coarsest mesh to the original fine mesh. The reader can refer to CFX solver theory [30] and to specific techniques in computational fluid dynamics [58] for more details.

Advection scheme

The discretization of the advection terms in CFX and TASCflow are as fellow:

$$\phi = \phi_{up} + \beta \nabla \phi \cdot \triangle \vec{r}$$

where ϕ_{up} is the value at the upwind node, $\vec{r}$ is the vector from the upwind node to the computed node, and $\beta \nabla \phi \cdot \triangle \vec{r}$ is called numerical advection correction and is as an anti-diffusive flux added to the upwind scheme. β=0 leads to the first order upwind difference scheme, and β=1 is formally second order accurate. The high resolution scheme computes β locally to be as close to 1 as possible (reducing to first order near discontinuities and in the free stream where the solution has little variation).

Boundary Conditions

Inflow Boundary Condition

Known as Dirichlet conditions, the inlet boundary conditions are set either in terms of velocity profile or mass flow rate. The boundary velocity components are specified, with a non-zero resultant into the domain as : $\vec{C} = C_x\vec{i} + C_y\vec{j} + C_z\vec{k}$. The mass flow rate is specified along with a direction component. The mass influx is calculated using : $\rho C = \dot{m} / \int_s dA$ where $\int_s dA$ is the integrated boundary surface area at a given mesh resolution.

The inlet turbulence quantities k and ε, are either specified directly or calculated using expressions which scale the distribution at the inlet according to the turbulence intensity $I = \frac{\tilde{C}}{C}$ (around 1 % for cavitation tunnels) and the eddy length scale L_t. The turbulence kinetic energy and dissipation are calculated using:

$$k_{inlet} = \frac{3}{2} I^2 C^2 \qquad \varepsilon_{inlet} = \frac{k^{\frac{3}{2}}}{L_t}$$

Pressure Boundary Condition

The relative static pressure over the boundary is specified generally for outlet regions. On the other hand, in order not to disturb the outlet flow field, the outlet relative static pressure is constrained such as the average value is specified,

$$\bar{p}_{spec} = \frac{1}{A} \int_s p_n dA$$

where the integral is applied over the entire outlet boundary surface. To enforce this condition, pressure at each boundary integration point is set as: $p_n = p_{spec} + (\bar{p}_{node} - \bar{p}_{node})$. In this way the exit boundary condition pressure profile can float, but the average value is constrained to the specified value.

Solid Boundary Condition

The velocity of the fluid at the wall boundary is set to zero, so the boundary condition for the velocity becomes: $C_{wall} = 0$. A Rotating wall can be specified in both stationary and rotating frames in hydraulic machines as : $C_{wall} = \omega R$.

The treatment of wall boundary conditions is used as automatic, the solver switches from the standard log-law wall conditions to the resolution of the viscous sublayer for low Reynolds numbers configuration, where the grid resolutions allows it [M1].

Symmetry Boundary Condition

The symmetry plane boundary condition imposes constraints which mirror the flow on either side of it. It is used to solve a part of â 2D domain with infinite span direction. The normal velocity component at the symmetry plane boundary is set to zero: $C_n = 0$ and the scalar variable gradients normal to the boundary are also set to zero: $\frac{\partial \phi}{\partial n}$=0.

3.2 Meshing

For the different case studies, multiblock structured meshes are generated with the help of ICEM CFD Hexa [M2] for the 2D hydrofoil case and CFX-TurboGrid [M4] mesh generator for hydraulic machines.

3.3 Interface Tracking Software

The interface tracking method is developed as a C programs unit and shells resolving cavitating flows Neptune [72; 19]. It was developed at the EPFL-LMH laboratory. For the present study, the program is integrated as a module with full interaction with CFX-TASCflow structured multi-block CFD code for resolving 3D cavitating flows for different flow configurations and geometries. The program includes the physical development of the interface tracking cavitation model coupled with TASCflow-Neptune routines for data pre/post-processing as well as remeshing/mesh-deformation routines.

Numerical Procedure

The Neptune software is divided in two parts. A set of programs for physical/numerical resolution, and another unit for geometry reconstruction (interaction of physical-discrete domains). First unit including an interface shaping procedure is governed by a Rayleigh-Plesset non linear differential equation (Runge-Kutta variable step algorithm) for initial cavity estimation and an iterative shaping algorithm (cavity deformation). Both procedures are supplied by B-spline reconstruction for the final cavity shape to avoid singular points at the reconstruction.

Mesh Deformation

Two different procedures are done. The first is the geometrical deformation based on surface normals of the blade for the cavity surface (the new solid) from each streamline computed in the physical domain. The second is based on the deformation of the existing structured grid using the new cavity shape. The method assumes the grid directions as an orthogonal basis of the flow directions (flow streamlines parallel to grid streamwise direction).

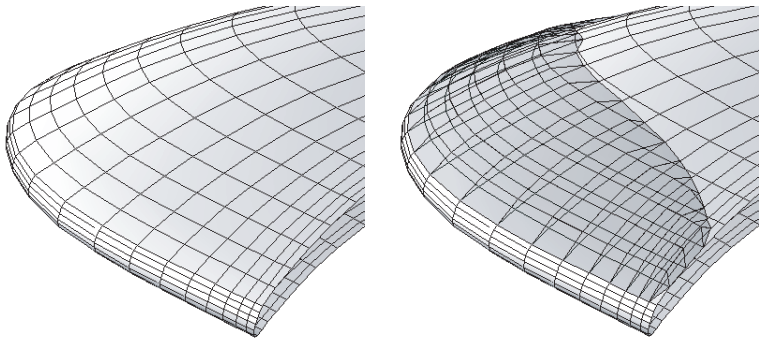

Figure 3.1: Original (cavitation free) and transformed (with cavitation) grids

First, an interpolation of the locations of the grid points is made to locate a cavity thickness at each point in streamlines directions of each span. Then, the computations of the closure and the detachment points of the cavity are performed by moving the closest point of the grid to them. Finally a deformation of the volume is made in linear way as:

$$\text{New-Grid-Point}=\text{Old-Grid-Point}+\frac{\eta_{max}-\eta}{\eta_{max}-\eta_0}\cdot e(\xi)$$

where $(\eta_{max}-\eta)$ is the maximum normal distance of the domain, $(\eta_{max}-\eta_0)$ is the distance of the deformed point to the upper bound of the domain, and $e(\xi)$ is the cavity thickness at the streamline location ξ. This equation gives the distance of the translation. A full algorithm is used to move the nodes only along mesh directions to overcome any intersections or negative volume generation.

It is clear that this method is solely dedicated when the grid mesh is adapted to the solid and flow directions. The procedure loses its efficiency when dealing with grids far from this hypothesis. In this case, a complete reconstruction of the mesh for the new blade shape (initial blade + cavity) is made. The procedure is also coupled with Turbo-Grid mesher, simply re-projecting the nodes on the new blade streamlines.

3.4 Computing Resources

The computing resources are provided by the EPFL. A standard PC P4 1Gb RAM is used for pre and post processing. Most of the computations (except test cases) are made in parallel environment using PVM mode in two different platforms based on Unix IBM-AIX 5 architecture.

The steady state computations for the 2D hydrofoil and 3D inducer are done with an IBM SP computing facility distributed as: 3 Silver Nodes of 4 CPUs PowerPC (332 MHz, 32-bit), 2 G Bytes of main memory each, and 4 Winterhawk of 4 CPUs Power3 (375 MHz, 64-bit), 2 G Bytes of main memory each.

The unsteady computations are done using another platform: IBM Blade Server JS20 having 14 x 2proc. PowerPC 970 (64-bit) with 4 G Bytes of RAM each.

3.5 Computations summary

Part III - Chapter 5

Case study: Leading edge cavitation on a 2D hydrofoil
Computations: 2D steady-state computations
Operating conditions: i=2.5°, C_{ref}=20m/s, σ=1.5-0.3

Cavitation models: Model 1, Model 2, Model 3
Turbulence models: k-ε

Multi-block structured grid: 3×25'000 mesh cells, $y^+ \sim 80$
Discretization: High resolution scheme

Convergence: $\varepsilon = 10^{-4}$
Conservation: Continuity and momentum imbalance in the domain satisfied
Mesh influence: 3×15'000, 3×25'000, 3×50'000 mesh cells

Part IV - Chapter 7

Case study: Cavitating von-Karman vortices in the wake of a 2D hydrofoil
Computations: 2D unsteady-state computations
Operating conditions: i=0.0°, C_{ref}=12–25m/s , σ=1.5-0.4

Cavitation models: Model 3
Turbulence models: SST

Multi-block structured grid: 3×50'000 mesh cells, $y^+ \sim 50$
Discretization: High resolution scheme
Time resolution scheme: Second order Euler scheme

Convergence: $\varepsilon = 10^{-4}$
Conservation: Continuity and momentum imbalance in the domain satisfied
Mesh influence: 3×50'000 mesh cells with $y^+ \sim 50$, 3×100'000 mesh cells with $y^+ \sim 1$
Time discretization influence: $0.40\,10^{-4}$, $0.30\,10^{-4}$, $0.15\,10^{-4}$ s

Part IV - Chapter 8

Case study: Cavitation instability on a 2D hydrofoil
Computations: 2D unsteady-state computations
Operating conditions: i=5.0°, C_{ref}=20m/s , σ=1.0

Cavitation models: Model 3
Turbulence models: k-ε, SST, Reynolds stress-ω, NH-SST, DES

Multi-block structured grid: 3×95'000 mesh cells, $y^+ \sim 1$
Discretization: Second order resolution scheme
Time resolution scheme: Second order Euler scheme

Convergence: $\varepsilon = 10^{-4}$
Conservation: Continuity and momentum imbalance in the domain satisfied
Time discretization influence: SST : 0.0050s, 0.0005s

Part IV - Chapter 9

Case study: Cavitation instability on a 2D hydrofoil
Computations: 2D unsteady-state computations
Operating conditions: i=5.0°, C_{ref}=20m/s , σ=1.2, 1.5

Cavitation models: Model 3
Turbulence models: NH-SST

Multi-block structured grid: 3×95'000 mesh cells, $y^+ \sim 1$
Discretization: Second order resolution scheme
Time resolution scheme: Second order Euler scheme

Convergence: $\varepsilon = 10^{-4}$
Conservation: Continuity and momentum imbalance in the domain satisfied

Part V - Chapter 10

Case study: Cavitation in an industrial inducer
Computations: 3D steady-state computations
Single machine passage in rotating frame of reference
Operating conditions: N=3000rpm ψ=0.20, 0.25, 0.30

Cavitation models: Model 1 (ψ=0.25), Model 3(ψ=0.20, 0.25, 0.3)
Turbulence models: k-ε

Multi-block structured grid: 260'000 mesh cells, $y^+ \sim 100$
Discretization: hybrid scheme (β=0.75)

Convergence: $\varepsilon = 10^{-4}$
Conservation: Continuity and momentum imbalance in the domain satisfied
Mesh influence: 150'000, 200'000, 260'000, 300'000, 400'000, 500'000 mesh cells

Chapter 4

Experimental Facilities

4.1 The Cavitation Tunnel

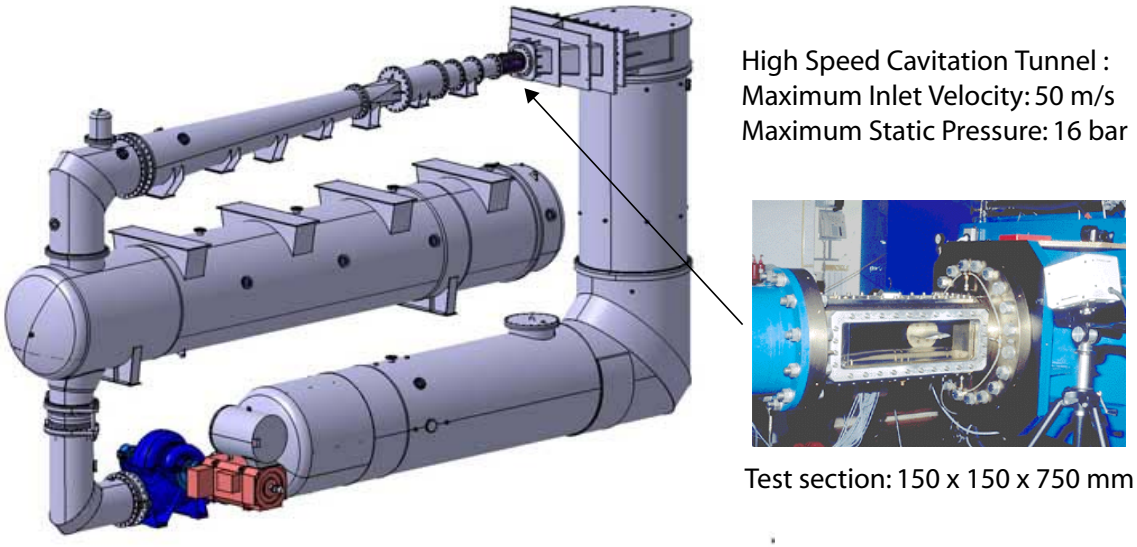

Figure 4.1: EPFL high speed cavitation tunnel

The cavitation tunnel (Fig. 4.1) of the EPFL is a closed loop of a very compact design built on three levels [16]. The flow from the resorber downstream the pump passes through a turn, which is combined with a settling chamber. Then it goes through a contraction nozzle of a ratio of about 40 to ensure the minimum flow fluctuations to the test section. The flow then passes through a horizontal diffuser, a vaned turn and downward through a diffuser-straightener elbow, which completes the deceleration and the uniformity of the flow before it reaches the bubble trap section at the 2nd level. After a complete circuit in this section the outgoing flow goes directly through the second vaned turn to the circulating pump at the 1st level.

The transit time resulting from a complete tunnel loop of one fluid particle is about 98 s at the maximum flow rate. This time value corresponds roughly to the resorption time of

a bubble of a 100 μm diameter. A double suction pump provides a total head of 36.5 m for 1.125 m^3/s at 885 rpm. This pump is directly driven by a 500 kW power DC-electric motor. The rectangular test section has inner dimensions of 150 x 150 x 750 mm, which corresponds, for the maximum flow rate, to 50 m/s. The hydrofoil sections usually tested have typical chord length of 100 mm and a maximum span of 150 mm, corresponding to the width of the test section. On each side of the test section one can mount various plates clamped by a strong rectangular frame, usually the hydrofoil support and three transparent windows. The hydrofoil support provides a precise adjustment of incidence angle reading of less than one minute of arc. The optical windows are built with a grounded perspex plate protected on the outside by a coated glass. These overcome light reflection in the wave length range corresponding to the light emission of the argon ion laser used when performing laser-Doppler velocimetry (LDV) measurements.

The macroscopic flow conditions are defined at the inlet of the test section. The mean flow velocity and the cavitation coefficient are derived from absolute pressure measurements at both ends of the contraction nozzle, and from temperature measurement in the higher part of the resorber.

4.2 The Experimental Hydrofoil

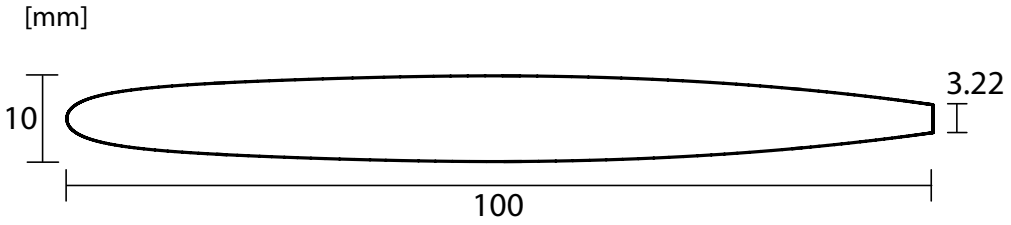

Figure 4.2: NACA0009 Hydrofoil

It concerns a modified NACA0009 hydrofoil, truncated at 90% of the original chord length. It has the final dimensions of 100 mm of chord length and 150 mm of span as illustrated in Fig. 4.2. The equations of the non truncated hydrofoil are:

$$0 \leq \frac{y}{c} \leq 0.45 \quad \frac{y}{c} = a_0 \left(\frac{x}{c}\right)^{\frac{1}{2}} + a_1 \left(\frac{x}{c}\right) + a_2 \left(\frac{x}{c}\right)^2 + a_3 \left(\frac{x}{c}\right)^3$$
$$0.45 \leq \frac{y}{c} \leq 1 \quad \frac{y}{c} = b_1 \left(1 - \frac{x}{c}\right) + b_2 \left(1 - \frac{x}{c}\right) + b_3 \left(1 - \frac{x}{c}\right)^3$$

with c being the chord length and :

$$\begin{cases} a_0 = +0.173688 & \\ a_1 = -0.244183 & b_1 = +0.1737 \\ a_2 = +0.313481 & b_2 = -0.185355 \\ a_3 = -0.275571 & b_3 = +0.33268 \end{cases}$$

4.3 Flow Field Measurements

Hydrodynamic Forces

The hydrodynamic force measurements are done by a five components hydrodynamic balance, mounted directly on the hydrofoil base, whose main characteristics are maximum lift of 10^4 N and maximum torque of 250 Nm. The hydrofoil is mounted on a "H" Section, mounted on cantilever on a rotating cylinder support of the test section. The deformations of the H structure which are measured by five strain gauges are treated, and transformed to the hydrofoil coordinates to finally extract the values corresponding to the lift and drag of the hydrofoil.

Pressure Measurement

A NACA0009 hydrofoil is especially instrumented for the pressure measurements [50]. 19 pressure lines are connected to pressure taps of 0.5 mm diameter each. The 19 x 3 pressure taps are distributed along the hydrofoil surface with a step of 5mm between 10 % and 90 % of the chord. The last sensor triplet is located on the blunt trailing edge.

The 19 pressure lines are connected to a electromagnetic pressure commutator (Scanivalve) which sequentially distributes each pressure line to a given pressure sensor (Digiquartz 2300-AS-002) which is isolated from the tunnel water by a silicone oil interface.

Velocity Profile Measurement

The velocity profiles are measured using two components LDV technique [50]. The measurement system includes an optical system, a treatment system and a measurement volume displacement management.

The used optical system of the velocimetry is based on Argon laser source of 6 Watts power, emitting over two dominant frequencies; green (514.5 nm) and blue (488 nm). The beam is separated on the main principal axis and a parallel one. The main beam is shifted in frequency by an acousto-optic module (Bragg cell) and splits in 2 beams of pure color with a prism, parallel to the third beam. The two pure color beams are located in a plane including the optical axis, and the third one is in a perpendicular plane to the first. The three parallel beams are at equal distance from the optical axis. They are then reflected by mirrors to form at the measurement point two perpendicular fringes, blue and green, in order to measure the two velocity components.

The system is used in retro-diffused mode, and a part of the optical system is used to return the signals of the measured window. The diffused particle light is collected by the focalization lens and introduced to the optics of the anemometer. Different photomultipliers and filters are used to separate the signals, and an acquisition system is used for the signal treatment.

Detailed informations about the procedure, including the different filtering and correction techniques, the acquisition system as well as the validations of the system in the turbulent multiphase behavior can be found in [50, chap.2-3].

Part III

2D Hydrofoil Time Independent Computations

Chapter 5

2D Hydrofoil Leading Edge Cavitation

Cavitation models evaluation is made through a 2D hydrofoil. For the purpose of comparison, the three main models presented as Model 1 (Mono-fluid, interface tracking model), Model 2 (multiphase, law state equilibrium model; based on Constant Enthalpy Vaporization hypothesis), and Model 3 (Multiphase, Rayleigh-Plesset transport equation based model) are assessed using the same solver [M1].

The main interest is the ability of the models to reproduce the cavitation flow in steady-state regime over a simple geometry. It concerns a NACA0009 hydrofoil, truncated at 90 % of the original chord length. It has the final dimensions of 100 mm of chord length and 150 mm of span. The hydrofoil is placed in the test section of the EPFL high-speed cavitation tunnel. The operating parameters are the flow incidence angle (i), the upstream velocity (C_{ref}), and the cavitation number (σ).

The chapter is divided in two parts; the first is an evaluation of the two multiphase models (Model 2 and Model 3) at a fixed incidence angle and various cavitation numbers. The results obtained with both models are compared with the experimental data in terms of pressure distribution on the hydrofoil.

The second part is the comparison of the three models for a fixed cavitation number in terms of flow field. The computation results are compared with the velocity profiles measurements at the hydrofoil along different transverse sections. The models are evaluated at lower cavitation numbers in terms of reproducing the hydrodynamic performances alteration due to the cavitation occurrence.

Since the experimental informations do not report time dependency, the steady-state model is adopted in the present computations. From the physical point of view, the steady-state assumption is sensible for sheet cavitation, which has a quasi-steady behavior at high enough cavitation numbers, with most of the unsteadiness localized in the rear closure region.

5.1 Numerical Setup

The 3D test section is modelled by a quasi 2D domain, with three rows of cells in spanwise direction for the numerical domain. The same mesh and numerical setup is used for the computations with the three models.

The domain is 9 blocks C-type grid of 3×25'000 mesh cells (Fig. 5.1). The steady state RANS simulations with the k-ε two equations turbulence model are performed in this case. The boundary conditions are set using a velocity inlet (C_{ref}=20 m/s) and an average static pressure at the outlet (the parameter which fixes the cavitation number). The turbulence is set to 1% of intensity and 0.001 m of eddy length scale. Both upper and lower section walls and the hydrofoil are modelled using non-slip conditions with classical log-law functions ($y^+ \sim 80$). Both lateral sides of the domain are modelled as symmetrical planes. Numerical convergence is set to a maximum of 10^{-4} for all the simulations.

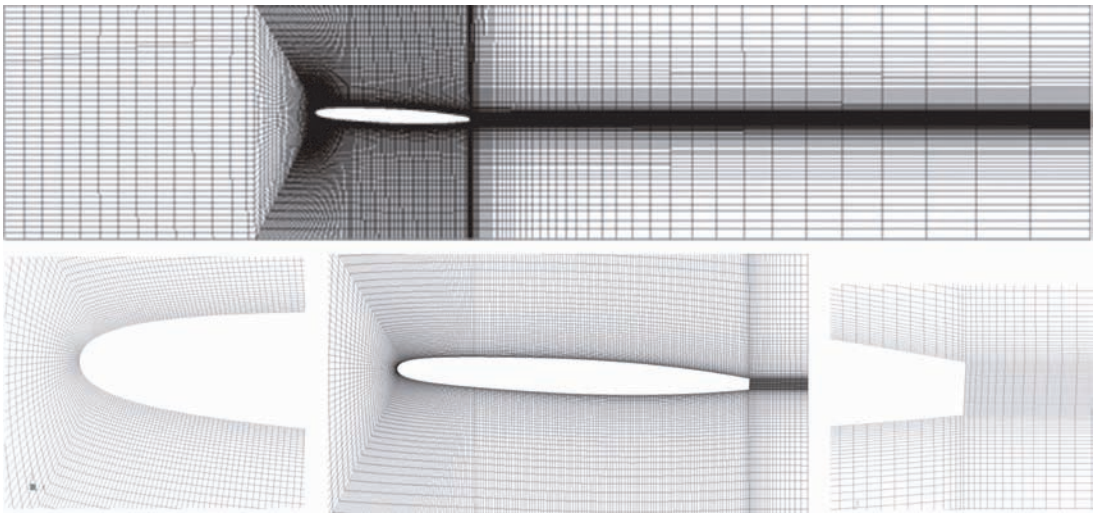

Figure 5.1: NACA0009 domain grid

5.2 Results and Analysis

5.2.1 Pressure Distribution

Experimental data concerning the NACA0009 hydrofoil are reported for different upstream velocities and cavitation numbers, and compared with the results of the computations (Model 2 and 3) in Figs. 5.2-5.5. We have presented in the same figures the vapor volume fraction computed by both models. From the experimental point of view, one can easily observe the strong influence of the upstream velocity on the cavitation closure region, which is significant for velocities higher than 20 m/s. For lower values the influence is not important. In the comparison with the simulations, we focus on the steady flow case C_{ref}=15–20 m/s, where the cavity closure fluctuations can be neglected.

Figures 5.2-5.5 show satisfactory results of the multiphase models in predicting the pressure distribution on the hydrofoil in the cavitation regime in terms of main cavity length

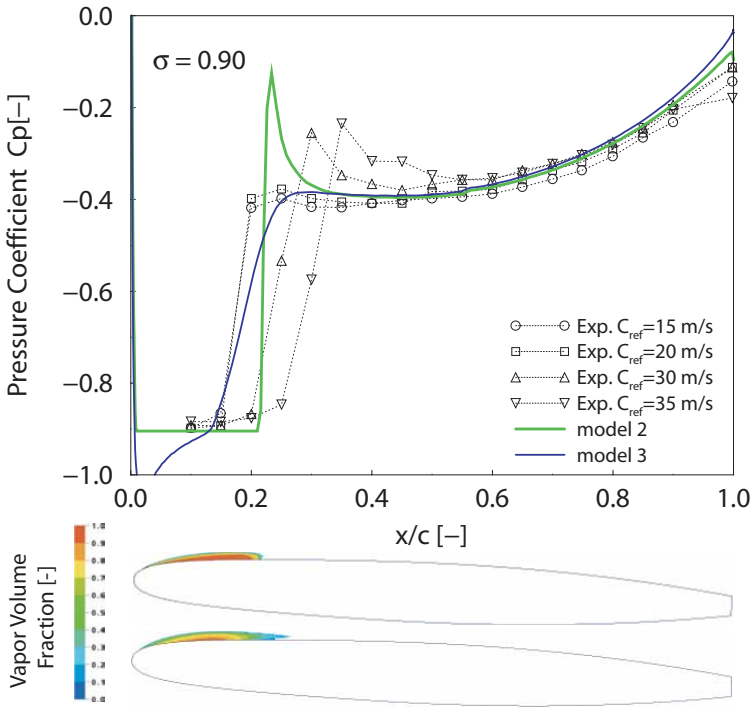

Figure 5.2: Pressure distribution and cavity shape on NACA0009
top : Model 2, bottom : Model 3, i=2.5°, σ=0.90

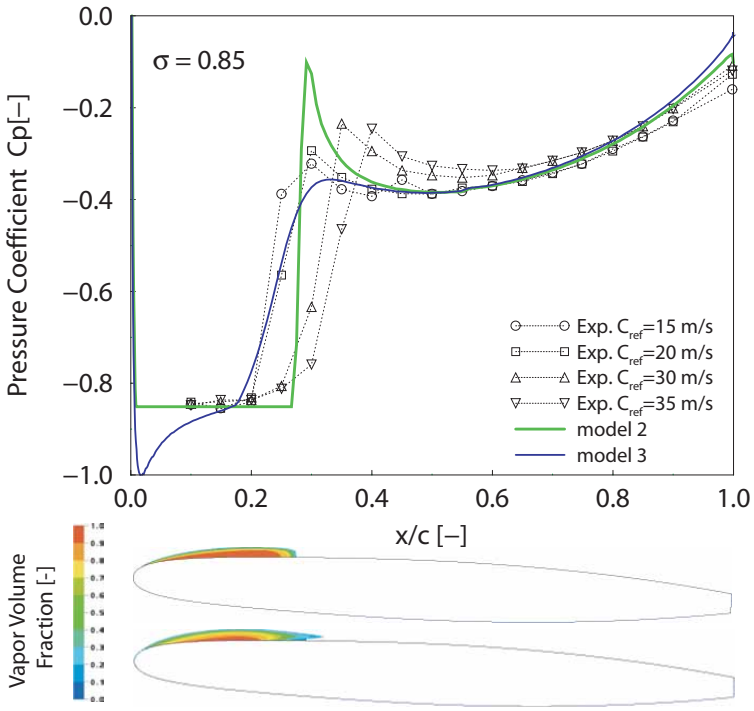

Figure 5.3: Pressure distribution and cavity shape on NACA0009
top : Model 2, bottom : Model 3, i=2.5°, σ=0.85

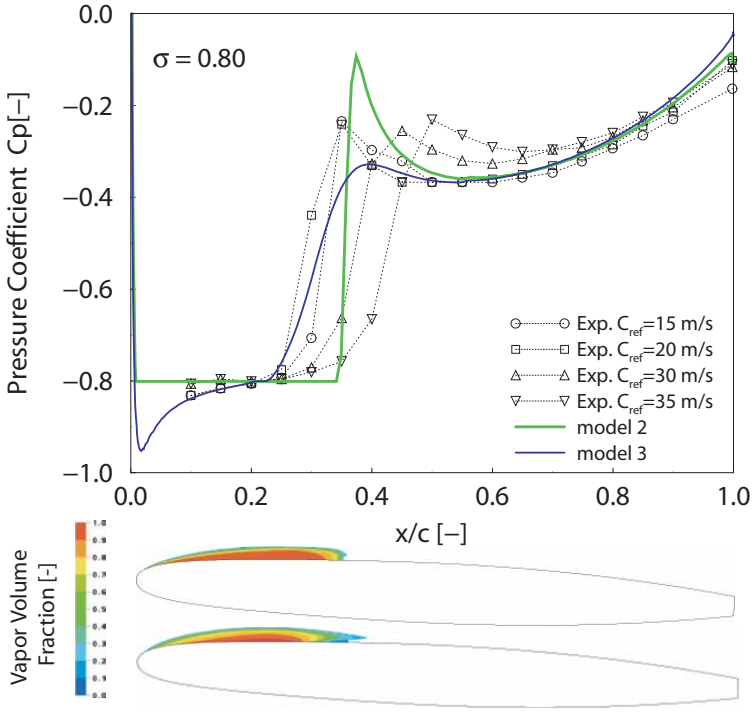

Figure 5.4: Pressure distribution and cavity shape on NACA0009
top : Model 2, bottom : Model 3, i=2.5°, σ=0.80

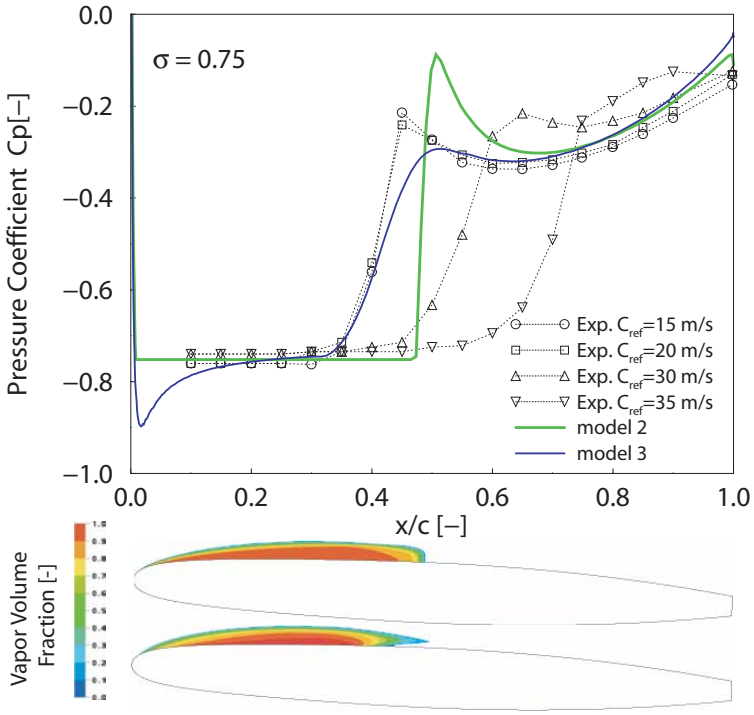

Figure 5.5: Pressure distribution and cavity shape on NACA0009
top : Model 2, bottom : Model 3, i=2.5°, σ=0.75

and pressure threshold. As expected, the cavity, , becomes larger with decreasing cavitation number. However the models exhibit very different flow behavior at the cavitation detachment and closure regions.

Model 2, based on a state equation ($\rho = \rho(p)$) assumes instantaneous phase change and leads to instantaneous cavity inception and closure. The pressure is always kept over the vapor pressure ($C_p \geq -\sigma$) and the pressure at the cavity closure shows a sharp peak. This is mainly due to the sudden pressure recovery which occurs principally at the confined region at the cavity closure.

Model 3, based on a transport equation for the phase change, leads to a smoother transition of the pressure field over the hydrofoil. Pressures below the vapor pressure ($C_p \leq -\sigma$) at the cavity detachment, shown in the graphic, are due to the inertia of the vaporization process. The closure region does not exhibit the sharp form as computed by the state-equation model. The closure region is smoother and closer to the experimental data. The transport equation formulation moderates the pressure rise within the cavity wake, and the pressure recovery is spread over a larger domain at the cavity closure.

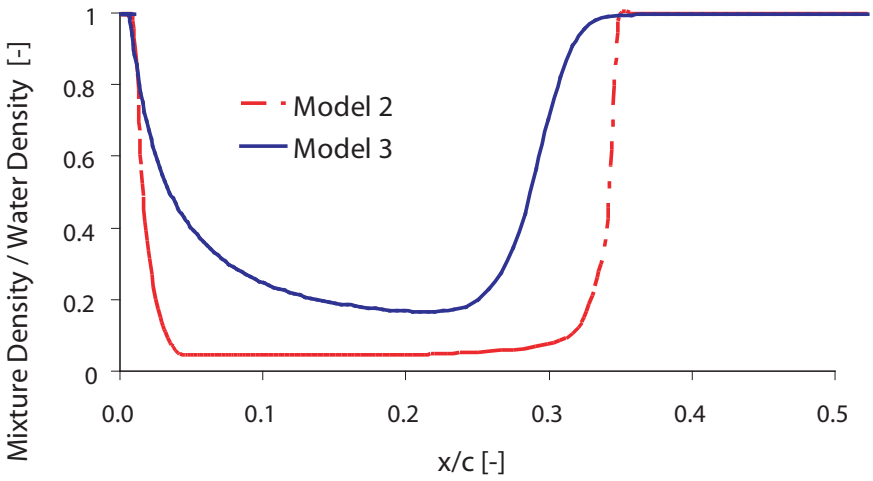

Figure 5.6: Dimensionless mixture density along the hydrofoil suction side at σ=0.80, i=2.5°, C_{ref}=20 m/s

The mixture density value in the cavity is reported in Fig. 5.6. The density computed by both models is noticeably different, even if the positions values of the detachment and the closure of the cavity are practically the same. For the state equation model (model 2) the density is driven by the pressure, meaning that the model recovers the vapor density inside the cavity for $p = p_v$. For the transport equation based model (model 3), the computed density ratios can be controlled through adjustment of the model parameters providing very different solutions.

For the transport equation based model (Model 3), and inside the cavity, the variable density field is generated through source terms for destruction and production of the vapor phase. As the resolution proceeds a balance between production and destruction terms, the solution is a cavity profile with uniform pressure and density field. The beginning

of the cavity shows low transition of the pressure, volume fraction and density. Due to the lack of detailed experiments concerning the mixture composition (vapor or liquid fractions) it is not possible to state a reasonable conclusion regarding this field.

5.2.2 Velocity Distribution

In this section, the velocity distribution around a developed leading edge cavity is analyzed. The case study concerns the NACA0009 hydrofoil at an incidence angle of i= 2.5°, a reference velocity of C_{ref}=20 m/s, with a cavitation number of σ=0.81 where the experimental data are reported by Dupont [50]. This regime is characterized by an attached cavity ($L_c/L \sim 33\,\%$). The pressure distribution and the cavity shape for the three used models are reported in Fig. 5.8.

As aforementioned in experimental procedure, velocity profiles from [50] (cf. Fig. 5.7) are obtained using the laser-Doppler velocimetry which allows to measure both components of the 2D flow velocities (C_x, C_y) at different locations on the hydrofoil. Three sections are located at the top of the cavity (x/L = 10, 20 and 30%) and seven stations in its wake (x/L = 40–100 %).

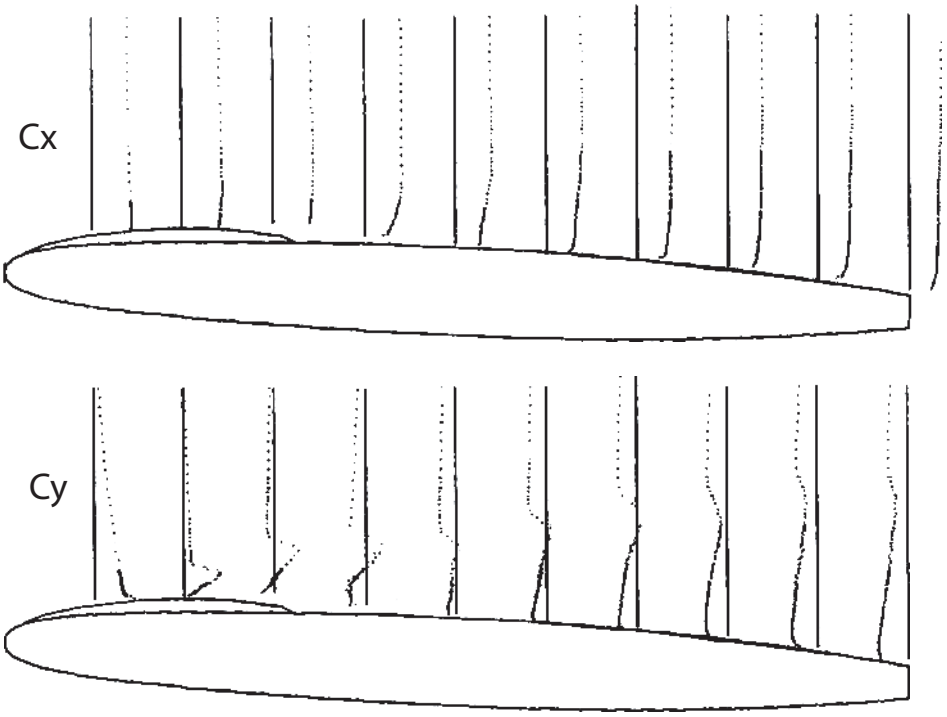

Figure 5.7: Averaged velocity profiles measurements on the NACA009 suction-side at 2.5° of incidence, 20 m/s of upstream velocity, and cavitation number of 0.81 [50].

Figure 5.7 reports the experimental data of both components of the velocity vectors C_x and C_y. In the wake of the cavity, a strong deviation of the flow due to the presence of the cavity is observed. This velocity perturbation can be seen at the first location (10%) and is amplified to the mid-chord distance where it starts to dissipate till the end of the hydrofoil.

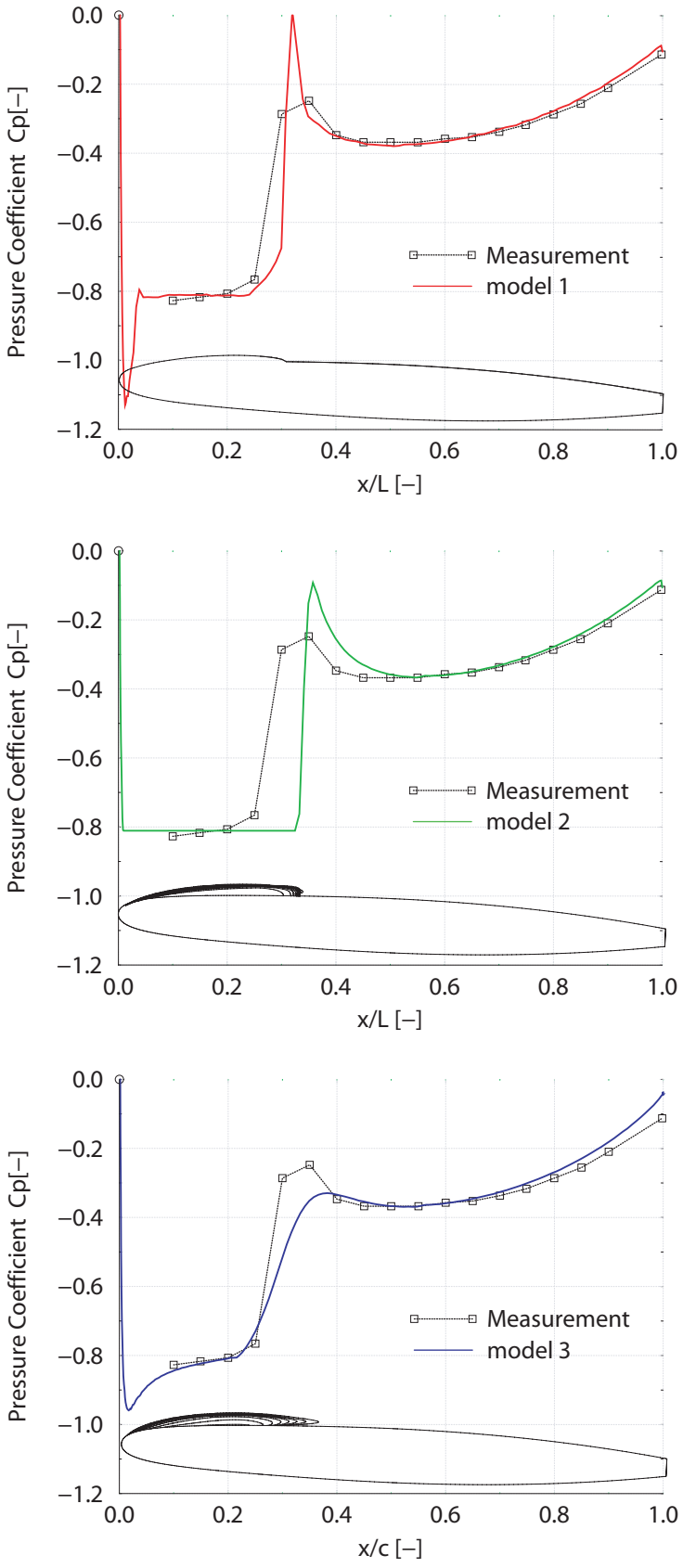

Figure 5.8: Pressure distribution and cavitation development for cavitation regime: i=2.5, C_{ref}=20 m/s, σ=0.81. Comparison between the used models

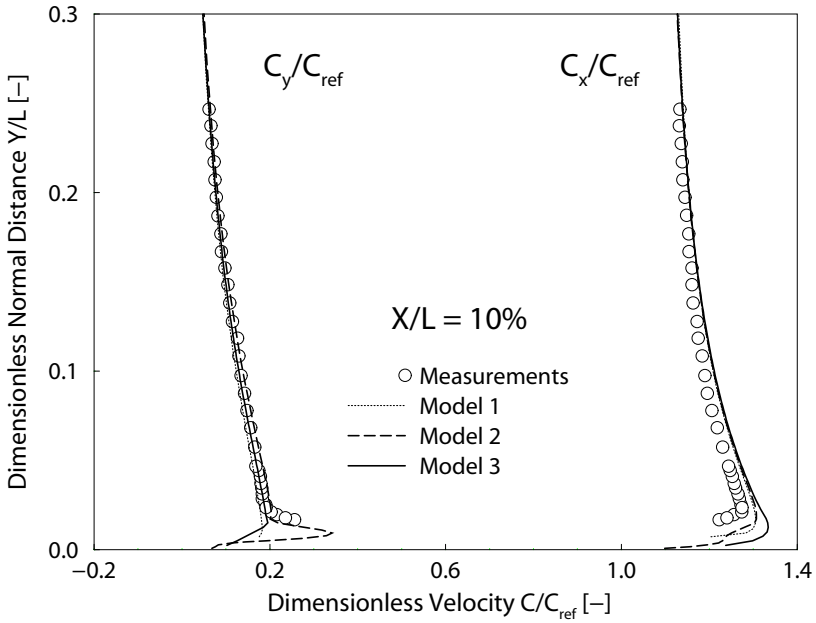

Figure 5.9: Computed and measured averaged dimensionless velocity profiles C_x/C_{ref} and C_y/C_{ref} on the NACA009 hydrofoil suction-side at 2.5° of incidence, 20 m/s of upstream velocity, and cavitation number of 0.81. Profiles at 10% of chord length

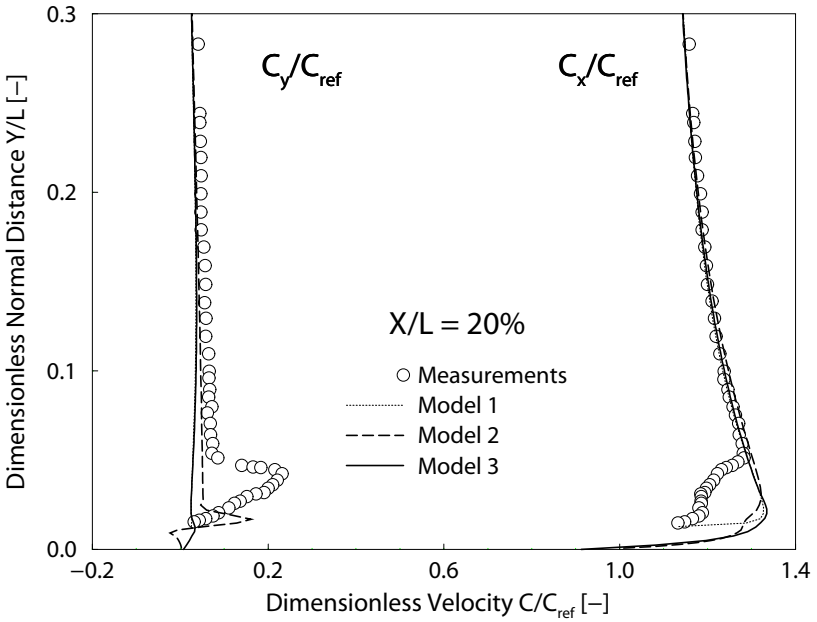

Figure 5.10: Computed and measured averaged dimensionless velocity profiles C_x/C_{ref} and C_y/C_{ref} on the NACA009 hydrofoil suction-side at 2.5° of incidence, 20 m/s of upstream velocity, and cavitation number of 0.81. Profiles at 20% of chord length

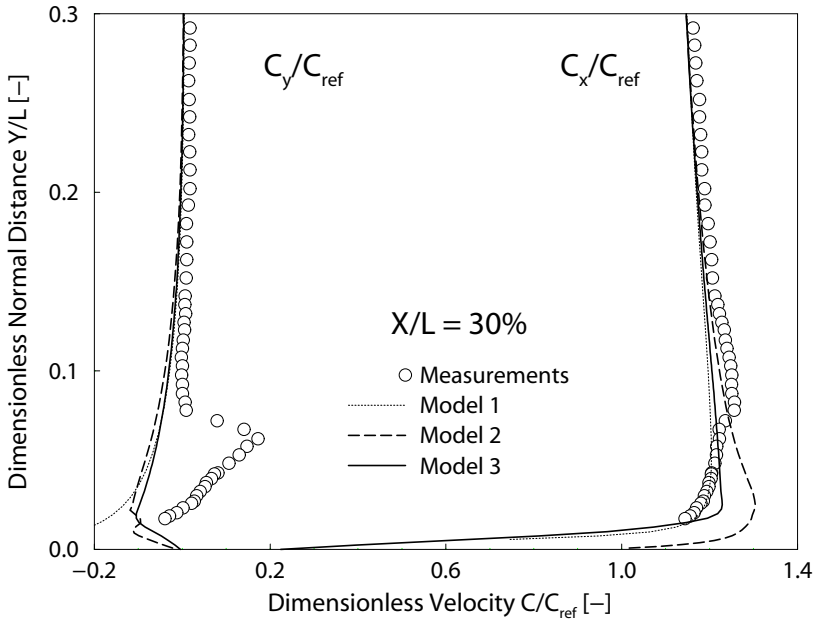

Figure 5.11: Computed and measured averaged dimensionless velocity profiles C_x/C_{ref} and C_y/C_{ref} on the NACA009 hydrofoil suction-side at 2.5° of incidence, 20 m/s of upstream velocity, and cavitation number of 0.81. Profiles at 30% of chord length

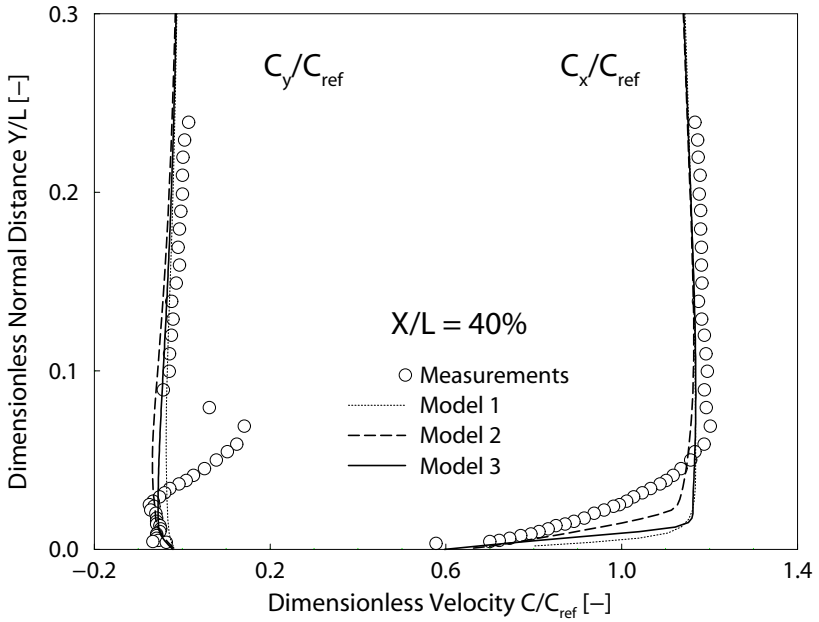

Figure 5.12: Computed and measured averaged dimensionless velocity profiles C_x/C_{ref} and C_y/C_{ref} on the NACA009 hydrofoil suction-side at 2.5° of incidence, 20 m/s of upstream velocity, and cavitation number of 0.81. Profiles at 40% of chord length

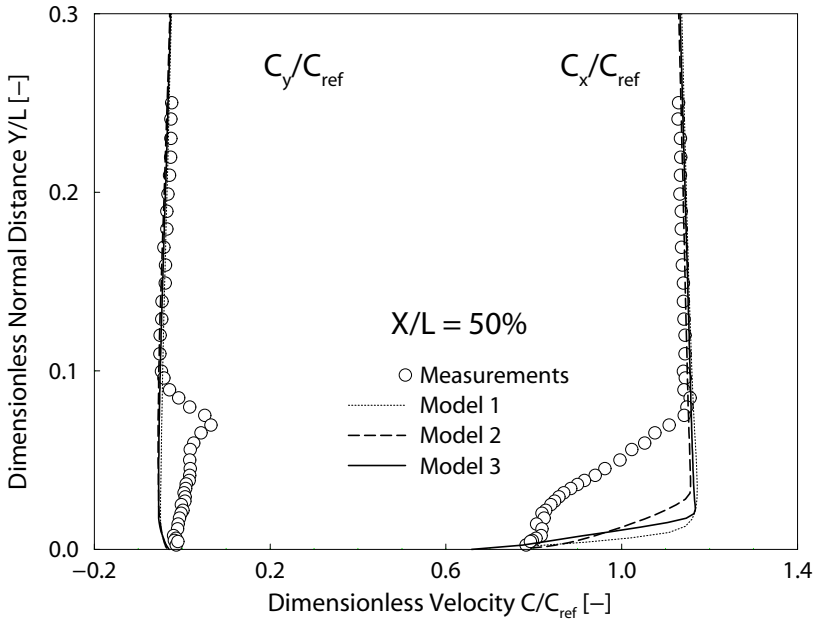

Figure 5.13: Computed and measured averaged dimensionless velocity profiles C_x/C_{ref} and C_y/C_{ref} on the NACA009 hydrofoil suction-side at 2.5° of incidence, 20 m/s of upstream velocity, and cavitation number of 0.81. Profiles at 50% of chord length

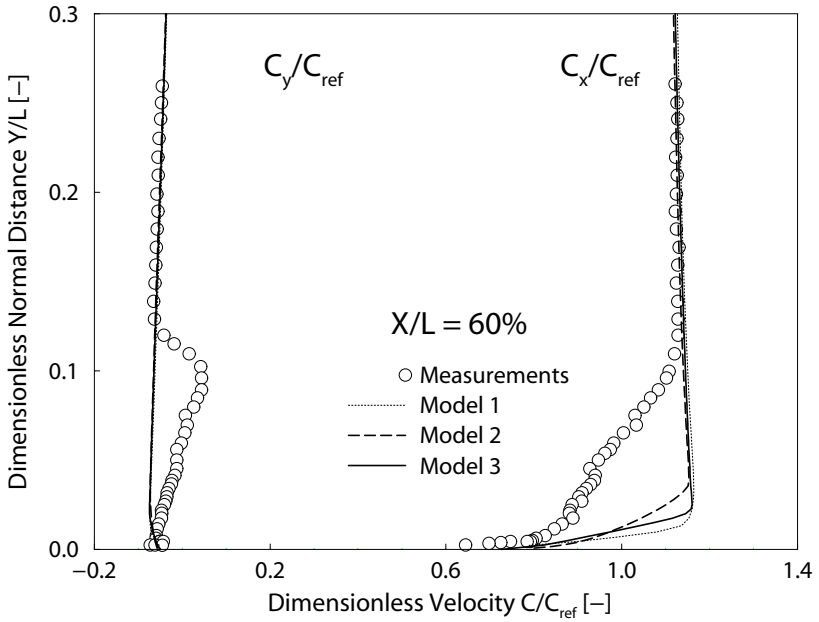

Figure 5.14: Computed and measured averaged dimensionless velocity profiles C_x/C_{ref} and C_y/C_{ref} on the NACA009 hydrofoil suction-side at 2.5° of incidence, 20 m/s of upstream velocity, and cavitation number of 0.81. Profiles at 60% of chord length

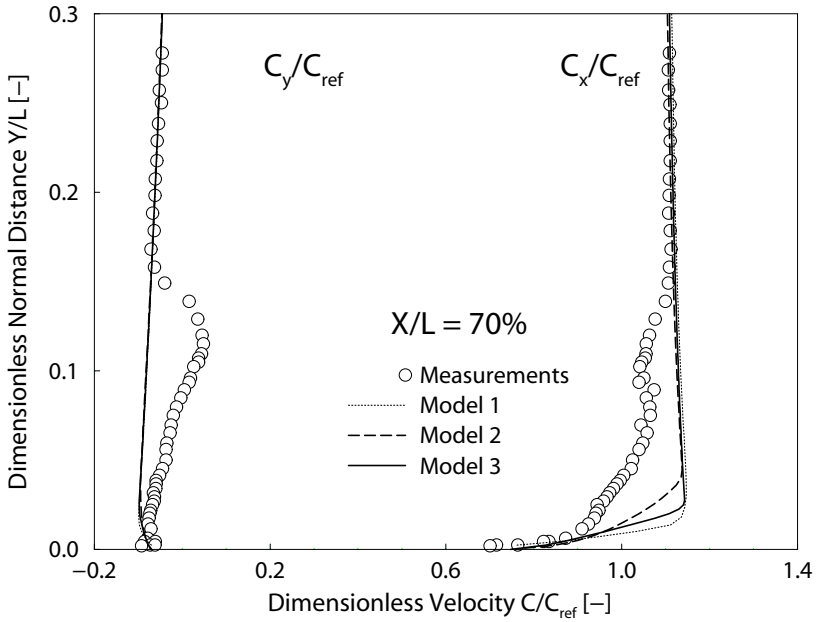

Figure 5.15: Computed and measured averaged dimensionless velocity profiles C_x/C_{ref} and C_y/C_{ref} on the NACA009 hydrofoil suction-side at 2.5° of incidence, 20 m/s of upstream velocity, and cavitation number of 0.81. Profiles at 70% of chord length

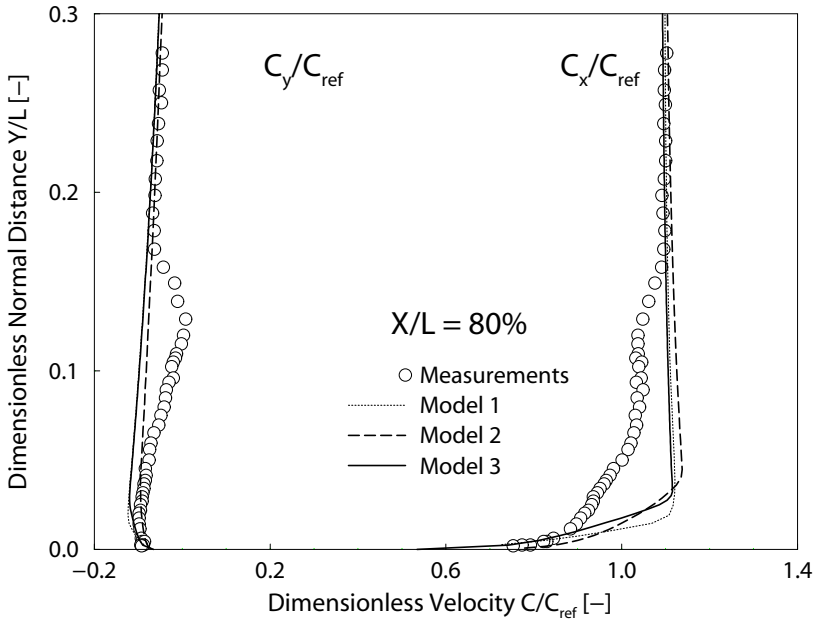

Figure 5.16: Computed and measured averaged dimensionless velocity profiles C_x/C_{ref} and C_y/C_{ref} on the NACA009 hydrofoil suction-side at 2.5° of incidence, 20 m/s of upstream velocity, and cavitation number of 0.81. Profiles at 80% of chord length

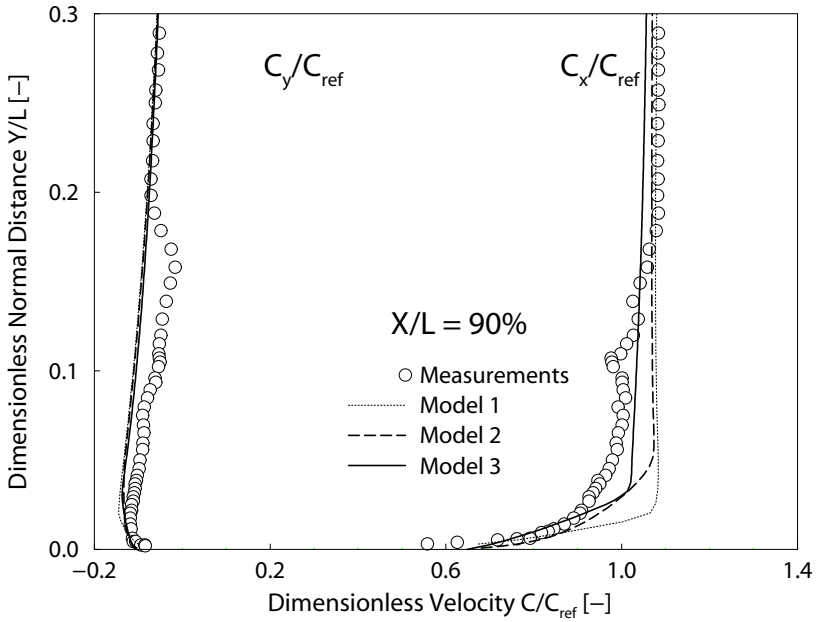

Figure 5.17: Computed and measured averaged dimensionless velocity profiles C_x/C_{ref} and C_y/C_{ref} on the NACA009 hydrofoil suction-side at 2.5° of incidence, 20 m/s of upstream velocity, and cavitation number of 0.81. Profiles at 90% of chord length

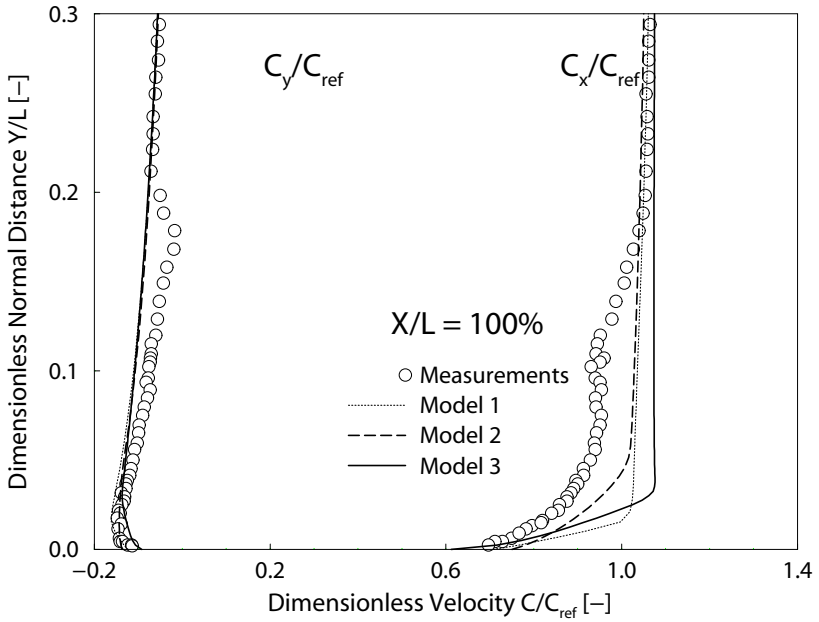

Figure 5.18: Computed and measured averaged dimensionless velocity profiles C_x/C_{ref} and C_y/C_{ref} on the NACA009 hydrofoil suction-side at 2.5° of incidence, 20 m/s of upstream velocity, and cavitation number of 0.81. Profiles at 100% of chord length

Figures 5.9 - 5.18 show the comparison between the measured velocity profiles and the simulations performed with the three models. The predicted velocity profiles of the main flow far from the wall is in good agreement with measurements. In the near-wall and in the wake region, the models fail to reproduce the complex cavitation flow-field. In fact, the wake of the cavity which can be highly unsteady, exhibits sharp velocity gradients which are very difficult, if not impossible to reproduce with steady state computations. The turbulence assumptions play also a major role in modelling these flow structures.

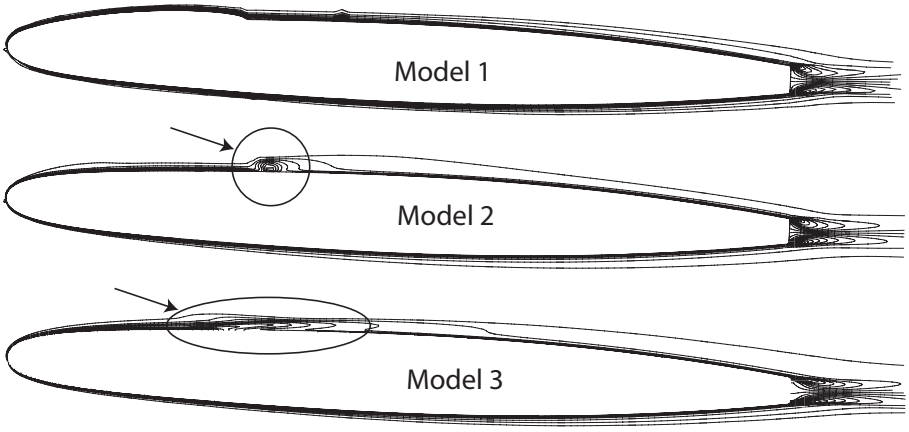

Figure 5.19: Iso-spanwise vorticity lines on the NACA0009, i=2.5°, C_{ref}=20 m/s, σ=0.81

Figure 5.19 displays the lines of iso-vorticity on the hydrofoil. Model 1 does not show any generation of vorticity in the wake of the cavity. Models 2 and 3 show a high vorticity level generation downstream of the cavity closure. It is diffused on a large domain for model 3 and well concentrated in the case of model 2. Considering the fact that adverse pressure gradients and the flow recovery at the cavity closure generates a recirculation zone behind an attached cavity, a vorticity zone generation takes place assuming that the pressure driven the baroclinic term is the main reason of this production (Eq. 5.1).

$$\frac{\partial \vec{\omega}}{\partial t} + \nabla \cdot (\vec{\omega} \cdot \vec{C}) = \frac{1}{\rho^2} \nabla p \cdot \nabla \rho + \nu \nabla^2 \vec{\omega} \tag{5.1}$$

Recent experiments [67] have shown that vorticity production occurs at the closure region of attached cavities due to the baroclinic torque. As shown in Fig. 5.19, the present computations indicate production of vorticity at the closure region for both multiphase cavitation models considered. These results are also in agreement with different experimental investigations highlighting the high vorticity flow in the wake of the cavity and the dynamics of generated vortices downstream of a leading edge cavitation [15; 14; 50; 91]. However, there is no additional production of vorticity at the front part of the cavity indicating that the density and the pressure fields are correctly computed. Their gradients are parallel without causing baroclinic vorticity generation which is in agreement with other transport equation based model investigations [125].

5.2.3 Hydrodynamic Forces

Developed cavitation can induce performance breakdown on hydrofoils. This is one of the main negative effects of cavitation. To evaluate the models concerning this issue, the cavitation number is decreased till reaching hydrodynamic performance alteration as observed in experiments.

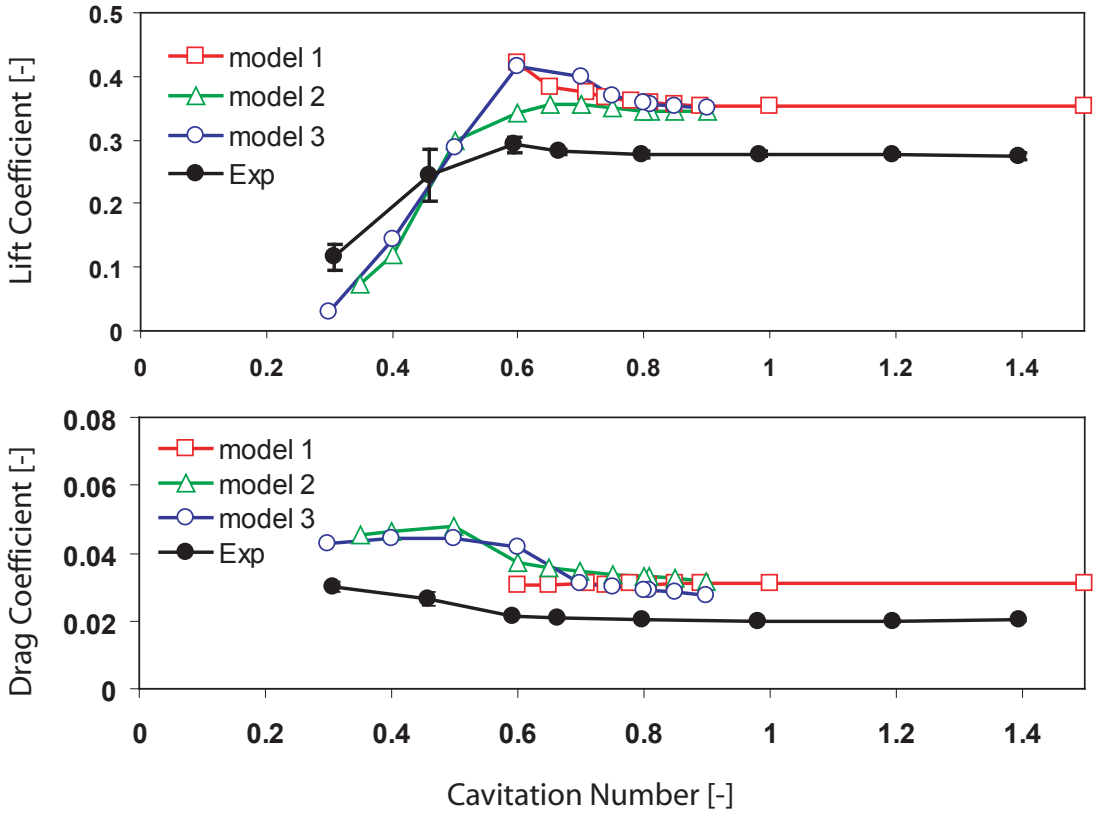

Figure 5.20: Hydrodynamic forces alteration with cavitation development

Figure 5.20 shows the lift (C_L) and the drag (C_D) evolution with the cavitation number σ. Without focussing on the absolute values and excluding Model 1 which can not compute the super-cavitation regimes, the Models 2 and 3 have a satisfactory threshold where hydrodynamic performance is altered by cavitation. The two models predict sooner lift and drag increase ($\sigma \sim 0.8$), and predict well the beginning of the lift drop ($\sigma \sim 0.6$).

The computations done with Models 2 and 3 are reported in Fig. 5.21 showing the cavitation flow for different cavitation number values. The super-cavitation regime is predicted up to $\sigma \sim 0.3$ and the cavitation numbers corresponding to the lift and drag decrease have thick partial cavities with large recirculating zones.

The decrease in performance can be explained by the alteration of the flow on the pressure side. This is easily shown by the location of the stagnation point moving upstream to the suction side. In fact, as the recirculation is only constant when the suction side flow is altered (in cavitation occurrence), it does not have perceptible change on the blade lift. As the cavity extends, the flow in its wake, disturbs the trailing edge flow, and thereby,

the suction side flow, altering the entire circulation around the hydrofoil and causing the sudden drop of the lift.

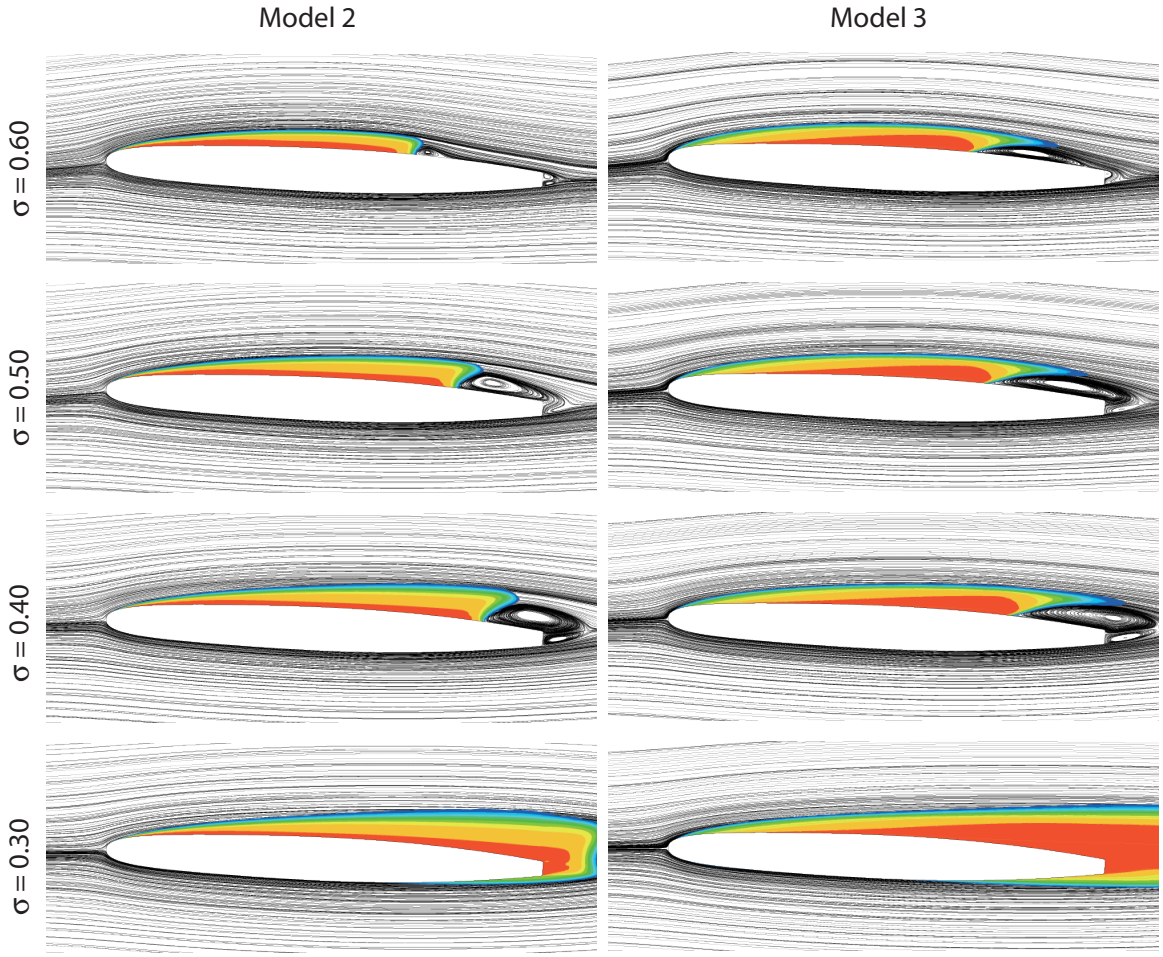

Figure 5.21: Cavitation development for different cavitation number values

5.3 Model Analysis

A typical attached partial cavity is presented in the case of a 2D hydrofoil. Computations of the steady-state flow for different cavitation regimes are done for the main three cavitation models one can find in literature and the results are compared to the experimental data. The pressure distribution and the cavity shape are well predicted by all the models. The transport equation based model shows the best agreement with experiments. The steady-state RANS computations with k-ε turbulence model fail to predict the measured velocity profiles in the wake of the cavity. Indeed, analyzing the flow, this region is characterized by high vorticity field, and seems to be hard to model in steady-state calculations. Both mixture models predict the strong vorticity generation in the wake of the cavity, which is in agreement with several experimental investigations. The models predict the cavitation induced performances alteration. Even if the computed values are different

from the measured ones, the processes behind the hydrodynamic performance alteration are captured by the models.

Model 1 based on interface tracking methodology reproduces the main leading edge cavitation flow field. The pressure distribution and cavity shape are well predicted. The model can predict the negative pressures upstream of the cavity. This is done by the imposition of the detachment point at the critical radius ($R = R_c$) in the Rayleigh-Plesset initial cavity estimation, instead of the standard formulation ($p = p_v$) [8; 9]. The main shortcomings of the model are that the vapor phase is not computed and the modelling of the closure region. This is the main reason for not predicting the vorticity in the wake of the cavity. However, for partial quasi-steady state cavities, the model's hypotheses are justified leading to satisfactory results as compared to multiphase flow models.

Model 2 based on instantaneous formulation of the phase change leads to a sudden change in the fluid properties and the calculations has numerical difficulties. The advantage of the model is its thermodynamic concept which does not need adjustable coefficients. However, this formulation based on static concept has a single formulation for both vaporization and condensation processes and does not take into account the timescale difference between the main flow and the local cavitation phenomenon preventing the possibility of simulating dynamic effects like cavitation delay.

Model 3 which is based on transport equation hypothesis, exhibits smoother transition leading to the possibility of predicting cavitation delay. The separation in condensation and vaporization processes has the advantage of localizing the collapse region as well as using the model with different formulation for both processes. The model shortcoming resides in empirical constants in the mass transfer term leading to an adjustable (tuned) model. The vorticity field, in agreement with the experiments, shows a generation only at the cavity closure.

Chapter 6

Maximum Tensile Stress Criterion for Cavitation Inception

Cavitation can take place in localized areas where the hydrodynamic parameters allow the rupture of the fluid continuum. Figure 6.2 shows the leading edge cavitation detachment over a 2D hydrofoil with $1\,\mu m$ rms value of the surface roughness, a constant incidence angle and a constant cavitation number. The only variable hydrodynamic parameter between the different pictures (a-d) is the reference velocity ($12-28\,\mathrm{m/s}$) highlighting the influence of the Reynolds number on a cavitation flow.

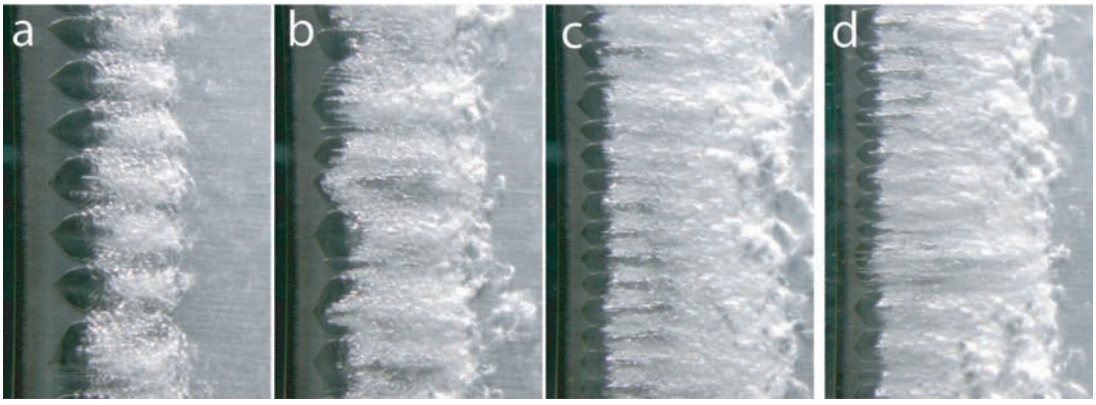

Figure 6.1: Isolated cavities (spots) over a non polished NACA0009 hydrofoil (σ=1, α=3°, rougness$\sim$1 μm) a) 12 m/s, b) 14 m/s, c) 18 m/s, d) 28 m/s, [69]

In theory, the hydrofoil has a uniform roughness height ($k_s \sim 1\mu m$), but a single roughness element can be at the origin of this phenomenon (cavities detach from a single point). At lower speeds (a), the first cavitation spots take place in the hydrofoil at a distance from the leading edge area which is far from the minimum pressure location and has a uniform spanwise distribution. By increasing the speed, these spots move upstream to the leading edge and their number is multiplied leading to uniform leading edge detachment near the minimum pressure.

If we analyze with dimensionless variables, the Cp and σ remain constant and the threshold of cavitation and its location should be constant. If we analyze with dimensional

variables, even if the pressure threshold decrease, the cavitation area which is concerned by cavitation is the same, and there is no reason for cavitation development changes with the velocity change. One may deduce that the cavitation inception threshold based on pressure alone is not sufficient to describe the cavitation development.

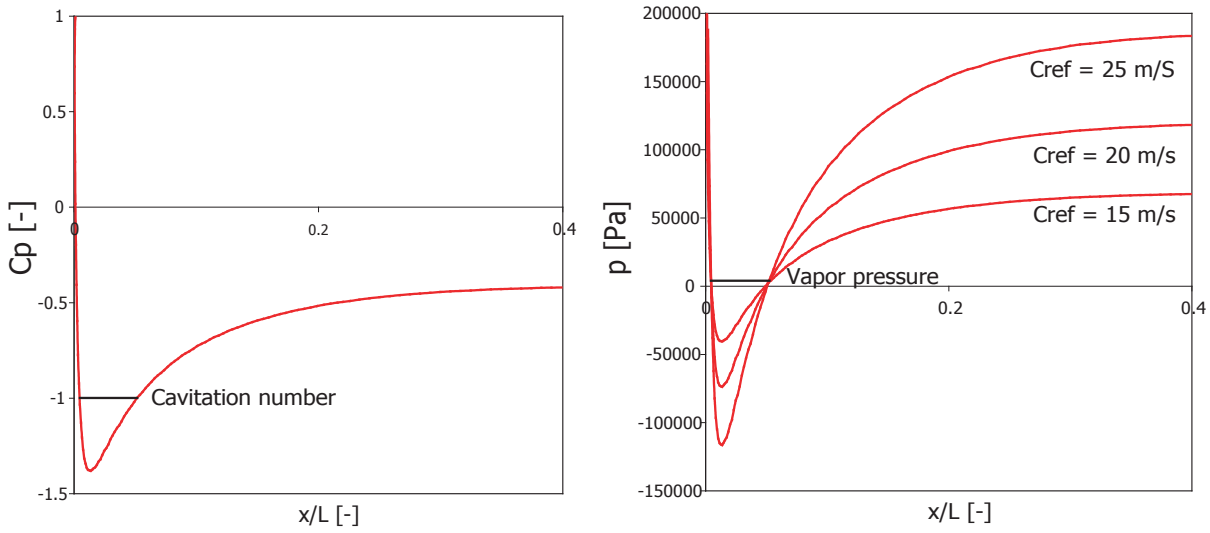

Figure 6.2: NACA0009 pressure profile at fixed σ and incidence angle

6.1 Maximum Tensile Stress Criterion

In moving incompressible liquids, the pressure is not the only fundamental dynamic variable, and the problem of the cavitation inception formulated in terms of breaking strength has been reported by Joseph et al. [79; 105]. At each point in a Newtonian liquid, the state of stress can be determined by:

$$\bar{\bar{T}} = -p\bar{\bar{I}} + \bar{\bar{S}}(\vec{C}) \tag{6.1}$$

$$\bar{\bar{S}}(C) = 2\mu\bar{\bar{D}}(\vec{C}) \tag{6.2}$$

where p is the pressure, μ the effective viscosity and $\bar{\bar{D}}(\vec{C})$ the deformation rate tensor (symmetric part of the velocity gradient), defined for a 2D flow as:

$$\bar{\bar{D}} = \begin{bmatrix} \frac{\partial C_x}{\partial x} & \frac{1}{2}\left(\frac{\partial C_x}{\partial y} + \frac{\partial C_y}{\partial x}\right) \\ \frac{1}{2}\left(\frac{\partial C_x}{\partial y} + \frac{\partial C_y}{\partial x}\right) & \frac{\partial C_y}{\partial y} \end{bmatrix} \tag{6.3}$$

$$\bar{\bar{S}} = \begin{bmatrix} S_{11} & S_{12} \\ S_{12} & -S_{112} \end{bmatrix} = 2\mu\ \bar{\bar{D}} = 2\mu \begin{bmatrix} \frac{\partial C_x}{\partial x} & \frac{1}{2}\left(\frac{\partial C_x}{\partial y} + \frac{\partial C_y}{\partial x}\right) \\ \frac{1}{2}\left(\frac{\partial C_x}{\partial y} + \frac{\partial C_y}{\partial x}\right) & \frac{\partial C_y}{\partial y} \end{bmatrix} \tag{6.4}$$

The idea that vapor cavities open to maximum tension is endemic in the cavitation community, but seems not to have been noticed before because it requires to consider the state of stress and to determine the principal axes coordinates in which the tension is maximum. The system diagonalization is given by the angle θ as:

$$\begin{cases} \sin(2\theta) = S_{12}/\sqrt{S_{12}^2 + S_{11}^2} \\ \cos(2\theta) = S_{11}/\sqrt{S_{12}^2 + S_{11}^2} \end{cases} \tag{6.5}$$

and:

$$\bar{\bar{S}} = \sqrt{S_{12}^2 + S_{11}^2} \begin{bmatrix} 1 & 0 \\ 0 & -1 \end{bmatrix} = \begin{bmatrix} S_1 & 0 \\ 0 & -S_1 \end{bmatrix} \tag{6.6}$$

The stress in the principal coordinate system will be:

$$\bar{\bar{T}} = \begin{bmatrix} -p + S_1 & 0 \\ 0 & -p - S_1 \end{bmatrix} \tag{6.7}$$

and, for incompressible 2D Newtonian fluid:

$$S_1 = \mu_{\text{eff}} \sqrt{\left(2\frac{\partial C_x}{\partial x}\right)^2 + \left(\frac{\partial C_x}{\partial y} + \frac{\partial C_y}{\partial x}\right)^2} = \mu_{\text{eff}} \dot{\gamma} \tag{6.8}$$

where:

$$\dot{\gamma} = \sqrt{\bar{\bar{D}} : \bar{\bar{D}}} \tag{6.9}$$

$$\begin{aligned} \dot{\gamma}^2 = 2 &\left[\left(\frac{\partial C_x}{\partial x}\right)^2 + \left(\frac{\partial C_y}{\partial y}\right)^2 + \left(\frac{\partial C_z}{\partial z}\right)^2 \right] \\ &+ \left(\frac{\partial C_x}{\partial y} + \frac{\partial C_y}{\partial x}\right)^2 + \left(\frac{\partial C_x}{\partial z} + \frac{\partial C_z}{\partial x}\right)^2 + \left(\frac{\partial C_y}{\partial z} + \frac{\partial C_z}{\partial y}\right)^2 \end{aligned} \tag{6.10}$$

$\dot{\gamma}$ is the so-called shear strain rate and related to the second invariant of $\bar{\bar{D}}[C]$ [110; M1; M7]. The formulation used in Eq. 6.8 can be derived using the 2D formulation and the continuity equation for incompressible fluid.

We call $(-p+S_1)$ the maximum tension and $(-p-S_1)$ the minimum tension. If cavitation opens, it will open in the direction of maximum tension.

If we compare the parameter $(T_{11} = -p+S_1)$ with $(-p)$ alone: T_{11} has the effect of stress-induced tension and is an anisotropic tension. In the theory of stress-induced cavitation, the inception criteria will be [79]:

$$\begin{cases} p - S_1 < p_v \\ p - \mu_{\text{eff}}\dot{\gamma} < p_v \end{cases} \tag{6.11}$$

instead of the classical parameter $p < p_v$.

These results show that a cavitation criterion based on the maximum tensile stress (Eq. 6.11) takes into account both the isotropic inviscid contribution (p) as well as the non-isotropic viscous contribution ($\mu_{\text{eff}}\dot{\gamma}$).

In dimensionless formulation, for cavitation inception, this is expressed by:

$$C_p - \frac{S_1}{\frac{1}{2}\rho C_{\text{ref}}^2} < -\sigma \tag{6.12}$$

The main goal of the present investigation is to evaluate the non-isotropic viscous term. Obviously, this term is important if either μ_{eff} and $\dot{\gamma}$ is large. For the flow around streamlined bodies, this is the case in the vicinity of the leading edge. For a hydrofoil at a given angle of attack, the flow is strongly accelerated starting from the leading edge stagnation point, then is more or less abruptly decelerated. When focussing on the leading edge region, the potential flow theory coupled with the boundary layer computation, which is well established methodology developed for more than one century, provides a good accuracy for the pressure, velocity and stress distribution. Moreover, these computations provide an excellent benchmark test case for evaluating the term $\mu_{\text{eff}}\dot{\gamma}$ using 3D CFD codes.

Maximum Tensile Stress in Boundary Layer Flow

In boundary layer flow, the maximum tensile stress term:

$$S_1 = \mu_{\text{eff}}\sqrt{\left(2\frac{\partial C_x}{\partial x}\right)^2 + \left(\frac{\partial C_x}{\partial y} + \frac{\partial C_y}{\partial x}\right)^2} = \mu_{\text{eff}}\dot{\gamma} \tag{6.13}$$

is simplified to:

$$S_1 = \mu_{\text{eff}}\left(\frac{\partial C_x}{\partial y}\right) = \mu_{\text{eff}}\dot{\gamma} \tag{6.14}$$

which is the stress in 2D incompressible Newtonian fluid and is equivalent to the shear stress τ.

This reduces the stress theory for the cavitation inception criterion to:

$$C_p - C_f < -\sigma \tag{6.15}$$

This simplification is given by the boundary layer theory (cf. Appendix A), and the main characteristics of the flow near the wall, where only the tangential stress coming from $\frac{\partial C_x}{\partial y}$ has a non negligible value according to:

$$\begin{cases} \dfrac{\partial C_y}{\partial x} \approx \varepsilon \\ \dfrac{\partial C_x}{\partial x} \ll \dfrac{\partial C_x}{\partial y} \end{cases} \tag{6.16}$$

Two case studies are presented: the flow around a parabolic body and the flow around a 2D hydrofoil leading edge. The flow around a parabolic body at a given angle of attack is a test case for the computational methodology evaluation and the relevance of the added correction. The analytical solution is developed and the computation of the boundary layer from the pressure profile as well as an estimation of the stresses at the parabola wall and inside the boundary layer are performed. The study based on conformal mapping comes with an orthogonal grid and used for CFD evaluation. A fully CFD turbulent computation is made to evaluate the accuracy of a general CFD code to evaluate/compute the maximum tensile stress criterion.

The second case is a NACA0009 2D hydrofoil at an angle of attack. An inviscid flow solution is coupled with a boundary layer computation using different turbulence models is made to evaluate the tensile stress. A roughness-strip method is used to simulate a rough wall and to evaluate the ability of the proposed model to account for roughness and Reynolds effects for cavitation inception.

6.2 Parabolic Nose Case Study: Methods Evaluation

6.2.1 Flow around a Parabola Body

This part addresses the problem of evaluating the shear strain rate, namely the determination of the evolution of this parameter near the leading edge of a streamlined body. It is clear that the 'rounder' the nose, the smaller the shear stresses are induced; sharp noses exhibit higher shear stresses induced in the flow [145; 146]. The purpose of the present developments is first to evaluate the order of magnitude of the shear strain rate, and secondly to evaluate the efficiency of a general CFD code to estimate correctly this parameter.

The body of interest is a parabola at a given radius. It gives the advantage of encompassing a family of needed nose shapes and is well suited to isolate the leading-edge receptivity mechanism from other mechanisms. The infinitesimally thin plate is a limiting solution of the parabola when the nose of curvature goes to zero. The formulation of the problem is a two-dimensional analytical solution using potential theory and is similar to those proposed by Tuck et al. [145] and Haddad et al. [71]. The complete solution procedure is given in appendix B.

6.2.2 Boundary Layer Computations

The pressure profile ($Cp(s)$) given by the inviscid flow computation is used for the boundary layer computations starting from the stagnation point. The boundary layer differential formulation is used for this case (cf. Appendix A). The integral initial parameters at this point are the default values for the stagnation point formulation [153].

Skin Friction Evaluation

Figure 6.3 gives the computation of the boundary layer flow using differential equation resolution at different angles of attack ($\beta = 1.0$ and $\beta = 1.15$) with laminar flow and three different turbulence models (algebraic Baldwin-Lomax model, k-ω and stress-ω)

formulations. The β parameter is the characteristic value of the stagnation point in the analytical solution.

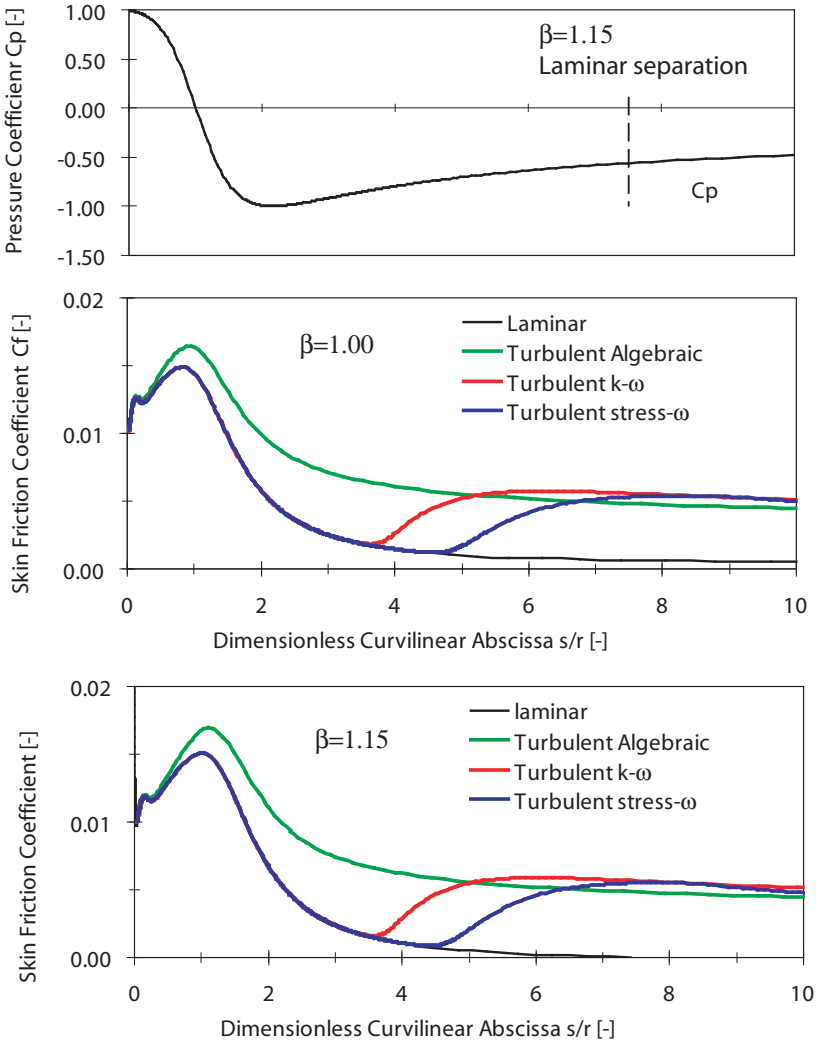

Figure 6.3: Skin friction evolution around the parabola body at $\beta = 1.0$, $\beta = 1.15$

Laminar boundary layer separation occurs at $\beta = 1.15$, which is similar to the results obtained by Werle and Davis (1972) and confirmed by Tuck et al. [145] giving the critical value of $\beta = 1.157$. Concerning the turbulence modelling, the k-ω and stress-ω models lead to very similar results, with the exception of the transition location, where the k-ω model exhibits sooner transition. The algebraic model, even if it is a simple way to describe a turbulent flow, shows a good agreement with the other turbulence models except in the transition region. The dimensionless skin friction coefficient based is reported for a value of $\beta = 1$ in Fig. 6.3. The graphs show the anisotropic stress value around $C_f = 0.01$ at the wall, leading to a dimensional value of the same order of vapor pressure (2000 Pa). This value is roughly the same around the region of minimum pressure. The value of the additive correction was also investigated for different nose radii ($R = 0.5$, 1.0, $2.0\,R_0$) and show that the correction has negligible change with the radius nose.

6.2.3 CFD Computations

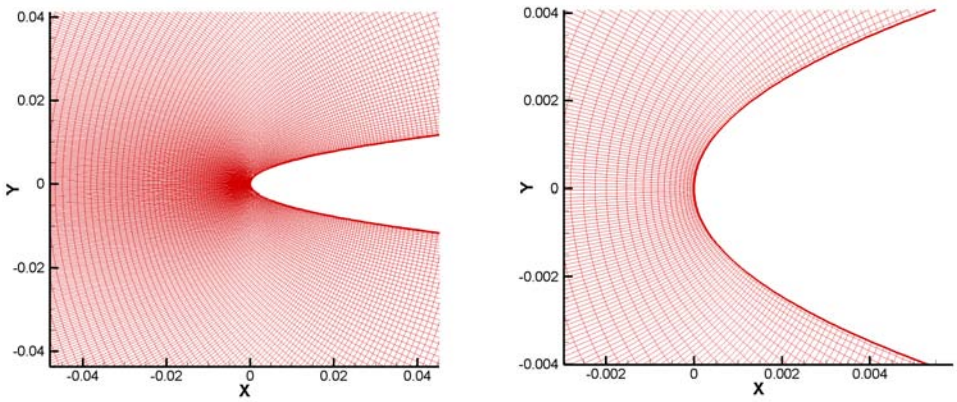

Figure 6.4: Parabola grid for the CFD computation

For the case of CFD computations, a grid stretched in both directions (power function for normal direction η, and centered hyperbolic sinus for ζ) is used (Fig. 6.4). An iterative way is done to find the appropriate angle of attack α for the CFD computations (for small values of the incidence angle, α is related to β via linear function, β=1 $\sim \alpha$=6.87). The pressure distributions on the parabola body are shown in Fig. 6.5 for the RANS [M1] and Euler [M7] computations and are compared to those obtained by the analytical solution. The graph shows a similar pressure distribution of the pressure for all the computations.

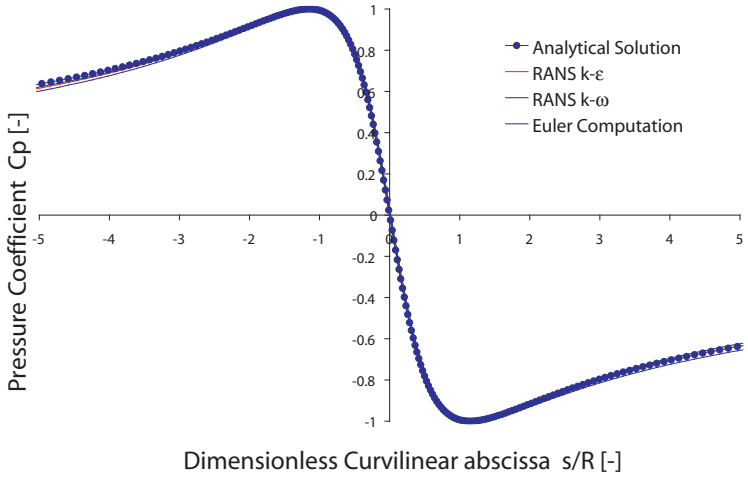

Figure 6.5: CFD Cp evaluation on the parabola body

The CFD computations which are for the same flow conditions as the analytical solution is then compared to the boundary layer computation in terms of viscous parameters. Two grids, having the same number of nodes and having different normal distribution are

reported for the RANS computation on the parabola body. (CFD-1: $10<y^+<60$, CFD-2: $y^+ \sim 2$).

The main differences between the two compared methods. The first is based on 2D parabolic equations of the boundary layer resoled 300 points in the normal direction in boundary layer thickness, the laminar, transitional and turbulent flow, using the boundary layer stagnation point hypothesis. The second resolves the 3D Navier-Stokes equations, assuming fully turbulent flow, and dealing with log-law hypothesis if necessary. Concerning the turbulence modelling, we used the k-ω model for the two simulation.

Figure 6.6 shows the distribution of the skin friction coefficient on the parabola suction side starting from the stagnation point and reports in different graphs two different skin friction computing methods. The first formulation is based on the shear strain rate computation (from the velocity gradients; $\tau = \mu_{\text{eff}}\dot{\gamma}$). The second is based on the formulation of the wall shear $\tau = \tau_{wall}$ (from log-law assumptions). It is obvious that the coarser the mesh is, the more different are the solutions between the two stress formulation evaluations. Fine meshes lead to closer solutions whereas the coarse mesh have large differences. Even if the wall shear gives a correction of the stresses at the wall when we are using the standard-mesh log-wall laws, the correct evaluation of the stress by a CFD computation needs a high resolution mesh at the boundary layer region. Figure 6.7 illustrates the neglected shear value obtained by the coarse mesh compared to the high resolution grid near the wall at the minimum pressure location.

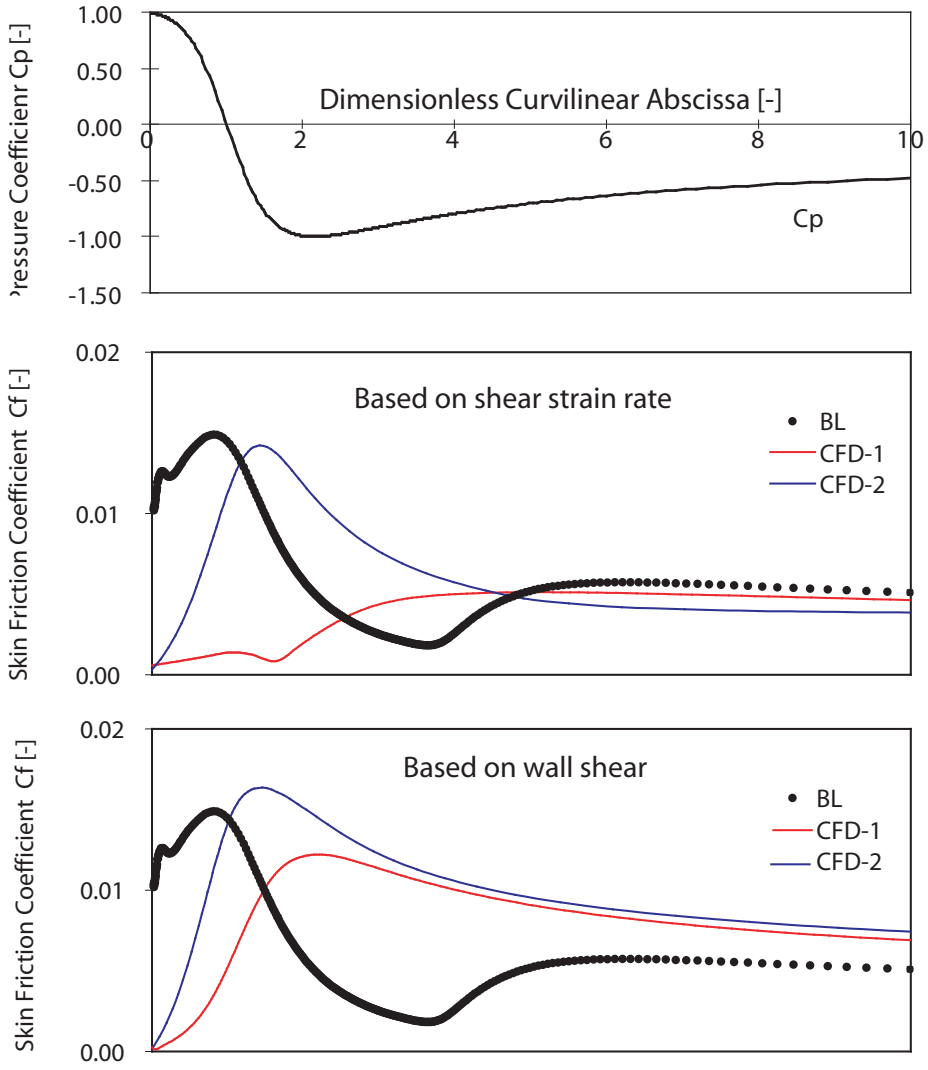

Figure 6.6: CFD stress evaluation on the parabola body

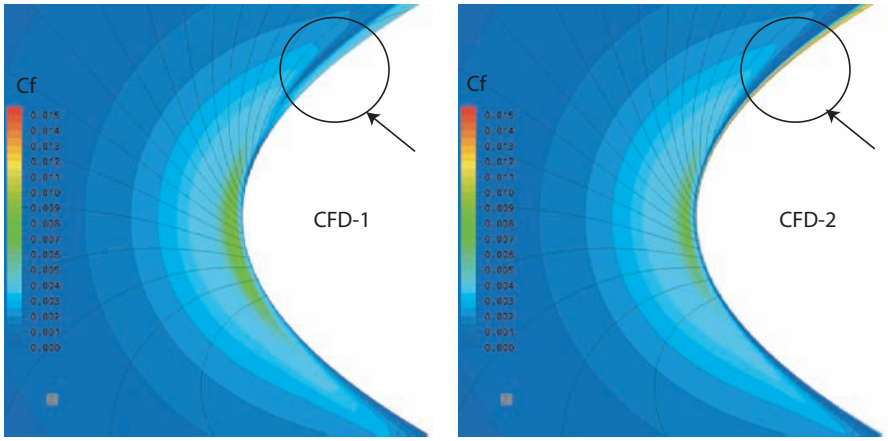

Figure 6.7: CFD stress evaluation around a parabola

6.3 NACA0009 Case Study: Roughness Effect

The case study concerns the 2D NACA0009 hydrofoil at 3° angle of attack. For the boundary layer integral formulation, the computation is directly given by the viscous/inviscid X-foil program [M5]. For the boundary layer differential formulation we use the Wilcox program [153]. The pressure distribution function of the dimension curvilinear abscissa is given by the inviscid computation. The pressure profile is transferred to the boundary layer computation starting from the stagnation point location.

6.3.1 Method Evaluation

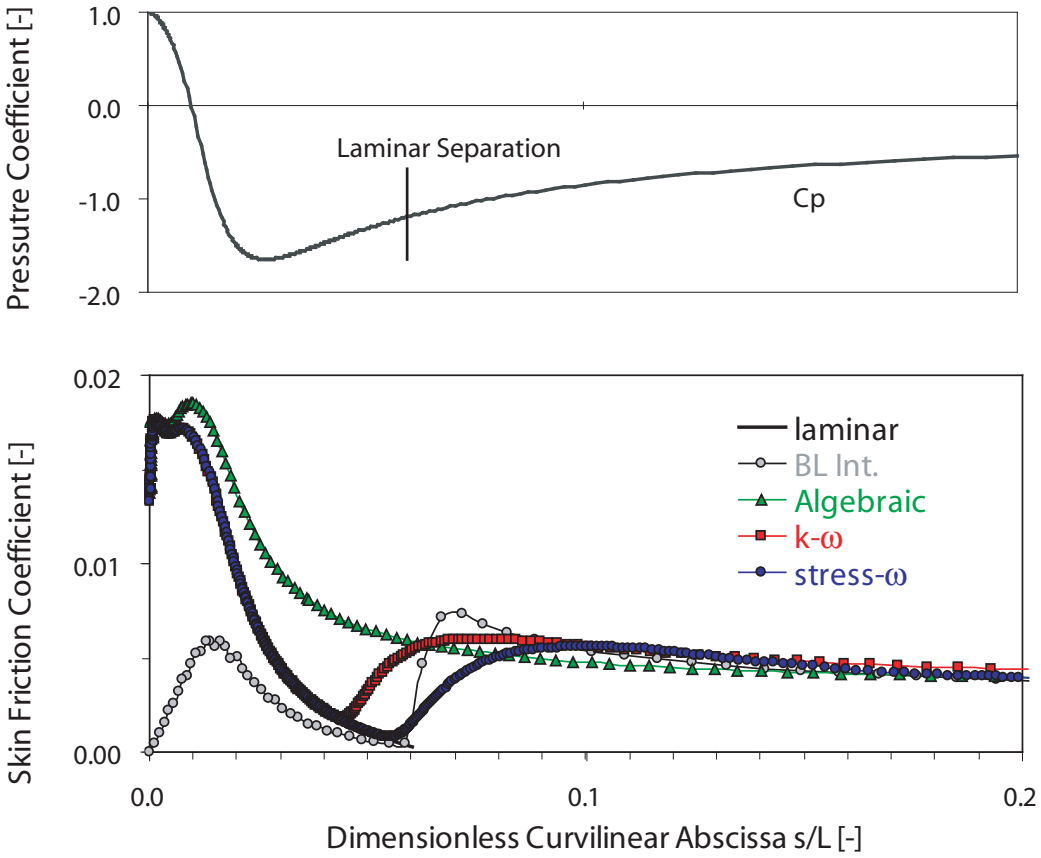

Figure 6.8: Skin friction evolution along the NACA0009 , C_{ref}=20 m/s, $\alpha = 3^{\circ}$

Two different methods are used to evaluate the skin friction on NACA0009 body at 3° angle of attack and stream-wise velocity of 20 m/s with a very small incoming turbulence intensity (less than 0.1%). The first method is the integral momentum method (BLI) proposed by Drela [M5; 48; 47], and the second is based on the solution of the differential equation of the boundary layer (BLD) including 3 turbulence models (algebraic model, k-ω and stress-ω) proposed by Wilcox [153].

Differential Equation Method (BLD)

- The computation gives a laminar boundary layer separation at $s/c = 0.06$ (downstream the minimum pressure and cavitation detachment).
- The two models k-ω and stress-ω have the same trend as the laminar computation before the separation and the transition for both models occurs at s/c = 4.5% and 6% respectively.
- The algebraic model, even if it gives the same results as the other turbulence models far from the stagnation point, exhibits a different solution close to the Cp_{min} location. The model does not show any transition.
- All turbulence models give the same evaluation of the skin friction far from the stagnation point, after the expected laminar-separation/transition.

Integral Momentum Method (BLI) The model, which is a simplified method of the boundary layer computation, has different estimation technique at the stagnation point in comparison with the differential equation method. Nevertheless, the model shows a transition exactly at the same location the of laminar separation predicted by the BLD method and shows the same behavior of the skin friction from this point.

Turbulence Level Influence

To avoid uncertainties concerning the upstream turbulence conditions, which can sensibly affect the turbulent boundary layer computation, the results of the computed skin friction for different incoming turbulence intensities, I = 1, 5, and 10, are investigated for the k-ω and stress-ω turbulence models. The computations show that increasing turbulence intensity moves the transition location upstream (earlier transition). As the location of cavitation interest (near Cp_{min}) is not affected by this parameter for I=1 to 10%, its influence is not taken into account in the further analysis.

Tensile Stress in the Boundary Layer

Figure 6.9 reports the skin friction coefficient, based on the stress $\tau = \mu_{\text{eff}} \frac{\partial C_x}{\partial n}$ as a function of the dimensionless normal distance y^+ for 20 m/s reference velocity at three different locations around the Cp_{min} (before and after with a shift $\varepsilon = 0.5\%$ L). The computations are done with laminar flow layer assumption.

The derivative of the stress with respect to the normal direction shows a negative slope before the Cp_{min} (accelerated flow), perpendicular one at the Cp_{min} location, and a positive slope thereafter (decelerated flow). At different locations, the maximum value of τ is always located either at the wall or inside the boundary layer for values of $y^+ \leq 10$. The order of magnitude of the additive term S_1 is of the same order of p_v ($C_f = 0.01$), which is similar to the one computed for the parabolic nose. In this region, the cavitation inception can be triggered by the shear flow and can reach the threshold of critical strength break even when the static pressure is higher than the vapor pressure.

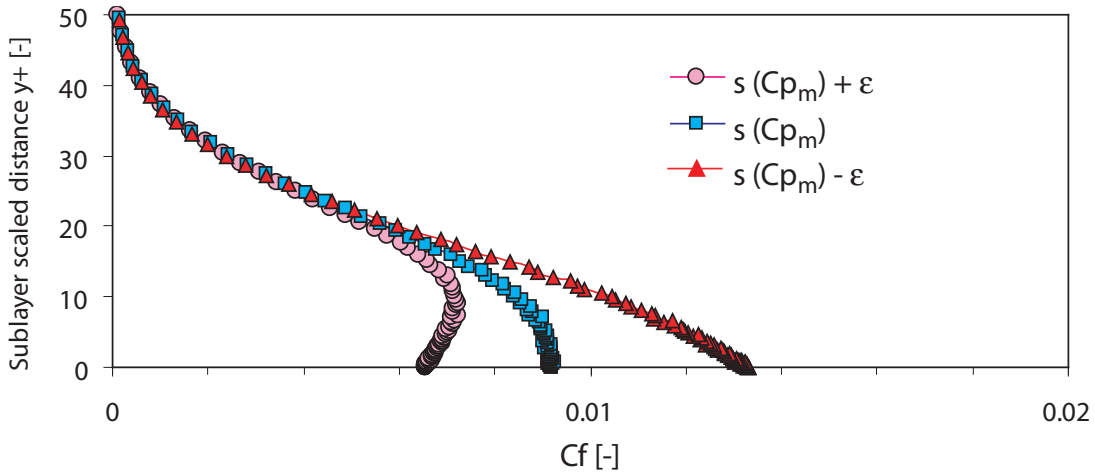

Figure 6.9: Evolution of the stress on the boundary layer flow at 3 stream-wise locations near the Cp_{min}. Reference speed, U=20 m/s

6.3.2 Effect of Surface Roughness

Knowledge of roughness effects is of practical importance since the degree of surface finish can be a controlling factor for the cavitation inception of a given configuration. Strictly speaking, roughness effects are a subset of viscous effects. Generally speaking, the roughness problem can be broken down into the effect of isolated asperities [5; 6].

Due to numerical stillness in direct modelling of a roughness element on the surface, a simple forced transition is made to have the desired transition before the Cp_{min} location. For any flow, we can always match the measured transition by adjusting the free-stream value of the turbulent kinetic energy k (or the turbulence Intensity I). This is satisfactory when the transition point occurs at a large Reynolds number. However, when transition is triggered at a relatively small Reynolds number, often unreasonable values of free-stream conditions are needed to cause transition, as seen in the turbulence intensity analysis.

Wilcox [153] offers an alternative calculation technique, known as the numerical roughness strip. The foundation of the concept rests upon the fact of using a finite value for ω at the surface, simulating surface roughness. Increasing surface roughness height correspond to decreasing surface value of ω according to:

$$\omega = \frac{C_\tau^2}{\nu} S_R \quad at \;\; y = 0 \tag{6.17}$$

with the roughness function correlations :

$$\begin{aligned} S_r &= (50/k_s^+)^2, \quad k_s^+ < 25 \\ S_r &= 100/k_s^+, \quad k_s^+ \geq 25 \end{aligned} \tag{6.18}$$

where $k_s^+ = C_\tau k_s/\nu$ is the dimensionless roughness height, and k_s the physical roughness height.

The second method, (BLI), offers a more practical way to use the model for transitional flows in describing the transitional region, as opposed to predicting transition onset. The method based on spatial amplification for the transition, the location can be chosen instead of the critical natural value. Due to the impossibility of extracting the needed values in the boundary layer outside the wall, this model is not investigated.

Figures 6.11 and 6.12 show the effect of simulated roughness in the stresses on the boundary layer. Figure 6.11 highlight the effect of roughness height on the transition of the boundary layer. This clearly affects the point of maximum tangential stress moving upstream. The reported values are not negligible and are related also to the Reynolds number characterizing the flow. Figure 6.12 shows an increase of the stresses by two main ways: surface roughness increase and reference speed increase (caused by change in transition location). Dimensional values of τ corresponding to the case of C_{ref}=20 m/s are: p_v for smooth wall, $2p_v$ and $3p_v$ for k_s=10μm and k_s=50μm.

Figure 6.10 illustrates a typical case of interest, comparing the isotropic inviscid parameter p alone, and with the anisotropic viscous τ correction in the case of flow over rough walls. Two points of importance can be deduced: first the added correction is not negligible ($C_f > 0.05$) and the cavitation inception is shifted for higher values of σ for the rough wall. Second, the supplied correction has no influence outside the Cp_{min} neighborhood, meaning that the developed cavitation pattern for both parameters for lower cavitation coefficients will be the same.

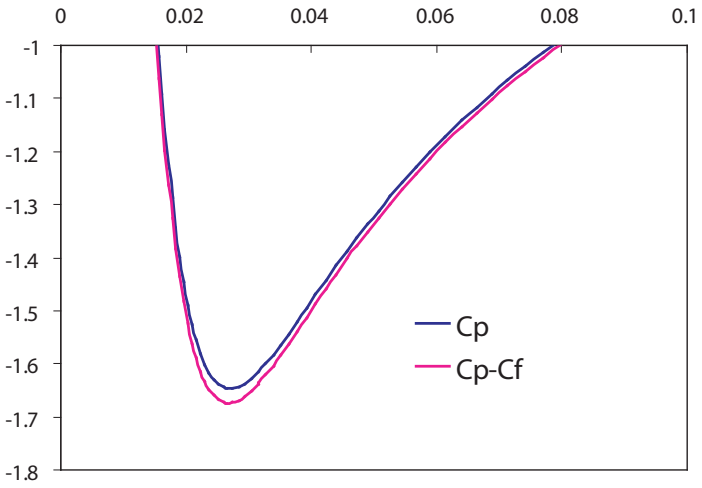

Figure 6.10: Effect of the added correction, C_{ref}=20 m/s, k_s=50μm

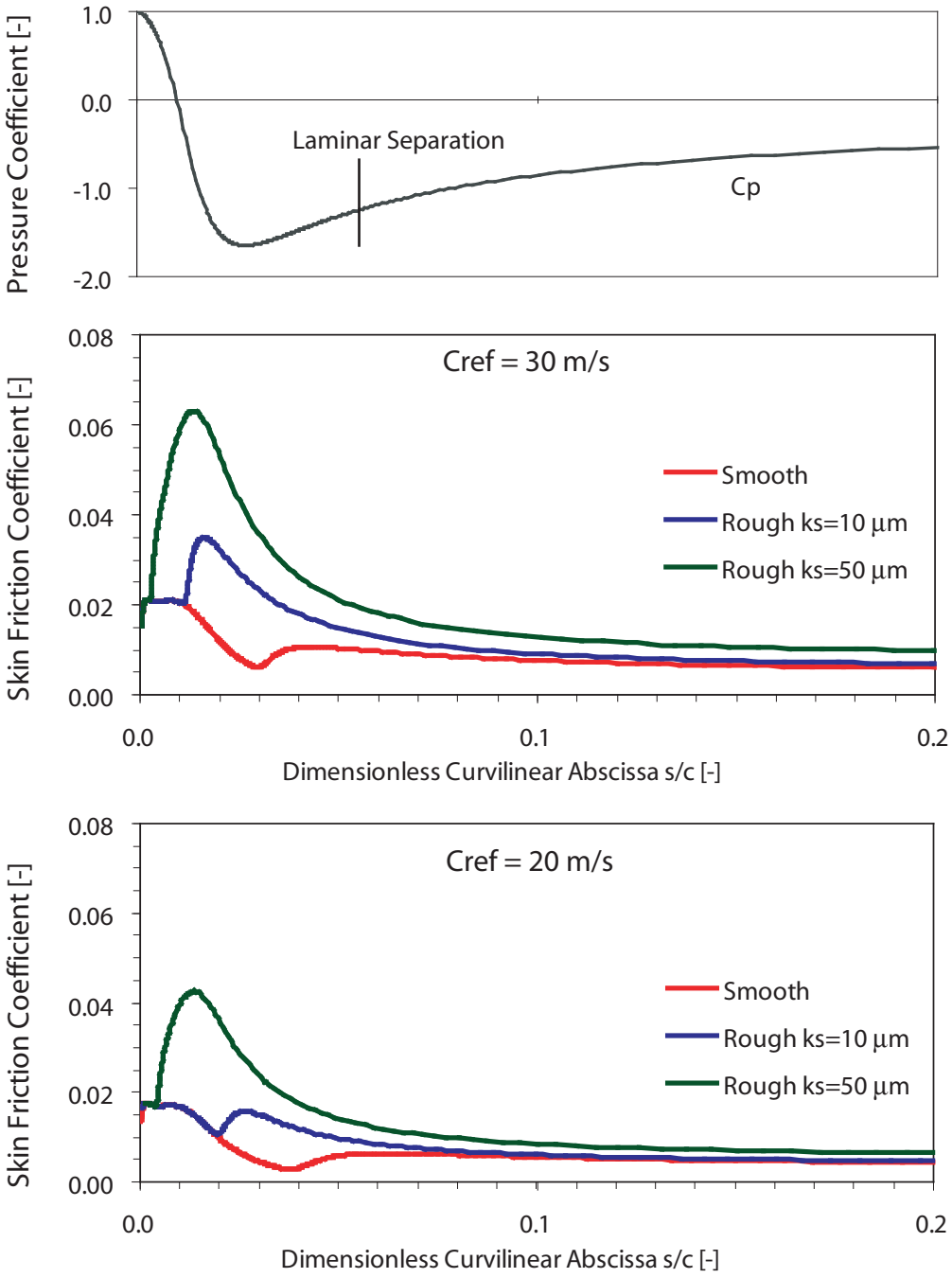

Figure 6.11: Evolution of the skin friction at the NACA0009 body due to forced transition of the boundary layer (rough strip)

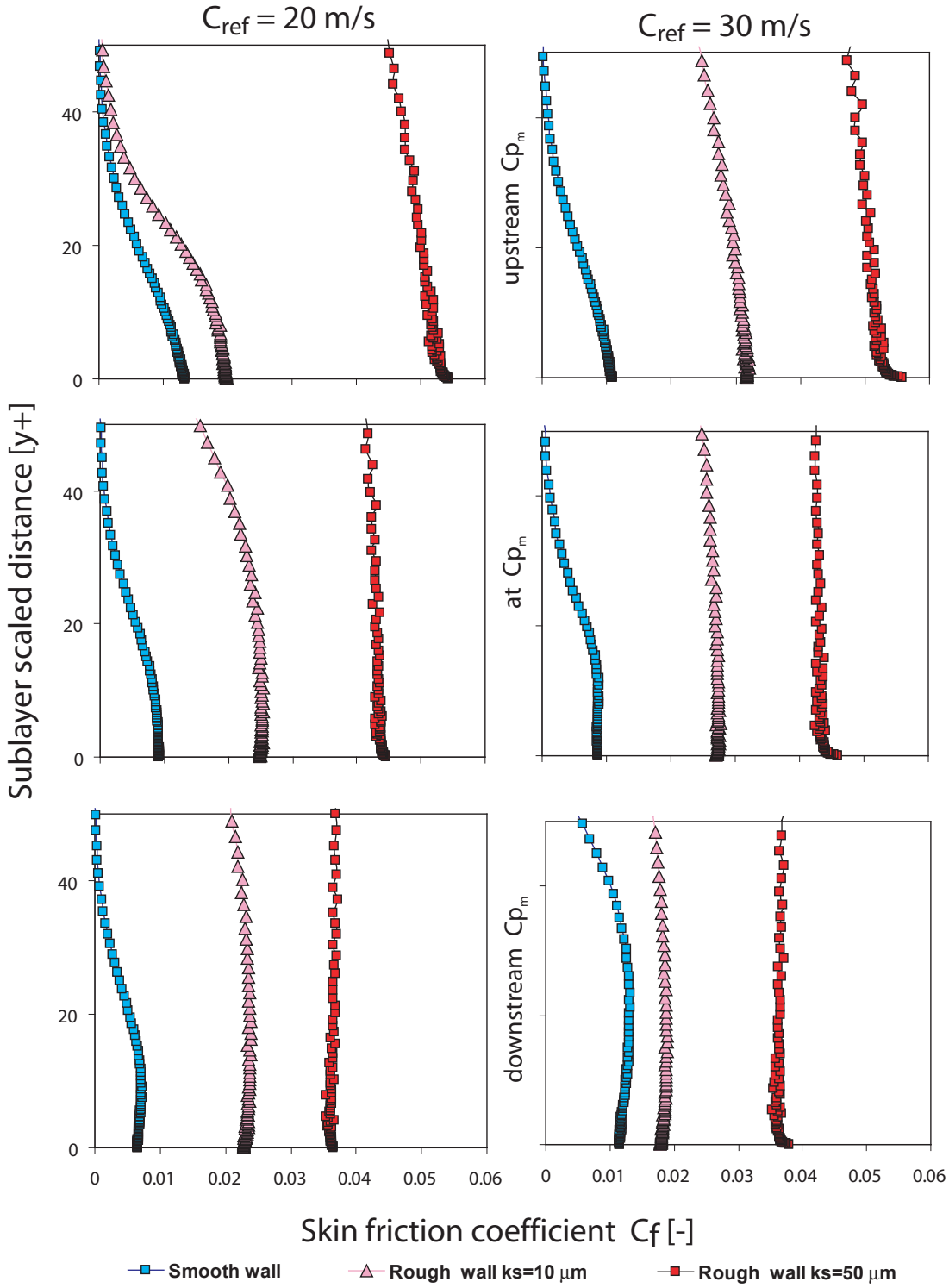

Figure 6.12: Evolution of the skin friction on the boundary layer flow at three stream-wise locations near the Cp_{min} for hydraulically smooth and rough wall ($k_s = 10$ and $50\,\mu$m) for two values of upstream reference velocity C_{ref}=20 and 30 m/s

Validations

Figure 6.13 reports experimental investigations of the roughness effect on cavitation inception [69]. The measurements are made for different speed values (12–23 m/s) and for different roughness elements on the NACA0009 leading edge on the spanwise direction (k_s=10–26 μm).

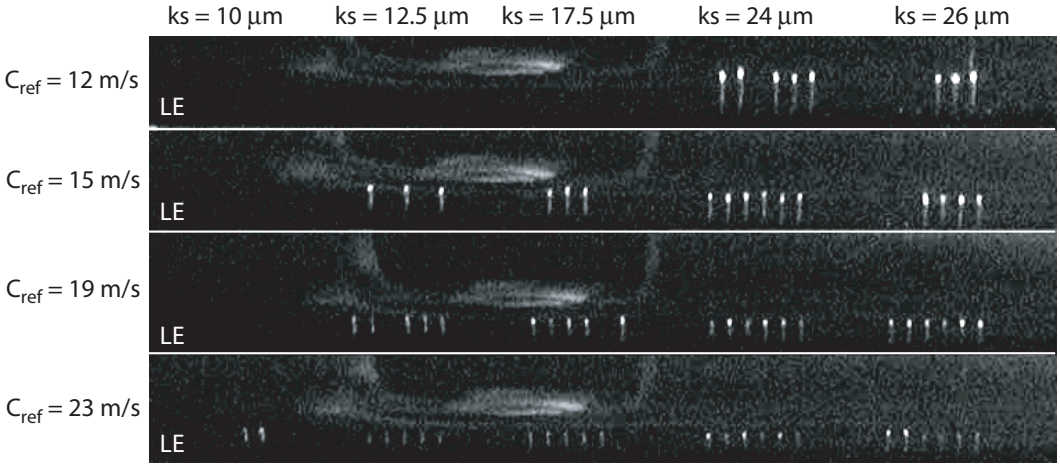

Figure 6.13: Isolated cavities on NACA0009 suction side at constant minimum pressure for different speed values and roughness height, [69]

The first observation is that cavitation detaches from the roughness elements whereas the rest of the foil remains without cavitation. At low speed value (12 m/s) the cavitation detaches only from the high roughness elements (24–26 μm). By increasing the velocity value to 15 m/s, cavitation occurs for the medium roughness elements (12.5–17.5 μm), and finally cavitation detaches from the low roughness elements (10μm) at higher velocity values (23 m/s), whereas the rest of the foil at the same operating conditions remains in the cavitation free regime. This is exactly what we have reported in this chapter by the numerical procedure of computing the maximum tensile stress for cavitation inception in the case of rough walls. However, the experimental difference observed is much higher than the computed one. This is due to the impossibility of computing single roughness elements without altering the boundary layer and flow computation hypothesis. It is clear, that isolated roughness elements have a complex pattern. On the other hand, modelling the effect of a roughness element is still a challenging topic. The difficulty is to reproduce the correct effect of a rough surface by an equivalent mathematical model based on a turbulence model modification. Different models referred in the literature may lead to sensitive differences depending on the case study [96].

The observations made in the experimental investigations (cf. Fig. 6.2) are highlighted in Fig. 6.14 reporting the results of the boundary layer computation (boundary layer thickness enlarged 10 times for analysis) in the case of the NACA0009. The added correction (C_f) is increasing with respect to the Reynolds number and the roughness height. In addition, the location of the cavitation inception based on the the maximum tensile stress criteria is not inevitably at minimum pressure location.

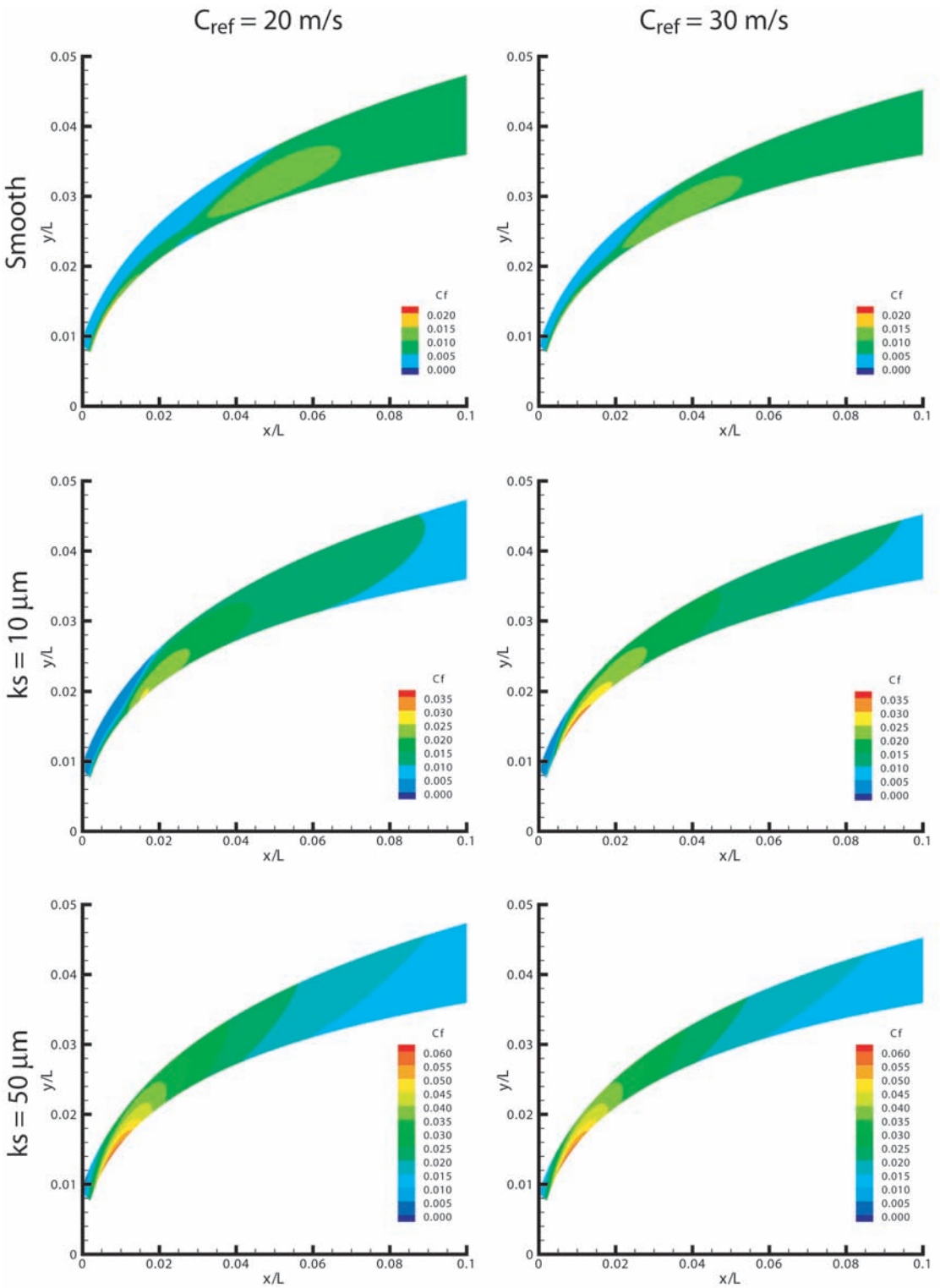

Figure 6.14: Evolution of the skin friction on the boundary layer flow near the Cp_{min} for hydraulically smooth and rough wall ($k_s = 10$ and $50\,\mu$m) for two values of upstream reference velocity C_{ref}=20 and 30 m/s. (Boundary layer thickness is enlarged 10 times)

Part IV

2D Hydrofoil Time Dependent Computations

Chapter 7

Typical Periodic Flow: Von-Kàrmàn Vortex Street

To validate the used solver algorithms for time-dependent flow problems (unsteady computations), a typical unsteady flow behind a blunt body is studied. The case of Von-Karman vortex shedding on the truncated NACA0009 trailing edge at 0° angle of attack is investigated.

The computational domain is the same as in Chapter 5. The domain is constructed of three rows of mesh in the spanwise direction (3 x 50'000 cells) with symmetry conditions at its border. A refined mesh at the trailing edge and near the hydrofoil body and the SST turbulence model are used. The inlet conditions are velocity which sets the Reynolds number, inlet turbulent intensity of 1 %, and a turbulence length scale of 0.001 m. The outlet is set to average static pressure, which sets the cavitation number. The top and bottom walls and the hydrofoil are set as non slip walls ($y^{+} \sim 50$). The simulations are done using a second order scheme for time and space.

The vortex shedding behind a structure induces vibrations and is of practical interest in hydraulic machines, since it can be at the origin of cracks. Figure 7.1 shows the Von Karman street in the wake of the NACA0009 hydrofoil under cavitation conditions that helps to identify the shed vortex structures. Even if the phenomenon has non negligible 3D character, the figure illustrates in a 2D side view the alternate vortex shedding from the upper and lower sides of the hydrofoil leading to two parallel rows of vortices with an opposite sense of rotation.

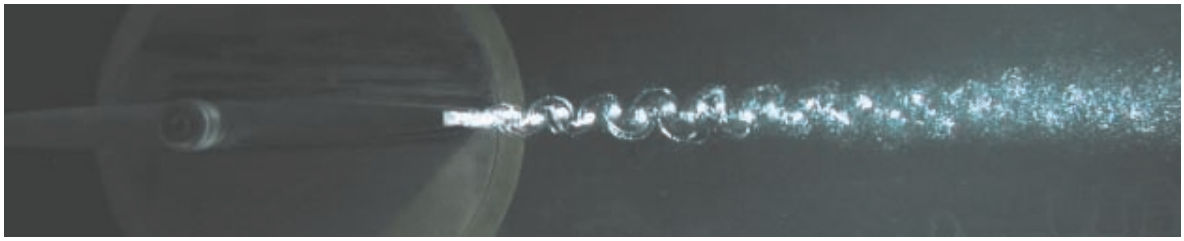

Figure 7.1: Shedding of Von-Kàrmàn street on NACA0009 hydrofoil [13]

The existence of a detailed experimental database has motivated our choice for this particular case study. The shedding process of von-Karman vortices in the wake of a NACA0009 hydrofoil has been investigated through various experiments at the LMH cavitation tunnel by Ausoni et al. [13]. A piezoelectric accelerometer fitted in the profile support to monitor the mechanical response of the vortex shedding as well as a portable digital vibrometer for non-intrusive vibration measurement (frequency shift measurement) at different location of the foil are used. Both measurement techniques lead to the same results and are compared with the numerical simulations.

7.1 Cavitation Free Regime

Figure 7.2 reports the computed lift coefficient as a function of dimensionless time t/t_{ref} (where $t_{\text{ref}} = \frac{L_{\text{ref}}}{C_{\text{ref}}}$) and shows a perfect periodic phenomenon, with the lift alternating between the positive and negative values due to the alternative vortex shedding at the pressure and suction sides behind the hydrofoil.

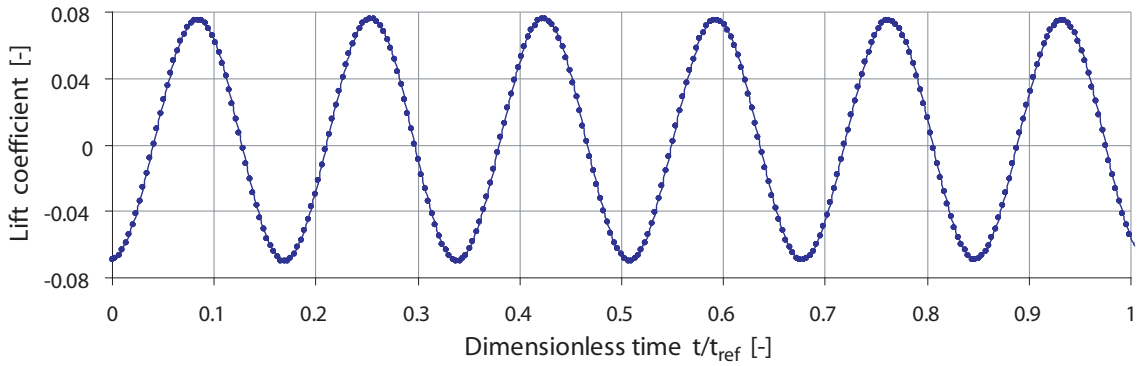

Figure 7.2: Time-dependent lift coefficient on NACA0009, C_{ref}=20m/s, i=0°

Figure 7.3 shows the spanwise vorticity field results of the numerical simulations illustrating the shed vortices, which form on the surface of the hydrofoil and shed downstream forming the well known von Kàrmàn vortex street. It is characterized by regions of high vorticity fields with alternate sense of rotation, with an upper row of negative vortices (black) and lower row of positive vortices (white). In contrast to the experimental visualizations, the numerical solution exhibit a strong vorticity diffusion in near wake of the hydrofoil leading to rapid decrease of the vorticity field.

Figure 7.4 reports the measured and computed values of shedding frequencies of Karman vortices for upstream velocities ranging from 5 to 30 m/s in cavitation free regime. A linear relationship between the shedding frequency and the upstream velocity is observed and found to be in agreement with the Strouhal law (dimensionless frequency based on hydrofoil trailing edge thickness of 3.22 10^{-3}m). The mean values are St=0.236 for the measurements and St=0.189 for the numerical simulations leading to a difference of 20%.

The observed linearity in measurements vanishes for upstream velocity ranging from 11 to 13 m/s, 7 to 9 m/s and 28 to 29 m/s. Within these velocity intervals, the so-called

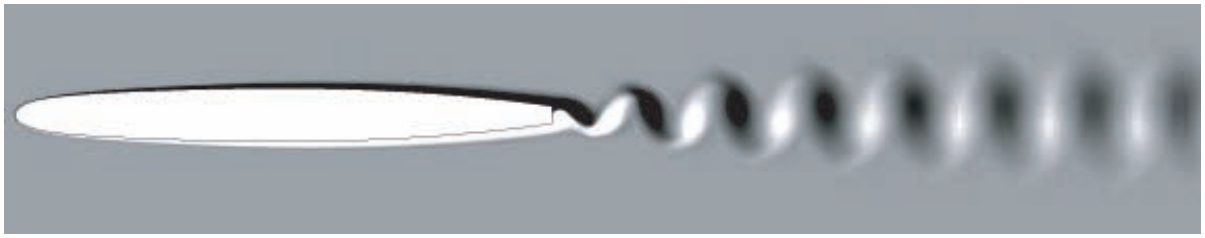

Figure 7.3: Computed spanwise vorticity (Von-Kàrmàn street) on NACA0009 hydrofoil positive : black, negative : white, C_{ref}=20m/s, i=0°, cavitation free regime

hydroelastic coupling occurs. In this case, the hydrofoil is excited at one of its resonance frequencies and the generation mechanism of Karman vortices is influenced by the fluid-structure interaction resulting from the hydrofoil's vibrations. In our attempt to model the von-Karman vortices generation, the fluid structure interaction is not taken into account.

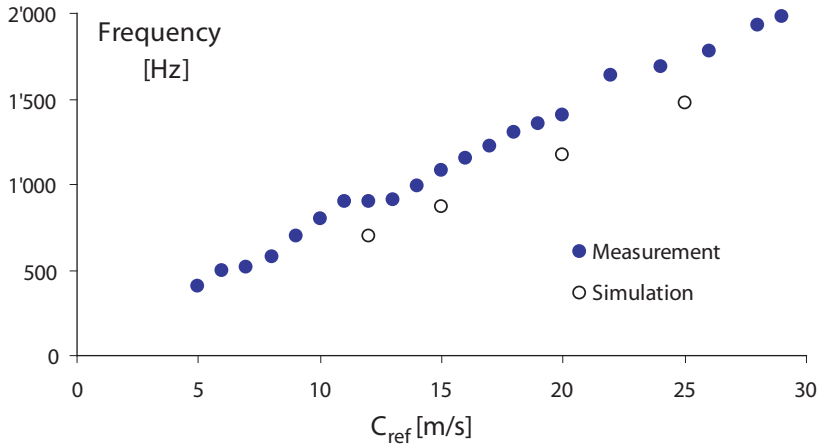

Figure 7.4: Shedding frequency of Kàrmàn vortices vs. the reference velocity

The differences found in the shedding frequencies between the simulations and the measurements are caused by the high Reynolds number of the case study (Re=2.0 10^6). The calculation can be affected by inadequate turbulence modelling and wall treatment resolution. In addition, the simulation does not take into account the three dimensionality of the phenomenon, and the vibrations of the hydrofoil.

7.2 Cavitation Regime

The cavitation influence on the vortex shedding frequency is studied for the same case configuration as for the cavitation free regime. The pressure level is lowered until cavitation occurs in the depression zone of the vortex core. Cavitation inception is found at σ=0.90, the measured value is σ=0.95.

Figure 7.5 shows the results of the numerical simulations for a cavitation number of $\sigma = 0.4$. The figure represents the spanwise iso-vorticity field and the vapor structures in the wake of the NACA0009 hydrofoil. The simulations results illustrate the creation of cavitation sites on the vortex core which are transported by the mean flow. The cavitation occurs near the hydrofoil trailing edge, it collapses completely and return to the liquid state very quickly at $x/L \sim 20\%$, whereas in the experiments, these cavities last much longer in the wake beyond the test section outlet as illustrated by Fig. 7.1.

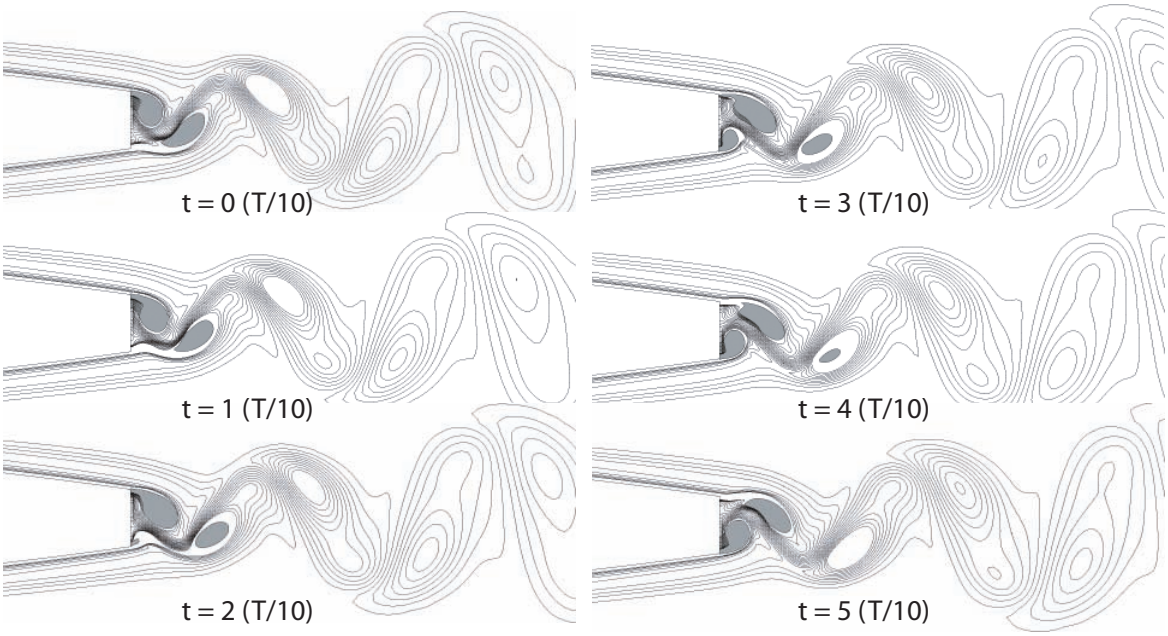

Figure 7.5: Computed spanwise vorticity (lines) and cavitation behavior (filled Grey; $\alpha_v > 1\%$) behind a NACA0009 hydrofoil, C_{ref}=20m/s, σ=0.4. (Time: semi-period, t=0; minimum lift, t=T/2; maximum lift)

Results of the experiments out of the hydro-elastic coupling are compared to the computed ones in Fig. 7.6. The shedding frequency is presented as a function of the cavitation number for an upstream velocity of 20 m/s. As soon as the cavitation appears in the core of the vortices, it is followed by a frequency increase. The graph displays an increase of the frequencies in the presence of cavitation of 10% for the computation and 14% for the measurements for σ=0.4, where the ratio of the frequency increase as a function of the cavitation number is the same in both experimental and numerical results. The computations reproduce the main change of the flow field induced by cavitation, which confirms the correct formulation of the model in reproducing this type of unsteady cavitation flow. The frequencies are changing in a linear way with respect to the cavitation number. This

frequency variation towards the cavitation number is consistent with the one reported in other studies on the wake of symmetric wedges [18].

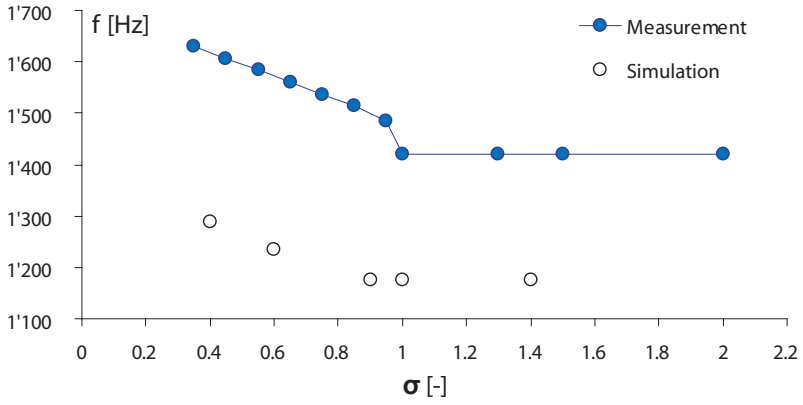

Figure 7.6: Shedding of Kàrmàn vortices function of the cavitation number

The results demonstrate that the cavitation is not a passive component in the mean flow but it modifies its major field. Cavitation occurrence does not only affect the shedding frequency of the vortices, but through mass conservation also their translational velocity. Further analysis on the flow structures may provide detailed explanations, but are out of the present scope. The case in which we are mainly interested, is to reproduce a typical physical instability by numerical simulations. More precisely to reproduce the periodicity of the phenomenon and the cavitation creation in the vortex core when the pressure threshold is favorable, the modelling of the cavity transport by the mean flow in time-dependent computations, and finally their interaction with the major flow structures as reported in experimental investigations.

Chapter 8

Cavitation Instability: Modelling Evaluation

We consider the non-truncated variant of the 2D NACA0009 hydrofoil at high incidence angles. The flow parameters are: i=5°, σ=1.0, and C_{ref}=20m/s, and reflected by a high pressure gradient over the hydrofoil leading to an unsteady state flow behavior and shedding of large transient cavities (Fig. 8.1).

Figure 8.1: Instantaneous pictures of unsteady cavitation on NACA0009 hydrofoil i=5°, σ=1.0, C_{ref}=20m/s. (top view: flow from up to down)

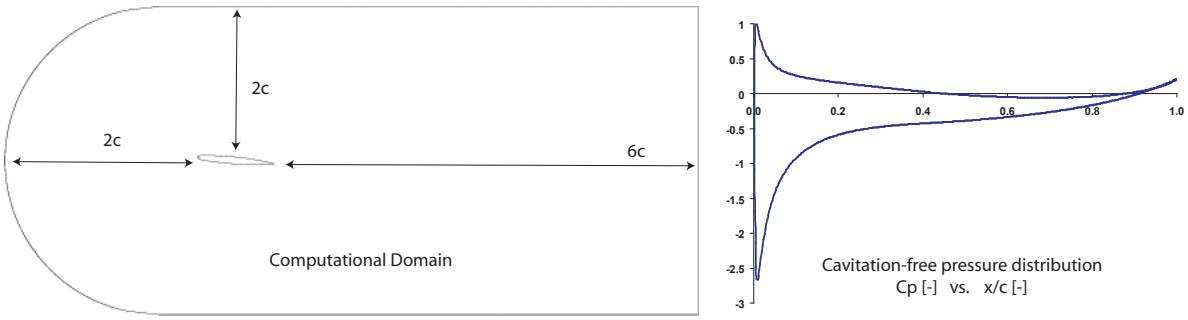

Figure 8.2: Computational flow configuration and pressure distribution on the non-truncated NACA0009 hydrofoil, i=5°

The domain is taken larger than the experimental test section to avoid numerical problem mainly due to reflections on the boundaries (Fig. 8.2). The domain is constructed of three rows of mesh in the spanwise direction (3 x 95'000 cells) with symmetry conditions at its border. The inlet conditions are velocity of (20m/s), inlet turbulent intensity of 1 %, and a turbulence length scale of 0.001 m. The outlet is set to average static pressure, which sets the cavitation number. The top and bottom walls are modelled as free slip

walls to avoid meshing restrictions. The hydrofoil is set as non slip wall with fine mesh at its border ($y^+ \sim 1$). The simulations are done using a pure second order scheme for momentum and continuity equations. Turbulence and volume fraction equations are set to a hybrid high resolution scheme. For this case, a comparative study is made for six different turbulence models: k-ε, SST, non homogeneous SST, Reynolds stress-ω, DES 1 and DES 2. The mesh is taken fine enough to compute the boundary layer flow near the hydrofoil boundary ($y^+ \sim 1$) for all the computations based on ω formulation near the wall, except for the k-ε model where a classical log-law is used.

The NH-SST model is the classical SST model, and we used the empirical correction adopted by Reboud et al. in k-ε model (cf. § 1.3.1) for the multiphase flows. The SST model, using both k-ε and k-ω models, this correction is used in both without discontinuities, because of the same formulation of μ_t (the correction is made on variable ρ, and C_μ=β^*). DES 1 and DES 2 models use same SST-LES hybrid formulation. DES 1 is based on geometrical filter (grid size), whereas the DES2 model has an additional constraint based on the SST blending functions (cf. §1.3.3, with DES 1 : F_{SST}=1, DES 2 : F_{SST}=F_1). The DES model which is theoretically based on 3D formulation, is used in this case as a forced 2D, in manner that all the flow components are set to zero in the spanwise direction. This is an attempt to use the DES model to investigate the ability of this type of model to reproduce the unsteady cavity behavior as observed along the experiments.

All the simulations (except cavitation free regime) were carried out in a time accurate way. The time steps are taken as : $t = (C/C_{\text{ref}})/100 = 0.0005\,\text{s}$ for the URANS simulations, and $t = (C/C_{\text{ref}})/500 = 0.0001\,\text{s}$ for the DES computations. 10 and 30 pseudo-time steps iterations are used for each physical time step respectively for URANS and DES computations. A maximum residual target of 10^{-4} is used as convergence criteria.

8.1 Results

Six sets of simulations are performed. Steady-state computation is used as an initial condition for the URANS computations, whereas for the DES computations, we have used the unsteady SST simulation after 10 times the reference time computation. The computations are performed up to 40 times the reference time period (40 passages of the hydrofoil) for most of the simulations (less in the cases where we do not observe unsteady shedding of transient cavities) which is equivalent to 4 times the total domain passage. Figure 8.3 illustrates the lift signal history starting from the steady state computations for the non homogeneous SST turbulence model. By this time, the simulations are not yet fully statistically stationary. These statements were also reported by several authors in the case of numerical simulations of unsteady cavitation flows [90][38][109], which can be attributed to the lack in space/time modelling (grid/time resolution) of the shed transient cavities. AN orthogonal fixed grid is not an efficient method to reproduce with accuracy the shed transient cavities (diffused cavities interfaces) which can interact with the phenomenon itself leading to very different transient cavities structure.

Figure 8.5 reports the lift coefficient signal for the different turbulence models used. Two different results are found: first, results without shedding of any transient cavities (attached cavity) reflected by quasi-steady regime for k-ε, SST, and DES 2 turbulence models, and a cavity pulsating regime without transient cavities shedding for the non isotropic homogeneous model Reynolds stress-ω. Second, unsteady flow results with the shedding

of transient cavities reflected by a cyclic fluctuations of the lift for the NH-SST and DES 1 turbulence models.

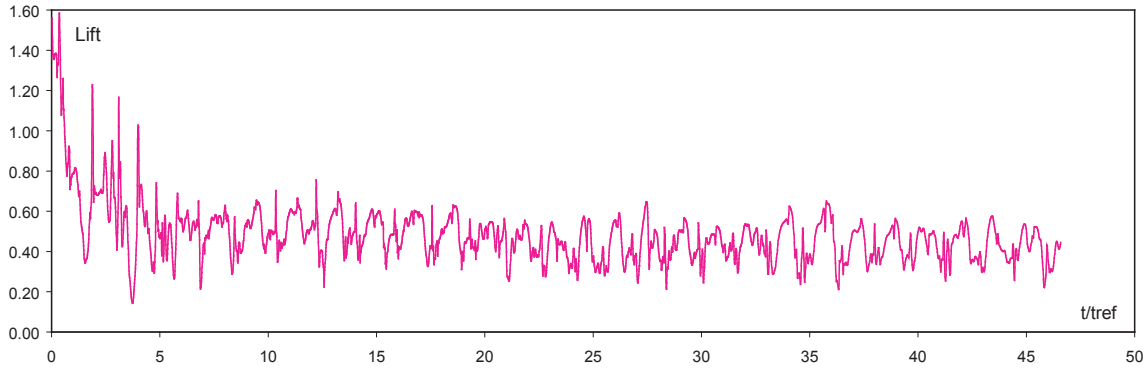

Figure 8.3: Lift coefficient time history

For the cavity shedding case (NH-SST and DES1), the lift has a cyclic time signal. Even if the periods are pretty clear, the fluctuations in a given period are very different from one to another. This phenomenon is mainly due to the dynamic of the shed cavities which are driven by the main flow-field downstream of the cavity closure. The growth and collapse mechanism of the cavity is driven by a cyclic phenomenon, whereas the dynamic of the cavity, when it is swept away can have very different non reproducible behavior. The transported vapor can have a single volume or divided into two or three cavities. The vapor can be attached to the wall or far from it. This different ways of cavities shedding have an important influence on the pressure field at the hydrofoil wall, and thereby on the lift values.

This statement is confirmed by the signal of the vapor source term ($\dot{m}$) on the domain reported in Fig. 8.4, which represents the total domain tendency in terms of vapor creation (positive) or destruction (negative). The signal is periodic and with lower noise level than the lift signal. It states that the general oscillatory system in terms of cavity growth and collapse is periodic at the origin of the phenomenon, and the interaction of the shed cavities with the main flow field is more complicated.

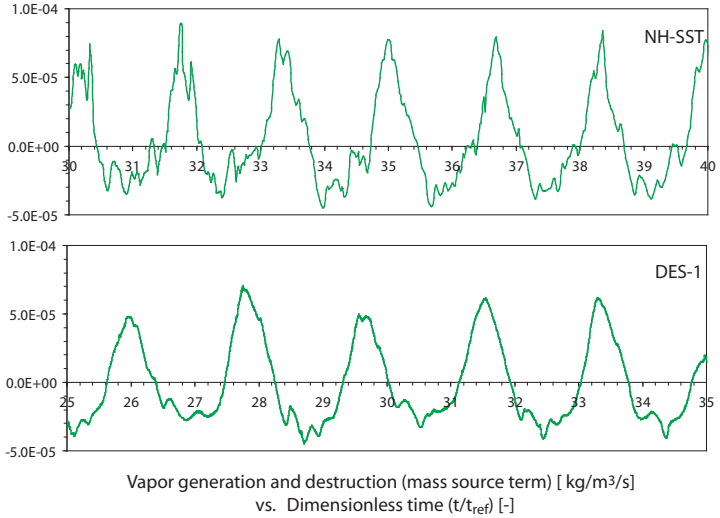

Figure 8.4: Vapor generation/destruction time history, period of t*=10

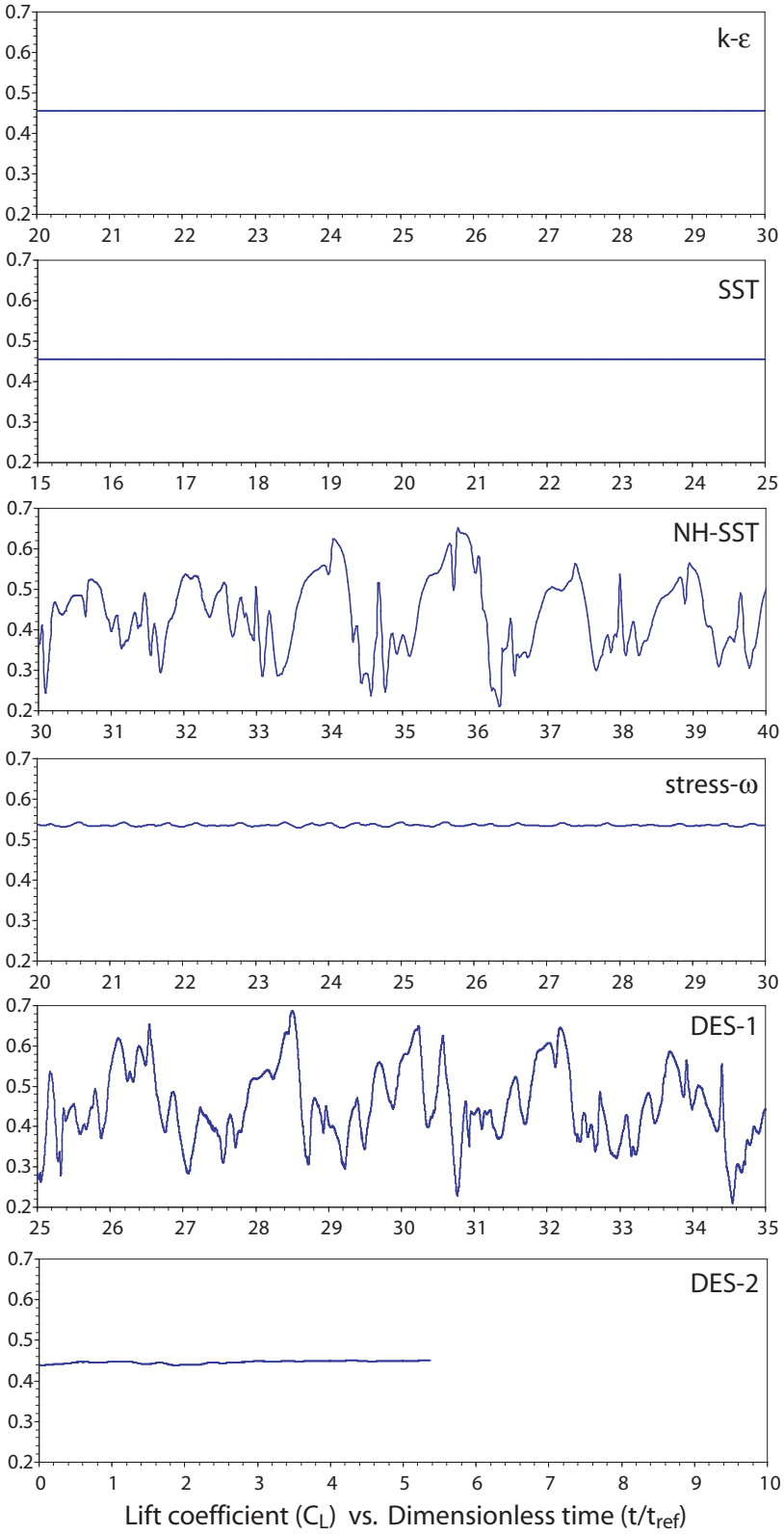

Figure 8.5: Lift coefficient time history, period of t*=10

8.1.1 Attached Cavity Results

In the case of k-ε, SST and DES 2 models, the unsteady-state results are the same as in steady state computations. Figure 8.6 shows a snapshot of the pressure distribution and cavity shape for this case.

The results of the k-ε model are expected and as reported by other authors. The results of the SST model evidence the fact that including a boundary layer zone computation ($y^+ \sim 1$) is not efficient in reproducing the unsteady cavitation flow. The k-ε and SST models fail to reproduce the shedding of transient cavities even when using fine mesh.

The DES 2 model fails to reproduce the flow unsteadiness. The used model based on zonal DES formulation uses the SST blending functions, and the SST model is used near the wall where the reentrant jet is important. The classical SST model fails to reproduce the reentrant jet instability, and the use of the LES model outside this zone is without any effect in this typical flow regime. The averaged values of the main flow characteristics are summarized in table 8.1.

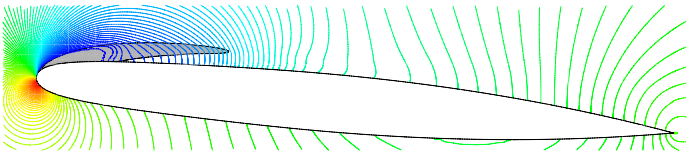

Figure 8.6: Cavity shape and iso-pressure contours, quasi-steady case

Model	$\overline{C_L}$	$\overline{C_D}$	$\overline{V_v}\,(\%)$
k-ε and SST	0.4554	0.02643	0.02175 %
DES 2	0.4486	0.02562	0.01962 %

Table 8.1: Predicted flow quantities, quasi-steady case

The Reynolds stress-ω turbulence model leads to an unsteady-state flow field without shedding of transient cavities. The cavity volume is oscillating on the hydrofoil surface and pure liquid structures with high vorticity level are shed downstream. This is reflected by transported iso-pressure structures (Fig. 8.7) which are at the origin of small lift fluctuations.

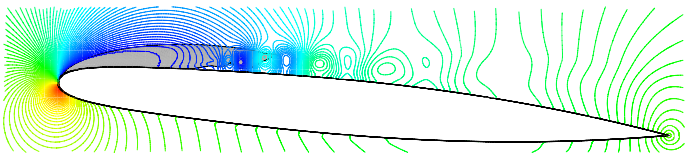

Figure 8.7: Cavity shape and iso-pressure contours, cavity pulsating case

Model	$\overline{C_L}$	C'_L	$\overline{C_D}$	C'_D	$\overline{V_v}\,(\%)$
Stress-ω	0.5360	0.0028	0.0316	0.0002	0.04472

Table 8.2: Predicted flow quantities, pulsating case

8.1.2 Cavity Shedding Results

Both NH-SST and DES 1 models lead to an unsteady flow with quasi periodic shedding of transient cavities. These are transported with the flow downstream where they collapse. The phenomenon can be represented by two cycles in the same period (Fig. 8.8 and 8.9): first, starting from the maximum cavity length, the reentrant jet enters the cavity at its closure leading to a wrenching of several small cavities (t=0.6–1.0T), and second, the reentrant jet reaches the hydrofoil leading edge where the whole main cavity is removed and transported downstream (t=0.1–0.6T).

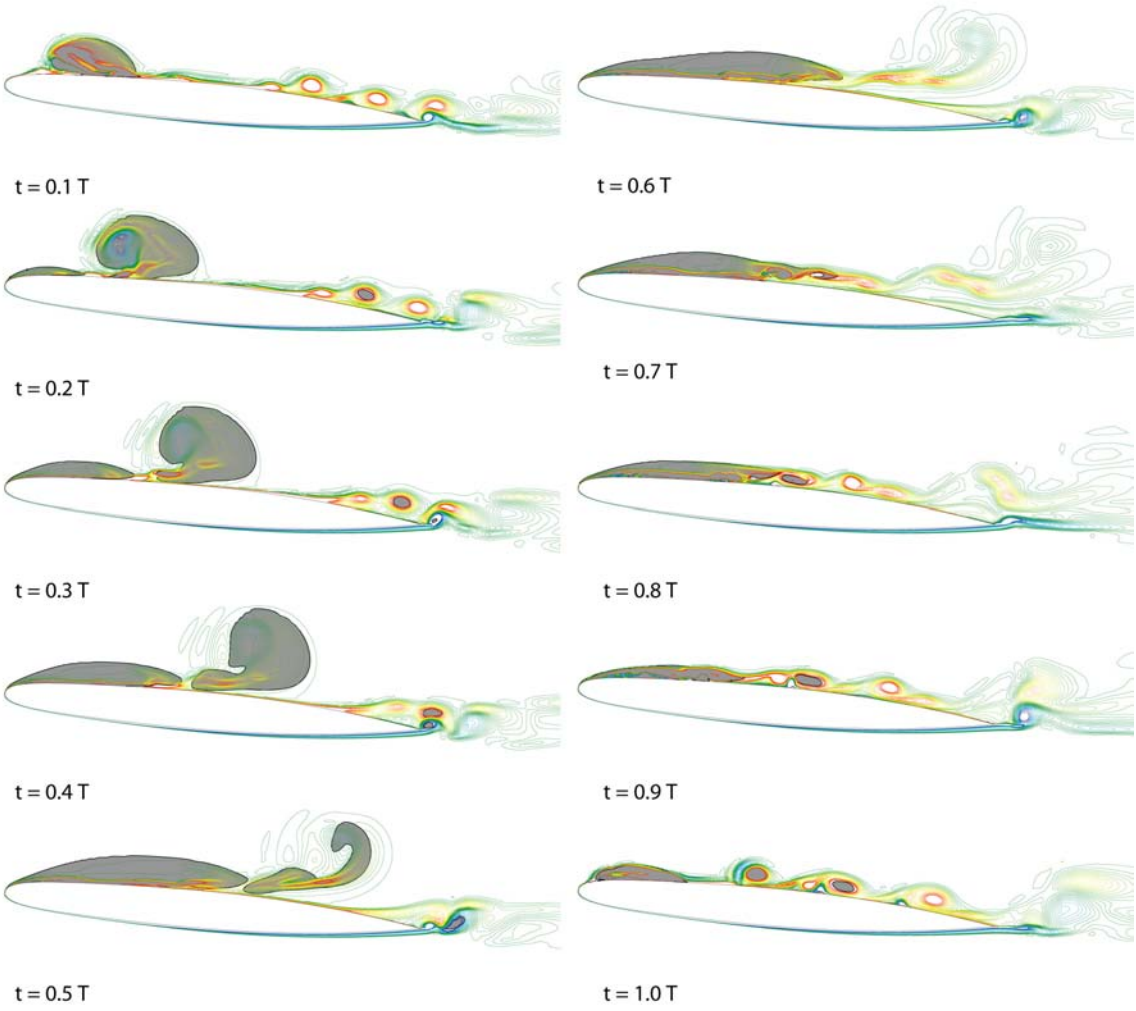

Figure 8.8: Cavity shape and iso-spanwise vorticity for a shedding life cycle i=5°, σ=1.0, turbulence model: URANS NH-SST

In comparison between the two simulations, the DES computation exhibits more scattered cavities and high vorticity field, whereas, the URANS simulation predicts larger volume vapor zones which are concentrated in single cavities. The grid induced switches from URANS to LES in DES model does not belong without problems, as shown near the hydrofoil trailing edge (region of fine mesh) for the vorticity field.

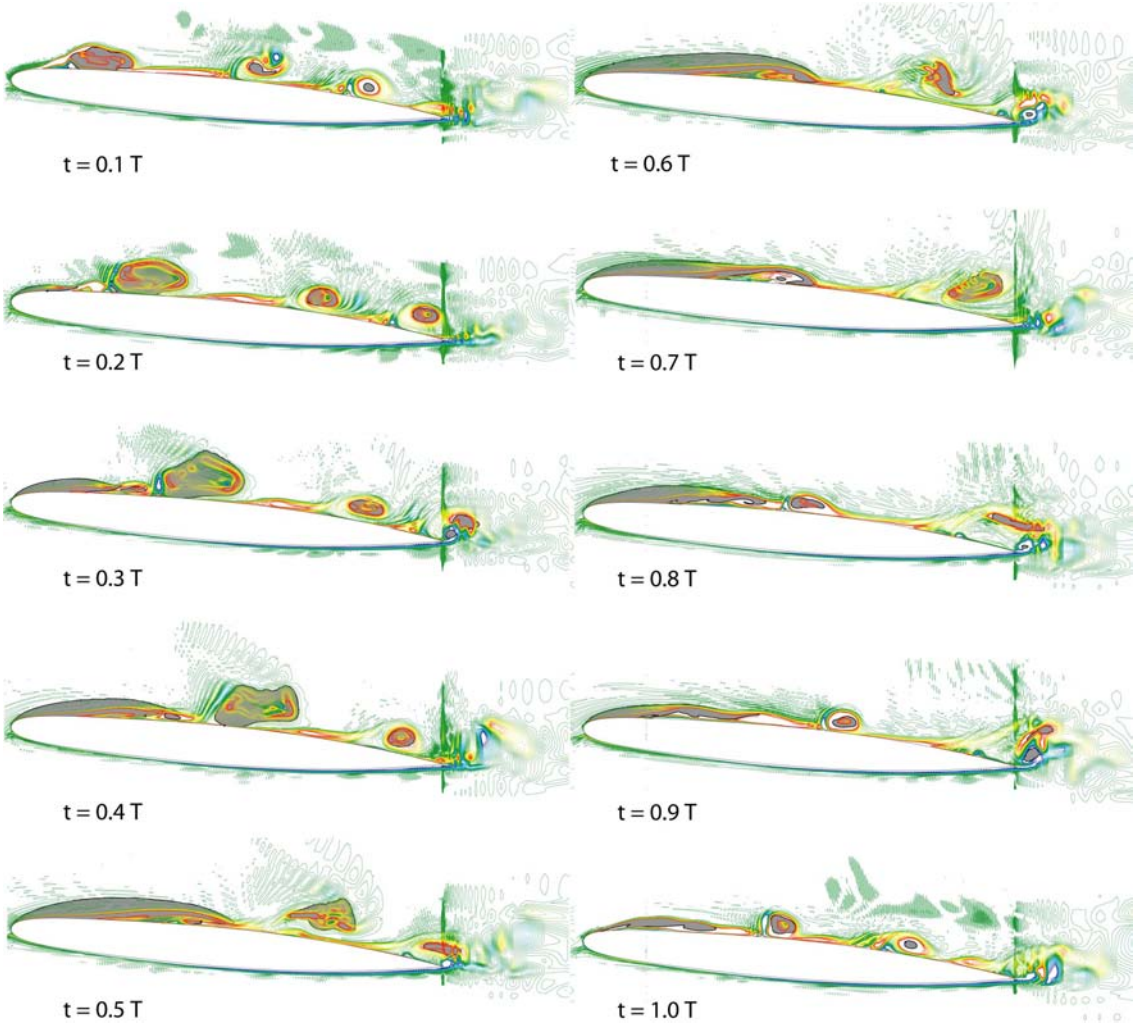

Figure 8.9: Cavity shape and iso-spanwise vorticity for a shedding life cycle i=5°, σ=1.0, turbulence model: DES 1

Figure 8.11 illustrates the amplitude spectrum of NH-SST and DES 1 simulations based on lift and vapor source time series. The frequency signal for both models have the same dominant frequency even if it is computed with lift or vaporization rate. This result confirms the periodicity of the phenomenon in terms of vapor source and lift fluctuations. The dominant frequencies are respectively 122 Hz and 112 Hz for URANS and DES models which gives, based on the maximum cavity length during one cycle, a Strouhal number of 0.3880 for the URANS computations and 0.3091 for the DES.

Table 8.3 reports the averaged and standard deviation values of the main flow field. Both models produce similar predictions in terms of averaged values and fluctuations of the lift and drag coefficients. The main differences are found in the shed transient cavities. The DES model leads to less vapor volumes formation (in terms of production and overall volume, and low frequency shedding.

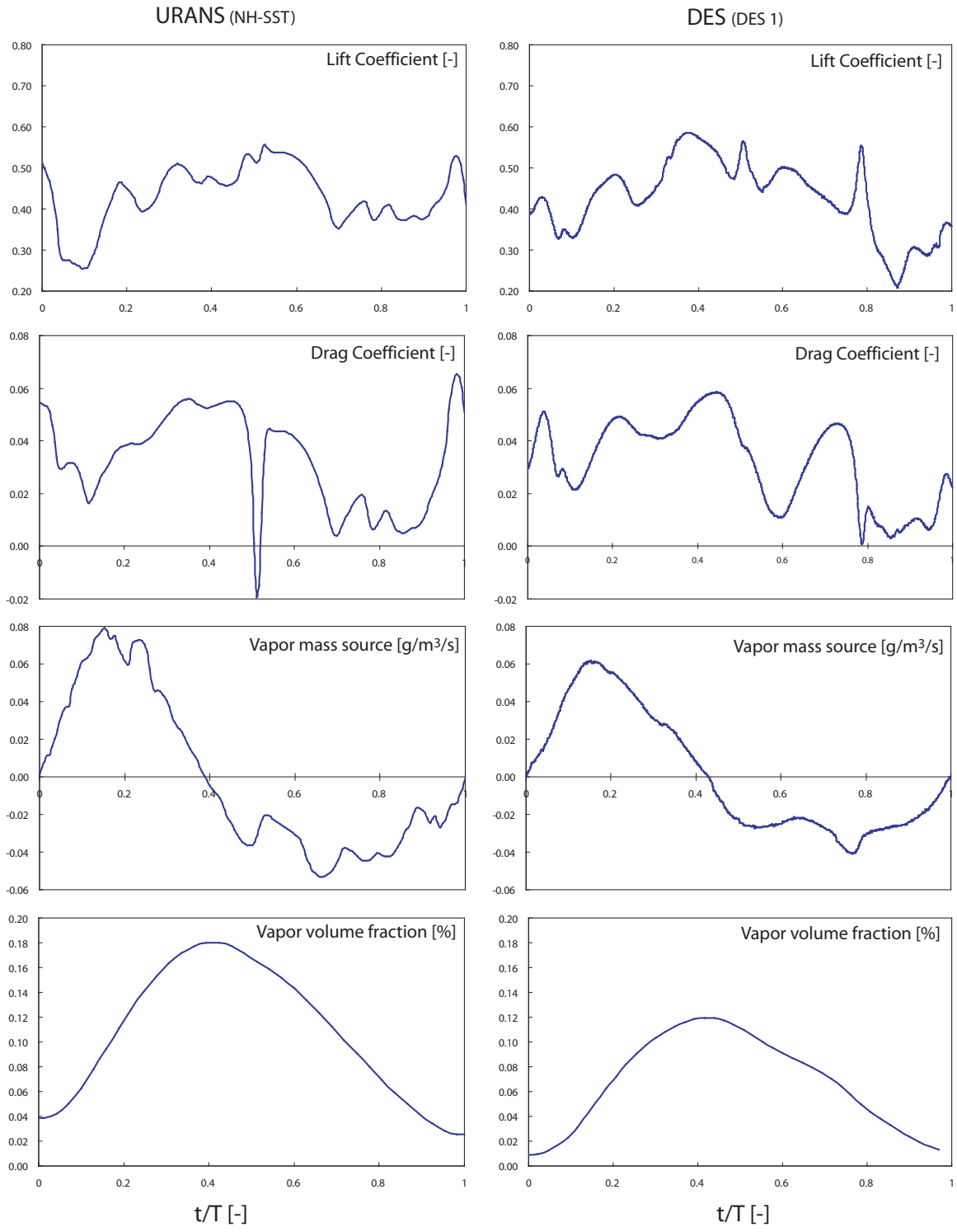

Figure 8.10: Main flow field signal for a typical period of cavity shedding URANS vs. DES; i=1°, C_{ref}=20m/s, σ=1

Model	$\overline{C_L}$ [-]	(C'_L) [-]	$\overline{C_D}$ [-]	(C'_D) [-]	$\overline{V_v}$ [%]	f [Hz]	(l_c/c) Max[-]	St [-]
NH-SST	0.4350	0.0981	0.0329	0.0148	0.1040	122	0.63	0.3880
DES	0.4550	0.0941	0.0327	0.0146	0.0699	112	0.55	0.3091

Table 8.3: Predicted flow quantities, cavity shedding case

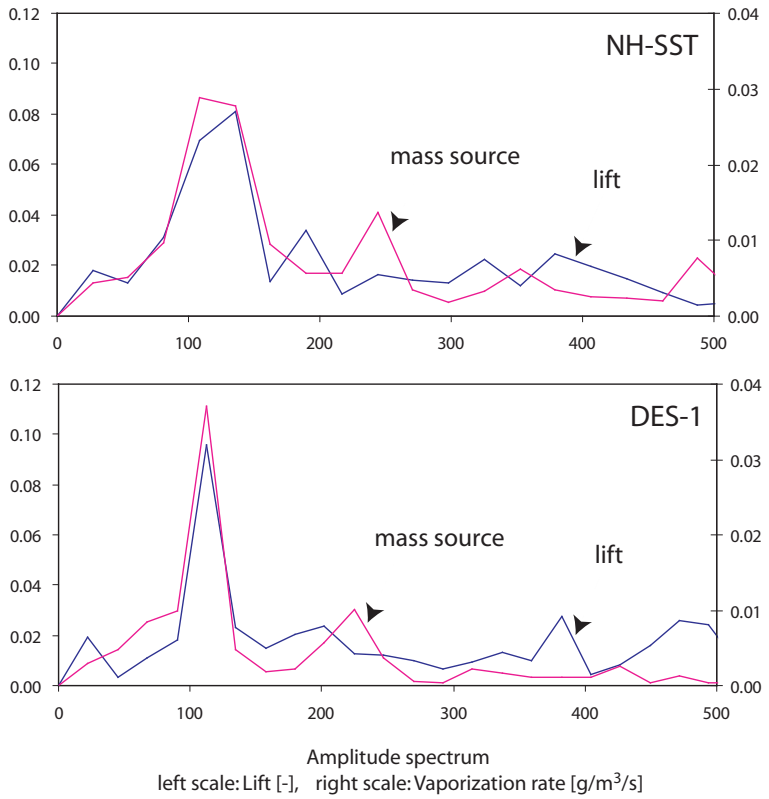

Figure 8.11: Amplitude spectrum of computed lift and measures vibration envelope

8.1.3 Lower Cavitation Numbers

A second investigation is made to evaluate the response of the turbulence models at lower cavitation numbers. The k-ε, SST, Reynolds stress-ω and DES 2 models are used to compute the same configuration at lower sigma value (σ=0.8) and are compared to the simulation obtained with the NH-SST model for the same case. The results are the same as the one obtained with the previous cavitation number for the URANS computations (the same as quasi-steady results for the k-ε and SST models, and pulsating cavity for the Stress-ω), whereas DES 2 leads to unsteady flow field with shedding of transient cavities.

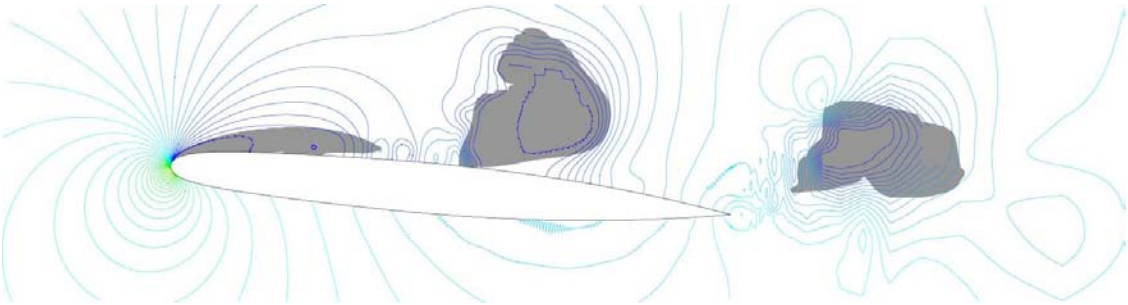

Figure 8.12: Cavity shape and iso-pressure contours for high shedding regime
Snapshot: i=5°, $C_{\text{ref}} = 20\,m/s$, σ=0.8 Turbulence model: DES 2

A snapshot of the cavitation flow obtained with DES 2 in the case of σ=0.8 is presented in Fig. 8.12. The regime is characterized by large transient cavities transported far from the hydrofoil. On the other hand, the differences shown at σ=1.0 are also obtained in the present case; the predicted vapor volume by the URANS NH-SST computation are more important than one predicted by DES one.

The difference between the two formulations of the DES model is only the one related to the blending functions. DES 2 model is limited at the wall region (enforced URANS at the wall) where DES 1 is only governed by the grid size. The formulation based on the SST blending functions gives more secure computations. The DES model does not return to LES near the wall, and it overcomes any unexpected separation. These model assumptions are based on the idea that SST model is adapted to predict the separations near the wall.

The problem in unsteady cavitation simulation is that the SST fails to reproduce the phenomenon (reentrant jet and cavity shedding). It turned out, that the use of DES 2 model is highly constrained by the efficiency of the SST model. In the case of lower cavitation numbers, the detached zones are so important that even the use of DES 2 formulation predict the reentrant jet. This case is characterized by thicker cavity and reentrant jet.

8.2 Models Evaluation Summary

The results obtained in this chapter highlight the importance of the turbulence modelling in unsteady cavitation simulation involving high level of interaction between the global flow and the cavity closure. The instability of the main cavity and the resulting shedding of transient cavities are mainly due, to the occurrence of the reentrant jet at the cavity closure. The reentrant jet is predicted by all the simulations. However, depending on the used model, it can or cannot lead to cavity wrenching and transient cavities shedding. The numerical model, based on incompressible formulation of the turbulence model, overestimates the mixture viscosity in the compressible zones, which results on high dissipation at the cavity closure. The additional viscosity in the eddy-viscosity concept, which is developed for single phase flow, does not include any compressibility effects.

It turned out that the unsteady-state cavitation flow modelling is strongly related to the turbulence formulation in the compressible zone. The DES simulations which uses a filter method is an alternative solution for the correct estimation of the eddy viscosity. Another solution is based on the non-homogeneous formulation for the eddy viscosity in the mixture, which highlights the importance of including the compressibility effects in the classical turbulence models when dealing with unsteady-state cavitation simulations. The resolution of the Reynolds stress components via Reynolds-stress models shows the anisotropic behavior of the cavity closure, reflected by high vorticity shedding in its wake, even if the model does not reproduce the transient cavity shedding.

Wilcox [153] has already highlighted the sensitivity of a mixing layer flow with a variable Mach number to the turbulence modelling. He observed that the Reynolds stress transport equation is directly concerned with the compressibility effects and it can not be corrected by simply taking into account the mean density change in the turbulence model. He proposed a compressible flow correction of the k-ω turbulence model based on the local Mach number.

Chapter 9

Unsteady Analysis of Leading Edge Cavitation Dynamics

In the previous chapter, we have shown the importance of turbulence modelling in simulating unsteady cavitation. Only DES and URANS NH-SST models were able to produce periodical shedding of transient cavities, while all the other turbulence models failed. In the present chapter, we present an unsteady-state analysis of the leading edge cavitation in the case of a flow around 2D hydrofoil with the help of the URANS NH-SST turbulence model.

9.1 Case Study and Experimental Setup

The case study is the NACA009 hydrofoil placed in the test section of the EPFL high speed cavitation tunnel. The computed domain corresponds to the test section and the mesh is of the same order as in the previous computations (3×95'000 cells, y^+ ∼1) The hydrodynamic conditions are 5° incidence angle, 20 m/s upstream velocity and two different cavitation numbers 1.2 and 1.5.

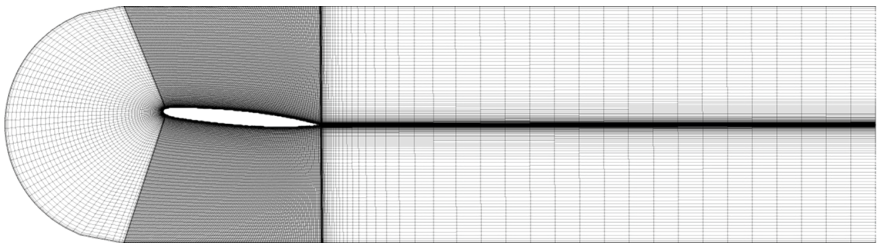

Figure 9.1: Domain mesh

The experimental setup is presented in Fig. 9.2. The flow visualization is ensured by a digital camera located on the top of the test section along with a Xenon flash light having a duration of 30 μs. A high frequency accelerometer is used to monitor the flow induced vibration of the hydrofoil. This sensor, having 54 kHz resonance frequency and 202 mV/g sensitivity, is fixed on the hydrofoil support outside of the test section. The signal acquisition is performed with the help of an HP1432A digitizer with 51.2 sampling frequency, 16 bits A/D resolution and 20 seconds recording time.

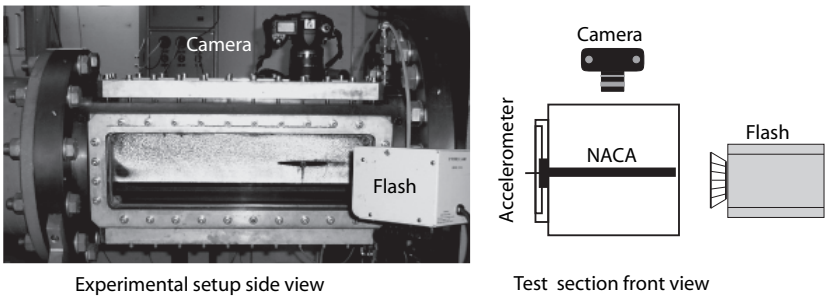

Figure 9.2: Experimental setup

9.2 Unsteady Analysis and Governing Frequencies

9.2.1 Experimental Results

We have presented in Fig. 9.3 and 9.4 the flow visualizations for both sets of hydrodynamic conditions. The cavity is highly unstable with a shedding of large transient cavities in an almost cyclic way. The transient cavities clearly originate from the main cavity break-up near its detachment location. As the transient cavities are transported by the outer flow to collapse downstream, the main cavity is reconstructed. As soon as the main cavity length reaches a maximum value, depending on the cavitation number and the incidence angle, the generation process of transient cavities restarts. During the main cavity growth, a re-entrant jet occurs, which travels beneath the main cavity in upstream direction to its detachment location. It should be noticed that the jet is due to the stagnation point located between the moving cavity closure and the transient cavity which is being shed. It is believed that this re-entrant jet governs the shedding frequency of transient cavities. The shorter cavity (σ=1.5) produces smaller transient cavities, since the time needed for the jet to reach the cavity detachment is smaller leading to a higher shedding frequency.

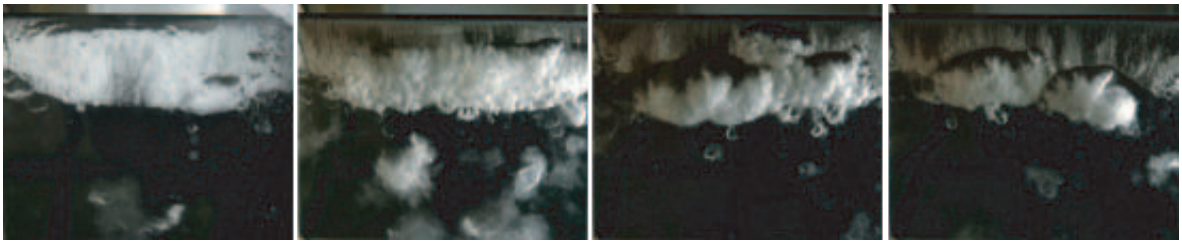

Figure 9.3: Instantaneous pictures of unsteady cavitation on NACA0009 hydrofoil i=5°, σ=1.2, C_{ref}=20m/s. (Top view: Flow from up to down)

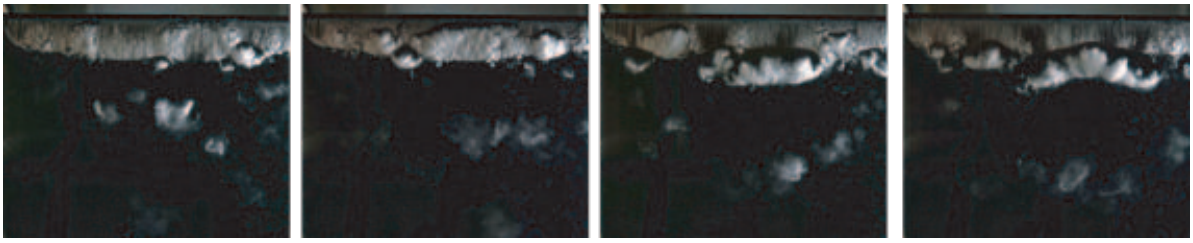

Figure 9.4: Instantaneous pictures of unsteady cavitation on NACA0009 hydrofoil i=5°, σ=1.5, C_{ref}=20m/s. (Top view: Flow from up to down)

The flow induced vibration is used to validate the shedding frequency of transient cavities. In fact, it is well known that cavitation instabilities highly modulate the vibration of the structure within a high frequency band. The envelope extraction from filtered broadband vibration is commonly used in the vibratory approach for cavitation detection in hydraulic turbines [54; 56; 21]. In our case study, the shedding frequency of transient cavities is derived from amplitude spectra of demodulated vibration within the frequency band of [5, 10 kHz]. The demodulation technique is based on Hilbert transform, which produces a phase shift of $+\pi/2$ and $-\pi/2$ for positive and negative frequencies respectively. Figure 9.5 show a record sample of the vibration signal band pass filtered as well as its envelope. Figure 9.6 reports the amplitude spectra of the raw vibration signal and of its envelope. The raw vibration spectrum exhibits several peaks at 0.7, 1.05 and 1.9 kHz. These particular frequencies are well known to be related to the first vibration modes of the hydrofoil (the bending, the torsion and bending-torsion modes respectively [13]). The excitation of the resonance frequencies of the hydrofoil is mainly due to the repeated collapses of transient cavities. Furthermore, a significant increase of the spectral energy may be observed within the frequency band of [5, 10 kHz]. This is also due to the response of the mechanical structure to the repeated violent collapses of transient cavities. As expected, this energy increase is higher with the lower cavitation index. The envelope spectra, allows to extract the modulated part of the vibration signal and filter all resonance frequencies. In the case of σ=1.2, the result shows only one sharp peak at 120 Hz related the shedding frequency of the transient cavities. For σ=1.5, a wider peak may be observed with a central frequency of 285 Hz. In this case, the energy scattering may be explained by the fact that the volume of transient cavities is smaller leading to less energetic collapses and also by the fact that the periodic shedding exhibits an intermittent behavior.

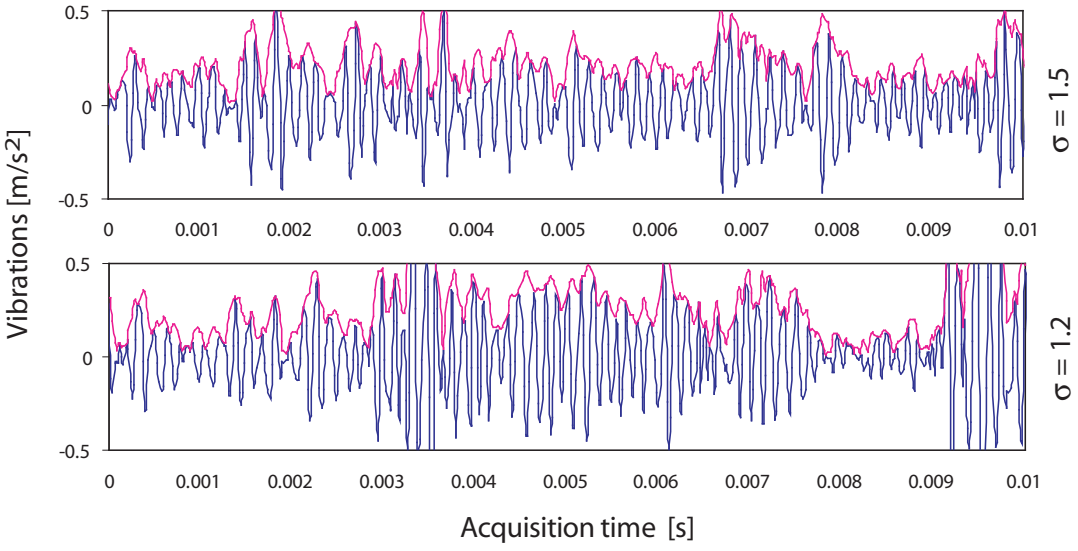

Figure 9.5: Vibration signal band-pass filtered between 5 and 10 kHz and its envelope

In order to investigate the effect of the hydrofoil vibration at its resonance frequencies on the cavitation dynamics, we have carried out an envelope extraction around the torsion mode frequency (namely [800, 1200 Hz]). The result shows no significant peak at the shedding frequency. This confirms that no interaction occurs between the hydrofoil modal

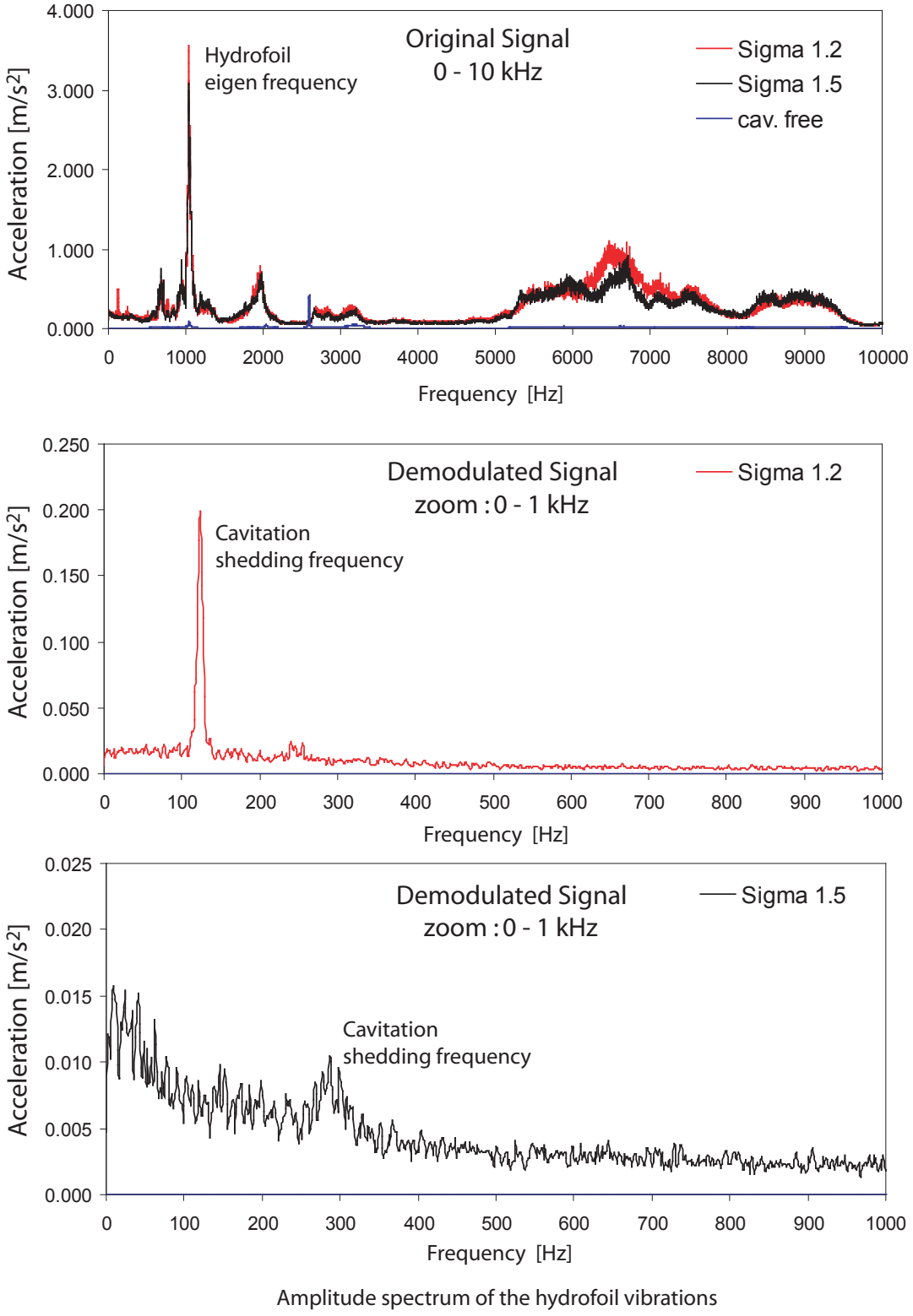

Amplitude spectrum of the hydrofoil vibrations

Figure 9.6: Spectra of raw vibration signals and their envelopes for σ=1.5 and σ=1.2

vibration and the shedding process. This is a major observation since it shows that there is no need to take such vibrations in the simulation of unsteady leading edge cavitation into account. Nevertheless, if the shedding frequency approaches one of the modal frequencies, one may expect the occurrence of a significant coupling between the two processes and the resulting fluid-structure interaction has to be considered in the CFD simulation.

9.2.2 Numerical Results and Validations

Figure 9.7 reports the time history of the lift, the drag, and the vaporization/condensation rate ($g/m^3/s$) for both cavitation numbers $\sigma = 1.5$ and 1.2 with a time window of $t/t_{ref} = 20$. After 30 reference time computations, the phenomenon is not yet fully statistically reproducible. The graphics of the analyzed variables show a periodic signal, even if the identified periods are very different from each others. The use of the vaporization/condensation rate signal is the easiest way to identify the periodicity of the vapor formation and collapse during a life cycle. The signal shows a different time characteristics between the vaporization and condensation rates. The vaporization process takes 40% of the total process, and is characterized by higher values of the interphase mass transfer rate. This is mainly due to the time of the shed cavities to collapse. Furthermore, the fluctuations amplitude are more important for the lower cavitation number, whereas the periods are larger, which is in agreement with the statements made in the experimental analysis.

Table 9.1 summarizes the averaged and standard deviation values of the lift, the drag, and the vapor volume in percent reported to the test section volume as well as the governing frequencies. Comparing the two cavitation regimes (σ=1.5 and 1.2), the lower cavitation regime is characterized by higher amplitudes of the fluctuations of the lift, the drag and the vaporisation/condensation rates. The $\sigma = 1.5$ regime is governed by a lower frequency phenomenon and larger cavities leading to very similar Strouhal numbers, such as $\sigma = 1.2$. The cavity length and the frequency are twice as large whereas the generated vapor volume is four times larger, which is qualitatively in agreement with experimental visualizations.

Model	$\overline{C_L}$ [-]	(C'_L) [-]	$\overline{C_D}$ [-]	(C'_D) [-]	$\overline{V_v}$ [%]	f [Hz]	(l_c/c) Max[-]	St [-]
σ=1.2	0.5048	0.0850	0.03715	0.0167	0.0862	120	0.60	0.360
σ=1.5	0.4837	0.0721	0.02855	0.0117	0.0266	250	0.30	0.375

Table 9.1: Predicted flow quantities, time interval=$30t_{ref}$

Figure 9.8 reports the measured and computed frequencies for both cavitation numbers. With our experimental facility, its is clear that we are only interested by the frequency driving the phenomena, as the amplitudes are not comparable. In the case of σ=1.5 it is not so obvious to characterize the flow governing frequency, because the period time of vapor formation and its transport is slightly changing from one period to another. Based on the vapor source time signal of the computations, the averaged frequency is 250Hz, and the experimental value is 285 Hz leading to a difference of 15%. For σ=1.2 the measured experimental frequency is 122 Hz, whereas the computed one is 120 Hz.

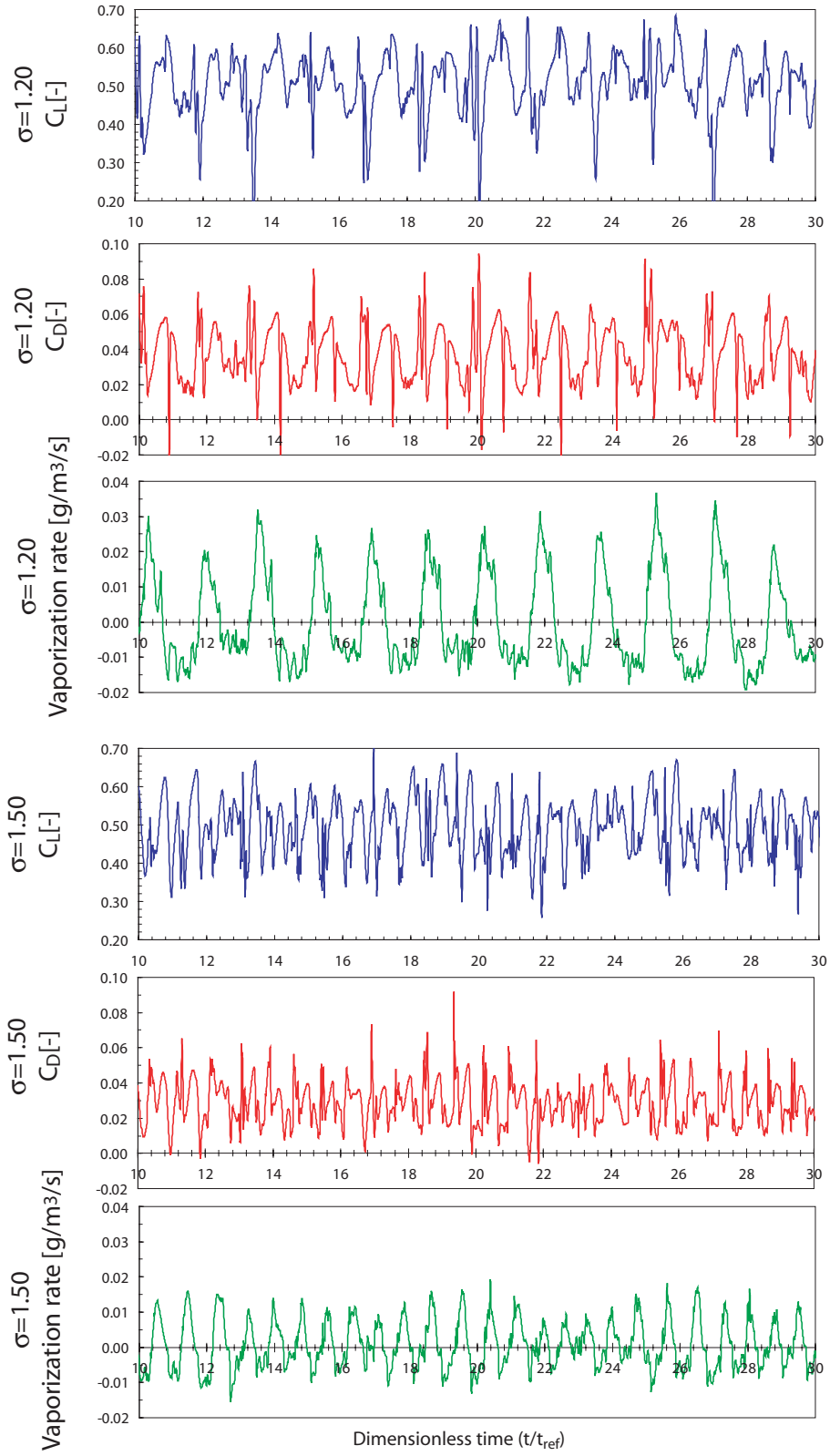

Figure 9.7: Flow variables time history, σ =1.2 and 1.5, period of t*=10

These excellent results obtained for both cavitation numbers confirm the correct assumptions of the model in terms of vaporization and condensation processes. In fact, the assumed time scale difference between the mean flow and the phase change processes are validated. The cavitation regime $\sigma = 1.2$ has a clear dominant frequency and it is the same as the measured one. Here, the secondary phenomena are negligible comparing to the main cavity shedding process, whereas at the higher cavitation number, the cavity shedding process is more sensitive to the rest of the flow fluctuations. This phenomena, already highlighted in the experiments is predicted by the model leading to a broad maximum in the amplitude spectrum.

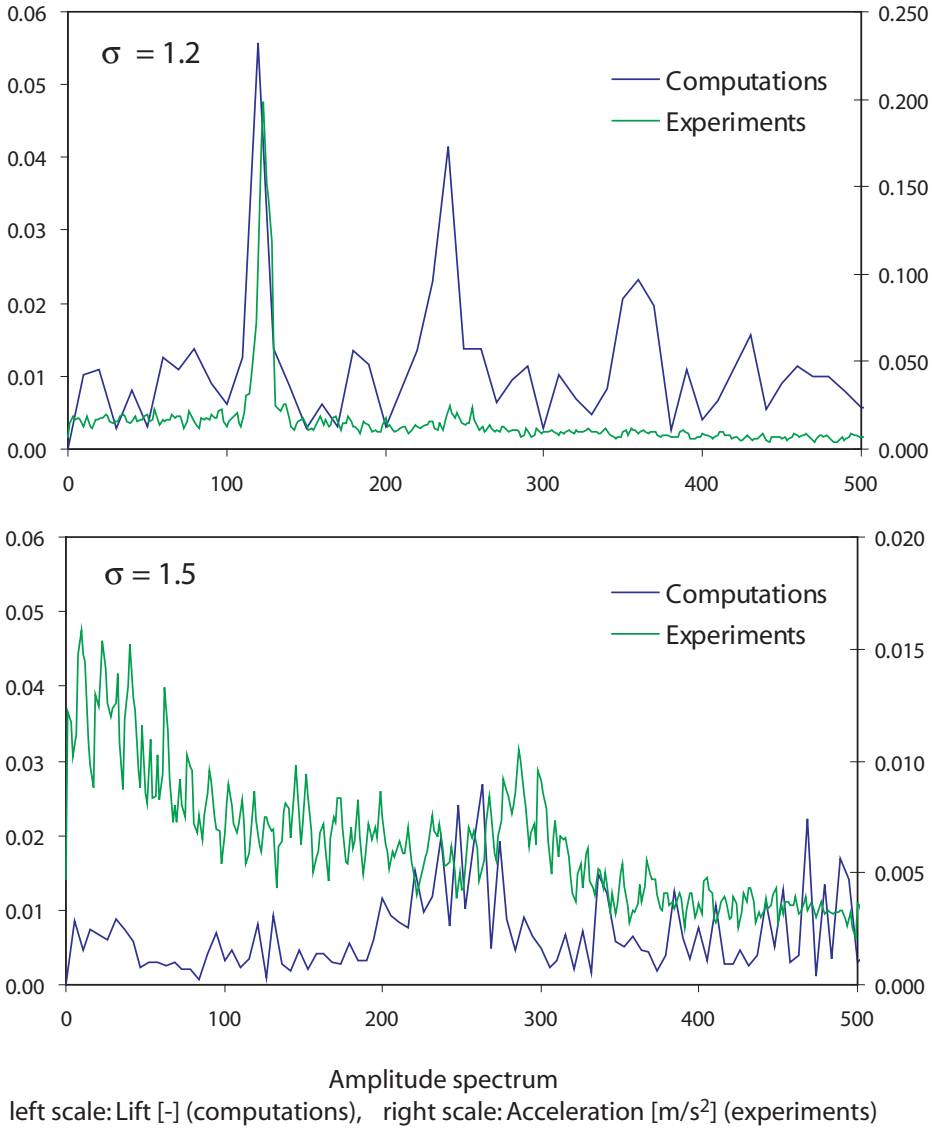

Figure 9.8: Unsteady cavitation amplitude spectrum

9.2.3 Unsteady Cavitation Dynamics

Figures 9.9 and 9.10 report a typical cavity life cycle for both computed cavitation regimes. The numerical simulations are qualitatively very similar to the experimental observations (cf. Fig. 9.3 and 9.4) regarding the main cavity dimensions and the transient cavities collapse region.

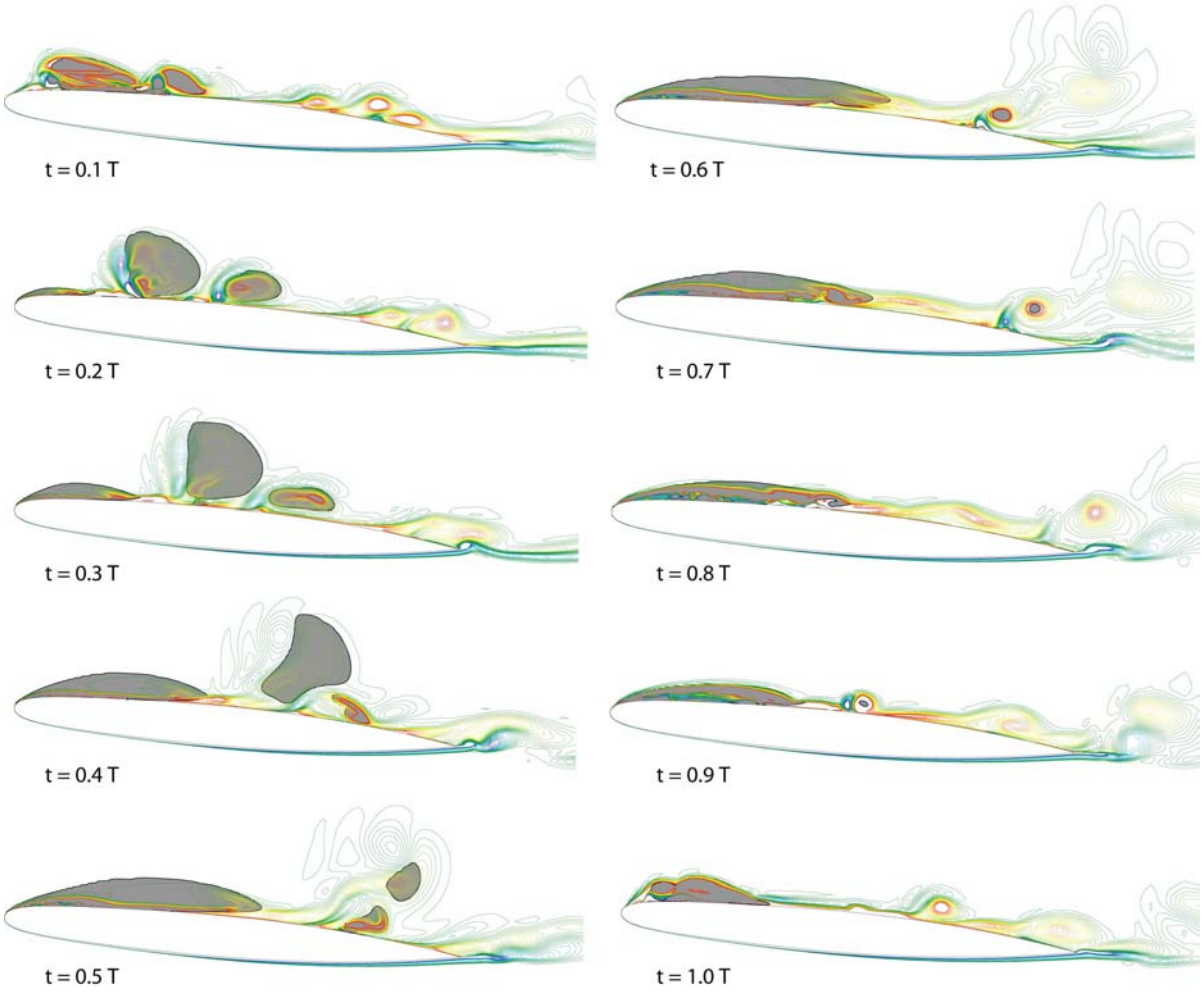

Figure 9.9: Cavity shape and iso-spnawise vorticity for a typical period shedding i=5°, σ=1.2, turbulence model: NH-SST

The case of $\sigma = 1.2$ is characterized by a thick main cavity and an important shed cavity volume in a disorganized way, such as the cavity can be divided into many small cavities. For one period of cavity creation and collapse, one can remark two distinct life cycles highlighted by the lift and drag signals. Firstly, starting from the maximum cavity length, the closure region is in the small adverse pressure gradient (low resistance) and the reentrant jet is too thin, such as the cavity closure region is continuously broken into small vapor volumes (T=0.7–1.0). Secondly, as the reentrant jet reaches the region of the high pressure gradient, the reentrant jet is more important and the whole cavity is extracted and shed downstream (T=0.0–0.6). This type of cavity shedding was described by Callenaere et al. [27] as the limit of the cloud cavitation when they observed a loss

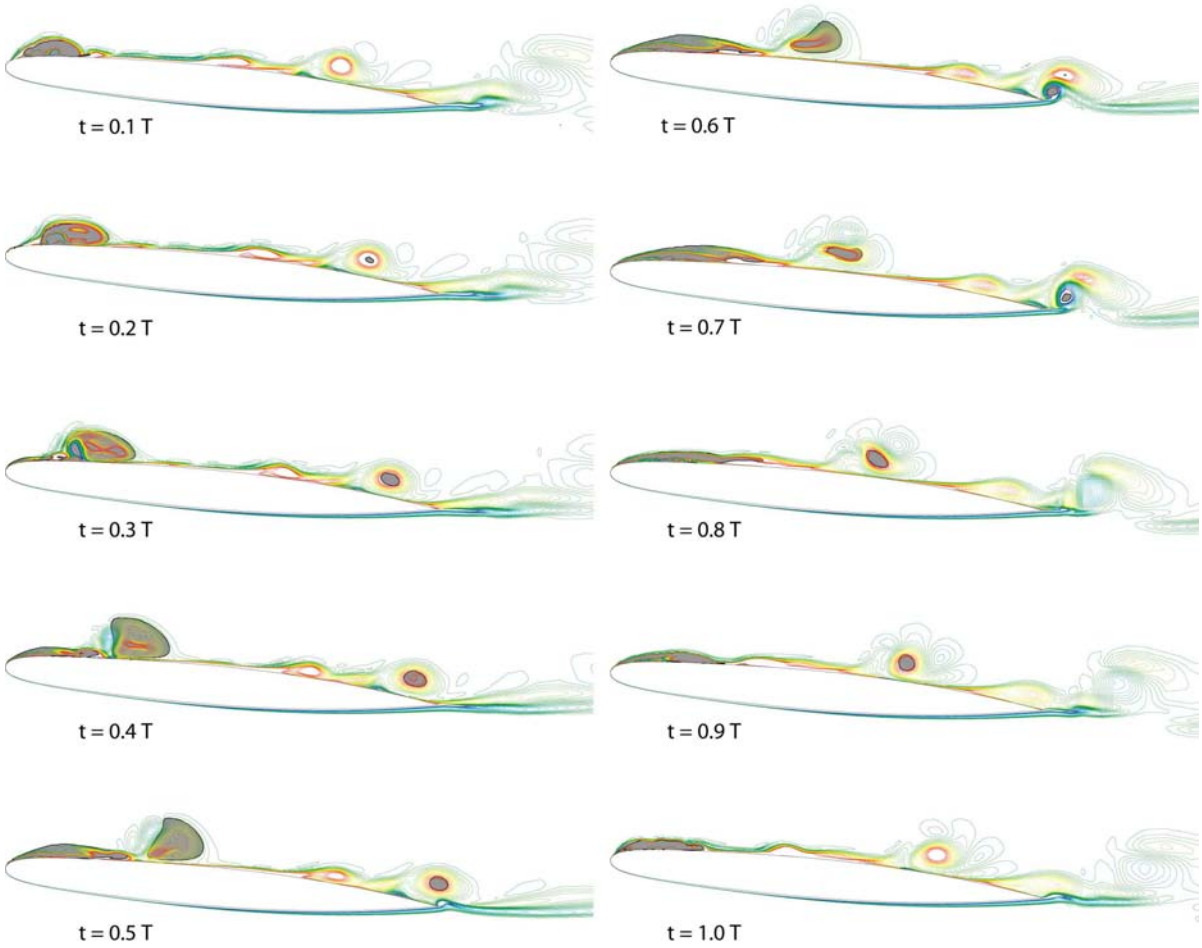

Figure 9.10: Cavity shape and Iso-spanwise vorticity for a typical period shedding i=5°, σ=1.5, turbulence model: NH-SST

in shedding regularity and an intermittency between coherent bursts of large clouds and chaotic entrainment of smaller vapor structures. $\sigma = 1.5$ is characterized by a thin main cavity and the shedding generally operates with a unique compact cavity.

For both cavitation regimes, it is hard to identify in one period the main characteristics of the unsteady flow field. Nevertheless lift coefficient time series and cavitation pictures indicate that t almosthe maximum lift occurs at the maximum cavity length ($t/T \sim 0.6$). Minimum lift occurs when the main cavity starts to leave the hydrofoil (reentrant jet reaches the leading edge, $t/T \sim 0.1$). At this time, the vapor generation is at its maximum. In parallel to this main sheet cavitation period other local secondary phenomena take place, which make the computed signals of lift and drag very different from one period to another.

9.3 Maximum Tensile Stress in Unsteady Cavitation

Visualizations of an attached cavity flow have shown different fields between the pressure field p and the pressure subtracted by the non isotropic shear strain $p - S_1$. It returns that the tensile stress criterion (cf. Chap. 6) may have an influence at the cavity closure.

We have substituted the tensile stress criterion as a threshold pressure in the used cavitation model instead of p_v. The correction is made only in the liquid phase as:

$$\dot{m}_l^v = -F^v \frac{3\rho_v \alpha_{nuc} \alpha_l}{R_0} \sqrt{\frac{2}{3} \text{Max}\left(\frac{p_c - p}{\rho_l}, 0\right)} \tag{9.1}$$

$$\dot{m}_l^c = F^c \frac{3\rho_v (1 - \alpha_l)}{R_0} \sqrt{\frac{2}{3} \text{Max}\left(\frac{p - p_c}{\rho_l}, 0\right)} \tag{9.2}$$

where :

$$p_c = p_v + \alpha_l \left(\dot{\gamma} \mu_{\text{eff}}\right) \tag{9.3}$$

In the first test the SST turbulence model was used. The correction in terms of pressure does not present any difference with the standard model and the computations have quasi-steady results as in the previous computations with the SST model. The second test is done by introducing the correction on unsteady computations of the NH-SST at $\sigma = 1.2$. The correction does not have any anti diffusive effect. It is used in conjunction with the correction of μ_t to identify if the tensile stress criterion have any major role in the unsteady cavitation pattern.

Figure 9.11 shows the history of the lift, drag, and vapor mass source generation in comparison with the first computation (NH-SST) based on p_v, where the thick solid lines are of the new computation, and the thin ones are from the first computation based on p_v as a pressure threshold for phase change.

Figure 9.12 shows the flow field results of a given period for the new simulation. The cavity life cycle is very close to the one obtained based on p_v criteria alone. However, it is not evident to make an adequate analysis concerning this topic because of the important differences between one given period to another.

Model	$\overline{C_L}$ [-]	(C'_L) [-]	$\overline{C_D}$ [-]	(C'_D) [-]	$\overline{V_v}$ [%]	f [Hz]	(l_c/c) Max[-]	St [-]
p_v	0.5048	0.0850	0.03715	0.0167	0.0862	120	0.603	0.3618
p_v+S_1	0.5254	0.0860	0.03811	0.0163	0.0959	113	0.654	0.3695
Difference	4%	1%	3%	2%	11%	6%	8%	2%

Table 9.2: Predicted flow quantities, tensile stress correction

Table 9.2 shows the comparison between the two computations, and highlights that the added correction based on the tensile stress criterion has an influence on the unsteady

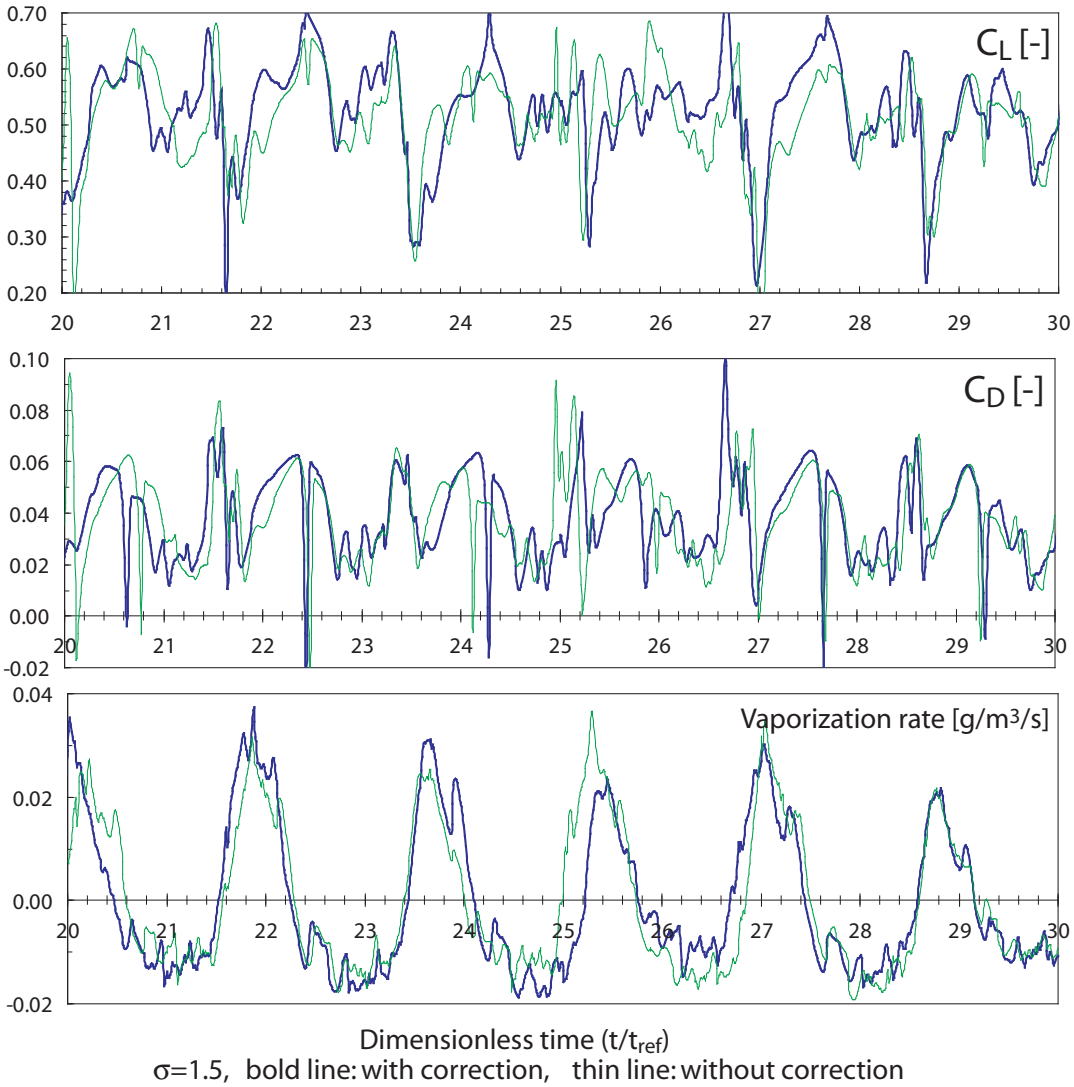

Figure 9.11: Flow history for cavitation regime σ =1.5, period of t*=10
Comparison between the simulations with and without tensile stress correction

cavitation. The main differences are found in the volume of the generated vapor (11%), the shedding frequency (6%), and the maximum cavity length (8%) leading to very close Strouhal frequencies.

The theoretical formulation of the tensile stress criterion evidences that it can have non negligible values in high shear or high vorticity flows, and this is the case in unsteady cavitation flows. However, further analysis is necessary to highlight its contribution in the non-isotropic turbulence model (as Reynolds stress models). In fact even if the formulation we have proposed is based on viscous and anisotropic formulation, its implementation through a turbulence model based on the Boussinesq eddy viscosity concept limits an important contribution of the term.

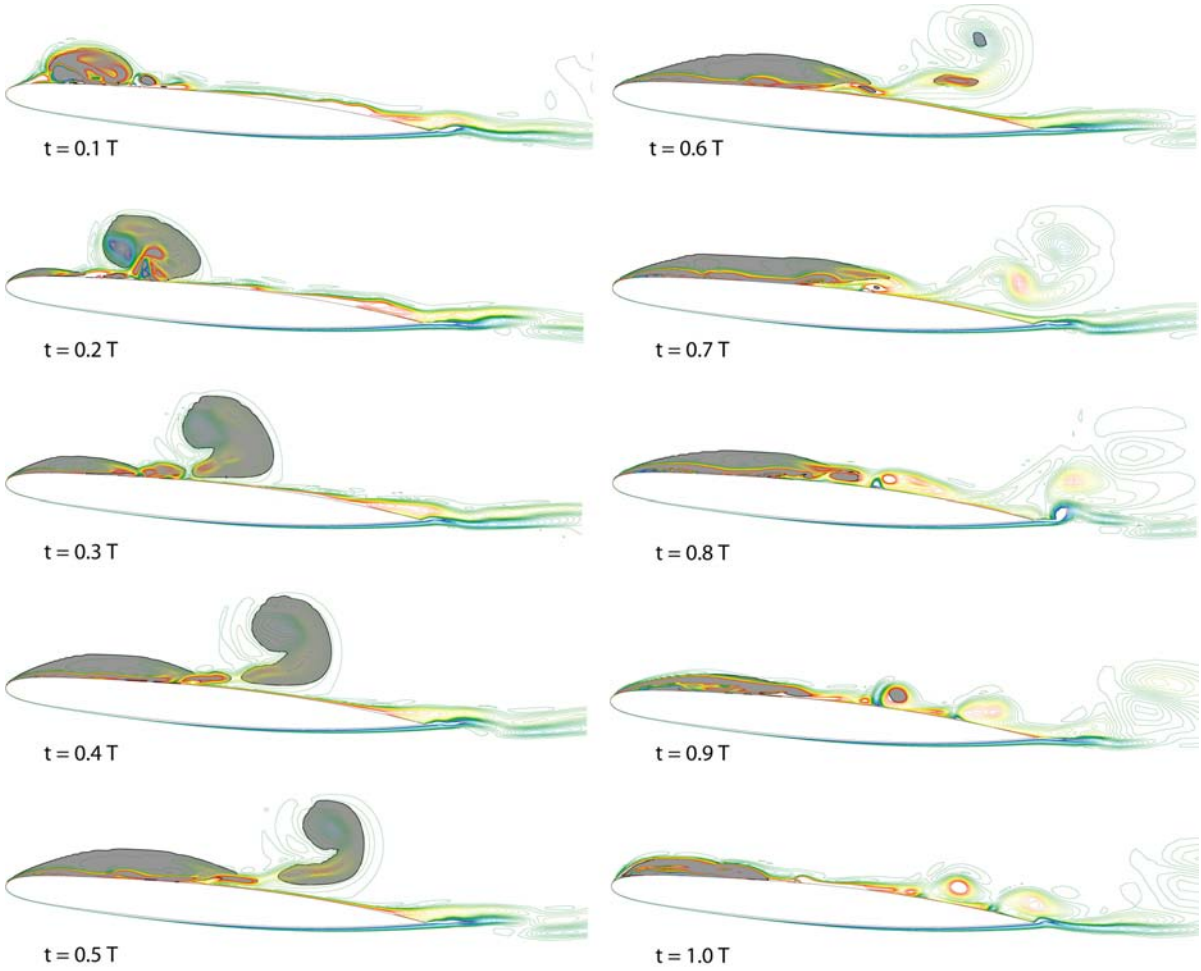

Figure 9.12: Cavity shape and Iso-spnawise vorticity for a typical period shedding i=5°, σ=1.5, turbulence model: URANS NH-SST with tensile stress correction

9.4 Unsteady Cavitation Modelling Summary

The cavitation instability involving two-phase flow with two different flow time scales is very sensitive to turbulence modelling, which plays the major role in modelling micro-scales perturbations of the flow. Classical models based on two-equations with homogeneous formulation fail to compute this typical case of cavitation, and the reason is the high values of introduced artificial viscosity. The incompressible formulation of the turbulence equations overestimates the effective viscosity in the compressible multiphase zone. More elaborate models as non-homogeneous formulations, reducing the mixture eddy viscosity are more suitable for this kind of simulations.

A recent turbulence model (Detached Eddy Simulation model) based on a hybrid URANS-LES formulation shows very promising results and reproduces the unsteady cavitation flow. The advantage of the model is that the computation is less expensive than LES and more accurate than URANS computations only for highly separated flow regions where the eddies are of the same order than the grid width. The computations with this model are presented as a test evaluation.

Two cavitation numbers (σ =1.2 and 1.5) are addressed and compared to the experimental data. The unsteady cavitation flow field including transient cavity shedding is reproduced. The cavity growth, detachment and collapse are predicted in a periodic way. Cavitation computations highlight the fact that for longer cavities, where the pressure gradient is not important, the cavity breaks into many random bubbles. As soon as the cavity closure reaches the region of high pressure gradient, the reentrant jet becomes thicker and pulls off the whole cavity. The predicted shedding frequencies are very close to the measured one, and the predicted Strouhal numbers are in range of 0.3$\sim$0.4 for the different cavitation regimes and are in agreement with different values reported in the literature [105][41]

Signals of the lift, drag, and vapor generation are reported and illustrate that in addition to the global primary events of the vapor formation, the cavity wrenching and collapse, local secondary events related to the pattern of the transient cavities are also observed. They are randomly distributed, changing from one period to another and correspond to the passage of the vapor volumes on the hydrofoil surface making the lift and drag signals different between the computed periods.

Part V

Cavitation in an Industrial Inducer

Cavitation is commonly observed when a hydraulic machine operates under off design conditions and is still a limiting factor in hydraulic design and operation. A special case of these machines is the inducer which is generally located upstream of the main impeller, and is designed to control cavitation and to pressurize the flow sufficiently allowing the principal impeller to operate in better operating conditions. The major characteristic features of an inducer are low flow coefficient (0.05 to 0.2), large stagger angle (70 to 80°), and high solidity blades (few blades of very long chords) of little or no camber. The inducer usually contains fewer blades (3 or 4) than conventional pumps and is designed to keep cavity thickness to minimum. Long and narrow passages provide the time and space for cavitation bubble collapse. The resulting configuration, although beneficial from a cavitation point of view, results in highly viscous, turbulent flow developed inside these passages. Lakshminarayana [92] provides a very comprehensive review of experimental and analytical investigations of the fluid dynamics in non-cavitating inducers.

Although the use of inducers is frequent today in petroleum, chemistry and cryogenic rocket fuel industries, several aspects of their operation still remain difficult to model, especially in unsteady-state two-phase flow cavitating regimes. The major studies of this topic are divided into two main lines: the first is interested in the system instability due to cavitation and are theoretical developments based on 1D models. The second undertakes 3D or quasi-3D Euler/NS simulations of the cavitation development in inducers.

The instabilities associated with cavitation in hydraulic systems can be divided into two categories: system instability and local instability. The first instability mode is associated with overall mass flow oscillations through the entire system and known as auto-oscillation or "cavitation surge". This phenomenon is observed during the boost phase of vehicle flight and named the POGO effect. Rubin [118] developed transfer functions with a linear mathematical model for instability analysis and highlighted the importance of the cavitation compliance in turbo-pumps (change of cavity volume with respect to suction pressure). Brennen and Acosta [23] and Brennen et al. [24] have characterized this effect by a positive "mass flow gain factor" (increase of cavity volume related to a decrease of the flow rate). An excellent review of these instabilities has been presented by Greitzer [68, pp 217-222]. The other type of instability is associated with the local flow in the inducer and the inlet flow and known as the "rotating cavitation". It manifests as unsteady cavitation at the inducer inlet that rotates with the inducer blades. This is related in the experimental works of Kamijo [80] to the flow conditions at the inlet. Tsujimoto et al. [143] have theoretically investigated this phenomenon and have highlighted the origin of rotating cavitation and rotating stall in inducers. They have stated that these are two different phenomena: the rotating cavitation is caused by the positive mass flow gain factor whereas the rotating stall is caused by the positive slope of the pressure performance, and the rotating stall is not significantly affected by the rotating cavitation.

Concerning the 3D model predictions of cavitation in turbo-pumps, they generally orig-

inate from the models used in 2D hydrofoil or in blade cascades. Cooper [36] has investigated an elaborated technique already in the sixties, using a mono-dimensional state equation for the vapor phase in a quasi 3D analysis of the flow field, unfortunately at this time, he was limited by the computation facilities. Kueny et al. [85] have used similar technique with a meridian/blade-to-blade external potential flow computation type, and have shown a good agreement in terms of the predicted cavity shapes in comparison to experimental data. In the last decade, different approaches have been proposed for cavitation simulation in hydraulic machinery using 3D Navier-Stokes solvers. The first approach based on fully 3D computation was undertaken by Hirshi et al. [72; 73] and was based on interface tracking strategy. Recently, cavitation modelling through a multi-phase mixture model have been introduced, using state equation models [40; 37] or transport equation for the phase change modelling [12; 97; 17; 10; 11].

Chapter 10

Methods Evaluation

10.1 Case Study and Experimental Setup

The present case study refers to a 3-bladed industrial inducer (Fig. 10.1). The inducer (model test) is designed for nominal operating conditions corresponding to a flow coefficient of $\varphi = 0.25$ with a rotational speed of 3'000 rpm, which corresponds to a specific energy coefficient of $\psi = 0.08$.

Measurements of hydraulic performances as well as cavitation visualizations have been achieved in the test rig of the Mitsubishi Heavy Industry R&D center (Fig. 10.2). It is composed of a large storage tank. An alternate current motor powered by a variable frequency controller was used to drive the tested inducer up to a rotational speed of 9'000 rpm. The inducer is equipped with a transparent acrylic cover for visualizations, and various measurement devices are used (pressure sensors at the inlet and outlet, flow-meter, torque-meter) to measure the operating conditions. The water temperature is kept constant with the help of a heat exchanger located in the return pipe.

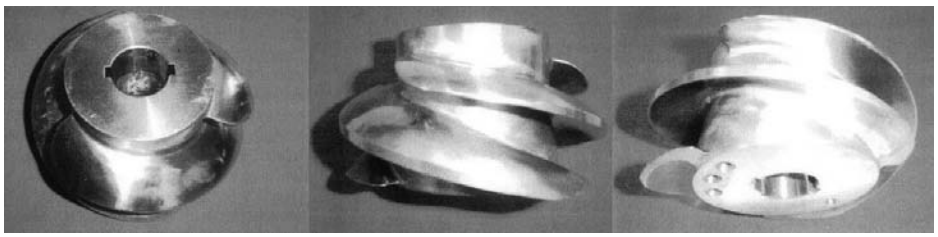

Figure 10.1: MHI Inducer case study

10.2 Numerical Setup

The CFX-TASCflow solver [M3], is used for the present work. A hybrid first/second order scheme associated with a modified interpolation coefficients is used for the convection term. A multiblock structured mesh is generated with the help of the TurboGrid [M4] mesh generator for hydraulic machines. Six different meshes ranging from 150'000 to 500'000 nodes were tested in cavitation free conditions and showed negligible grid influence

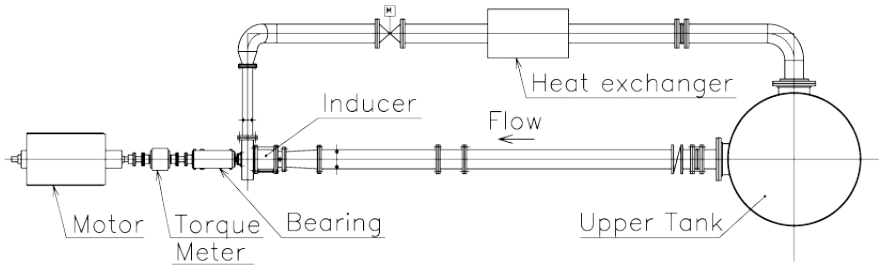

Figure 10.2: MHI Inducer test loop facility

in terms of the head evaluation and the pressure distribution on the blade beyond the 260'000 nodes mesh. This mesh is used for the computations. The computing domain, which corresponds to a single machine passage (1/3 of the machine), is made of nine O-blocks and H-blocks as well as 3 evolution layers of cells around the blade surface in the hub-to-shroud, blade-to-blade and meridional directions are used to ensure good grid orthogonality and cells evolution factor (Fig. 10.3). A refined mesh with ten nodes in the hub to shroud direction is used in the tip clearance region and connected to the rest of the domain with a generalized grid interface (GGI) connection type.

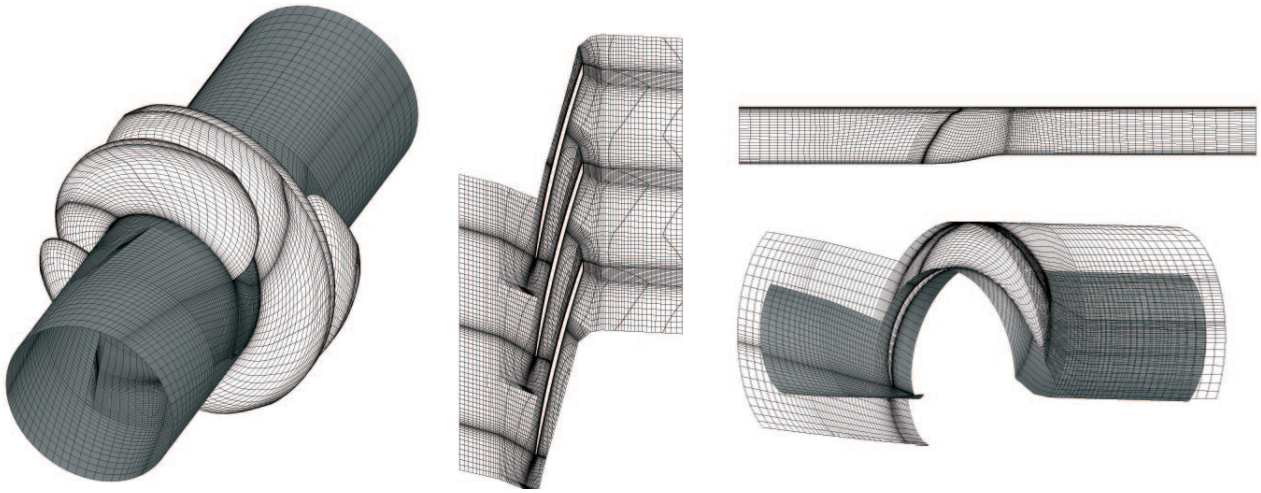

Figure 10.3: Inducer grid

Steady-state solutions are obtained for different regimes by setting the flow rate at the inducer inlet and the average static pressure at its outlet as boundary conditions (the needed σ value is set based on the outlet pressure and head of the inducer stage). Single channel geometry in rotating frame of reference is used and periodicity conditions are applied to the channel connections. The hub and the inducer blade are set to rotating walls whereas the shroud is set to stationary. The k-ε turbulence model is used for the computations. Computations are made in the cavitation free regime, then the pressure condition at the inducer outlet is lowered until reaching a substantial drop of hydraulic performance. A maximum numerical residual is kept below 10^{-4} as convergence criteria.

Numerical simulations are performed for three operating points corresponding to $\varphi^{**} =$

$\varphi/\varphi_{\text{design}} = 0.8, 1.0$ and 1.2. The design point is the best efficiency operating point (BEP). The multiphase transport equation based model (Model 3) is used for the three operating points whereas the interface tracking model (Model 1) is only used for the BEP as methods evaluation and comparison.

10.3 Methods Evaluation

The ability of the interface tracking (Model 1) and the multiphase flow (Model 3) models to predict the performance of the inducer under cavitation condition is evaluated for different values of the cavitation number ψ_c for the best efficiency point $\varphi = \varphi_{\text{design}}$. The results obtained with both models are compared to the experimental data in terms of cavity shape and performance drop. It should be noticed that for the interface tracking model, any cavitation which is not attached to the blade surface is not computed. Only the cavitation which occurs at the blade surface boundary can be predicted. Therefore, the tip clearance cavitation is not considered.

It should be noticed that in the comparison between the numerical computations and experiments, a correction (shift) of the head is made for the numerical results. Measurements which are based on the difference between the total pressure, downstream of the diffuser and far upstream of the inducer inlet, include more hydraulic losses than the computational domain which is confined to a smaller region (inducer inlet-outlet). The computed value ($\Delta E = E_{\text{exp}} - E_{\text{num}}$) in cavitation free regime for each operating point (φ^{**}=0.8, 1.0, 1.2) is used as a shift value for the numerical results. This hypothesis is justified by the fact that the losses remain constant in fixed (non rotating) and non cavitating hydraulic parts of the system at fixed flow rate.

10.3.1 Cavitation Visualization

Cavitation figures corresponding to different values of ψ_c are reported in Fig. 10.4. Photographs of the flow taken through the transparent acrylic cover of the test rig are compared to the predictions of both models (a value of $\alpha_v = 0.1$ is taken for the multiphase model cavity interface).

The cavitation inception is observed experimentally at ψ_c=0.6, which corresponds to the numerical prediction. Nevertheless, while the experiment shows a simultaneous inception of cavitation in the tip clearance region and in the leading edge, both models predict cavitation inception only in the tip clearance region at ψ_c=0.6. The occurrence of the leading edge cavitation is predicted at ψ_c <0.4 by both models. For values of ψ_c <0.15, cavitation extends to the channel region and reaches the throat leading to a flow blockage. The corresponding flow visualization clearly shows strong unsteadiness of the cavity dynamics.

10.3.2 Head Drop Prediction

In Fig. 10.5, the specific energy coefficient is shown as a function of the cavitation number. Experimental results are compared to the calculations one and show good agreement concerning the threshold of performance alteration at ψ_c 0.12. At this operating condition, the suction side cavitation develops beyond the throat and an attached cavitation

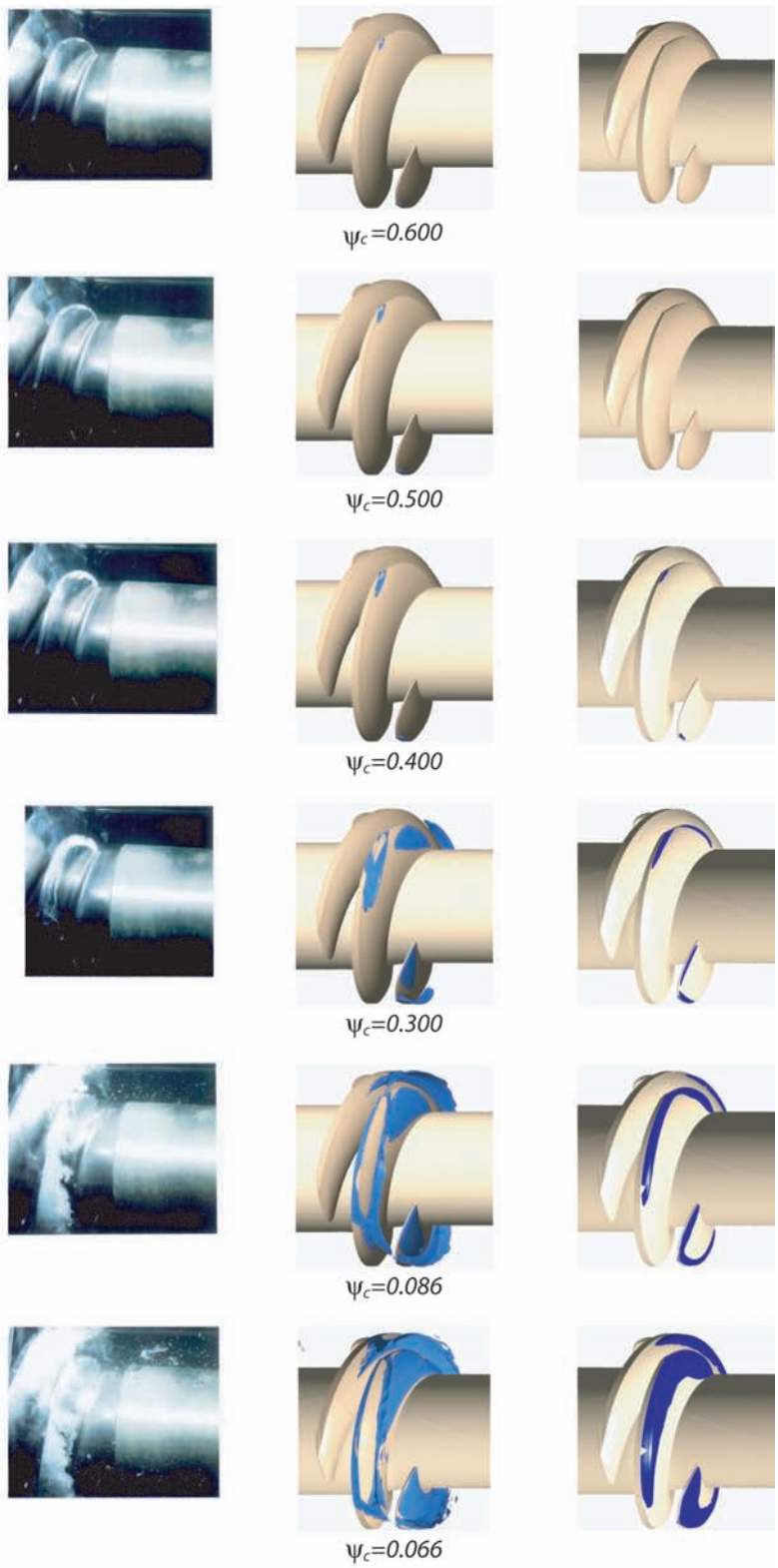

Figure 10.4: Cavitation development for different cavitation regimes, φ^{**}=1.0
left : experiments, center : model 3 (α_v=0.1), right : model 1 (deformed grid)

is observed on the pressure side. The predicted breakdown value agrees well with experimental results when it comes to the beginning of performances drop. For lower values of the cavitation number, the predicted drop is underestimated. For these flow regimes, the unsteady character of the flow which may have an influence in the flow characteristics is not taken into account by the steady-state computation.

Both interface tracking and multiphase flow mixture models predict the same results for the head drop phenomenon. It results for this case that the small region of tip cavitation has no major influence in the head drop. The head drop is mainly due to leading edge cavitation and the resulting flow disturbances. For the rest of the work, we will use the multiphase flow mixture model, mainly due to the ability of the model to capture more cavitation types than the mono-fluid model as the non-attached cavities.

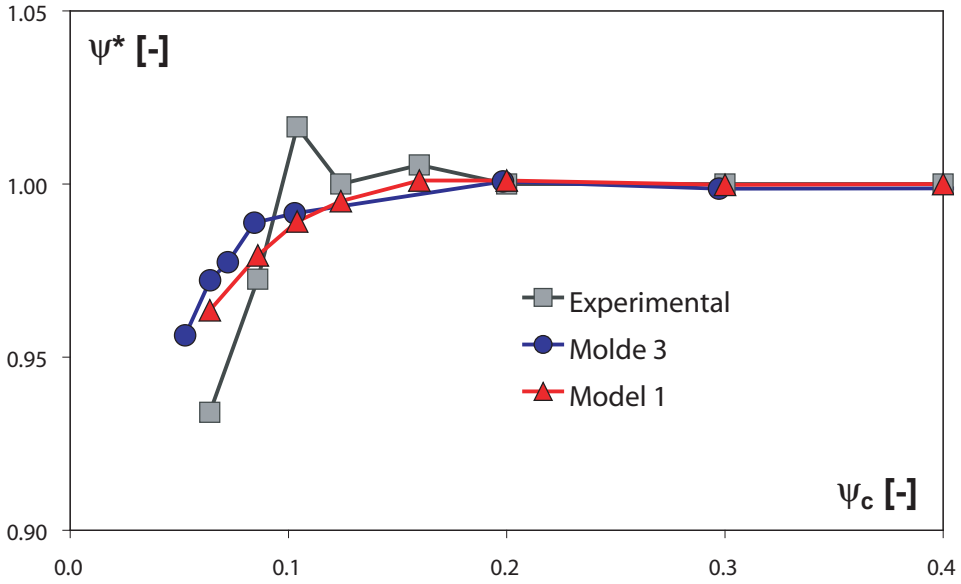

Figure 10.5: Predicted and measured inducer head ψ vs. cavitation number ψ_c

10.4 Cavitation Behavior

10.4.1 Cavitation Visualization

Cavitation figures corresponding to different stages of cavitation development for the three values of φ are reported in figs. 10.4, 10.6, and 10.7. The predicted cavitation flow is in good agreement with experiments, and shows the typical cavitation development in the inducer. The numerical simulations underestimate the tip vortex cavity. The predicted tip vortex cavitation is less important and shorter than measured one. The computed main leading edge cavity agrees well with the data, even if its inception is predicted at lower cavitation numbers.

- For the partial flow rate ($\varphi^{**} = 0.8$), cavitation mainly occurs at the shroud and tip regions, and the back-flow vortex cavitation is returning upstream of the inducer. The flow induced by the cavitation occurrence is unstable and the cavity region occupies the entire channel near the shroud region at lower ψ_c.
- At the nominal flow rate ($\varphi^{**} = 1.0$), cavitation develops along the blade surfaces and the tip region. For lower values of ψ_c, cavitation extends to the channel region and reaches the throat leading to a flow blockage.
- For the high flow rate ($\varphi^{**} = 1.2$), stable and thin cavities develop principally on the blade surfaces. The tip vortex cavitation is less important.

Inducer design requirements lead to geometries where the best (adapted) flow incoming angle design point is different from the best efficiency operating point, the latter being located at lower flow rates. The shape as well as the stability of the cavity attached to the blade is directly related to the incidence angle of the flow at the leading edge of the blade. The high flow rate ($\varphi^{**} = 1.2$) corresponds to the adapted flow incidence which leads to thin and stable cavities mainly at the blade leading edge. In contrast, at low flow rates ($\varphi^{**} = 0.8$), the leading edge cavity exhibit an unstable behavior and the main cavitation occurs at the shroud region leading to a large tip vortex occurrence close to the gap.

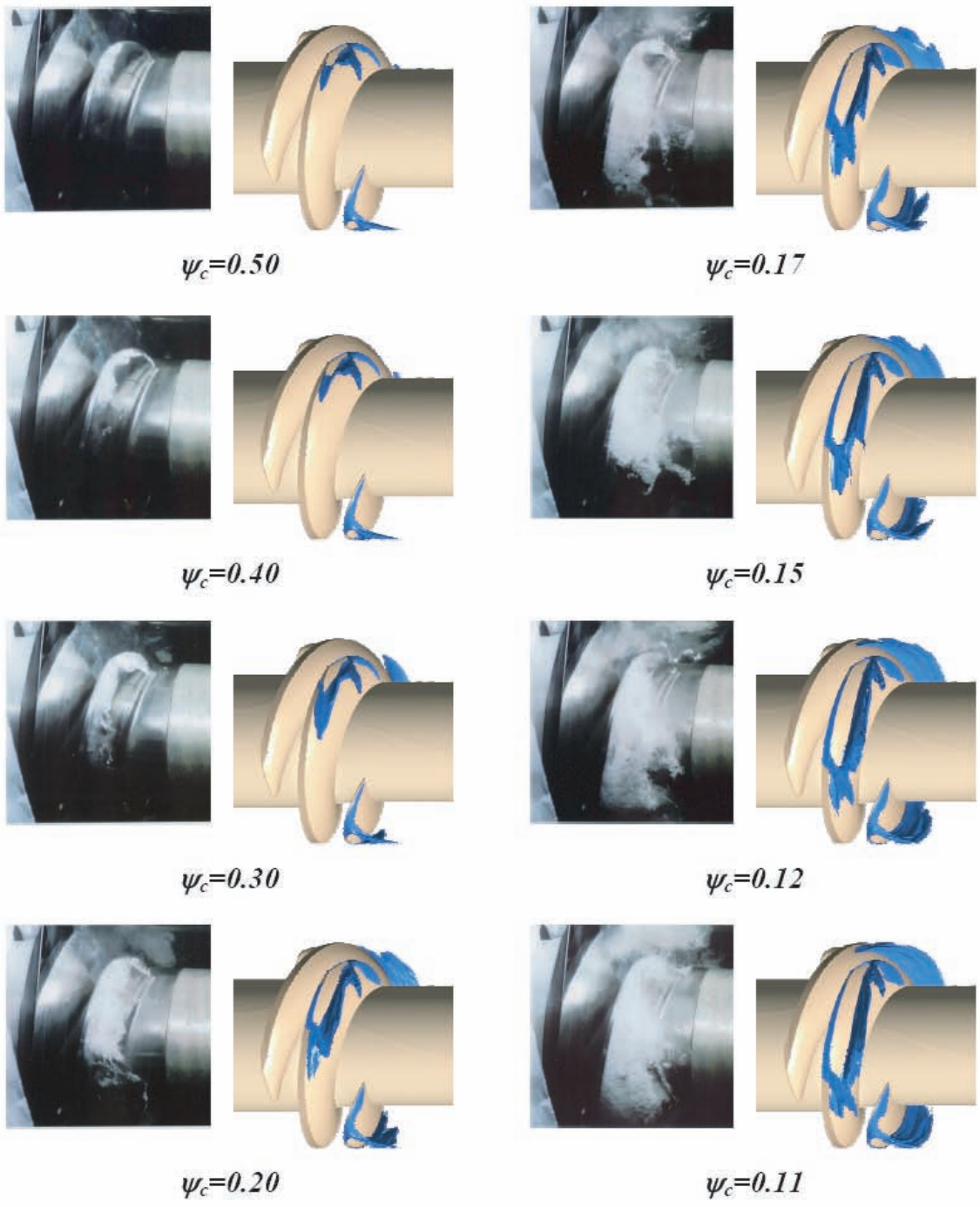

Figure 10.6: Cavitation development for different cavitation regimes, $\varphi^{**} = 0.8$ (left : experiments, right : model 3 (α_v=0.1))

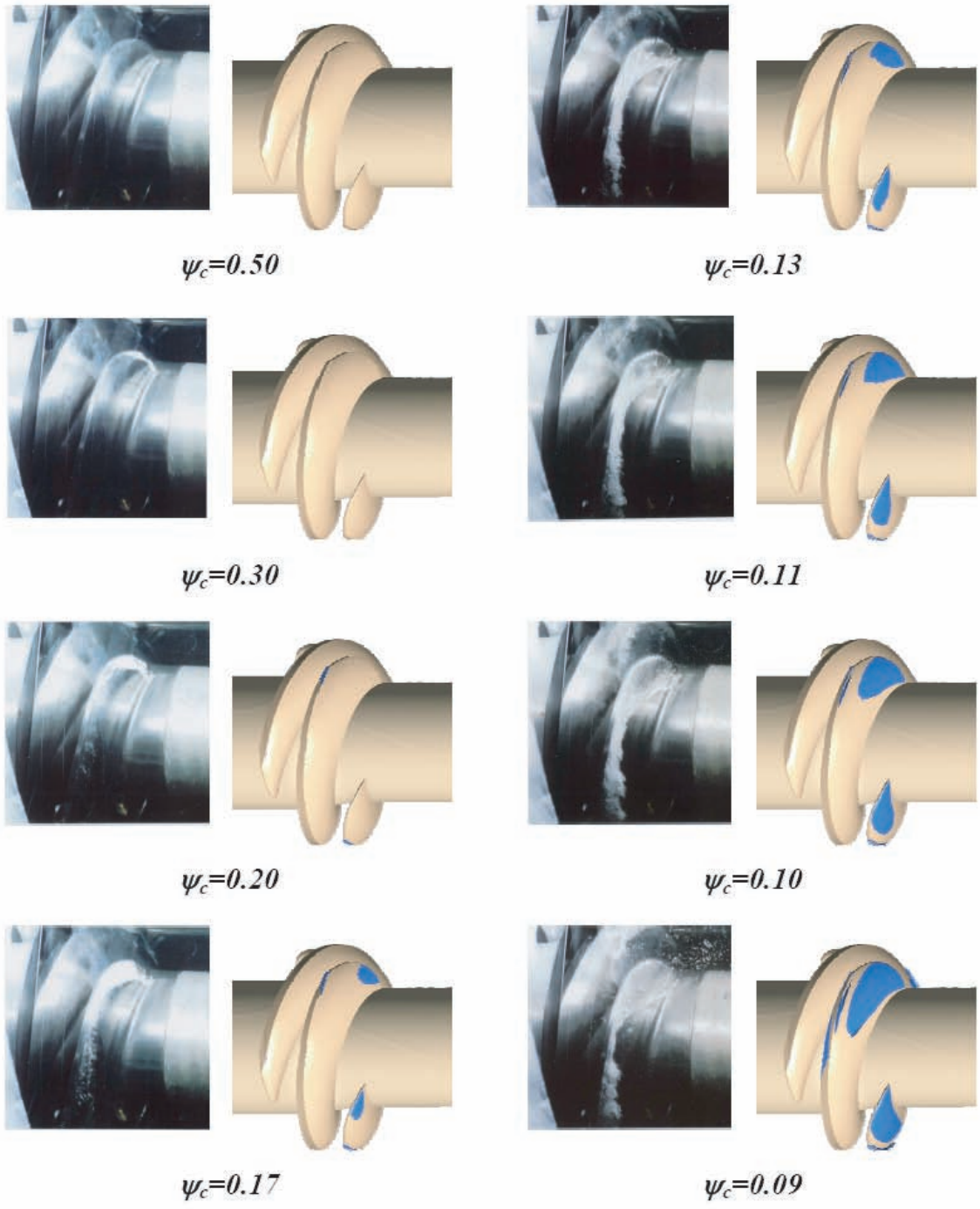

Figure 10.7: Cavitation development for different cavitation regimes, $\varphi^{**} = 1.2$ (left : experiments, right : model 3 (α_v=0.1))

10.4.2 Head Drop Prediction

We plotted in Fig. 10.8, the dimensionless specific energy coefficient ψ^{**} function of the cavitation number ψ_c. Experimental results are compared to the predicted ones and show good agreement concerning the threshold of performance alteration for the design operating point. For off design points the head drop threshold is predicted at lower values of ψ_c. At the breakdown value, the suction side cavitation develops beyond the throat and an attached cavitation is observed on the pressure side. For lower cavitation numbers, the predicted drop is underestimated. For these flow regimes, the unsteady character of the flow is not taken into account by the computation.

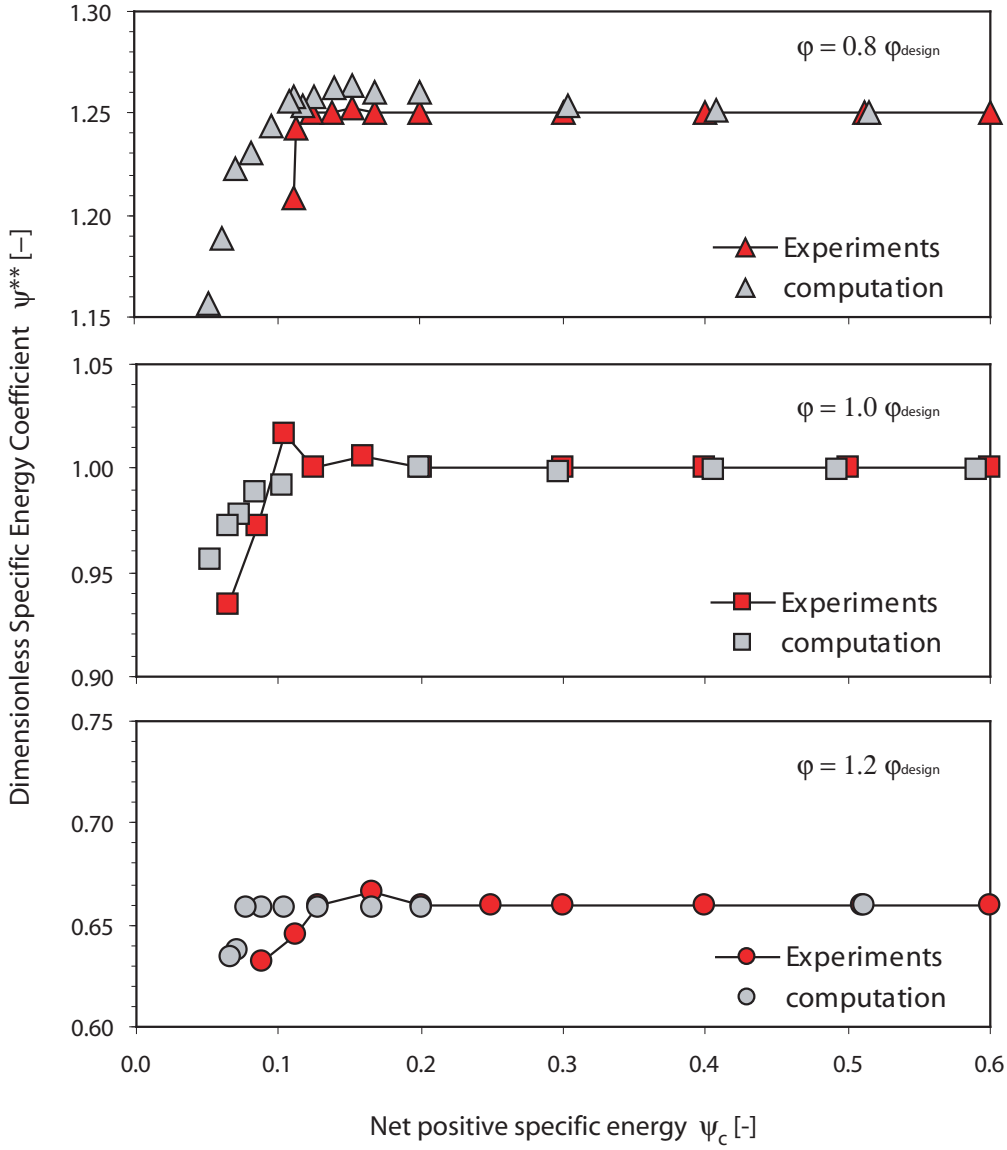

Figure 10.8: Predicted and measured inducer head function of the cavitation number filled: experiments, opaque: computation. Operating points: $\varphi^{**} = 0.8,\ 1.0,\ 1.2$

Chapter 11

Head Drop Analysis

The head drop in hydraulic machines occurs at values of ψ_c which correspond to a given cavitation development in the machine. The interest is to understand the mechanism of this phenomenon through an energetic transfer point of view and to set an understandable threshold of cavitation development which causes the head drop. The need is to understand the origin and the onset of the head drop as well as to locate the sensitive areas affected by the cavitation.

11.1 Energy Balance

The energy loss E_r in the system is determined by comparing E_t, the energy supplied to the inducer, with E_b, the specific energy effectively transferred to the fluid by the inducer stage. This is expressed by:

$$E_b = E_t - E_r \tag{11.1}$$

Supplied Specific Energy

The specific energy supplied to the inducer is defined by:

$$E_t = \frac{\vec{T_t}\vec{\Omega}}{\rho Q} \tag{11.2}$$

where $\vec{\Omega}$ is the angular rotation speed and $\vec{T_t}$ represents the resulting moment of the flow forces acting on the inducer and may be derived from the integration of the pressure and the viscous forces on the blades and the hub surfaces (torque of the rotating parts).

Inducer Energy

The energy E_b transferred to the fluid by the inducer blades is defined by the energy balance between low pressure and high pressure sections of the inducer domain.

$$E_b = gH_1 - gH_{\bar{1}} \tag{11.3}$$

We have reported in the same graph (Fig. 11.1) the evolution of the specific energy supplied by the machine ψ_t^* as well as the specific energy transferred to the fluid ψ_b^*

as a function of cavitation number ψ_c. According to Fig. 11.1, the drop of specific energy corresponds to a drop of both supplied and transferred energies. This observation evidences that the flow field is strongly changed as the cavitation extends beyond the throat region, leading to lower value of the torque. For operating regimes $\varphi^{**} = 0.8$ and $\varphi^{**} = 1.0$, the transferred energy decreases faster than the supplied energy, which demonstrates that the hydrodynamic losses due to cavitation development play a major role in this case. For the high flow rate ($\varphi^{**} = 1.2$), the torque decrease is the principal reason of the beginning of the head drop.

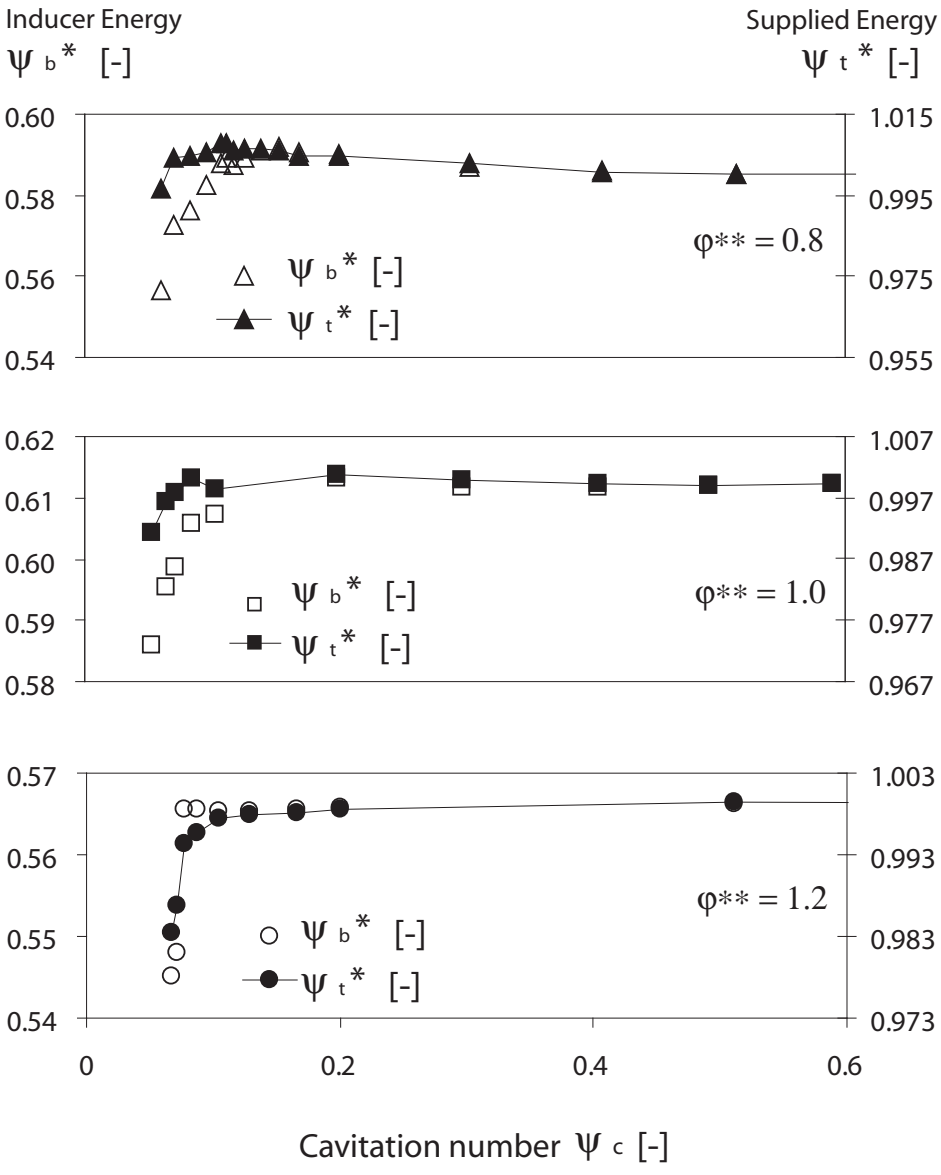

Figure 11.1: Evolution of the supplied (ψ_t^*; filled) and transferred (ψ_b^*; opaque) specific energy coefficients function of the cavitation number (ψ_c)

Table 11.1 summarizes the values of the head drop origin for the three regimes corresponding to the operating point of 3% of energy loss (φ^{**}, ψ_c): (0.8, 0.070), (1.0, 0.064),

(1.2, 0.072). This point is mainly the threshold taken for the head drop criterion by the manufacturer. For the high flow rate ($\varphi^{**} = 1.2$), where the cavity is thin, the losses are mainly due to both torque reduction and hydraulic losses. The attached cavity on the blade plays the main role of torque limiter. When reducing the flow rate ($\varphi^{**} = 1.0, 0.8$), the most important part of the head drop origin are the flow-induced losses due to the high disorganization of the flow field (tip cavitation, back-flow cavitation). For $\varphi^{**} = 0.8$ a special case where the torque is more important (increase in the efficiency) than the cavitation free regime is shown at the head drop operating point.

Operating point	Torque loss (%)	Hydraulic losses (%)
$(\varphi^{**} = 0.8, \varphi_c = 0.070)$	-20	120
$(\varphi^{**} = 1.0, \varphi_c = 0.064)$	13	87
$(\varphi^{**} = 1.2, \varphi_c = 0.072)$	51	49

Table 11.1: Summary of the head drop origin

11.2 Blade-Fluid Transfer

In order to eliminate the fraction of pressure, which does not contribute to the torque (axial contribution part), we may define the following coefficients for any given location M on the blade surface:

$$Cp_{t\_T}(M) = \frac{\vec{U}}{\|\vec{U}\|}\vec{n}Cp_t(M) \tag{11.4}$$

$$Cp^*_{t\_T}(M) = \left[\frac{\vec{U}}{\|\vec{U}\|}\vec{n}Cp_t(M)\right]_{PS} + \left[\frac{\vec{U}}{\|\vec{U}\|}\vec{n}Cp_t(M)\right]_{SS} \tag{11.5}$$

where Cp_t is the total pressure coefficient. $Cp_{t\_T}(M)$ is the total pressure density which contributes in the torque direction, and $Cp^*_{t\_T}(M)$ will be the blade load. $\vec{U}$ the peripheral velocity and $\vec{n}$ the normal to the blade surface at a given location (M). PS and SS refers respectively to pressure and suction sides.

Figure 11.2 shows the distribution of the coefficient $Cp^*_{t\_T}$ for the cavitation-free regime and cavitating regime corresponding to 3% of the head drop at the best efficiency point ($\varphi^{**} = 1.0, \varphi_c = 0.064$) as an example of the torque evolution on the blade. Figure 11.3 shows the evolution of the coefficient Cp_{t_T} along the chord for two different values of the span, 0.1 (near the hub) and 0.9 (near the shroud).

As the cavitation parameter is decreased, a decrease of the $Cp^*_{t\_T}$ coefficient in the leading edge area followed by an increase at the cavity closure zone is observed. Since no alteration of the torque is observed, the loss and gain in $Cp^*_{t\_T}$ coefficient are balanced. As soon as the cavity reaches the throat, the resulting drop of the torque illustrates that the loss in the $Cp^*_{t\_T}$ coefficient is no longer balanced by the gain at the cavity closure. Indeed, the cavitation occurrence in the pressure side, near the hub, fixes the value of the pressure leading to a decrease in the pressure side Cp_{t_T} (Fig. 11.3, span=0.1) which is no longer balanced by the flow mechanisms.

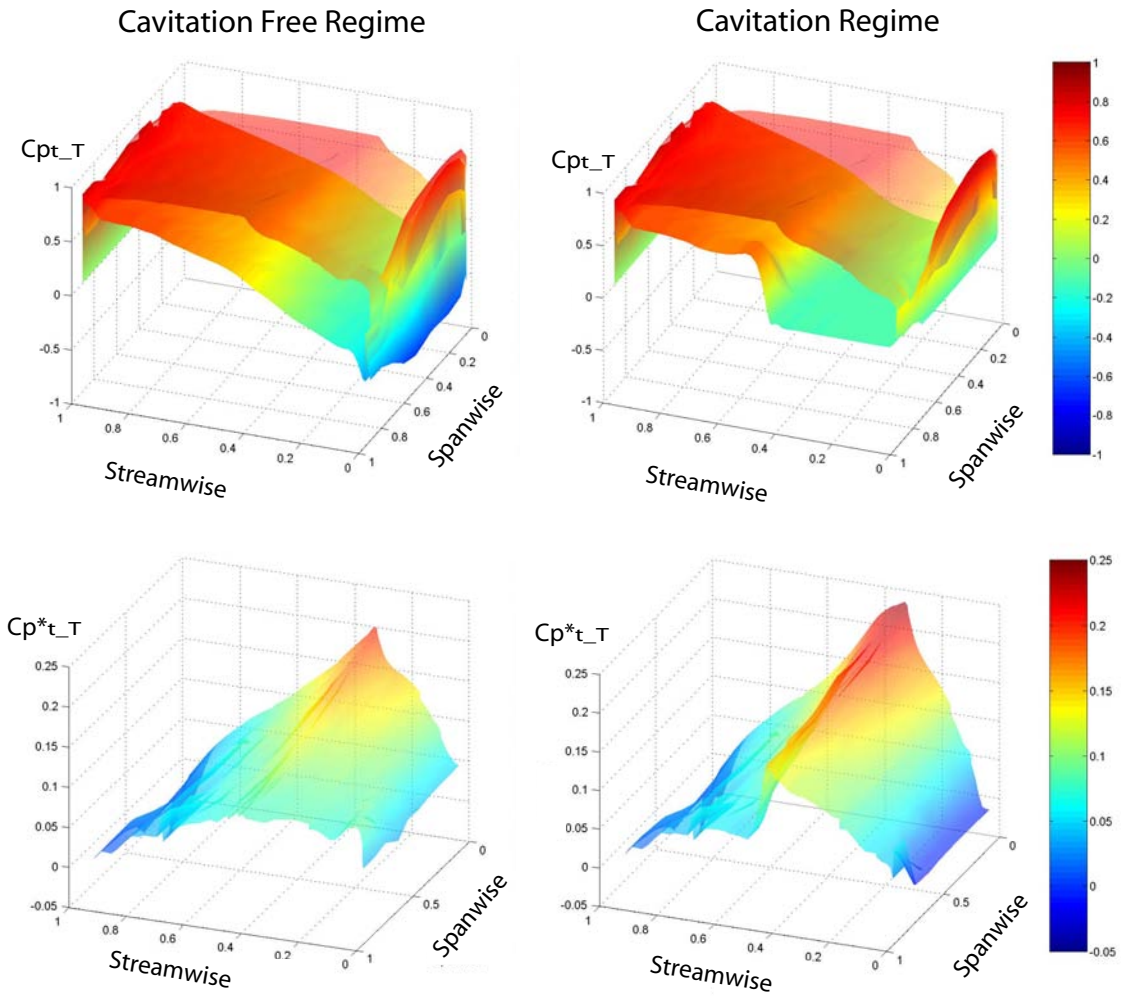

Figure 11.2: $Cp^*_{t\_T}(M)$ distribution on the inducer blade

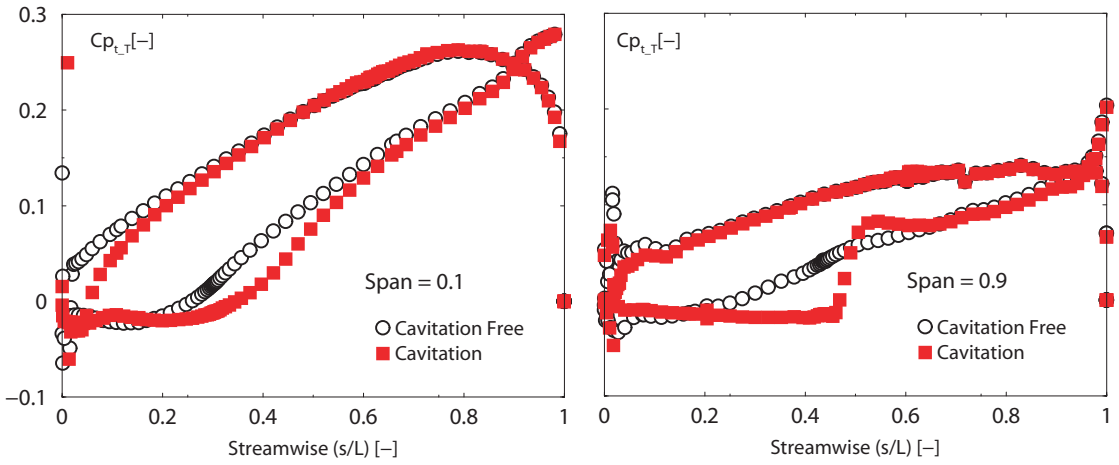

Figure 11.3: Evolution of $Cp_{t\_T}(M)$ coefficient on the suction and pressure sides near the hub (span = 0.1) and the shroud (span = 0.9) areas

Furthermore, the occurrence of leading edge cavitation on the pressure side is due to a significant decrease of pressure coefficient in this area, since in the cavitation free regime the pressure value at the pressure side is higher than the vapor pressure (Fig. 11.3, span=0.1). This illustrates the modification of the flow field in the channel as soon as the main cavitation reaches the throat area. The cavitation occurrence in pressure side could be the main reason of the torque loss in this case. Using a potential flow simulations, and without predicting the head drop, Kueny & Desclaux [85] have already reported that the measured head drop corresponds to the cavity reaching the blade passage in their simulations. They supposed that the main reasons of head drop are the losses which are not predicted by the model.

11.3 Energy Evolution in the Meridian Channel

For an understanding of the mechanisms of the head drop and a localization of relevant areas affected by cavitation, we have carried out an analysis of the specific energy evolution through the meridian channel. We have considered fifteen surfaces located in the meridian channel (Fig. 11.4).

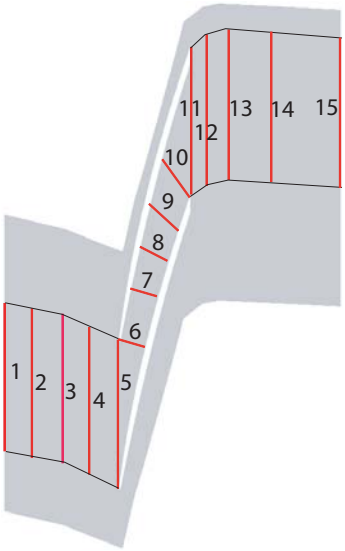

Figure 11.4: Meridian channel subdivision

The evolution of three energetic variables is analyzed: the specific energy (ψ), potential energy (ψ_s), and kinetic energy (ψ_k) from the inlet to the outlet of the domain is presented. Figure 11.5 represent this evolution for the cavitation-free flow and cavitating flow corresponding to 3% of the head drop, which illustrate the operating condition pairs (φ^{**}, ψ_c) : (0.8, 0.070), (1.0, 0.064), (1.2, 0.072). The total energy transferred to the fluid in the cavitation free regime, computed as a difference between total energies at sections 15 and 1, is used to normalize all plotted variables.

Several observations may be done through the evolution of the energy and its transfer in the machine due to the cavitation development:

Sections 1–5 (upstream to the blade leading edge): Since no energy is yet transferred to the fluid, the total energy in sections 1 through 5 remains almost constant.

Furthermore, no cavitation effect on the energy evolution can be observed in this area.

Section 6 (throat, cavity closure): The leading edge cavitation causes a decrease of the potential energy and an increase of the kinetic energy. This may be explained by the fact that the flow is accelerated in the non cavitating region to ensure mass conservation.

Sections 6–8 (first part of the channel): The excess of the kinetic energy due to cavitation at section 6 is totally dissipated at sections 7–8, but partially transformed to a potential energy, since the potential and total energy losses are reduced but not totally recovered.

Sections 8–10 (second part of the channel): The lack of total energy observed in the mid-channel (section 8) is no more recovered in the rest of the channel.

Sections 11–15 (blade wake, inducer outlet): The cavitation has no significant effect on energy distribution and the lack of energy observed in previous sections is almost maintained.

To highlight the effect of cavitation losses, the evolution of the rothalpy parameter I in the meridian channel using the same domain subdivision os analyzed. The rothalpy is defined by:

$$I = \frac{p}{\rho} + gz - \frac{U^2}{2} + \frac{W^2}{2} \tag{11.6}$$

To focus on the cavitation influence alone, the induced cavitation effects may be related to rothalpy evolution as follows:

$$\text{Cavitation induced Losses} = \frac{[I_{\text{ref}} - I]_{\text{cav.}} - [I_{\text{ref}} - I]_{\text{cav.free}}}{[I_{\text{ref}} - I]_{\text{cav.free}}} \tag{11.7}$$

where I_{ref} denotes a reference rothalpy averaged over the section 1. Figure 11.6 shows the evolution of the energy losses in the meridian channel for the same operating points as discussed above.

The graphics illustrates that total losses in the inducer (inlet to outlet) are important with the decreasing flow rate. This confirms the statement made in the energy analysis (Fig. 11.1). As shown in cavitation behavior (figs. 10.4, 10.6, 10.7) the cavities are thinner, and mainly attached to the blade at high flow rates, where they exhibit a very unstable behavior with very thick cavities and back-flow region at low flow rate. One may be able to suppose that the flow is more disorganized by cavitation at low flow rates. For the operating points (φ^{**}=1.0, 1.2), between sections 1 and 4, no significant change in energy losses is observed, illustrating that the flow upstream of the blades is not affected by the cavitation. For the operating point (φ^{**}=0.8), significant losses are located upstream of the blade leading edge. This is due to the back-flow cavitation regions which characterize the cavitation behavior of inducers at low flow rate (Fig. 10.6).

The negative value of relative losses obtained in section 6 (6-8 for φ^{**}=1.2) shows a better energy transfer (low losses values) between the blade and the fluid, in the space

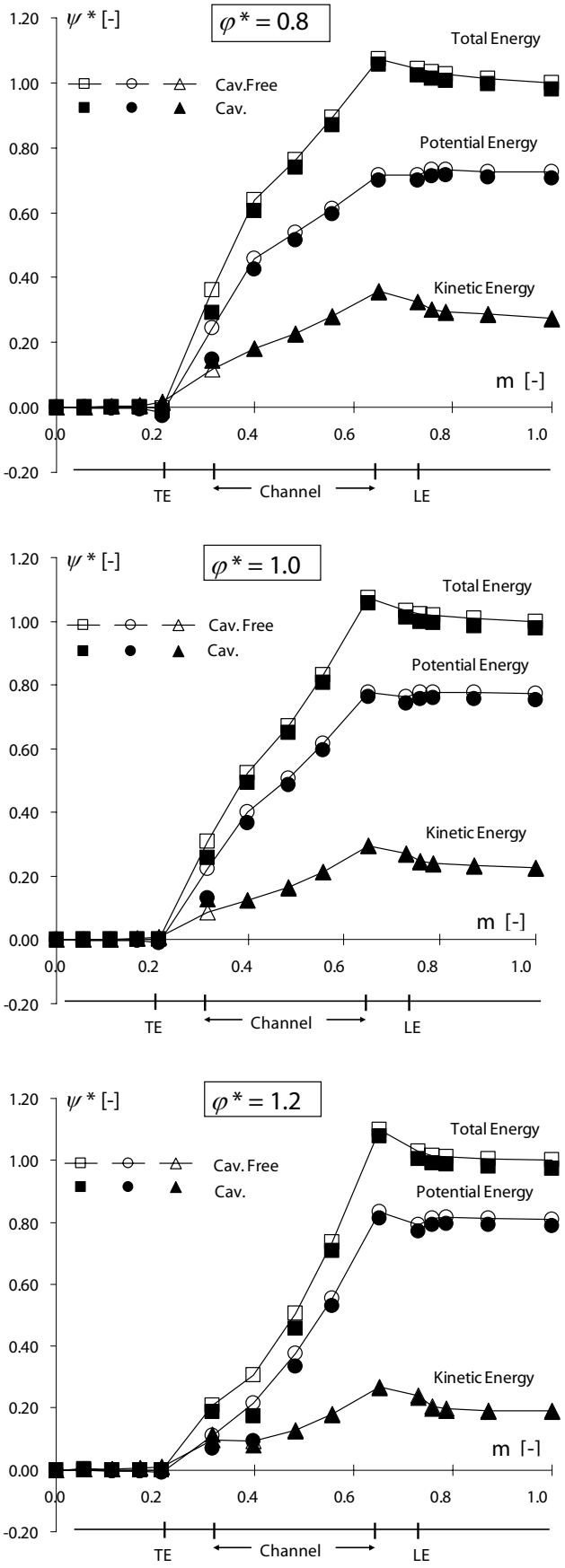

Figure 11.5: Evolution of the specific energy in the meridian channel

between the leading edge and the channel inlet. In contrast, from the channel inlet up to the trailing edge (sections 6 to 10), the flow exhibits an increasing energy loss due to cavitation. No further relative losses are observed up to the inducer outlet. Note that the results of the losses based on the rothalpy evolution are different from those of Tab. 11.1, and should not be transposed. The table shows the main origin of the head drop at a certain cavitation regime reported to the cavitation free regime. The graph based on the rothalpy represents the added losses due to cavitation occurrence (data reported to cavitation free regime where the losses already exist).

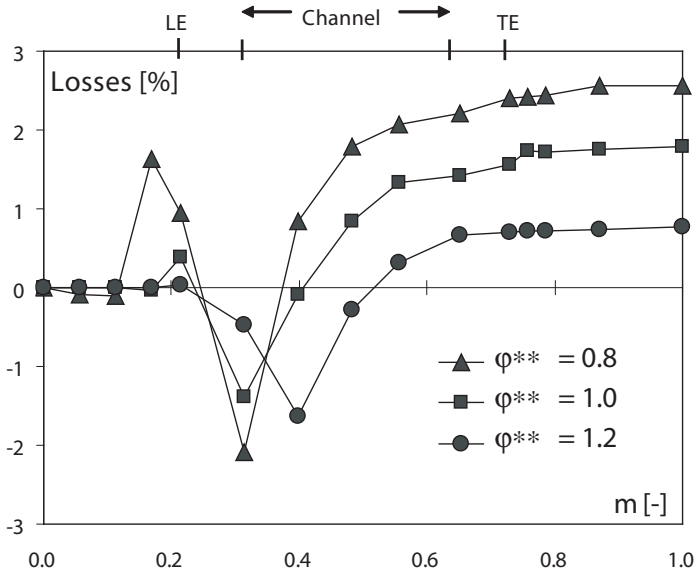

Figure 11.6: Evolution of the losses induced by cavitation in the meridian channel

11.4 Flow Unbalance and Reorganization of the Secondary Flow

Results of the cavitation regime corresponding to 3% of the head drop at the design operating point ($\varphi^{**} = 1.0, \varphi_c = 0.064$) are presented. Figure 11.7 shows local values of static pressure (p), relative speed (W), and cavitation induced change in relative speed ($W_{\text{cav}} - W_{\text{cav.free}}$) in blade-to-blade view at two different spanwise locations; near the hub, and near the shroud. The figures confirm the statements made before, showing a region of low pressure at pressure side of the blade near the hub. This region is characterized by a local high relative speed (W), whereas the shroud region shows very low relative speed at the cavitation closure. This is mainly due to the flow reorganization caused by the passage blockage near the shroud as illustrated in the last set of figures showing the increase of the flow relative speed near the hub region.

Figure 11.8 shows the distribution of the normal speed, losses, and kinetic energy in two plans located near the throat (channel entrance) and the mid channel. To these graphs the distribution of net tangential velocity vectors due to cavitation superposed. It should be noticed that the plans are constructed as normal as possible to the main flow direction (we use $\vec{U}$ as normal to the plan). All the reported variables including the velocity projected vectors ($\vec{C}_t$) are the cavitation induced values in % as $\bar{\Phi} = (\Phi_{\text{cav}} - \Phi_{\text{cav.free}})/\Phi_{\text{cav.free}}$.

The distribution of relative energy losses clearly shows that maximum losses are concentrated near the shroud region, mainly in the vicinity of the cavity closure as well as above the cavity interface prior to channel inlet. Another location is clearly shown to be the tip area characterized by the back-flow phenomenon. This character is emphasized at low flow rates. The normal velocity distribution in the throat clearly shows that the leading edge cavity causes an important change in the flow repartition. A significant decrease of the normal velocity in the cavity wake (shroud side) is balanced by an increase of the normal velocity in the hub region. At mid channel, although the flow unbalance is mitigated, the flow does not recover completely. The superposed vector field of the tangential velocity (surface projection of the velocity vectors) illustrates the secondary flow reorganization to achieve the flow recovery. The inducer fails in recovering the velocity distribution which remains perturbed up to its outlet.

The flow patterns reported in figs. 11.7 and 11.8 are in agreement with other studies which evidence the reverse flow and vorticity generation at the cavity closure [15; 67]. The cavitation causes a substantial increase of the energy losses in its wake and, this is made by a vorticity generation and flow unbalance. The rotating machine fails to transform the high kinetic energy to potential one in the case of vortex flows.

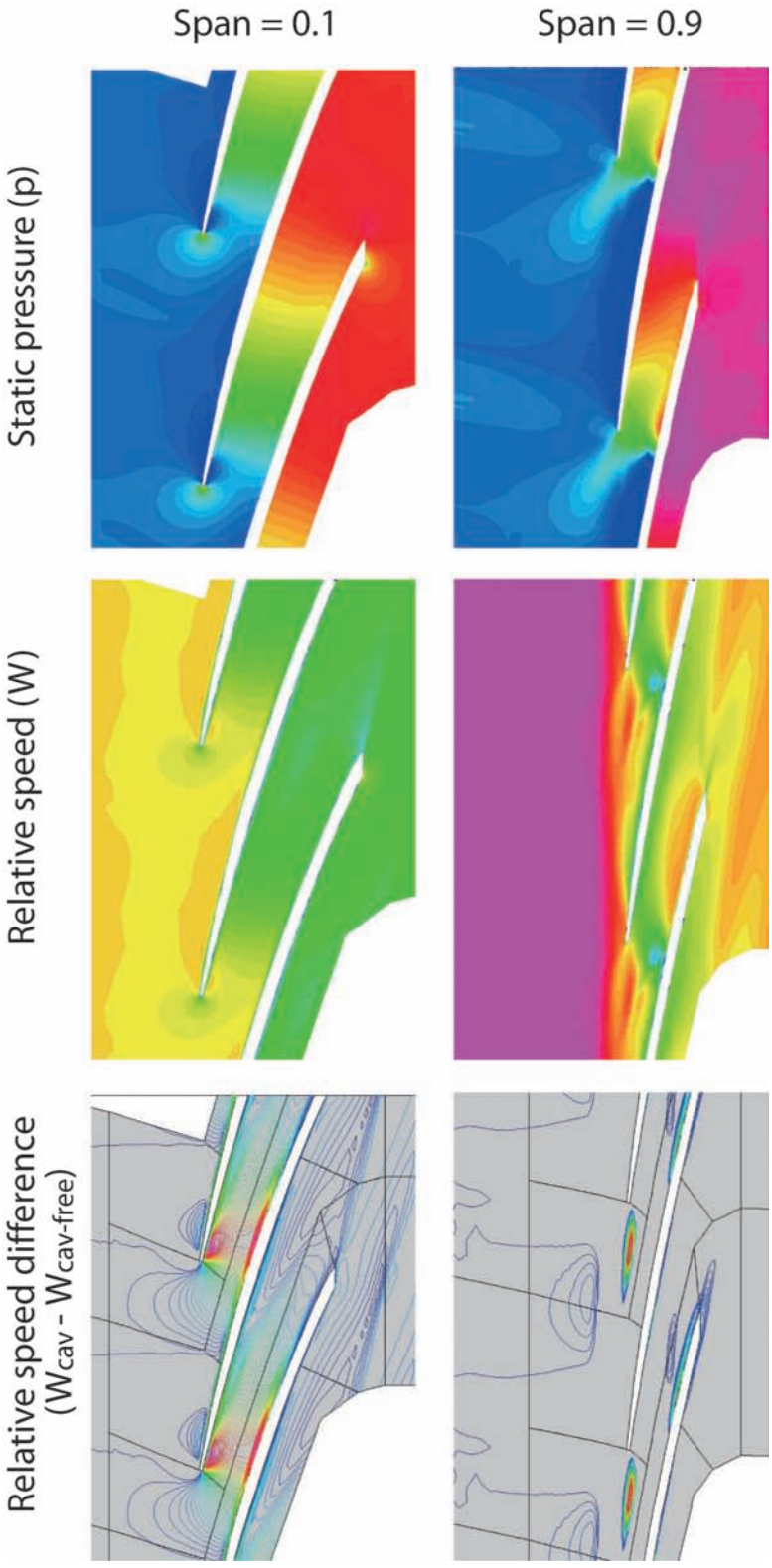

Figure 11.7: Distribution of the static pressure (p) and relative speed (W) in blade-to-blade view at two locations of the span; near the hub (0.1) and the shroud (0.9)

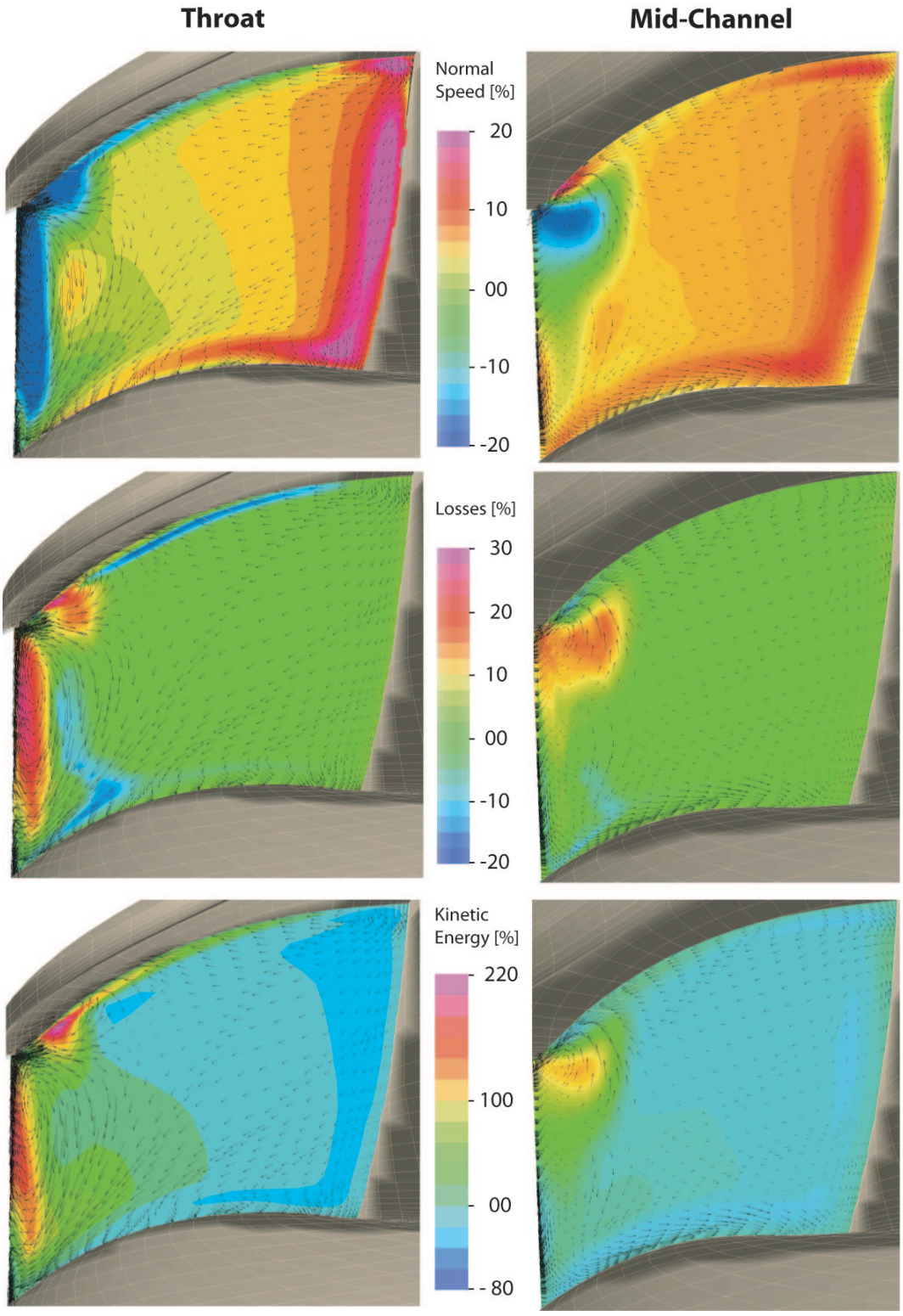

Figure 11.8: Distribution of normal speed and losses at two locations in the channel (values are the difference between cavitation free regime and cavitation regime)

11.5 Summary of the Head Drop Phenomenon

The cavitation induced head drop is mainly due to an increase of energy losses. A secondary reason of the head drop phenomenon is a decrease of the supplied energy resulting from the torque generation reduction. High flow rate regime is characterized by both and equal decrease of the torque and increase of the losses, whereas the main reason for the head drop under low flow rates conditions are the cavitation induced losses, even if the values of the torque (supplied energy) are more important than those of cavitation free regime.

The cavitation occurrence induces an increase of the kinetic energy at the channel inlet while the potential energy is decreased. Part of the gained kinetic energy is then transformed into potential energy in the channel while the other part is definitively lost. Furthermore, the rothalpy evolution analysis demonstrates that the main energy losses are located in the channel downstream of the cavity closure.

As soon as the leading edge cavitation reaches the throat, it causes a flow blockage. The lack of velocity in the flow direction in the cavity wake, near the shroud, is balanced by an increase of the velocity in the hub region. The pressure distribution on the pressure side of the opposite blade is significantly reduced at the leading edge, which allows cavitation occurrence and thereby the reduction of the torque. This is the first mechanism besides the performances drop. Although the flow unbalance is mitigated further in the channel, the flow does not recover completely. A high vortex flow is generated downstream and influences the energy transfer. This is the second mechanism of head drop and is more important for low flow rates.

In spite of the fact that this analysis provides an explanation of the hydrodynamic origin of the head drop; it should be noticed that the actual solution of the flow is steady-state and the flow rate is fixed in the computations, which is far from the realistic pumping systems where the cavitation may induce significant flow unsteadiness and large fluctuation of the cavity length as well as the flow rate.

Conclusions & Perspectives

Conclusions & Perspectives

The present work is a contribution to the physical modelling and numerical simulation of cavitation flows. A comprehensive theoretical approach is done, and detailed formulations of the existing models for cavitation flows are presented. A comparative study is made using steady-state and time-dependent computations of a 2D hydrofoil. A typical case of cavitation in an industrial inducer is investigated with regards to the head drop mechanisms in hydraulic machines

The main three model formulations: Mono-Fluid Interface Tracking Model, Mixture State-Equation Model and Mixture Transport-Equation based Model are used in the case of a 2D NACA0009 hydrofoil. Computations with the three models are compared with experimental data and show the ability of the models to reproduce the steady-state developed cavitation flow fields. In addition, the transport-based model presents the advantages of reproducing the cavitation delay by an effect of inertia in phase change modelling and the baroclinic vorticity generation at the cavity wake. The model is used in the case of a 3D rotating inducer and predicts well the cavitation development and the head drop threshold for different flow regimes. An analysis of global energy balance and flow field highlighted the mechanisms behind the performance losses in cavitating machines.

An innovative approach based on the maximum tensile criterion for cavitation inception is presented. A boundary layer computation, coupled with potential flow theory for a parabolic body leading-edge is used to evaluate the CFD computations. The technique is employed in order to include the roughness and Reynolds effects in cavitation inception for a 2D hydrofoil and shows very promising results compared to the experimental observations.

The time-dependent problem is illustrated with a 2D hydrofoil unsteady cavitation regime to detect the origin of cavitation intrinsic instability, and several turbulence models are used. Classical models fail to represent the unsteady cavitation flow, while the space filtered and modified two-equation models display cavitation instabilities in accordance with the observations. The computed phenomena frequencies agrees well with the measured one, and matches the Strouhal law.

Cavitation Inception and Detachment

The classical cavitation inception criterion is based on the macroscopic equilibrium thermodynamic criterion $p < p_v$. It was observed in practice, that the cavitation inception as well as the developed cavitation are triggered by additional parameters. It is useful to call these phenomena cavitation scale effects, which are the water nucleation, surface roughness, and Reynolds scale effects. The commonly used classical isotropic threshold

p_v, coming from potential computations fails in taking into account the specific phenomena mentioned. An innovative approach based on the maximum stress formulation in the liquid is proposed. The non-viscous anisotropic stress is taken into account through the maximum tensile stress criterion for cavitation inception.

The model developed, takes into account the surface roughness and the Reynolds effects. Experimental investigations show clearly the strong correlation between surface roughness, incoming velocity and cavitation inception. A strip roughness method is used in combination with the tensile stress criterion and confirms the ability of the model to take into account the surface roughness effects in triggering the cavitation inception. As our best knowledge, this is the first attempt in this field.

Cavitation Instability

Cavity closure is characterized by a two-phase flow field, sudden change in flow characteristics and unsteady flow regime. Using several turbulence models, we have highlighted the strong interactions between the main flow and the local phenomena at the cavity closure region. The suitable models to reproduce the unsteady flow are those using an accurate filtering technique to capture correctly the large eddies or taking into account the compressibility effects of the mixture in turbulence modelling.

The main mechanisms of the cavity instability in our case are found to be the occurrence of the reentrant jet at the cavity closure. This instability occurs at a certain cavity length where the cavity closure is located at the high pressure gradient region. The phenomenon is found to be cyclic, and parallel to the main cavity shedding, local phenomena related to the structure of the shed transient cavities are observed making the lift and pressure signals very random. For lower cavitation numbers, the cavity shedding is the dominant phenomenon in the system leading to a clear dominant frequency, while for higher cavitation numbers, local phenomena associated to the system arise, leading to a wider frequency domain.

Cavitation In Hydraulic Machines

The model presented in this work predicts successfully the inception and cavitation development in a rotating inducer. Both leading edge and tip vortex cavitation were predicted. An analysis based on the energy balance shows that major reasons of the head drop are related to the torque generation reduction and the losses induced by the change in flow structure. Energy and rothalpy evolutions in the machine have located the sensitive zone of the throat to be the location of the flow field disorganization .

Local flow analysis proves that extend of the cavitation to the throat reduces the channel section entrance. The fluid is accelerated in the non-blocked part, and is the origin of cavitation occurrence on the opposite blade. These phenomena explain the torque reduction, because the cavity defines a minimum pressure level. Furthermore, the presence of the cavity disorganizes the flow structure, and its wake is a region of important secondary flows. This is shown by a recirculating zone in the channel, which affects the energy transfer mechanisms leading to increased hydraulic losses.

Perspectives

The transport-equation based model with the mixture formulation accurately predicts the leading edge cavitation flow as its inception, pressure distribution, and velocity flow field. The used model is efficient in the case of hydrofoil cascade and turbomachinery, when the studied scales are recovered with this formulation. However, there are three important issues which should be clearly detailed and studied to improve the model:

Multiphase Modelling The used mixture model formulation present today the best compromise between the numerical effort and the solution accuracy for general multiphase flows. The shortcoming of this model is the homogeneous averaging procedure. The need to locate the interface is of great importance; first to control the diffusivity of the interface, and second to improve and control the interfacial transfer.

Cavitation Modelling Most of the models use empirical constants to compute the interphase mass transfer. These results are satisfactory, at least for the class of flows we are interested in, where the time scale ratio between the main flow field and the time scales governing the phase change remains in a given interval. Dedicated experimental investigations should be done to identify and quantify the main parameters controlling the phase change in order to obtain more generalized models. Other improvements could be achieved by deriving a consistent energetic model which takes into account the thermodynamic effects of the phase change and to include the vapor and gas compressibility.

Numerical Procedure The main difficulty of modelling cavitation flows is the numerical algorithm because of the discontinuities in the mixture, and local abrupt jump in the flow conditions on the one hand and to have two different scales in time and space on the other hand. Another difficulty is to have a supersonic flow in the mixture and a subsonic flow in the rest of the domain. A correct formulation of the Mach number and adapted algorithms for this kind of flow would be highly appreciable.

Toward Multi-Scale Modelling

The main cavitation models are focused on ensemble-averaged conservation equations for multiphase flows. One of the difficulties associated with such averaging are the closure relationships which are largely empirical and lead to many adjustable constants.

As in turbulence modelling where the system geometry affects the large eddy structures and makes it difficult to close with ensemble-averaged models, the same statement can be done regarding the multiphase flows.

Now, when the large-eddy and hybrid simulations for turbulence are gaining popularity, there is a hope that interface configuration for scales larger than those associated with the computational grid will be resolved and for those smaller than will be averaged. The use of fine sub-grid and adaptative grid resolution procedures as Embedded Interface, and Level Set methods should open a new way in cavitation modelling.

Appendix

Appendix A

Boundary Layer Flows

Prandtl L. (1904) has clarified the essential influence of viscosity in flows at high Reynolds numbers and shows how the Navier-Stokes equation could be simplified to yield approximate solutions for this case. The bulk of flow is nearly irrotational and the viscous force is significant only within boundary layers that line the surface of the body. In this manner there are two regions to consider even if the division between them is not very sharp:

Boundary Layer : A very thin layer in the immediate neighborhood of the body in which the velocity satisfies the non slip condition and the velocity gradient, normal to the wall is very large. In this region the very small viscosity of the fluid exerts an essential influence insofar the shear stress may assume large value

External Flow : In the remaining region no such large velocity gradients occur and the influence of viscosity is not important. In this region the flow is potential

Boundary Layer Equations

Considering two-dimensional boundary layer, developing around a mildly curved body, that held stationary in an irrotational flow. We choose a system of coordinates (x, y) that x-direction coincide with the wall and the y-direction being perpendicular to it.

In order to achieve the simplification of the equations of motion, we shall estimate the order of magnitude of each term, and assume that the thickness is very small compared with unspecified linear dimension, leading to $\delta \ll L$ and assuming :

$$\begin{array}{ll} L & \text{Typical dimension of the body} \\ \delta & \text{Typical thickness of the boundary layer} \\ C_{x\infty} & \text{Typical magnitude of the velocity of the irrotational flow} \\ C_{y\infty} & \text{Typical magnitude of the velocity component normal to the body} \end{array} \tag{A.1}$$

The Continuity Equation

$$\frac{\partial C_x}{\partial x} + \frac{\partial C_y}{\partial y} = 0 \tag{A.2}$$

The Navier-Stokes Equations

$$\begin{aligned}\frac{\partial C_x}{\partial t}+C_x\frac{\partial C_x}{\partial x}+C_y\frac{\partial C_x}{\partial y}&=-\frac{1}{\rho}\frac{\partial p}{\partial x}+\nu\left(\frac{\partial^2 C_x}{\partial x^2}+\frac{\partial^2 C_x}{\partial y^2}\right)\\ \frac{\partial C_y}{\partial t}+C_x\frac{\partial C_y}{\partial x}+C_y\frac{\partial C_y}{\partial y}&=-\frac{1}{\rho}\frac{\partial p}{\partial y}+\nu\left(\frac{\partial^2 C_y}{\partial x^2}+\frac{\partial^2 C_y}{\partial y^2}\right)\end{aligned} \tag{A.3}$$

and reduced to the simplified form:

$$\begin{aligned}\frac{dC_x}{dt}+C_x\frac{dC_x}{dx}+C_y\frac{dC_x}{dy}&=-\frac{1}{\rho}\frac{\partial p}{\partial x}+\nu\frac{\partial^2 C_x}{\partial y^2}\\ \frac{\partial p}{\partial y}&=0\end{aligned} \tag{A.4}$$

with the assumptions:

$$\delta \ll L \qquad \frac{C_{x\infty}}{L}\approx\frac{C_{y\infty}}{\delta} \qquad \delta\approx\sqrt{\frac{\nu L}{C_{x\infty}}}=\frac{L}{\sqrt{Re}} \tag{A.5}$$

Finally, the simplified Navier-Stokes equations, known as Prandtl's boundary layer equations are [124; 110; 28]:

$$\begin{aligned}\frac{\partial C_x}{\partial x}+\frac{\partial C_y}{\partial y}&=0\\ \frac{\partial C_x}{\partial t}+C_x\frac{\partial C_x}{\partial x}+C_y\frac{\partial C_x}{\partial y}&=-\frac{1}{\rho}\frac{\partial p}{\partial x}+\nu\frac{\partial^2 C_x}{\partial y^2}\end{aligned} \tag{A.6}$$

with the boundary conditions:

$$y=0 \qquad C_x=C_y=0 \tag{A.7}$$

$$y=\infty \qquad C_x=C_{x\infty}(x,t) \tag{A.8}$$

Evaluating the pressure gradient at the edge of the boundary layer using Euler's equation for the incident irrotational flow, we can write the equations as:

$$\begin{aligned}\frac{\partial C_{x\infty}}{\partial t}+C_{x\infty}\frac{\partial C_{x\infty}}{\partial x}&=-\frac{1}{\rho}\frac{\partial p}{\partial x}\\ \frac{\partial C_x}{\partial t}+C_x\frac{\partial C_x}{\partial x}+C_y\frac{\partial C_x}{\partial y}&=\frac{\partial C_{x\infty}}{\partial t}+C_{x\infty}\frac{\partial C_{x\infty}}{\partial x}+\nu\frac{\partial^2 C_x}{\partial y^2}\end{aligned} \tag{A.9}$$

Computation of the Boundary Layer Flows

Although the boundary layer equations have been simplified, as compared to Navier-Stokes equations, they are still difficult from the mathematical resolution point of view. It is also important to notice that NS equations are of elliptic type with respect to the coordinates, whereas Prandtl's boundary layer equations are parabolic. It is a consequence of the simplifying assumptions in the boundary layer theory. The equations provides us with a system of two parabolic nonlinear partial differential equations with respect to the arc length that may be resolved numerically using standard space-marching, or finite difference methods.

Boundary Layer Differential Formulation (BLD)

For this formulation, we used the Wilcox program [153], which is a 2D and axisymmetric, compressible boundary-layer program for laminar, transitional and turbulent boundary layers. The program uses conventional Leevy-Lees variables, and a second order Blottner (1974) variable grid method as numerical procedure.

The governing equations in body-oriented coordinates (s, n) of mass and momentum and mean energy are (simplified 2D formulation is given below instead of the axisymmetric formulation of Wilcox):

$$\begin{aligned} \frac{\partial}{\partial s}(\rho C_x) + \frac{\partial}{\partial n}(\rho C_y) &= 0 \\ (\rho C_x)\frac{\partial C_x}{\partial s} + \rho C_y \frac{\partial C_x}{\partial n} &= \frac{dp}{ds} + \frac{\partial}{\partial n}\left(\mu \frac{\partial C_x}{\partial n} + \rho\tau\right) \\ (\rho C_x)\frac{\partial h}{\partial s} + \rho C_y \frac{\partial h}{\partial n} &= C_x \frac{dp}{ds} + \mu\left(\frac{\partial C_x}{\partial n}\right)^2 + \rho\varepsilon + \frac{\partial}{\partial n}\left[\left(\frac{\mu_l}{Pr_l} + \frac{\mu_t}{Pr_t}\right)\frac{\partial h}{\partial n}\right] \end{aligned} \tag{A.10}$$

The perfect-gas law is used as the equation of state and the fluid is assumed calorically perfect so that:

$$p = \rho R T \qquad \text{and} \qquad h = c_p T \tag{A.11}$$

where C_x, C_y are the stream-wise and normal mass-averaged velocity components; ρ, the fluid density; h, the enthalpy; τ, the specific Reynolds shear stress; Pr_l, Pr_t, the laminar and turbulent Prandtl numbers ; and T , the mass averaged temperature.

Algebraic Baldwin-Lomax Turbulence Model

It uses the Boussineq Eddy-viscosity approximation to compute the Reynolds stress tensor as the product of an eddy viscosity and the mean strain-rate tensor. For computational simplicity, the eddy viscosity is often computed in terms of mixing length.

The Baldwin-Lomax model (1978) was formulated for use in computations where boundary-layer proprieties such as δ ,δ^* and C_e are difficult to determine. The model uses a two-layer model, and the eddy viscosity is given for the inner and outer layer [153].

k-ω and Stress-ω Turbulence Models

For both k-ω and Stress-ω models, the dissipation ε , is given by:

$$\varepsilon = \beta^* \omega k \tag{A.12}$$

where k is the kinetic energy and ω is the specific dissipation rate. The equations for k and ω applicable to the boundary layers are :

$$\rho C_s \frac{\partial k}{\partial s} + \rho C_n \frac{\partial k}{\partial n} = \rho\tau \frac{\partial C_s}{\partial n} - \beta^* + \frac{\partial}{\partial n}\left[(\mu + \sigma^* \mu_t)\frac{\partial k}{\partial n}\right] \tag{A.13}$$

$$\rho C_s \frac{\partial \omega}{\partial s} + \rho C_n \frac{\partial \omega}{\partial n} = \frac{\omega}{k}(\alpha\rho\tau \frac{\partial C_s}{\partial n} - \rho k \omega \beta) + \frac{\partial}{\partial n}\left[(\mu + \sigma \mu_t)\frac{\partial \omega}{\partial n}\right] \tag{A.14}$$

For the k-ω model. The Reynolds shear stress is given by

$$\rho\tau = \alpha\mu_t \frac{\partial C_x}{\partial n} \tag{A.15}$$

For the Stress-ω model. The Reynolds shear stress is computed by a set of equations:

$$\rho C_s \frac{\partial \tau}{\partial s} + \rho C_n \frac{\partial \tau}{\partial n} = \frac{\partial}{\partial n}\left[(\mu + \sigma^* \mu_t)\frac{\partial \tau}{\partial n}\right] - C_1 \beta^* \rho \omega \tau + \left[(1-\hat{\alpha})\sigma_y - \hat{\beta}\sigma_x + \frac{2}{3}(1 - \hat{\alpha} - \hat{\beta} + \frac{3}{4}\hat{\gamma})k)\right]\rho \frac{\partial C_s}{\partial n} \tag{A.16}$$

$$\rho C_s \frac{\partial \sigma_x}{\partial s} + \rho C_n \frac{\partial \sigma_x}{\partial n} = \frac{\partial}{\partial n}\left[(\mu + \sigma^* \mu_t)\frac{\partial \sigma_x}{\partial n}\right] - C_1 \beta^* \rho \omega \sigma_x + \frac{2}{3}\left[2(1-\hat{\alpha}) + \hat{\beta}\right]\rho\tau \frac{\partial C_s}{\partial n} \tag{A.17}$$

$$\rho C_s \frac{\partial \sigma_y}{\partial s} + \rho C_n \frac{\partial \sigma_y}{\partial n} = \frac{\partial}{\partial n}\left[(\mu + \sigma^* \mu_t)\frac{\partial \sigma_y}{\partial n}\right] - C_1 \beta^* \rho \omega \sigma_y - \frac{2}{3}\left[2(1-\hat{\alpha}) + 2\hat{\beta}\right]\rho\tau \frac{\partial C_s}{\partial n} \tag{A.18}$$

Quantities δ_x and δ_y are the stress deviator components. Closure coefficients for fully turbulent incompressible flow (subscript ∞) are given in chapter **??**. If low-Reynolds number correction are excluded from the models we use the same constants ($\Phi = \Phi_\infty$). Low-Reynolds corrections of the k-ω and Stress-ω can be found in [153].

Transformed Equations

The boundary-layer equations are singular at the leading edge of a body. As mentionned, conventional Levy-Lees variables (ξ, η) are used to remove this singularity. Body oriented physical coordinates (s, n) are related to transformed coordinates according to:

$$d\xi = \rho_e C_{xe} \mu_e ds \qquad d\eta = \frac{\rho_e C_{xe} dn}{\sqrt{2\eta}} \tag{A.19}$$

The relations between derivatives in the physical (s, n) and transformed (ξ, η)coordinate system are as follows:

$$\begin{aligned} \left(\frac{\partial}{\partial s}\right)_n &= \rho_e C_{xe} \mu_e \left(\frac{\partial}{\partial \xi}\right)_\eta + \left(\frac{\partial n}{\partial s}\right)_n \left(\frac{\partial}{\partial \eta}\right)_\xi \\ \left(\frac{\partial}{\partial n}\right)_n &= \frac{\rho_e C_{xe}}{\sqrt{e\xi}} \left(\frac{\partial}{\partial \xi}\right)_\eta + \left(\frac{\rho}{\rho_e}\right) \left(\frac{\partial}{\partial \eta}\right)_\xi \end{aligned} \tag{A.20}$$

The dependent variables and the transformed equations for the turbulence modelling can be found in [153].

Compressibility Effect

The Wilcox [153] boundary layers computation program is developed for compressible flows. The input parameters are the fluid proprieties and stagnation point parameters (pressure, Temperature, Mach number). For our case, using an incompressible fluid, the simplifications and adaptations are obtained as follows [95; 120; 42].

From the energy equation of a perfect gas:

$$c_p T + \frac{C^2}{2} = c_p T_0 \tag{A.21}$$

and from gas perfect law:

$$\frac{p^{\frac{\gamma-1}{\gamma}}}{T} \tag{A.22}$$

we can obtain:

$$\frac{C^2}{2} = c_p \left(T_0 - T\right) = c_p T_0 \left(1 - \left(\frac{p}{p_0}\right)^{\frac{\gamma-1}{\gamma}}\right) \tag{A.23}$$

where suffix "0" refers to stagnation conditions. The influence of compressibility can be illustrated by using Mach number and noting that:

$$a^2 = \gamma R T = (\gamma - 1) c_p T \tag{A.24}$$

we obtain:

$$\frac{T}{T_0} = 1 + \left(\frac{\gamma - 1}{2}\right) M^2 \tag{A.25}$$

$$\frac{p_0}{p} = \left(1 + \left(\frac{\gamma - 1}{2}\right) M^2\right)^{\frac{\gamma}{\gamma-1}} \tag{A.26}$$

For subsonic flow $\left(\frac{\gamma-1}{2} M^2 \ll 1\right)$ the right hand may be expanded by the binomial theorem:

$$\begin{aligned} \frac{p_0}{p} &= \left\{1 + \frac{\gamma}{2} M^2 + \frac{\gamma}{8} M^4 + \frac{\gamma(2-\gamma)}{48} M^6 + \ldots\right\} \\ p_0 - p &= \frac{p\gamma M^2}{2} \left\{1 + \frac{1}{4} M^2 + \frac{2-\gamma}{24} M^4 + \ldots\right\} \\ &= \frac{pC^2}{2} \left\{1 + \frac{1}{4} M^2 + \frac{2-\gamma}{24} M^4 + \ldots\right\} \end{aligned} \tag{A.27}$$

Comparing this equation to incompressible fluid equations, the bracket quantity in Eq. A.27 represents the effect of compressibility (so-called the Compressibility Factor) .

For our case, and by setting isothermal conditions ($\gamma = 1 + \varepsilon$), the compressibility factor affect the pressure difference as follow for our computations:

$C_{\text{ref}} = 20\, m/s$	$M = 0.06321$	Compressibility Factor = 1.001
$C_{\text{ref}} = 30\, m/s$	$M = 0.09482$	Compressibility Factor = 1.002

As a result, with this analysis, we can use the incompressible BLD solution algorithm in the case of incompressible flows (water in our case) without altering the computation physics.

Boundary Layer Integral Formulation (BLI)

The method is an approximate one, based on the idea of satisfying the differential equations of boundary layer flow only in the average and over the boundary layer thickness. This is obtained as an integral of the equations of motion of the boundary layer thickness. We have used the X-foil [M5] program, developed by Drela [48; 47], which employs the standard compressible integral momentum and kinetic energy shape parameter equations:

$$\begin{aligned} \frac{d\theta}{d\xi} + (2 + H - M_e^2)\frac{\theta}{C_e}\frac{dC_e}{d\xi} &= \frac{C_f}{2} \\ \theta\frac{dH^*}{d\xi} + (2H^{**}(1-H)))\frac{\theta}{C_e}\frac{dC_e}{d\xi} &= 2C_D - H^*\frac{C_f}{2} \end{aligned} \tag{A.28}$$

The closure equations are the formulations of the Falkner-Skan one-parameter profile family for the laminar flow, and an equation from Whitifield (1978) for the density shape parameter H^{**} . The turbulent closure relations are derived using the skin-friction and velocity profile formulas of Swaford (1983) [48; 47].

For the compressibility , Xfoil uses the Kàrmàn-Tsien [47] correction for the compressibility formulation. The compressible speed Q and the pressure coefficient Cp in a compressible flow are approximately determined from the incompressible flow values. Setting the Mach number equal to zero gives automatically the incompressible formulation.

The general X-foil methodology and viscous/inviscid coupling can be found in [47]. Further details about the boundary layer formulation in [48], and the specific blunt trailing edge treatment in [46].

Appendix B

Analytical Flow Around Parabola Body

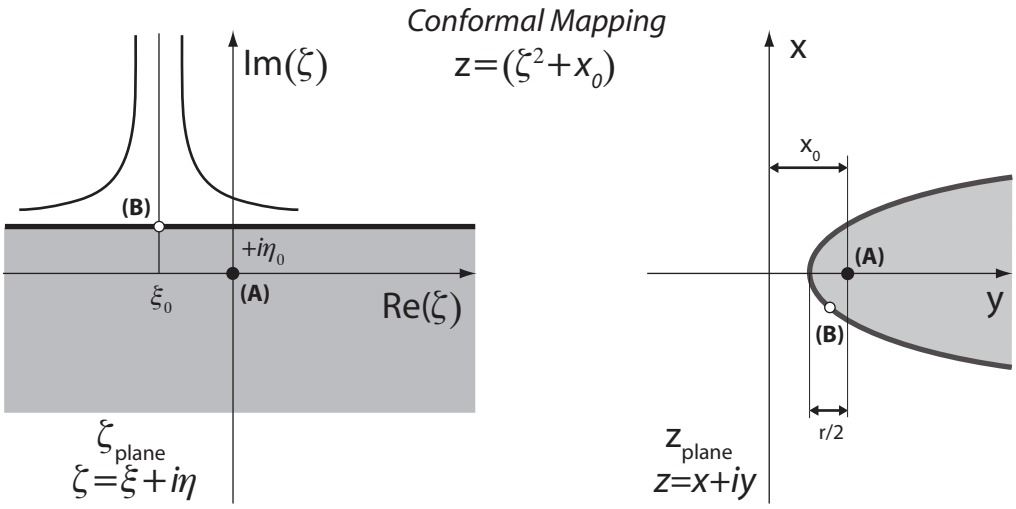

Figure B.1: Parabola conformal mapping

The parabola conformal mapping transforming the ζ plane to z plane is given by :

$$z = \frac{1}{2}(\zeta^2 + x_0) \tag{B.1}$$

where; x_0 is the parabola shift parameter and $r/2 = \sqrt{\eta_0}/2$, is the parabola radius.
From the complex potential theory; a flow with a stagnation point is defined by:

$$f(\zeta) = \frac{1}{2}(\zeta - \zeta_0)^2 = \frac{1}{2}(\zeta + \zeta_0 - i\eta_0^2) \tag{B.2}$$

The parabola conformal mapping is given by $z(\zeta)$ and the flow with a stagnation point by $f(\zeta(z)) \equiv F(z)$. The complex velocity potential can derived for the flow around the parabola as:

$$f' \equiv \frac{df}{d\zeta} = \frac{df}{dz}\frac{dz}{d\zeta}$$

Special Cases ($\eta_0 = 1$, $X_0 = 1$) : Tuck et al. [145], conformal mapping: $Z = \frac{1}{2}(\zeta^2 + 1)$
($\eta_0 = \sqrt{R}$, $X_0 = 0$) : Haddad et al. [71], conformal mapping: $Z = \frac{1}{2}(\zeta^2)$

Analytical Solution and Complex Potential

We consider the two-dimensional laminar, inviscid and incompressible flow with constant fluid proprieties over a parabolic body such as schematically represented in fig. B.1

Complex Velocity Potential

The parabola conformal mapping is given by:

$$z(\zeta) = \frac{1}{2}(\zeta^2 + x_0) \rightarrow \zeta(z) = (2z - x_0)^{1/2} \tag{B.3}$$

and the potential flow with stagnation point by:

$$f(\zeta) = \frac{1}{2}(\zeta - \zeta_0)^2 = \frac{1}{2}(\zeta + \zeta_0 - i\eta_0^2) \tag{B.4}$$

with the initial value $\zeta_0 = \sqrt{r}(-\beta + i)$ for the stagnation point. The potential can be written as:

$$f(\zeta) = \frac{1}{2}(\zeta - \zeta_0)^2 = \frac{1}{2}(\zeta + \beta\sqrt{r} - i\sqrt{r})^2 \tag{B.5}$$

From the complex velocity potential and using Eq. (B.5) and the value of ζ_0 :

$$F(z) = \frac{1}{2}\left(\zeta(z) + \sqrt{r}(\beta - i)\right)^2 = \frac{1}{2}\left(\sqrt{2z - r_0} + \sqrt{r}(\beta - i)\right)^2 \tag{B.6}$$

which gives with the stagnation point formulation:

$$F(z) = \left(z + \sqrt{2z - x_0}\sqrt{r}(\beta - i) + \frac{(\beta - i\sqrt{r})}{2} + x_0\right) \tag{B.7}$$

and can be expressed as:

$$F(z) = \left(z + (2z - x_0) + \sqrt{r}(\beta - i) + const.\right) \tag{B.8}$$

Dimensionless Formulation

The dimensionless formulation is made with respect to the parabola nose radius r, as proposed by Tuck et al. [145]. The dimensionless conformal mapping can be expressed as:

$$Z = \frac{z}{r} = \frac{1}{2}\left(\left(\frac{\zeta}{\sqrt{r}}\right)^2 + \frac{x_0}{r}\right) \tag{B.9}$$

with the variable change:

$$Z = \frac{z}{r} \qquad X = \frac{x}{r} \qquad Y = \frac{y}{r} \qquad X_0 = \frac{x_0}{r} \tag{B.10}$$

The complex velocity potential is then defined as:

$$F(Z) = F\left(\frac{z}{r}\right) = r(Z + (2Z - X_0)^{1/2}(\beta - i)) \tag{B.11}$$

and the complex velocity as:

$$F'(Z) = \frac{1}{r}F'\left(\frac{z}{r}\right) = C_{ref}(1 + (2Z - X_0)^{-1/2}(\beta - i)) \tag{B.12}$$

These equations describe the flow around a parabola body. The geometry of the body suggests that the problem be formulated in terms of parabolic coordinates. The parabolic coordinates (ζ, η) are related to the dimensionless Cartesian coordinates(x, y) by:

$$\begin{cases} X = \frac{x}{r} = \frac{\zeta^2 - \eta^2}{2r} + \frac{X_0}{2} \\ Y = \frac{y}{r} = \frac{\zeta\eta}{r} \end{cases} \tag{B.13}$$

Note that the line $\eta = iR^{1/2}$ in (ζ) plane is the parabola body surface in (z) plane, and defined as:

$$x(y) = \frac{(y^2 - r^2 + rx_0)}{2r} \quad \rightarrow \quad y^2(x) = 2rx + r^2 - rx_0 \tag{B.14}$$

or, in dimensionless coordinates:

$$X(Y) = \frac{(Y^2 - 1 + X_0)}{2} \quad \rightarrow \quad Y^2(x) = 2X + 1 - X_0 \tag{B.15}$$

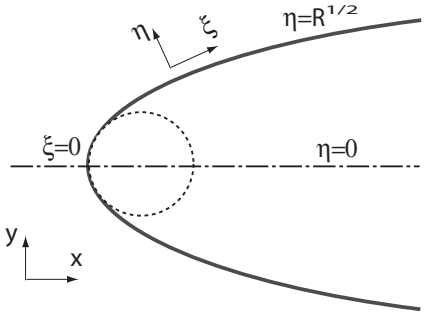

Figure B.2: Schematic representation of the parabolic body in Cartesian coordinates

Analytical Solution

The analytical computation of flow around a parabola and results post-processing is made via numerical program. We generate the mesh in the parabolic coordinates (ζ, η) including the mesh stretching in both directions if needed. A conformal mapping gives the transformed grid in the Cartesian domain (x,y). The complex velocity potential is then computed including the results in all the domain of the: Stream and Potential functions, the different speed components, and the pressure coefficient distribution. The results as the speed and pressure along the parabola body can be extracted. The grid generation is only used as post processing facility. The grid which is perfectly orthogonal (conformal mapping) will be used later for a CFD computation.

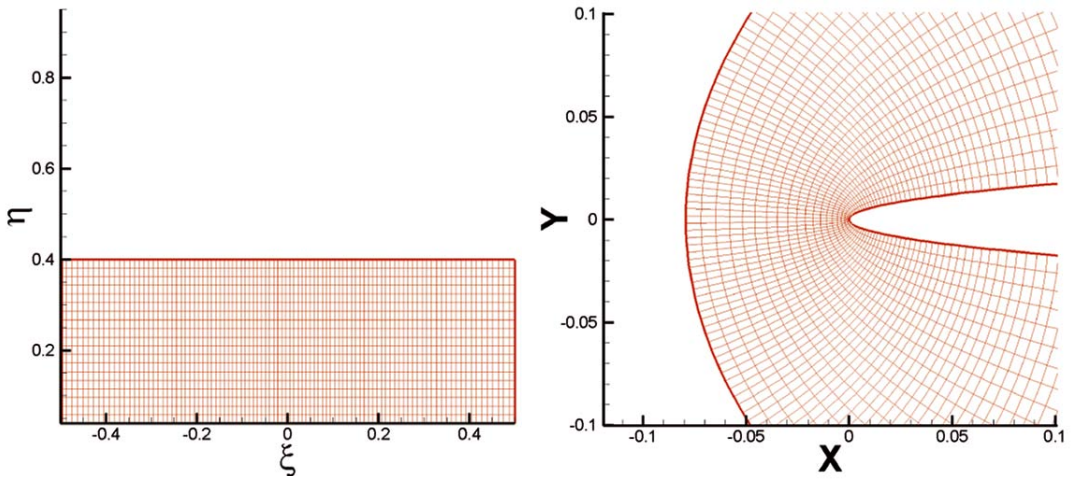

Figure B.3: Grid conformal mapping, left; parabolic coordinates ($\zeta = \xi + i\eta$), right: cartesian orthogonal coordinates ($z = x + iy$)

Complex Velocity Potential

The complex potential is defined as:

$$F(Z) \equiv F\left(\frac{z}{r}\right) = rC_\infty \left(Z + (2Z - X_0)^{1/2}(\beta - i)\right) \tag{B.16}$$

By introducing the variable $Z = X + iY$, the complex potential can be written as :

$$F(Z) = \phi + i\psi = rC_\infty \left((X + \beta a + b) + i(Y + \beta a - a)\right) \tag{B.17}$$

with:

$$\begin{cases} a = \frac{y}{b} \\ b = \left(\frac{-(2X-X_0)+\left((2X-X_0)^2+4Y^2\right)^{1/2}}{2}\right)^{1/2} \end{cases} \tag{B.18}$$

The complex velocity potential is defined as:

$$F'(Z) = \frac{1}{2}F'\left(\frac{z}{r}\right) = C_\infty(1 + (2Z - X_0)^{-1/2}(\beta - i)) \tag{B.19}$$

By introducing the variable $Z = X + iY$ and rearranging the terms, we have the form:

$$F'(Z) = C_x - iC_y = C_\infty \left(\left(1 + \frac{\beta b + a}{a^2 + b^2}\right) + i\left(-\frac{\beta b + a}{a^2 + b^2}\right)\right) \tag{B.20}$$

Fig.B.3 shows the Cartesian grid (parabolic domain) and its transformation by conformal mapping to the parabolic domain (x, y). Fig.B.4 presents the streamlines in the ζ and z planes for the zero angle of attack around a parabola. Obviously, in this case the flow is symmetric with respect to the abscissa.

A flow at an angle of attack is shown in fig. B.5, corresponding to $\beta = 1$ in Eq. B.17 and B.20. The flow losses the symmetry and the stagnation point moves on the "pressure side". One can easily see that the streamline and pressure patterns strongly resembles the flow around the leading edge of a hydrofoil at an angle of attack.

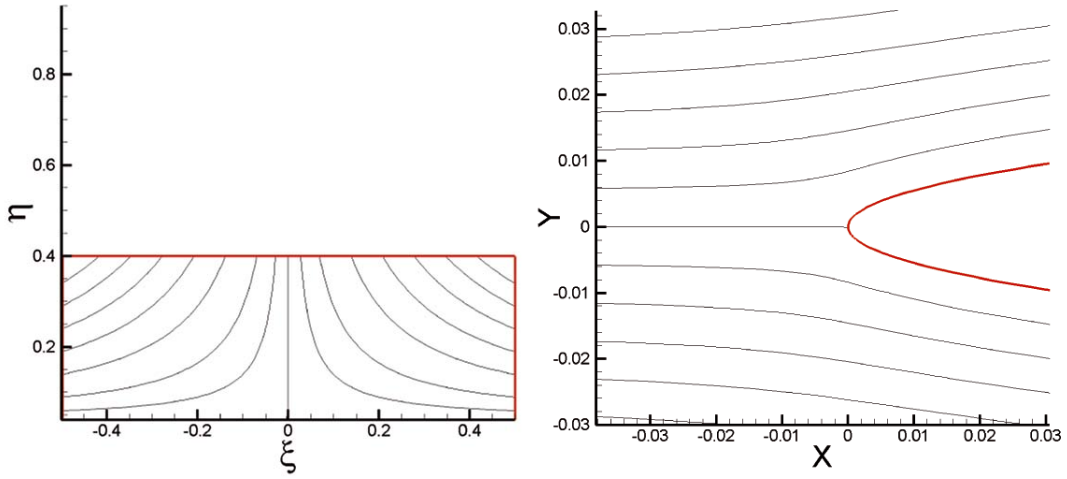

Figure B.4: Conformal mapping and streamlines around the parabola body, $\beta = 0$

Flow on the Parabola Body

The general complex potential velocity is given by Eq. B.19, with ($2X = Y^2 - 1 + X_0$) and ($\eta = \sqrt{r}$) on the parabola surface. Using these simplifications, at the parabola body, the Complex velocity will be:

$$\text{Complex velocity:} \quad F'(Z) = C\frac{Y+\beta}{Y+i} \tag{B.21}$$

$$\text{Velocity magnitude:} \quad Q = C\frac{Y+B}{(Y^2+1)^{1/2}} \tag{B.22}$$

At the maximum pressure location (Stagnation point s_0): Q=0:

$$U(s_0) = Q = 0, \qquad Y(s_0) = -\beta \tag{B.23}$$

At the minimum pressure location : $\frac{dQ}{dY} = 0$

$$Y(s_1) = 1/\beta, \qquad Cp_{min} = -\beta^2 \qquad C_{max} = C\sqrt{1+\beta^2} \tag{B.24}$$

The tangential and normal speeds are :$C_T = \eta C_x - \zeta C_y \qquad C_N = \zeta C_x + \eta C_y$

As an example, fig. B.6 shows the pressure and velocity distribution on the parabola body at an angle of attack corresponding to $\beta = 1$ function of the dimensionless curvilinear abscissa (The origin is the geometric symmetry point of the parabola ($x = 0, y = 0$)). The pressure filed shows the locations of the stagnation point and the minimum pressure. One can remark that the special case of $\beta = 1$ giving a symmetric pressure distribution. The velocity filed also reported in fig. B.6 shows a decelerating flow in the pressure side of the parabola, and a zero velocity at the stagnation point. In the pressure side, the flow is accelerated to the minimum pressure location and then decelerated after. The special value of $R = 1.5\ 10^{-3}$ is chosen to fit the NACA0009 nose.

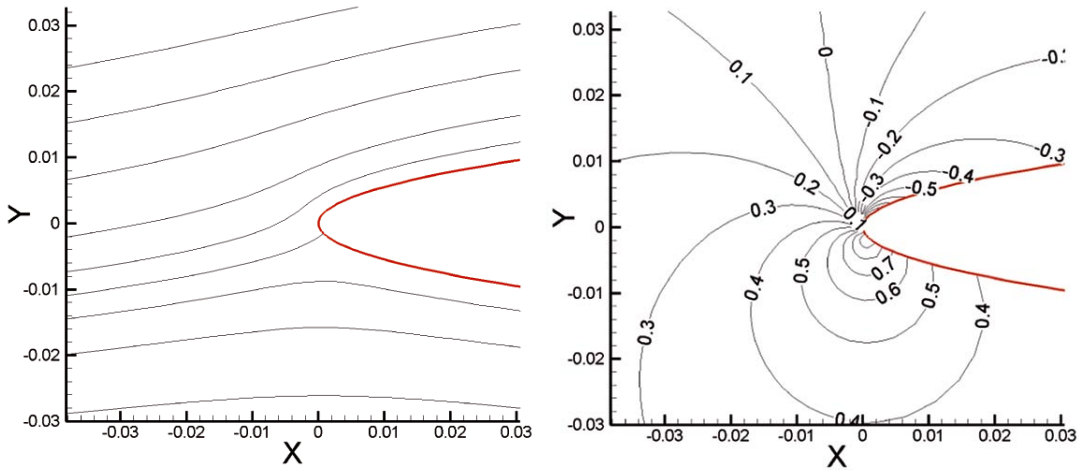

Figure B.5: Streamlines and C_p distribution at an angle of attack (β=1)

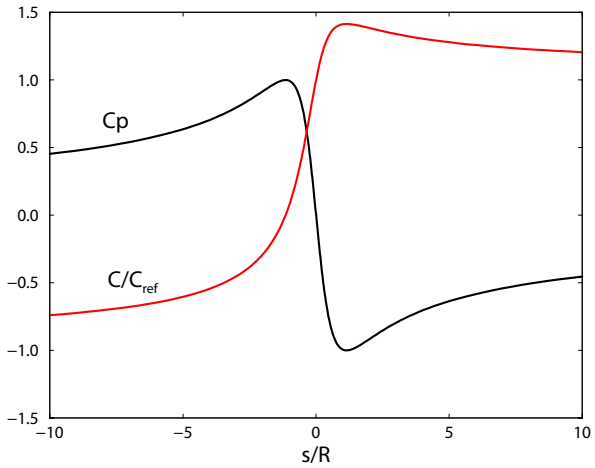

Figure B.6: Dimensionless velocity and pressure coefficient distribution on the parabola body for β =1, r=1.51 10^{-3} m, function of the dimensionless curvilinear abscissa s/r

Bibliography

References

[1] Ahuja, V., Hosangadi, A., and Arunajatesan, S. Simulations of Cavitating Flows Using Hybrid Unstructured Meshes. *Trans. of ASME, J. Fluids Eng. 123* (June 2001), 331–340.

[2] Alajbegovic, A., Grogger, H. A., and Philippe, H. Calculation of transient cavitation in nozzle using two-fluid model. In *12th Annual Conf. on Liquid Atomization and Spray Systems* (Indianapolis, may 16-19 1999), pp. 373–377.

[3] Arakeri, V. H. Viscous effects on the position of cavitation separation from smooth bodies. *J. Fluid Mech. 68* (1975), 779–800.

[4] Arakeri, V. H., and Acosta, A. J. Viscous effects on the inception of cavitation on axisymmetric bodies. *Trans. of ASME, J. Fluids Eng. 95* (1973), 519–546.

[5] Arndt, R. E. A. Cavitation in fluid machinery and hydraulic structures. *Ann. Rev. Fluid Mech. 13* (1981), 273–328.

[6] Arndt, R. E. A. Recent advances in cavitation research. *Advances in Hydroscience 12*, Tecnical paper N°110 (1981), 1–78. ISBN 0-12-021812-7.

[7] Arndt, R. E. A., and Ippen, A. T. Rough surface effects on cavitation inception. *Trans. of ASME, J. Basic Eng. 90*, D (1968), 249–261.

[8] Aït-Bouziad, Y., Guennoun, F., Farhat, M., and Avellan, F. Numerical simulation of leading edge cavitation over 2d hydrofoil. In *Proc. of the 21st IAHR Symposium on Hydraulic Machinery and Systems* (Lausanne, Switzerland, September 9-12 2002), pp. 403–410.

[9] Aït-Bouziad, Y., Guennoun, F., Farhat, M., and Avellan, F. Numerical simulation of leading edge cavitation. In *Proc. of FEDSM'03 4th ASME-JSME Joint Fluids Engineering Conference* (Honolulu, Hawaii, USA, July 6-11 2003), no. FEDSM2003-45312.

[10] Aït-Bouziad, Y., Guennoun, F., Farhat, M., Kueny, J.-L., Miyagawa, K., and Avellan, F. Physical modelling and simulation of leading edge cavitation : Application to an industrial inducer. In *Proce. of the 5th Int. Symposium on Cavitation CAV2003* (Osaka, Japan, November 1-4 2003), no. Cav03-OS-67-014.

[11] Aït-Bouziad, Y., Guennoun, F., Farhat, M., Kueny, J.-L., Miyagawa, K., and Avellan, F. Experimental and numerical cavitation flow analysis of

an industrial inducer. In *Proceedings of the 22nd IAHR Symposium on Hydraulic Machinery and Systems* (Stockholm, Sweden, June 29 - July 2, 2004 2004).

[12] Athavale, M. M., Li, H.-Y., Jiang, Y., and Singhal, A. K. Application of the full cavitation model to pumps and inducers. *Int. J. of Rotating Machinery 8* (2002), 45–56.

[13] Ausoni, P., Farhat, M., Avellan, F., Escaler, X., and Egusquisa, E. Cavitation effects on fluid structure interaction in the case of a 2d hydrofoil. In *Proc. ASME FEDSM2005, Houston, TX, FEDSM05-77477* (June 19-23, 2005).

[14] Avellan, F., and Dupont, P. Etude du sillage d'une poche de cavitation partielle se développant sur un profil hydraulique bi-dimensionnel). *La Houille Blanche*, 7 (august 1988), 507–524.

[15] Avellan, F., Dupont, P., and Rhyming, I. Generation mechanism and dynamics of cavitation vortices downstream of a fixed leading edge cavity. In *17th O.N.R Symposium on Naval Hydrodynamics* (The Hague, Netherlands, aug. 29 - sept. 1 1988), Office of Naval Research, pp. 317–329.

[16] Avellan, F., Henry, P., and Ryhming, I. L. A new high-speed cavitation tunnel for cavitation studies in hydraulic machinery. In *Proc. of Int. Symposium on Cavitation Research Facilities and Techniques* (1987), ASME Winter Annual Meeting, pp. 49–60.

[17] Bakir, F., Rey, R., Gerber, A. G., Belamri, T., and Hutchinson, B. Numerical and experimental investigations of the cavitating behavior of an inducer. *Int. J. of Rotating Machinery 10* (2004), 15–25.

[18] Balahadji, B., Franc, J. P., and Michel, J. M. Cavitation in the rotational structures of a turbulent wake. *J. Fluid Mech. 287* (march 1995), 282–403.

[19] Bordier, Y.-A., Farhat, M., and Avellan, F. Etude du code de prediction de la cavitation par poches attachées: Application au cas de l'inducteur snecma. Tech. rep., LMH-EPFL, Jul. 2000. Confidential.

[20] Borel, L. *Thermodynamique et Energétique*. Presses polytechnique romandes, ISBN 2-88074-025-8, 1984.

[21] Bourdon, P. *Détection Vibratoire de l'érosion de cavitation des turbines Francis*. PhD thesis, EPFL, 2000 (N°2295).

[22] Brackbill, J., Kothe, D., and Zemach, C. A continuum method for modelling surface tension. *J Comput. Physics 100* (1992), 335–354.

[23] Brennen, C., and Acosta, A. J. Theoretical, quasi-static analysis of cavitation compliance in turbopumps. *J. Space Craft 10*, 3 (march 1973), 175–180.

[24] Brennen, C., Meissner, C., Lo, E., and Hoffman, G. Bubbly flow model for the dynamic characteristics of cavitating pumps. *Trans. of ASME J. Fluid Eng. 104* (december 1982), 428–433.

[25] Brennen, C. E. *Cavitation and Bubble Dynamics*. Oxford University Press, New-York, 1995.

[26] Callenaere, M., Franc, J.-P., and Michel, J.-M. Influence of cavity thickness and pressure gradient on the unsteday behavior of partial cavities. In *Proc. Third Int. Symposium on Cavitation* (Grenoble, France, April 7-10 1998), J. Michel and H. Kato, Eds., vol. 1, pp. 209–214.

[27] Callenaere, M., Franc, J.-P., Michel, J.-M., and Riondet, M. The cavitation instability induced by the development of a re-entrant jet. *J. Fluid Mech 444* (2002), 223–256.

[28] Cebeci, T., and Bradshaw, P. *Momentum Transfer in Boundary Layers*. McGraw-HILL Series in Thermal and Fluid Engineering. Hemisphere Publishing Corp., 1997. ISBN 0-07-010300-3.

[29] CFX-AEA Canada Ltd. *CFX-TASCflow 2.12: Theory Documentation*. Waterloo, Canada.

[30] CFX-ANSYS Canada Ltd. *CFX-5.7: Solver Theory*. Canada, 2004.

[31] Chahine, G., Duraiswami, R., and Rebut, M. Analytical and numerical study of large bubble/bubble and bubble/flow interactions. In *19 th ONR Symp. of Naval Hydrodynamics* (Seoul, 1992), pp. 195–206.

[32] Chahine, G. L. Strong interactions bubble/bubble and bubble/flow. In *Bubble Dynamics and Interface Phenomena* (1994), Kluwer Academic Publishers, pp. 195–206.

[33] Chen, Y., and Heister, S. D. A numerical treatment for attached cavitation. *Trans. of ASME, J. Fluids Eng. 116* (september 1994), 613–618.

[34] Chen, Y., and Heister, S. D. Two-phase modeling of cavitated flows. *Computers and Fluids 24*, 7 (1995), 799–809. Elsevier Science Ltd.

[35] Chen, Y., and Heister, S. D. Modeling hydrodynamic nonequilibrium in cavitating flows. *Trans. of ASME, J. Fluids Eng. 118* (march 1996), 172–178.

[36] Cooper, P. Analysis of single and two phase flows in turbopump inducers. *Trans. of ASME, J. Eng. Power 104* (1967), 577–588.

[37] Coutier-Delgosha, O. *Modelisation des Ecoulement Cavitants: Etude des Comportements Instationnaires et Application Tridimensionnelle aux Turbomachines*. PhD thesis, LEGI-INPG, Grenoble, France, Nov. 2001. UMR 5519.

[38] Coutier-Delgosha, O., and Astolfi, J. A. Numerical prediction of the cavitating flow on a two-dimensional symmetrical hydrofoil with a single fluid model. In *5th Int. Symposium on Cavitation, Workshop on physical models and CFD tools for computation of cavitating flows* (2003).

[39] Coutier-Delgosha, O., Fortes-Patella, R., and Reboud, J.-L. Evaluation of the turbulence model influence on the numerical simulations of unsteady cavitation. *Trans. of ASME, J. Fluids Eng. 125* (january 2003), 38–45.

[40] Coutier-Delgosha, O., Fortes-Patella, R., Reboud, J.-L., Hofmann, B., and Stoffel, B. Experimental and numerical studies in a centrifugal pump with two-dimensional curved blades in cavitating condition. *Trans. of ASME, J. Fluids Eng. 125* (november 2003), 970–978.

[41] Couty, P. *Physical Investigation of Cavitation Vortex Collapse.* PhD thesis, EPFL, 2001 (N°2463).

[42] CURRIE, I. J. *Fundamental Mechanics of Fluids*, 3rd edition ed., vol. Part IV; Compressible Flow of Inviscid Fluids of *Mechanical Engineering series.* McGraw-HILL International Editions, 1979. ISBN 0-07-113242-2.

[43] Delannoy, Y., and Kueny, J.-L. Two phase flow approach in unsteady cavitation modelling. In *ASME Cavitation and Multi-phase Flow Forum* (1990), vol. 109, pp. 153–159.

[44] Deshpande, M., Feng, J., and 1994, C. L. M. Cavity flow predicitions based on the euler equations. *Trans. of ASME, J. Fluids Eng. 116* (march 1994), 36–44.

[45] Deshpande, M., Feng, J., and 1997, C. L. M. Numerical modeling of the thermodynamic effects of cavitation. *Trans. of ASME, J. Fluids Eng. 119* (june 1997), 420–427.

[46] Drela, M. Integral boundary layer formulation of blunt trailing edge. *AIAA-89-2200* (August 1989).

[47] Drela, M. Xfoil: An analysis and design system for low reynolds number airfoils. In *Conf. on low Reynolds number Aerodrodynamics* (University of notre dame, 1989).

[48] Drela, M., and Giles, M. B. Viscous-inviscid analysis of transonic and low reynolds number airfoils. *AIAA Journal 25*, 10 (oct. 1987), 1347–1355.

[49] Dumont, N., Simonin, O., and Habchi, C. Numerical simulation of cavitating flows in diesel injectors by homogeneous equilibrium modeling approach. In *4th Int. Symposium on Cavitation* (Pasadena, California, USA, june 20-23 2001), no. CAV2001:B6.005.

[50] Dupont, P. *Étude de la Dynamique d'une Poche de Cavitation Partielle en Vue de la Prédiction de l'Érosion dans les Turbomachines Hydrauliques.* PhD thesis, École Polytechnique Fédérale de Lausanne, 1991 (N°931).

[51] Dupont, P., and Avellan, F. Numerical computation of a leading edge cavity. In *Proceedings of the Cavitation Symposium "Cavitation'91", 1st ASME-JSME Fluid Eng. Conf.* (1991), vol. 116.

[52] Duttweiler, M. E., and Brennen, C. Surge instability on a cavitating propeller. *J. Fluid Mech. 458* (2002), 133–152.

[53] Edwards, J. R., Franklin, R. K., and Liou, M.-S. Low-diffusion flux-splitting methods mfor real fluid flows with phase transition. *AIAA Journal 38*, 9 (september 2000), 1624–1633.

[54] Farhat, M. *Contribution à l'étude de l'érosion de Cavitation: Mécanismes Hydrodynamiques et Prédiction*. PhD thesis, École Polytechnique Fédérale de Lausanne, 1994 (N°1273).

[55] Farhat, M., and Avellan, F. On the detachment of a leading edge cavitation. In *4th Int. symposium on cavitation* (Pasadena, California, june 2001).

[56] Farhat, M., Bourdon, P., Lavigne, P., and SIMONEAU, R. The hydrodynamic aggressiveness of cavitating flows in hydro turbines. In *Proc. of the ASME FEDSM-97* (Vancouver, Canada, June 22-26 1997).

[57] Farhat, M., Guennoun, F., and Avellan, F. The leading edge cavitation dynamics. In *Proc. of ASME FEDSM, Fluids Eng. Division Meeting* (2002).

[58] Ferziger, J. H., and Perić, M. *Computational Methods for Fluid Dynamics*, 2nd ed. Springer, 1999.

[59] Franc, J.-P., Avellan, F., Belhadji, B., Billard, J.-Y., Briançon-marjolet, L., Fréchou, D., Fruman, D. H., Karimi, A., Kueny, J.-L., and Michel, J.-M. *"La Cavitation: Mécanismes Physiques et Aspects Industriels"*. Collection Grenoble Sciences. Presse Universitaires de Grenoble, Grenoble, 1995.

[60] Franc, J. P., Janson, E., Morel, P., C., R., and Riondet, M. Visualizations of leading edge cavitation in an inducer at different temperatures. In *3rd symposium on Cavitation* (2001). CAV2001:B7.002.

[61] Franc, J.-P., and Michel, J.-M. Attached cavitation and the boundary layer: Experimental investiguation and numerical treatment. *J. Fluid Mech. 154* (1985), 63–90.

[62] Franc, J. P., Rebattet, C., and Coulon, A. An experimental investigation of thermal effects in a cavitating inducer. *Trans. of ASME, J. Fluids Eng. 126* (september 2003), 716–723.

[63] Fruman, D. H. Review of thermal effects in the cavitation of inducers. In *4th Int. Conf. on Launcher Technology "Space Launcher Liquid Propulsion"* (Liege Belgium, december 3-6 2002).

[64] Fruman, D. H., Benmansour, I., and Sery, R. Estimation of the thermal effects on cavitation of ceyogenic liquids. In *Cavitation and Multiphase Flow Forum* (1991), F. ASME, Ed.

[65] Fruman, D. H., Reboud, J.-L., and Stutz, B. Estimation of thermal effects in cavitation of thermosensible liquids. *Int. J. Heat Mass Transfer 42* (1999), 3195–3204.

[66] Furness, R., and Hutton, S. Experimental and theoritical studies of two dimensional fixed type cavity. *Trans. of ASME, J. Fluids Eng.* (1975), 515–522.

[67] Gopalan, S., and Katz, J. Flow structure and modelling issues in the closure region of attached cavitation. *Phys. of Fluids 12(4)* (2000), 186–192.

[68] Greitzer, E. M. The stability of pumping systems — the 1980 freeman scholar lecture. *Trans. of ASME, J. Fluids Eng. 103* (june 1981), 193–242.

[69] Guennoun, F. *Etude physique de la cavitation du bord d'attaque.* PhD thesis, EPFL, 2005.

[70] Guennoun, F., Aït-Bouziad, Y., Farhat, M., Pereira, F., and Avellan, F. Experimental investigation of a particular traveling bubble cavitation. In *Proce. of the 5th Int. Symposium on Cavitation CAV2003* (Osaka, Japan, November 1-4 2003), no. Cav03-OS-67-012.

[71] Haddad, O. M., and Corke, T. C. Boundary layer receptivity to free-stream sound on parabolic bodies. *J. Fluid Mech. 368* (1998), 1–26.

[72] Hirschi, R. *Prédiction par Modélisation Numérique Tridimensionnelle des Effets de la Cavitation à Poche dans les Turbomachines Hydrauliques.* PhD thesis, École Polytechnique Fédérale de Lausanne, 1998 (N°1777).

[73] Hirschi, R., Dupont, P., and Avellan, F. Centrifugal pump performance drop due to leading edge cavitation : Numerical predictions compared with model tests. *Trans. of ASME, J. Fluids Eng. 120* (december 1997), 705–711.

[74] Hirschi, R., Dupont, P., and Avellan, F. Centrifugal pump performance drop due to leading edge cavitation : Numerical predictions compared with model tests. In *ASME Fluid Eng. Division, Summer meeting* (Grenoble, France, june 1997), pp. 22–26.

[75] Horigushi, H., Watanabe, S., and Tsujimoto, Y. Theoretical analysis of cavitation in inducers with unequal blades with alternate leading edge cutback. *Trans. of ASME, J. Fluids Eng. 412* (1982), 412–424.

[76] Iga, Y., Nohml, M., Goto, A., and Ikohagi, T. Numerical analysis of cavitation instabilities arising in the three-blade cascade. *Trans. of ASME, J. Fluids Eng. 126* (2004), 219.429.

[77] Ishii, M. *Thermo-Fluid Dynamic Theory of Two-Phase Flow.* Eyrolles, 1975.

[78] Jones, S., Evans, G., and Galvin, K. Bubble nucleation from gas ccavities — a review. *Advances in Colloid and Interface Science 80* (1999), 27–50.

[79] Joseph, D. D. Cavitation and the state of stress in a flowing liquid. *J. Fluid Mech. 366* (1998), 367–378.

[80] Kamijo, K., Shimura, T., and Watanabe, M. An experimental investigation of cavitating inducer instability. *ASME paper 77-WA/FW*, 14 (1977).

[81] Kawanami, Y., Kato, H., and Yamagushi, H. Three dimensional charachristics of the cavities formed on a two-dimensional hydrofoil. In *Proc. Third Int. Symposium on Cavitation* (Grenoble, France, April 7-10 1998), J. Michel and H. Kato, Eds., vol. 1, pp. 191–196.

[82] Keller, A. P. Cavitation scale effects empirically found relations and the correlation of cavitation number and hydrodynamic coefficients. In *4th Int. Symposium on Cavitation* (Pasadena, California, USA, june 20-23 2001), no. CAV2001: Lecture 1.

[83] Knapp, R. T., Daily, J. W., and Hammitt, F. G. *Cavitation.* McGraw-Hill Inc., New York, 1970.

[84] Kubota, A., Kato, H., and Yamaguchi, H. A new modelling of cavitating flows : A numerical study of unsteady cavitation on a hydrofoil section. *J. Fluid Mech. 240* (March 1992), 59–96.

[85] Kueny, J.-L., and Desclaux, J. Theoretical analysis of cavitation in rocket engine inducers. In *ASME Pumping Machinery Symposium* (San DiegoA, 1989).

[86] Kunz, R. F., Boger, D. A., Stinebring, D. A., Chyczewski, T. S., and Gibeling, H. J. A preconditioned navier-stokes method for two-phase flows with application to cavitation prediction. *AIAA-99-3329* (1999), 1–9.

[87] Kunz, R. F., Boger, D. A., Stinebring, D. A., Chyczewski, T. S., Gibeling, H. J., and Govindan, T. R. Multi-phase cfd analysis of natural and ventilated cavitation about submerged bodies. In *Proc. of FEDSM'99* (San Francisco California USA, july 18-23 1999), 3rd ASME-JSME Joint Fluids Engineering Conf., Ed., no. FEDSM99-7364.

[88] Kunz, R. F., Boger, D. A., Stinebring, D. A., Chyczewski, T. S., Gibeling, H. J., Venkateswaran, S., and Govindan, T. R. A preconditioned navier-stokes method for two-phase flows with application to cavitation prediction. *Computers & Fluids 29* (2000), 849–875. Elsevier Svcience Ltd.

[89] Kunz, R. F., Lindau, J. W., Billet, M. L., and Stinebring, D. R. Multiphase cfd modeling of developed and supercavitating flows. Applied Research Laboratory State College, None.

[90] Kunz, R. F., Lindau, J. W., Kaday, T. A., and Peltier, L. J. Unsteady rans and detached eddy simulations of cavitating flow over a hydrofoil. In *5th Int. Symposium on Cavitation, , Workshop on physical models and CFD tools for computation of cavitating flows* (Osaka Japan3, november 1-4 2003), no. Cav03-OS-1-12.

[91] Laberteaux, K. R., and Ceccio, S. L. Flow in the closure region of closed partial attached cavitation. In *Proc. Third Int. Symposium on Cavitation* (Grenoble, France, April 7-10 1998), J. Michel and H. Kato, Eds., vol. 1, pp. 197–202.

[92] Lakshminarayana, B. Fluid dynamics of inducers—a review. *Trans. of ASME, J. Fluids Eng. 104* (1982), 411–427.

[93] Lemonnier, H., and Rowe, A. Another approach in modelling cavitating flows. *J. Fluid Mech. 195* (1988), 557–580.

[94] Lindau, J. W., Kunz, R. F., Boger, D. A., Stinebring, D. A., and Gibeling, H. J. High reynolds number, unsteady, multiphase cfd modeling of cavitating flows. *Trans. of ASME, J. Fluids Eng. 124* (september 2002), 607–616.

[95] Massey, B. S. *Mechanics of Fluids*, 4th van nostrand reinhold company ed., vol. Chap 12; Flow with appreciable change of density. Litton Educational Publishing, N.Y., 1979. ISBN-0-442-30247-9 ELBS.

[96] McKeel, S. A. *Numerical Simulation of the Transition Region in Hypersonic Flow*. PhD thesis, Virginia Polytechnic Institute and State University, Blacksburg, Virginia, 1996.

[97] Medvitz, R. B., F.Kunz, R., A.Boger, D., W.Lindau, J., Yocum, A. M., and Pauley, L. L. Performance analysis of cavitating flows in centrifugal pumps using multiphase cfd. *Trans. of ASME, J. Fluids Eng. 124* (june 2002), 377–383.

[98] Menter, F. Two-equation eddy-viscosity turbulence models for engineering applications. *AIAA-Journal 32*, 8 (1994).

[99] Menter, F., and Kuntz, M. Adaptation of eddy-viscosity turbulence models to unsteady separated flow behind vehicles. In *Proc. Conf. The Aerodynamics of Heavy Vehicles: Trucks, Busses and Trains* (RAsilomar, Ca, 2002).

[100] Menter, F., and Kuntz, M. Development and application of a zonal des turbulence model for cfx-5. Tech. rep., ANSYS-CFX Canada Ltd., CFX-Validation Report, CFX-VAL17/0503.

[101] Merkle, C. L., Feng, J. Z., and Buelow, P. E. Computational modeling of the dynamics of sheet cavitation. In *Proc. Third Int. Symposium on Cavitation* (Grenoble, France, april 1998), pp. 307–311.

[102] Moore, R. D., and Ruggeri, R. S. Prediction of thermodynamic effects on develloped cavitation based on liquid-hydrogen and freon-114 data in scaled venturis. Tech. Rep. TN D-4899, NASA, 1969.

[103] Numachi, F., Oba, R., and Chida, I. Effect of surface roughness on cavitation performance of hydrofoils; report ii. *Trans. of ASME, J. Basic Eng.* (1965).

[104] Osher, S., and Fedkiw, R. P. Level set methods: An overview and some recent results. *J. Comput. Phys. 169*, 2 (may 2001), 463–502.

[105] Pereira, A., McGrath, G., and Joseph, D. D. Flow and stress induced cavitation in a journal bearing with axial throughput. *J. of Tribology 123* (october 2001 2001), 742–754.

[106] Pereira, F. *Prédiction de l'érosion de la cavitation: Approche Energétique*. PhD thesis, École Polytechnique Fédérale de Lausanne, 1997 (N°1592).

[107] Pope, S. B. *Turbulent Flows*. Cambridge University Press, 2000.

[108] Popinet, S., and Zaleski, S. Bubble collapse near a solid boundary: A numerical study of the influence of viscosity. *J. Fluid Mech. 464* (2002), 137–163.

[109] Pouffary, B., Fortes-Patella, R., and Reboud, J. Numerical simulation of cavitating flow around a 2d hydrofoil: A barotropic approach. In *5th Int. Symposium on Cavitation, Workshop on physical models and CFD tools for computation of cavitating flows* (Osaka Japan3, november 1-4 2003), no. Cav03-OS-1-005.

[110] Pozrikidis, C. *Introduction to Theoritical and Computational Fluid Dynamics*, vol. Chap. 8; Boundary Layers. Oxford University Press, 1997.

[111] Qin, Q., Song, C. C. S., and Arndt, R. E. A. A near field study of a non-cavitating and cavitating hydrofoil. In *5th Int. Symposium on Cavitation* (Osaka, Japan3, november 1-4 2003), no. Cav03-GS-9-003.

[112] Qin, Q., Song, C. C. S., and Arndt, R. E. A. A numerical study of an unsteady turbulent wake behind a cavitating hydrofoil. In *5th Int. Symposium on Cavitation* (Osaka, Japan, november 1-4 2003), no. Cav03-GS-9-001.

[113] Qin, Q., Song, C. C. S., and Arndt, R. E. A. A virtual single-phase natural cavitation model and its application to cav2003 hydrofoil. In *5th Int. Symposium on Cavitation, Workshop on physical models and CFD tools for computation of cavitating flows* (Osaka, Japan, november 1-4 2003), no. Cav03-OS-1-004.

[114] Rapposelli, E., and d'Agostino, L. A barotropic cavitation model with thermodynamic effects. In *5th International Symposium on Cavitation; CAV03)* (Osaka, Japan, november 1-4 2003), no. Cav03-GS-16-004.

[115] Reboud, J.-L., and Delannoy, Y. Two-phase flow modelling of unsteady cavitation. In *Proc. 2nd Int. symposium on cavitation* (Tokyo, Japan, April 1994), H. Kato, Ed., pp. 203–208.

[116] Reboud, J.-L., Stutz, B., and Coutier-Delgosha, O. Two-phase flow structure of cavitation : Experiment and modeling of unsteady effects. In *Proc. Third Int. symposium on cavitation* (Grenoble, France, April 1998), vol. 1, pp. 39–44.

[117] Rouse, H., and McNown, J. S. Cavitation and pressure distribution, head forms at zero angle of yaw. Tech. rep., Iowa Institute of Hydraulic Research, Iowa City, 1948.

[118] Rubin, S. Longitudinal instability of liquid rockets due to propulsion feedback (pogo). *J. Space Craft 3*, 8 (august 1966), 1188–1195.

[119] Ruggeri, R. S., and Moore, R. D. Method for prediction of pump cavitation performance for various liquids, liquid temperatures, and rotative speeds. Tech. Rep. TN D-5292, NASA, 1969.

[120] Ryhming, I. L. *Dynamique des Fluides*, 2nd ed. Presses Polytechniques et Universitaires Romandes, Lausanne, 1991.

[121] Saito, Y., Nakamori, I., and Ikohagi, T. Numerical analysis of unsteady vaporous cavitating flow around a hydrofoil. In *5th Int. Symposium on Cavitation, Workshop on physical models and CFD tools for computation of cavitating flows* (Osaka Japan3, november 1-4 2003), no. Cav03-OS-1-006.

[122] Sauer, J., and Schnerr, G. H. Unsteady cavitating flow – a new cavitation model based on modified front capturing method and bubble dynamics. In *Proc. of FEDSM'00 4th Fluids Engineering Summer Conference* (2000, FEDSM2000-11095).

[123] Scardovelli, R., and Zaleski, S. Direct numerical simulation of free-surface and interfacial flow. *Annu. Rev. Fluid Mech. 31* (1999), 567–603.

[124] Schlichting, H. *Boundary-Layer Theory*, 7th ed. McGraw-Hill Series in Mechanical Engineering. McGraw-Hill, New-York, Etats-Unis, 1979.

[125] Senocak, I. *Computational Methodology for the Simulation Turbulent Cavitating Flows*. PhD thesis, University of Florida, 2002.

[126] Senocak, I., and Shyy, W. A pressure-based method for turbulent cavitating flow computations. In *31st AIAA Fluid Dynamics Conference and Exhibit* (Anaheim, june 11-14 2001), vol. AIAA 2001-2907.

[127] Senocak, I., and Shyy, W. Evaluation of cavitation models for navier-stokes computations. In *Proc. of FEDSM'02* (Montreal, Canada, july 14-18 2002), vol. FEDSM2002-31011.

[128] Senocak, I., and Shyy, W. A pressure-based method for turbulent cavitating flow computations. *J. Comput. Phys. 176* (2002), 363–383.

[129] Shen, Y., and Dimotakis. The influence of surface cavitation on hydrodynamic forces. In *Proc 22nd ATTC* (1989), pp. 44–53.

[130] Shin, B. R., and Ikohagi, T. A numerical study of unsteady cavitating flows. In *Proc. Third Int. Symposium on Cavitation* (Grenoble, France, April 7-10 1998), J. Michel and H. Kato, Eds., vol. 2, pp. 301–306.

[131] Singhal, A. K., Athavale, M. M., Li, H., and Jiang, Y. Mathematical basis and validation of the full cavitation model. *Trans. of ASME, J. Fluids Eng. 124* (2002), 617–624.

[132] Singhal, A. K., Athavale, M. M., and Yang, H. Recent advances (ventilated cavitation) with the full cavitation model. In *ECCOMAS 2004, European Congress on Computational Methods in Applied Sciences andEngineering* (2004).

[133] Singhal, A. K., Li, H. Y., Athavale, M. M., and Jiang., Y. Mathematical basis and validation of the full cavitation model. In *ASME FEDSM'01* (New Orleans, Louisiana, USA, 2001).

[134] Singhal, A. K., Vaidya, N., and Leonard, A. D. Multi-dimensional simulation of cavitating flows using a pdf model for phase change. In *The 1997 ASME FEDSM* (june 22-26 1997), no. FEDSM'97-3272.

[135] Song, C. C. S., and HE, J. Numerical simulation of cavitating flows by single-phase flow approach. In *Proc. Third Int. Symposium on Cavitation* (Grenoble, France, April 7-10 1998), J. Michel and H. Kato, Eds., vol. 2, pp. 295–300.

[136] Spalart, P., Jou, W.-H., Strelets, M., and Allmaras, S. Comments on the feasibility of les for wings, and on a hybrid rans/les approach. In *1st AFOSR Int. Conf. On DNS/LES* (Ruston, LA. In Advances in DNS/LES, C. Liu and Z. Liu Eds., Greyden Press, Colombus, OH, Aug.4-8 1997).

[137] Strelets, M. Detached eddy simulation of massively separated flows. *AIAA Paper 2001-0879* (1997).

[138] Stutz, B. *Analyse de la Structure Diphasique et Instationnaire de Poches de Cavitation.* PhD thesis, Institut National Polytechnique de Grenoble, France, 1996.

[139] Stutz, B., and Reboud, J. Two-phase flow structure of sheet cavitation. *Phys. Fluids 9*, 12 (1992), 3678–3686.

[140] Tani, N., and Ngashima, T. Numerical analysis of cryogenic cavitating flow on hydrofoil: Comparison between water and cryogenic fluids. In *4th Int. Conf. on Launcher Technology "Space Launcher Liquid Propulsion"* (Liege Belgium, december 3-6 2002).

[141] Tassin, L., and Ceccio, S. L. Examination of the flow ear the leading edge of attached cavitation. part 1; detachment of two-dimensional and axisymmetric cavities. *J. Fluid Mech. 376* (1998), 61–90.

[142] Tryggvason, G., Bunner, B., Esmaeeli, A., Juric, D., Al-Rawahi, N., Tauber, W., Han, J., Nas, S., and Janz, Y.-J. A front-tracking method for the computations of multiphase flow. *J. Compt. Physics 169* (2001), 708–759.

[143] Tsujimoto, Y., Kamijo, K., and Yoshida, Y. A theoretical analysis of rotating cavitation in inducers. *Trans. of ASME, J. Fluids Eng. 115* (1993), 135–141.

[144] Tsujimoto, Y., Yoshida, Y., Mekawa, Y., Watanabe, S., and Hashimoto, T. Observations of oscillating cavitation of an inducer. *Trans. of ASME, J. Fluids Eng. 119* (december 1997), 775–781.

[145] Tuck, E. O., and Dostovalova, A. A criterion for leading-edge separation. *J. Fluid Mech. 222* (1991), 33–37.

[146] Tuck, E. O., and Dostovalova, A. Aerofoils nose shapes delaying leading-edge separation. *The Aeronautical Journal 104* (2000), 433–437.

[147] Tulin, M. Linearized theory for flows about lifting foils at zero cavitation number. Tech. Rep. C-638, DTMB Report, Navy Department, Washington, D.C., february 1955.

[148] Vaidyanathan, R., Senocak, I., Wu, J., and Shyy, W. Sensitivity evaluation of a transport-based turbulent cavitation model. *Trans. of ASME J. Fluids Eng. 125* (may 2003), 447–458.

[149] Ventikos, Y., and Tzabiras, G. A numerical method for the simulation of steady and unsteady cavitating flows. *Computers and Fluid 29* (2000), 63–88.

[150] Versteegand, H. K., and Malalasekera, W. *An introduction to Computational Fluid Dynamics: The finite volume method*, vol. Pearson Prentice Hall. 1995.

[151] Watanabe, S., and Brennen, C. E. Dynamics of a cavitating propeller in a water tunnel. *Trans. of ASME, J. Fluids Eng. 125* (march 2003), 283–292.

[152] Watanabe, S., Tsujimoto, Y., Franc, J.-P., and Michel, J.-M. Linear analyses of cavitation instabilities. In *Proc. Third Int. Symposium on Cavitation* (Grenoble, France, April 7-10 1998), J. Michel and H. Kato, Eds., vol. 1, pp. 347–352.

[153] Wilcox, D. C. *Turbulence Modeling for CFD*, 2nd edition ed. DCW Industries Inc., 1998.

[154] Wu, J., Utturkar, Y., and Shyy, W. Assessment of modeling strategies for cavitating flow around a hydrofoil. In *5th Int. Symposium on Cavitation, Workshop on physical models and CFD tools for computation of cavitating flows* (Osaka Japan3, november 1-4 2003), no. Cav03-OS-1-007.

[155] Wu, T. Y.-T. A free streamline theory for two-dimensional fully cavitated hydrofoils. *J. Math. Phys. 35* (1956), 236–265.

[156] Yamagushi, H., and Kato, H. On application of nonlinear cavity flow theory to tick foil sections. In *Proc. Of Second Int. Conf. on Cavitationg* (1983), pp. 167–174.

[157] Yu Po-Wen, S. L. C., and Tryggvason, G. The collapse of a cavitation bubble in shear flows-a numerical study. *Phys. Fluids 7*, 11 (november 1995), 2608–2616.

[158] Zhang, S., Duncan, J. H., and Chahine, G. L. The bahavior of a cavitation bubble near a rigid wall. In *Bubble Dynamics and Interface Phenomena* (1994), Kluwer Academic Publishers, pp. 429–436.

Manuals

[M1] ANSYS Canada Ltd.
CFX-5.7© Documentation, Canada, 2004

[M2] ANSYS Canada Ltd.
ICEM CFD 4.3© User Guide, Canada, 2004

[M3] AEA Technology
CFX-TASCflow© V 2.12 Primer Documentation, Waterloo, Canada, 2000

[M4] AEA Technology
CFX-TurboGrid© V 1.2 User Guide, Canada, 2000

[M5] MIT Aero Astro and Aerocraft Inc., Mark Drela and Harold Youngren
Xfoil© 6.94 User Guide, 2001

[M6] Tecplot Amtec Engineering, Inc.
Tecplot© Ver.10, Bellevue, Washington, 2003

[M7] Fluent Inc.
Fluent6© Documentation, 2003

[M8] Numeca International,
Fine™/Turbo 6.2 User Guide, 2004

[M9] CFD-RC Group
CFD-ACE+ Users Manual, 2001

[M10] CD-adapco Group
Star-CD 3.15 User Guide, 2003

[M11] DynaFlow Inc., Georges L. Chahine
DynaFS©; Bubble and Free Surface Hydrodynamic Interaction Modelling,1988

Index

Youcef AÏT BOUZIAD

LMH - EPFL
Av. de Cour 33bis
CH-1007 Lausanne (VD)

Tél. Prof.: +41 21 693 3917
Portable: +41 78 639 9937
E-mail: youcef.aitbouziad@epfl.ch

Né le 13 mars 1975
Célibataire

FORMATION

2001-2005:	**Doctorat ès sciences techniques** École Polytechnique Fédérale de Lausanne (EPFL), Suisse
1999-2000:	**DEA en conversion de l'énergie** ENSAM de Paris - Université de ParisVI, France
1998-1999:	**DEA en Mécanique. Option: Mécanique des fluides et transferts** Université de BordeauxI, France
1992-1997:	**Ingénieur d'état en hydraulique** Ecole Nationale Polytechnique d'Alger, Algérie
1989-1992:	**Baccalauréat type C (mathématiques)**

EXPÉRIENCES

2001-2005:	**École Polytechnique Fédérale de Lausanne (EPFL), Suisse.** **Laboratoire de Machines Hydrauliques (LMH).** Thèse de Doctorat: Modélisation physique et simulation numérique des écoulements en régime de cavitation: application aux machines hydrauliques
2000:	**Laboratoire d'Energétique et de Mécanique des Fluides Interne (LEMFI), Paris** DEA: Simulation numérique de ventilateurs centrifuges à action
1999:	**Laboratoire de Modélisation Avancée des Systèmes Thermiques et Ecoulements Réels (MASTER), Bordeaux** DEA: Etude de traitement et de valorisation des sédiments du réseau des eaux pluviales
1997:	**Laboratoire d'Hydraulique, ENP, Alger** PFE: Contribution à l'étude du charriage sous l'effet combiné de la houle et du courant

COMPÉTENCES INFORMATIQUES

Systèmes:	Windows, MS-DOS, Unix (IBM-AIX).
Program.:	C, Fortran.
CFD:	CFX, Fluent, Fine/Turbo, ICEM, Tecplot.
CAO:	Catia, SolidWorks.
Bureautique:	MS-Office, Latex.
Multimédia:	MS-Office, Suite Adobe, HTML.

LANGUES

Berbère	Langue maternelle.
Arabe	Parlé, lu et écrit: couramment.
Français	Parlé, lu et écrit: couramment.
Anglais	Parlé, lu et écrit: bien.